Chronostratigraphy of the Beaufort Formation, western Canadian Arctic Archipelago

by

Léa C. Braschi

Submitted in partial fulfilment of the requirements
for the degree of Master of Science

at

Dalhousie University
Halifax, Nova Scotia
April 2015

Dedication Page

For all those dearest to me

Table of Contents

List of Tables

List of Figures

Abstract

The Beaufort Formation (BF) braided river deposit contains exceptionally well-preserved logs, leaves, peat, insects, and vertebrate fossils that provide key evidence for Arctic environmental conditions during the Pliocene. Its wide geographic range along the western edge of the Canadian Arctic Archipelago suggests that its deposition and incision history were dictated by regional drivers of sediment transport (e.g., eustatic sea-level, permafrost thaw, ice sheet erosion, and dynamic topography). Hence, the BF provides clues about both environmental and depositional conditions, but available chronology in the last few decades has not been able to identify these as having occurred either 1) during the polar amplification of global warming (Pliocene Climate Optimum, 3.3-3.0 Ma) or 2) during the onset of northern hemisphere glaciations (Plio-Pleistocene transition, 2.6 Ma). We use cosmogenic nuclide burial dating at the southernmost BF locality (Ballast Brook on Banks Is.) to obtain: a) a minimum age of 2.72 $^{+0.34}/_{-0.24}$ (1 σ) Ma, and b) a maximum catchment-wide paleo-erosion rate of 49-86 ± 2 cm/ka. The description of a previously unreported glaciofluvial gravel (which occurs at the same stratigraphic level as a potential ice-wedge pseudomorph and coincides with the base of a previously-mapped 3-km wide cut-and-fill channel) dates the earliest evidence of CAA glaciation, at 2.72 Ma. The presence of a large channel that runs parallel to the northern coast of Banks Is. also suggests that M'Clure Strait (and the Northwest Passage) was not open at that time. Furthermore, such a large (correlative with part of the 3-km Iperk Formation offshore) and quick (49-86 ± 2 cm/ka) deposition event must have required the stripping of unconsolidated material (e.g, part of the Eureka Sound Group or Hassel and Isachsen Formations). The deposition system was likely a transport-limited system, and like the White Channel Gravels of the Yukon (Hidy et al. 2013), may have been controlled by changing climate in the Pliocene (e.g., melting permafrost, increased precipitation).

List of Abbreviations Used

AMS – Accelerator Mass Spectrometer

BF – Beaufort Formation

CAA – Canadian Arctic Archipelago

TCN – Terrestrial Cosmogenic Nuclide

BBF – Ballast Brook Formation

CAMS – Center for Accelerator Mass Spectrometry

CIS – Cordilleran Ice Sheet

DGC – Dalhousie Geochronology Center

ICP-OES – Inductively Coupled Plasma Optical Emission Spectrometer

IRD – Ice-Rafted Debris

LIS – Laurentide Ice Sheet

LLNL – Laurence Livermore National Laboratory

MAT – Mean Annual Temperature

Acknowledgements

With more gratitude and affection than I can well put down here, I owe special thanks to many people who made this experience what it really was.

I am grateful to my supervisor, John Gosse, for being a dedicated scientist and teacher and doing everything he can to be the best in what he believes in. Thank you for giving me the opportunity to be a part of this research. I have benefited greatly as a person, as a student and as a professional as a result my experience at Dalhousie.

Thank you also to Tom Lakeman for the time and effort you put into this project, and to the rest of my committee, Natalia Rybczynski and Martin Gibling, for their knowledge, expertise, and overall good will. I am sincerely appreciative for the learning opportunities you provided. I am also indebted to Boz Wing, Earth Systems Science professor at McGill University, for introducing me to the addictive world of research.

I would like to express my deep appreciation and gratitude to my many colleagues and friends who, in a diverse set of ways, have made my time in Halifax phenomenal. Annina, thank you for being someone I look up to. Thank you for your strength, your wisdom, your kindness, and for bringing the graduate student community together. Gabe – you kept me sane. I am lucky to have had you as my M.Sc. partner and office partner while at Dal. It would not have been the same experience if you had not been there to hear my rants and share yours with me. Thank you Alan for always having smart and insightful answers to my cosmo questions, and for reminding me how much I do not know. Guang, thank you for your steady support and your constantly happy, friendly face.

I am grateful to lifelong friends whose support is unending, including the core group of graduate students (Stefanie, Glenn, Jocelyn, Sam, Bertha, Janice, Ricardo,

Bertha…).Heather, you are one of the kindest people I know, thank you for being my friend, I still have so much to learn from you. Ale, thank you for reviving my need to be outdoors and on the road, and thank you for pushing my boundaries. Alaa, my dear, thank you for being so fun to be around, and so accepting of others. Mel, thank you for being non-judgemental and down to earth, thank you for your love and your patience. Al, thank you for your endless support and encouragement. Louise, it is so easy to spend time with you, your carefreeness and spontaneity is contagious, I miss you constantly. Marina, thank you for sticking around and for being my lifelong friend, I love our conversations and your creativity and thoughtfulness, you are just amazing.

Lastly, I could not ask for a more wonderful family. I realize this again and again each time we share time together. Maman, Papa, et Emélie, thank you for being individuals I truly look up to. I am in great debt to you for your love, your strength, and your kindness.

***

This project would not have been possible without the generous financial support of the W. Garfield Weston Foundation, the Canadian Museum of Nature, NSERC, the Killam Trust, the Association of Canadian Universities for Northern Studies, and the Aurora College.

Chapter 1 : Introduction

1.1 Importance of the Beaufort Formation

The Pliocene Beaufort Formation (BF) is part of a subaerially exposed, dissected wedge of unconsolidated braided river deposits that stretches 1200 km along the western Canadian Arctic Archipelago (CAA; Fyles 1990). It thickens westward towards the Beaufort Sea; previous researchers have proposed correlative deposits in the lower Iperk Sequence (using seismic profiles and biostratigraphy; Blasco *et al.* 1990, McNeil *et al.* 1990). Today, outliers of the BF (average widths of 50 km) are separated by inter-island straits (Fyles 1990; Figure 1.1). To test hypotheses regarding past erosion, transport, and deposition of sediment, including sediment fluxes to oceans during significant Earth system changes, a better understanding of the deposition and incision of the BF is needed. The BF and related sediments contain exceptionally well preserved plants, peat, insects, and vertebrate fossils (Matthews and Ovenden 1990, Matthews and Telka 1997) that have provided quantitative estimates of Arctic environmental change during the Pliocene (Ballantyne *et al.* 2010, Csank *et al.* 2011). Apparent paleoenvironmental differences across the wide geographic range of the BF and related deposits have triggered hypotheses regarding the role of latitude, continentality, and age in influencing environmental conditions during the Pliocene (e.g., Fyles 1990).

The BF is hypothesised to have been deposited along a formerly contiguous coastal plain (Tozer 1956, Trettin 1989, Fyles 1990). A contiguous coastal plain would have required the extant channels of the CAA to have been absent or much narrower than today (Fyles 1990). Such a major difference in regional physiography likely influenced contemporaneous paleoenvironments in a number of ways: (1) a more continental climate and vegetation in all or parts of the CAA, (2) a lowering of albedo from sea ice (due to increased land area), (3) a decrease in moisture supply to glaciers and ice caps, (4) a major reorganization of Arctic Ocean circulation, and (5) an increase in sediment flux to the Beaufort Sea margin (and associated isostatic subsidence).

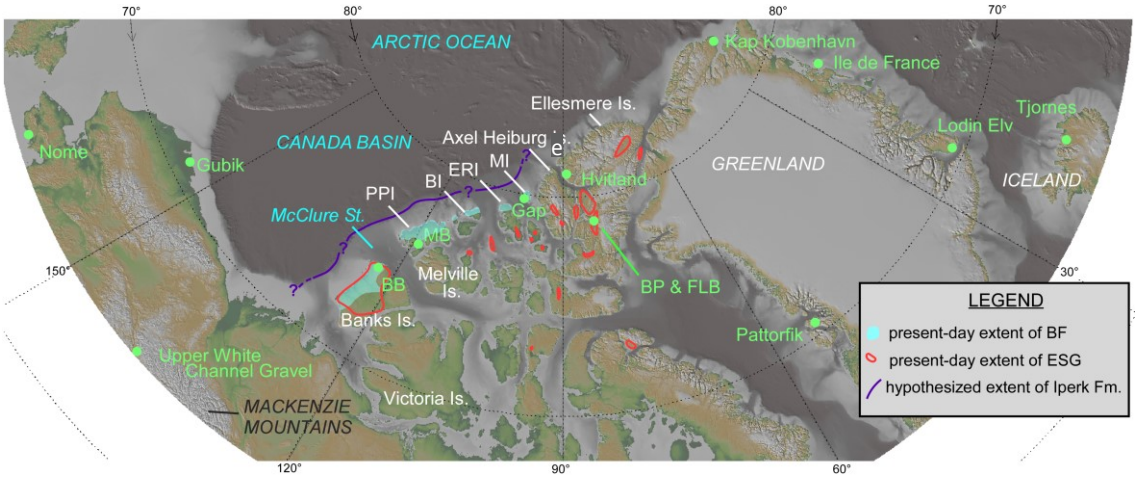

Figure 1.1 – Map of the Canadian Arctic and surrounding regions, showing the BF and related deposits. The extent of the BF (not including the High Terrace Sediments) is shown in transparent light blue (Fyles 1990). The extent of the Eureka Sound Group, a likely source material for the BF, is shown in red (after Miall 1986). The approximate extent of shelf facies in the lower Iperk Sequence offshore is shown in purple (Helwig *et al.* 2011). Island names are shown in white: PPI – Prince Patrick Island, BI – Borden Island, ERI – Ellef Ringnes Island, MI – Meighen Island. Study sites are shown in green: BB – Ballast Brook site, MB – Mould Bay site, BP – Beaver Pond site, FLB – Fyles Leaf Bed site. Basemap from GeoMappApp.

1.2 Lack of chronostratigraphy

The absolute age of the BF must be determined before previously compiled paleoenvironmental records can be fully understood and first-order hypotheses tested. For example, it is unknown whether latitudinal variations in climate or differences in the ages of the deposits account for the apparent variability in proxy records (Matthews and Ovenden 1990). Further, the pre-conditions that were necessary and the changes or events that acted as triggers for sediments to be eroded, transported, and deposited to form the BF over more than 1200 km also cannot be determined without knowing the timing and rate of deposition of the BF. For example, it is possible that the BF was deposited in less than 100 ka. Alternatively, it may have been deposited over a much longer interval (e.g., greater than 1 Ma), which would imply a significantly different set of variables responsible for its deposition. Lastly, if the BF formerly comprised a contiguous braid plain, significant dissection must have occurred, since it is now fragmented by the wide channels of the CAA. Dissection may have started at the same

time everywhere (due to a drop in relative sea-level and subsequent river incision or mantle-generated dynamic topography), or started diachronously. Therefore, establishing the temporal dynamics and spatial characteristics of sediment transport in the Pliocene is a valuable contribution towards improving our understanding of how landscape and environmental changes in the Arctic were connected to other Earth system phenomena.

Only a few facies and stratigraphic descriptions of the BF have been published (Craig and Fyles 1965, Fyles 1988, Fyles 1990, Devaney 1991, Fyles *et al*. 1991, Fyles *et al.* 1994). No studies have been published on the sedimentology and stratigraphy of the BF since 1994, although investigations on the well-preserved paleoenvironmental records of the related High Terrace Sediments on Ellesmere Is. have continued (e.g. Matthews and Fyles 2000, Ballantyne *et al.* 2010, Csank *et al.* 2011, Rybczynski *et al.* 2013). Therefore, it is unclear whether the BF contains greater facies variation than previously considered. As well, the precise stratigraphic relationship among the many localities of the BF in the CAA is unknown. Hence, in addition to chronology, a more thorough understanding of the sedimentology and stratigraphy of the BF and its correlatives is warranted.

1.3 Previous chronological studies

Although the establishment of a chronostratigraphic framework for the BF and related deposits has been a focus of research since the 1960s, the absolute ages of late Cenozoic strata on different islands of the CAA have not been determined with sufficient precision to test many of the above hypotheses (e.g., Fyles *et al.* 1994). Several of the dating techniques that have been used are restricted to the marine sediments on Meighen Is.: Sr isotope analyses on marine shells (2.5 -5.1 Ma; Kaufman *et al.* 1990), biostratigraphic correlation of foraminifera with other northern sites (younger than Miocene but older than 2.4 Ma; McNeil *et al.* 1990), association of Pacific molluscs with the opening of the Bering Strait (3 Ma; *Fyles et al.* 1991), and correlation of a marine transgression on Meighen Is. with relative sea level records from northern Alaska (older than 2.48 Ma; Brigham-Grette and Carter 1992). This previous research has been

supplemented by paleomagnetic studies of fine-grained facies of the BF and related deposits on Banks, Meighen, and Ellesmere islands (Fyles *et al.* 1994). Although multidisciplinary and broad in scope, these studies were unable to develop a robust chronostratigraphy. Thus, many fundamental questions remain unanswered, such as whether the BF represents a single phase of deposition across the western CAA. Rybczynski *et al.* (2013) demonstrated that ^{26}Al-^{10}Be terrestrial cosmogenic nuclide (TCN) burial dating can provide robust age constraints on High Arctic Pliocene sediments, improving upon previous age estimates.

1.4 Study area

The Ballast Brook locality on northwest Banks Is. offers a high potential for the successful application of TCN burial dating of the BF. It is one of the southernmost exposures of the BF and may thus comprise an instructive correlative to the dated sediments on Meighen and Ellesmere Island (Fyles 1990). Furthermore, it has the thickest and most laterally extensive stratigraphic exposures of any locality. Finally, the general stratigraphy has already been established by earlier researchers, and an abundance of paleoenvironmental research has been conducted, which will give context to TCN burial ages.

1.5 Objectives and methods

This thesis focuses on the BF exposures at Ballast Brook, Banks Is., and contributes to a collaborative research program with the long-term goal of addressing many of the outstanding questions and hypotheses outlined above. The primary objectives of this thesis are to: i) determine the age of the BF at multiple stratigraphic exposures, ii) describe the sedimentology and stratigraphy of the BF and compare new observations with previously published results, iii) provide an estimate of catchment-wide average paleoerosion rates and sediment flux rates at the time of BF deposition, and iv) consider the influence of the adjacent M'Clure Strait on the sedimentology of the BF on northern Banks Island (Figure 1.2).

Multiple techniques were attempted depending on the stratigraphy, sedimentology, and depth of the strata. These include simple burial dating (i.e. sampling the deepest possible sediments; Granger and Muzikar 2001), muon exposure profile dating (i.e. sampling up-section), and isochron burial dating (i.e. sampling below potential exposure surfaces; Balco and Rovey 2008). Sedimentological and stratigraphic observations (including texture, bedding surfaces, hiatuses, unconformities, organics, lithology, clast form and roundness, fossil flora and fauna, and lateral continuity of subunits) helped characterize depositional environments, the number of depositional events, and paleoflow directions.

1.6 Results

These investigations have resulted in a revision of previously published stratigraphy and a classification of the organic facies within the BF at Ballast Brook. Certain revisions have significant implications for CAA paleoceanography and the analysis of the landscape response to climate change. A previously unreported shift in paleoflow has been documented in the BF at Ballast Brook, which has implications for the timing of the establishment of the M'Clure Strait. A potential ice-wedge pseudomorph reveals that permafrost was at least discontinuous, like at other localities of the BF, despite the close presence of contemporaneous forests. Previous field investigations did not report glacial facies in the BF at Ballast Brook. The glacial sediments described here represent the earliest recorded presence of ice on Banks Is., and perhaps the earliest terrestrial evidence of CAA glaciation.

The geochronology of the BF sediments was challenging compared to previous TCN dating on Ellesmere and Meighen Is. The main source of difficulty was the low TCN concentration in quartz at the time of deposition. Nevertheless, a minimum age of 2.72 $^{+0.34}/_{-0.24}$ (1 σ) Ma was obtained for the BF at Ballast Brook. This allowed the dating of a previously mapped channel parallel to the northern coast of Banks, with potential implications for the timing of the last opening of the M'Clure Strait. Short-term (800-1500 years) maximum paleo-erosion rates for the catchments that sourced the BF were also calculated (49-86 ± 2 cm/ka). Catchment-wide erosion rates have never been

measured before in the Canadian Arctic. This work has provided important guidelines for future use of TCN burial dating at Ballast Brook in particular (e.g., the feasibility of sampling requirements for certain techniques).

1.7 Thesis structure

This thesis is organized into eight chapters: Chapter 2 explains the characteristics and importance of the BF and outlines the scientific uncertainties stemming from poor chronological control. Two contrasting hypotheses are presented on the former connectivity of different BF exposures, and the important aspects of the BF are discussed (chronology, paleoecology, spatial extent of the braid plain, time span and source of sediment, hypothetical causes and consequences of deposition, and incision of the braid plain). Chapter 3 discusses previous work conducted in the field area, including work on the lithology, paleoflow direction, and provenance of the sediment, physical descriptions of the organic deposits, plant assemblages and tree ring widths, biostratigraphy and comparison to other deposits, magnetostratigraphy, unconformity below the BF, and extent of the BF on Banks Island. Chapter 4 details the field geology methods and results, outlining the details of two measured sections, as well as descriptions of organic material, unconformities, and paleoflow measurements. Chapter 5 explains the TCN burial dating method, including the theoretical background, sampling methods, sample preparation and analyses, and data reduction. The TCN results, both isochron profiles and sampling up-section, are then presented. Chapter 6 discusses multiple interpretations of the TCN results and how they bear on the considered hypotheses. Chapter 6 also presents the final interpretation of the BF age at Ballast Brook, as well as calculated paleo-erosion rates. Chapter 7 discusses the geological and TCN results and their importance. Chapter 7 also details future work to be done both at Ballast Brook and in the BF and related deposits in general. Finally, Chapter 8 summarizes the primary conclusions from this study.

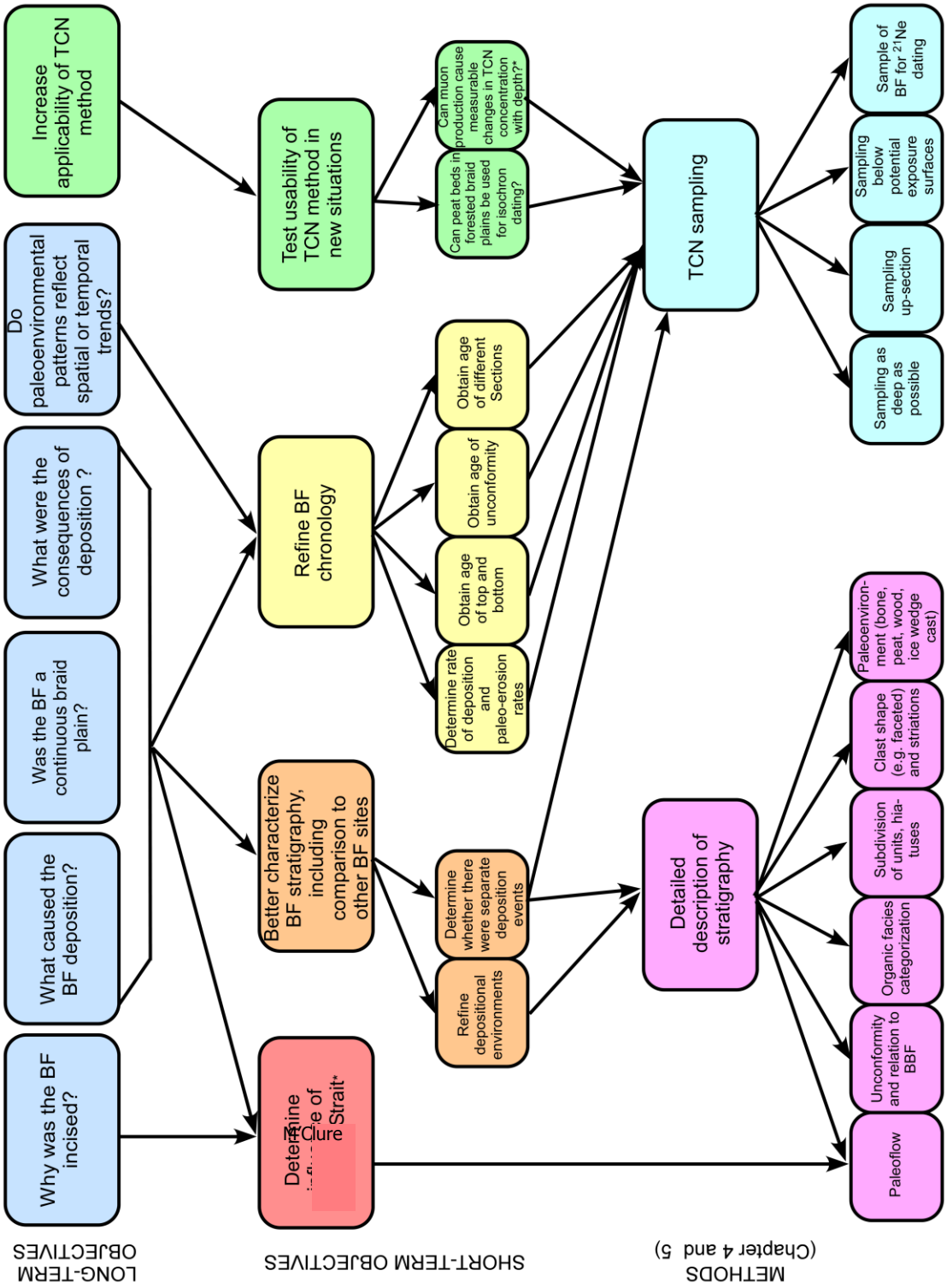

Figure 1.2 – Flow-chart of the long-term objectives, short-term objectives, and methods of the present research. The links between objectives and methods are illustrated. The asterix identifies objectives which were established after field investigations.

Chapter 2 : Background - The Beaufort Formation in the Western Canadian Arctic Archipelago

2.1 The Beaufort Formation in the context of Plio-Pleistocene global change

The Pliocene Beaufort Formation (BF) is part of a dissected wedge of unconsolidated fluvial deposits extending ~1200 km along the western CAA (Fyles 1990; Figure 1.1). Potentially correlative deposits (part of the 3 km-thick Iperk Sequence; Blasco *et al.* 1990, McNeil 1990, Helwig *et al.* 2011) thicken westward onto the Beaufort Sea Shelf and Slope and extend into Canada Basin (Mosher *et al.* 2012). Today, outliers of the BF are separated by inter-island straits and on average constitute a 50 km-wide band bordering the northwest margin of the CAA (Fyles 1990; Figure 1.1). Geological evidence for the deposition and incision of the BF provide clues about the erosion, transport, and deposition of sediment –including sediment delivery to oceans– during Earth system changes such as those that occurred during the Pliocene.

The Plio-Pleistocene boundary was a very interesting time in Earth's history when the global climate system was reorganized from a state of restricted local ice sheets on Greenland and Antarctica (Pliocene greenhouse conditions) to a state of extensive global ice sheets (Pleistocene icehouse conditions; Lisiecki and Raymo 2005, Brigham-Grette *et al.* 2013; Figure 2.1). This definition of the Plio-Pleistocene boundary has had a long and controversial history since the 1980, and is now defined (on a purely climatic change) at 2.58 Ma, within 20,000 years of the Gauss-Matuyama geomagnetic reversal (Cohen *et al.* 2014; Gibbard *et al.* 2009). The Pliocene Climate Optimum, an anomalously warm excursion from ~3.3 to 3.0 Ma (De Schepper *et al.* 2013) preceded the climate deterioration that marked the Pliocene-Pleistocene transition (Lisiecki and Raymo 2005; Figure 2.1). During the Pliocene Climate Optimum, the exact timing of which is also debated (Haywood *et al.* 2009), CO_2 concentrations were similar to today (between 350-385 ppm; Pagani *et al.* 2010; Figure 2.1) and the global mean temperature was ~2°C warmer than today. However, high-latitude records (e.g., Csank *et al*. 2011) and climate models (e.g., Haywood *et al.* 2009) show that the Arctic was ~15°C warmer, due to the

polar amplification of climate change. The Intergovernmental Panel on Climate Change forecasts future global warming of ~2°C; therefore, the Pliocene constitutes a useful analogue for investigating how anticipated rates and magnitudes of climate warming will be manifest in the Arctic (Stoker *et al.* 2013). For example, more knowledge of Pliocene environmental change in the Arctic will provide a long-term geological context to accurately assess the significance and implications of current permafrost thaw and sediment mobilization.

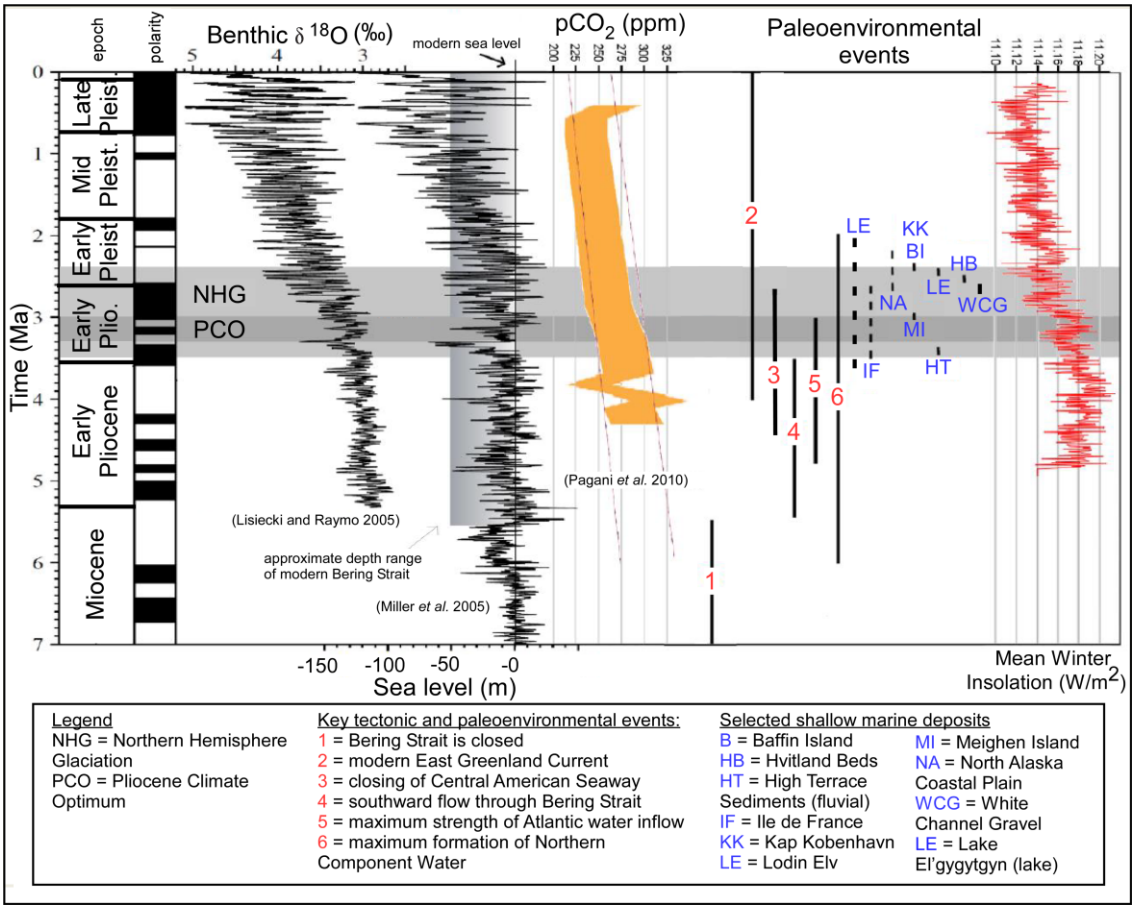

Figure 2.1 – Time series of global and Arctic changes that occurred during the Late Eocene. The BF on Meighen Is. (MI) and the High Terrace Sediments on Ellesmere Is. (HT) are shown in context of these changes (Rybczynski *et al.* 2013). The Mean Winter Insolation (red) is modified from Rybczynski *et al.* (2013) and is for 78°N. The compilation of time series is modified from Matthiessen *et al.* (2009). Atmospheric CO_2, shown in yellow, is modified from Pagani *et al.* (2010). The timescale is from Cohen *et al.* (2014).

The reopening of or reversal of flow through the Bering Strait (4.5 Ma; Marincovich *et al.* 2001; Figure 2.1) and the shoaling of the Central American Seaway between 4.7 and 4.2 Ma (Verhoeven 2011; Figure 2.1) occurred during the Pliocene. Such tectonic and sea-level changes controlled the size and geometry of ocean gateways and continental drainage systems in the Arctic Ocean, which exerted a major influence on ocean circulation and water mass characteristics (Dixon *et al.* 1992, Matthiessen *et al.* 2009).

The BF sediments contain exceptionally well preserved logs, leaves, peat, insects, and vertebrate fossils, which provide key evidence for Arctic environmental conditions during the Pliocene (Matthews and Ovenden 1990, Matthews and Telka 1997). The wide geographic range of these paleoenvironmental records (e.g., the more temperate Banks Is. to the south and the more depauperate Meighen Is. to the north; Figure 1.1) has triggered hypotheses regarding the role of latitude, continentality, and age in determining environmental conditions in the Pliocene (e.g., Fyles 1990, Matthews and Ovenden 1990).

2.2 Previous stratigraphic analyses

2.2.1 Discovery and definition of the BF

Sediments of the BF were first recognized by explorers in the mid-19th century. M'Clure noted the presence of abundant fossil wood at Ballast Beach in 1851. According to Fyles (1990), wood collected by Mecham (1855) was described by Heer (1868). The deposits were formally named by Tozer (1956) in the Mould Bay area of Prince Patrick Is. (Figure 1.1). In the next decades, largely as a result of reconnaissance studies by Tozer (1956) and Tozer and Thorsteinsson (1962, 1964), BF sediments were recognized and described on all the islands bordering the Canada Basin from Meighen Is. to Banks Is. (Figure 1.1). By the early 1990s, several facies and stratigraphic descriptions for Banks and Meighen Is. were published (Craig and Fyles 1965, Hills 1969, Fyles 1990, Devaney 1991, Fyles *et al*. 1991; Figure 2.2), but most research papers to this point focused on

the unique and exquisitely preserved paleoenvironmental records (e.g. Vincent 1983, Matthews 1987).

Fyles (1990) was instrumental in revising the formal definition of the BF. Devaney (1991), in collaboration with J. G. Fyles (regional stratigraphy) and J. V. Matthews, Jr. (paleobotany), outlined a more detailed classification of sedimentary facies at the type locality on Prince Patrick Is. In 1991, Fyles *et al.* published a detailed sedimentological and stratigraphical analysis from Meighen Is. (Figure 2.2), the marine strata of which set this locality apart from all other known BF exposures. No major studies have been published on the sedimentology and stratigraphy of the BF and related deposits in the last two decades, although investigations have continued on the fossil record, especially in the Pliocene fluvial sand and gravel of the High Terrace Sediments on Ellesmere Is. (e.g. Matthews and Fyles 2000, Dawson and Harington 2007; Figure 1.1).

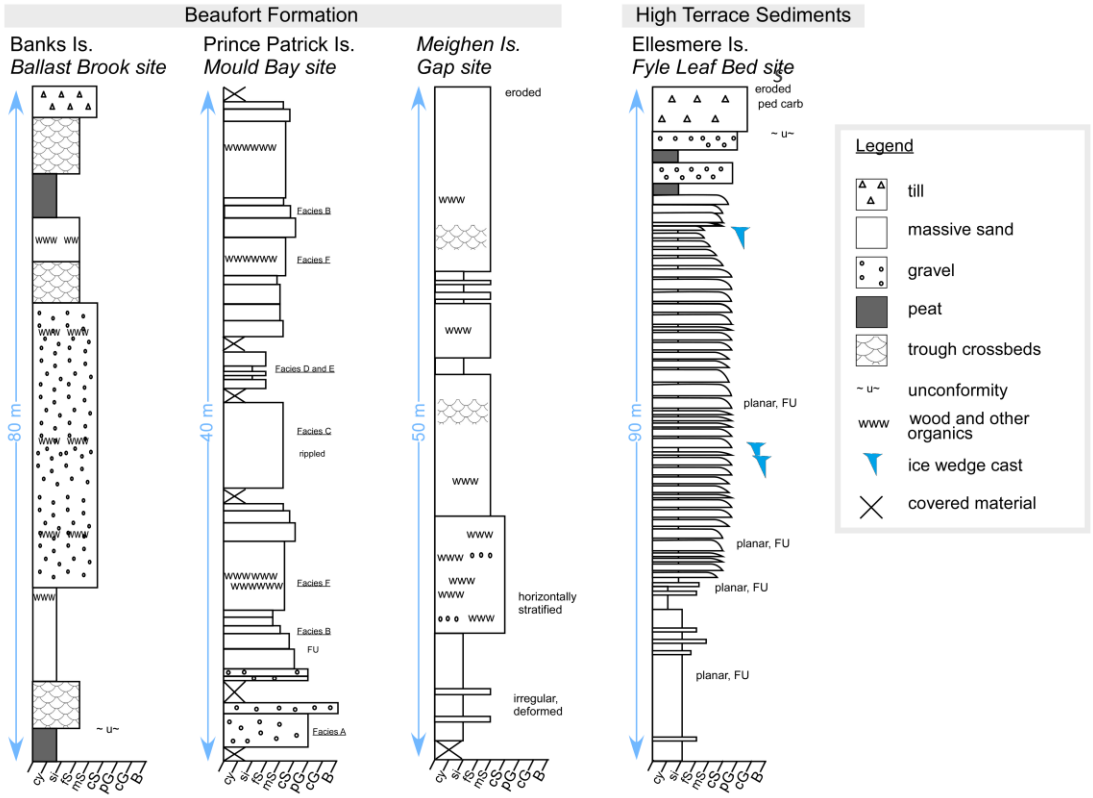

Figure 2.2 – Combined stratigraphic log of BF and related deposits on Banks, Prince Patrick, Meighen, and Ellesmere Is. Abbreviations: FU = fining upward, cy = clay, si = silt, fS = fine sand, mS= medium sand, cS = coarse sand, pG = pebble gravel, cG = cobble gravel, B = boulder gravel.

The High Terrace Sediments on Ellesmere Is. were likely contemporaneous to the BF (confirmed by recent TCN chronology; see below § 2.2.3; Figure 2.2). The High Terrace Sediments are likely a more continental alluvial fan depositional environment associated with the BF coastal plain depositional environment (Fyles 1990). For simplicity in this thesis, the term BF is used to indicate both the BF *sensu stricto* sites (Banks, Prince Patrick, Borden, and Meighen Is.) and the High Terrace Sediments (Ellesmere Is.), unless otherwise specified.

2.2.2 Extent of the BF inland and offshore

Pliocene sediments are rare in the interior of the CAA (Harrison *et al.* 2011), so little is known about the extent of the BF inland. Thin and discontinuous deposits of gravel on Melville Is., which locally contain wood, may be erosional remnants of the BF (Hodgson 1984, Fyles 1990; Figure 1.1).

The extent, thickness, and character of the BF and correlative deposits on the Beaufort Sea Shelf and Slope are largely uncertain due to a paucity of regional seismic data and sediment cores (Fyles 1990). The exposed BF beds on Meighen Is. (>100 m thickness exposed above sea level) form the uppermost part of approximately 3000 m of Plio-Pleistocene clastic sediment penetrated by a petroleum exploration well beneath the island (well Crocker I-53, not entirely of the same age as the exposed deposits; Asudeh *et al.* 1989). The BF on Prince Patrick Is. seems to be the thin southeast edge of a westward-thickening sedimentary wedge on the island (Devaney 1991). Exploration wells demonstrate that Pliocene to Pleistocene clastic strata thicken from tens of meters to more than 1000 meters within 50 km west of the Prince Patrick Is. coast (Asudeh *et al.* 1989, Helwig *et al.* 2011). The Plio-Pleistocene offshore Iperk Formation thickens to 3000 m, and part of this sequence is thought to correlate with the BF (Blasco *et al.* 1990, McNeil *et al*. 2001). McNeil *et al.* (2001) describe a first-order regional paleosurface which extends from the deep basin onto the continental rise, shelf, and cratonic margin in the Mackenzie Delta area and Richardson Mountains. They suggest that this Mio Pliocene unconformity is correlative with the unconformity at the base of the BF (described below in § 3.9).

2.2.3 Variability within the BF

Despite clear biostratigraphic correlations, attempts at lithostratigraphic or chronostratigraphic correlations have been impeded by limited exposures of the sediments. Any of the studied exposures could have been deposited earlier or later during the broader depositional history of the BF (i.e., their precise stratigraphic relationship is unknown). No regionally extensive bounding surfaces (10,000-100,000 years; James and Dalrymple 2010) have been described in the BF, and the BF has not been subdivided into correlatable units. Other than the marine strata on Meighen Is. (Fyles *et al.* 1991), the descriptions of the BF on other islands are not sufficiently distinct (or characterized sufficiently precisely) to be contrasted. It would be useful to understand how these different sites relate to each other, because trends or patterns between sites may help characterize that of depositional processes and paleoenvironments.

The source of BF sediment is known to vary across the CAA. For example, the observed volcanic clasts on Meighen Is. suggest source material from Axel Heiberg Is. (Fyles 1990). In contrast, the BF on Prince Patrick Is. contains lithologies similar to eastern Prince Patrick Is. (orange Devonian sandstone), northwestern Melville Is. (black chert of the Ibbet Bay Formation), and northeastern Banks Is. (Fyles 1990, Devaney 1991). At Ballast Brook on Banks Is., fossil palynomorphs including both terrestrial and marine taxa indicate that a primary sediment source was the Late Cretaceous to Eocene Eureka Sound Group. Chert clasts may be derived from Proterozoic bedrock on Victoria Is. or eastern and southern Banks Is. (Fyles *et al.* 1994).

The fossil floras and faunas are similar across the present-day latitudinal extent of the BF and related sediments, but they are not identical. The Prince Patrick Is. assemblage represents a coniferous forest, while that of Meighen Is. suggests forest-tundra boundary conditions (Matthews and Ovenden 1990, Fyles *et al.* 1994). Additionally, several quantitative temperature estimates have been calculated for the Beaver Pond and Fyles Leaf Bed sites on Ellesmere Is. (High Terrace Sediments) based on fossil beetles (growing season temperature = 10 ± 2 °C warmer than present; Elias and

Matthews 2002), oxygen isotopes in tree cellulose (MAT=14-19°C warmer than present; Ballantyne *et al.* 2006), plant macrofossils and molecular techniques (MAT=19°C warmer than present; Ballantyne *et al.* 2010), and oxygen isotopes in freshwater molluscs and carbonate isotope thermometry on freshwater mollusc shells (growing season temperature = 11-16°C warmer than present; Csank *et al.* 2011). These temperature estimates for the High Terrace Sediments are higher than those in the BF *sensu stricto* because of higher winter temperatures (less seasonality) at the High Terrace Sediment sites on Ellesmere Is.

2.2.4 Chronology

The establishment of a chronostratigraphic framework for the BF has been a focus of research over several decades. Most of the techniques that have been used were restricted to the marine beds on Meighen Is. The age uncertainty for most of these techniques is too large to distinguish whether the BF was deposited in the early-, mid-, or Late Pliocene and to establish the relative timing of BF deposition at different localities. Furthermore, the interpretations of some of the methods used need to be revised.

Until Rybczynski *et al.* (2013), the only BF sediment with absolute age constraints was the marine facies present on Meighen Is. The rest of the BF was correlated to Meighen Is. based on paleontological characteristics (extrapolation could not be decisively achieved based on stratigraphy alone; e.g., no stratigraphic marker beds). Recently, Rybczynski *et al.* (2013) used ^{26}Al and ^{10}Be TCN burial dating to show that the related High Terrace Sediments on Ellesmere Is. were deposited 3.4 $^{+0.6}/_{-0.4}$ Ma (average of 4 measurements, Beaver Pond site) and 3.7 $^{+1.0}/_{-0.7}$ Ma (1 measurement, Fyles Leaf Bed site; Figures 2.1 and 2.2). The BF on Meighen Is. was also dated using TCN, yielding an age of 3.3 $^{+0.19}/_{-0.22}$ Ma (average of 8 measurements, Gap site; Gosse pers. comm. 2015). The TCN burial ages are consistent with previous biostratigraphic estimates for the same deposits. This demonstrates that ^{26}Al/^{10}Be TCN burial dating can provide age constraints for Pliocene sediments in the high Arctic. However, the cosmogenic burial age interpretation was simplified at these two sites. At the Beaver

Pond and Fyles Leaf Bed sites, the locally high altitude makes burial (and decay of TCN) before deposition unlikely. On Meighen Is., the proximity to an ice cap reduces likeliness of post-depositional exposure to TCN production. Burial before permanent deposition and post-depositional exposure are two factors that complicate the interpretation of TCN burial ages, and these factors cannot be ignored at Ballast Brook (discussed in Chapter 6).

2.2.5 Other western CAA sedimentation events

There is an important history of sedimentation in the western CAA. The Eurekan Orogeny, which developed fully during the Paleogene, contributed to the basinward dispersal of sediment (Harrison *et al.* 1999; Figure 2.3). Sediment was eroded from the emerging Arctic Platform and transported to the northwest across the coastal plain on which the BF is now exposed (Trettin 1991; Figure 2.3). Deposition occurred between the central Sverdrup Basin and the Mackenzie Delta, and built the continental terrace that now lies along the northwestern margin of the CAA (Miall 1986; yellow in Figure 2.3). The diachronous formations and units of the Eocene Eureka Sound Group reflect the complex paleogeographic evolution of the CAA during this Orogeny (Miall 1986). The Eureka Sound Group was likely reworked and redeposited as the BF in the Pliocene (Fyles 1990).

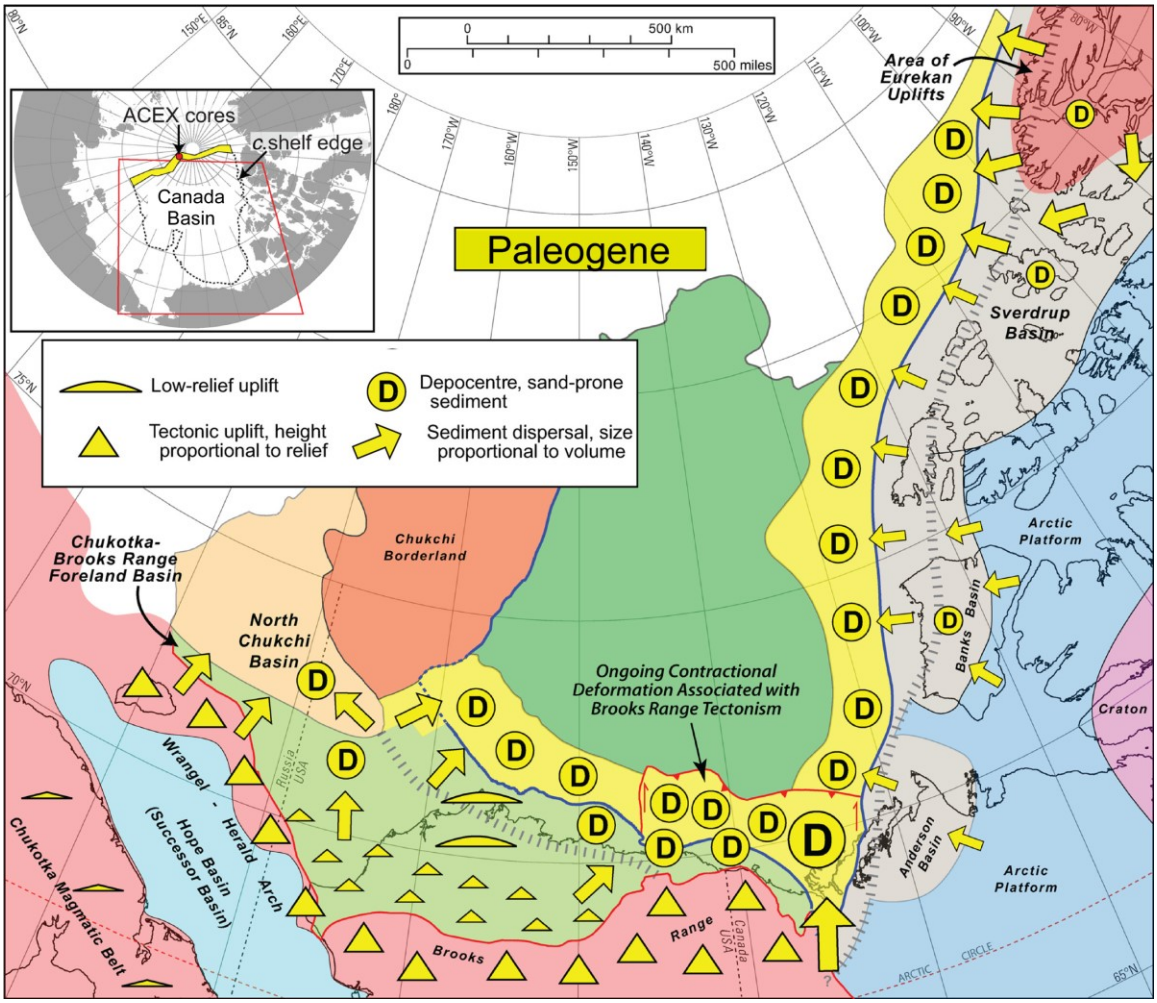

Figure 2.3 –Map of Paleogene deposition onto the Arctic Coastal plain and into the Beaufort Sea. The deposition originated from the Eurekan Uplifts and the Arctic Platform. Sediment was deposited mainly in the Canada Basin but also on a former coastal plain extending along the north slope of Alaska and the western margin of the CAA (modified from Houseknecht and Bird 2011). The dark green area is the deep Canada Basin, and yellow areas are continental terraces along the rifted margins of Alaska and Canada. The remainder of the colours represent geological provinces discussed in Houseknecht and Bird (2011).

Although the Plio-Pleistocene portion of the offshore sedimentary record (Iperk Formation) is by far the thickest (McNeil *et al.* 2001), there are several Late Miocene deposits in the western CAA and surrounding areas which show similar warm-climate characteristics as the BF (e.g., abundant sub-fossil wood), but are not identical to the BF (e.g., wood is more compressed, or greater abundance of meandering stream facies). On Ellef Ringnes and Borden Is. (Figure 1.1), the fluvial deposits are physically and

paleontologically similar, although the wood is more altered (i.e., partially decomposed and compressed), mossy beds are absent, and thin beds of dark brown and black silt and clay are common (Fyles 1990). Additionally, fluvial sand and gravel is present on Ellesmere and Axel Heiberg Is. (High Terrace Sediments), although it is coarser than the BF *sensu stricto* (Fyles 1989; Figure 1.1). The Ballast Brook Formation (BBF), which underlies the BF on Banks Is., consists of sandy, meandering river sediments, with peat and clay deposited in floodplain swamps and lakes (Vincent 1990, Fyles *et al.* 1994). The wood is more compressed and altered than BF wood (similar to the Ellef Ringnes and Borden Is. wood), and differences in plant macrofossils are thought to signal a Miocene age (Fyles *et al*. 1994). The Mary Sachs Gravel on southwestern Banks Is. is glaciofluvial, with abundant reworked organic matter of Miocene and Pliocene age (Evans *et al.* 2014), including similar taxa to the upper BBF (Fyles 1990). Pleistocene sites include the Worth Point Formation on Banks Is. (Vincent 1990, Vaughan *et al.* 2014), the Bylot Is. deposits (Csank *et al.* 2013), and the Hvitland Beds on Ellesmere Is. (2.4 Ma, Fyles *et al.* 1998). Fyles (1990) recommended excluding Miocene (e.g., BBF and Mary Sachs gravels) and Pleistocene (e.g., Worth Point Formation) from the BF proper and restrict the BF to a Pliocene age.

2.2.6 The BF as part of a circum-Arctic sedimentation event?

The BF and High Terrace Sediments may be one of several contemporaneous Pliocene sedimentation events that occurred throughout the circum-Arctic (Figure 2.1). This would suggest that there was a period of time during the Pliocene that was conducive to sedimentation across the Arctic. Several other well-studied Arctic sites demonstrate warm Pliocene conditions, including: Baffin Is. deposits (fluvial sediments, 2.5 Ma; Harrison *et al.* 2011), Île de France in northeastern Greenland (shallow water marine sediments, 2.60-3.58 Ma; Bennike *et al.* 2002), Kap København in northern Greenland (shallow marine nearshore sediments, 2.4 Ma; Funder *et al.* 2001), Lodin Elv in eastern Greenland (2.6 Ma; Feyling-Hanssen *et al.* 1983), the Gubik Formation in the northern Alaska coastal plain (marine, fluvial, lacustrine, and eolian sediments, 2.48-2.7 Ma; Brigham-Grette and Carter 1992), the Upper White Channel Gravel in the Yukon

(2.64 Ma, Hidy *et al.* 2013), and the Tjornes Section in Iceland (near-shore and terrestrial deposits, 3.8-5.3 Ma; Verhoeven *et al.* 2011). However, correlation with the BF is uncertain due to large chronology uncertainties. For instance, the ages of the sites do not preclude a synchronous pan-Arctic event.

2.3 Hypothesis 1: The BF was deposited along a contiguous coastal braid plain

The uppermost beds of the BF are typically parallel to the modern surface over many kilometers and dip westward, which is consistent with regional indicators of westward stream flow, eastward sources of sediment (variable across the islands), and offshore thickening (Trettin 1989; Figure 1.1). A major disconformity (with local angular unconformities) separates the BF from underlying sediment of Paleozoic to Miocene age (Blasco *et al.* 1990). This basal contact also dips to the northwest (Fyles 1990). Based on the sedimentology, stratigraphy, and geographic distribution of the BF, Fyles (1990) suggested that the BF originated as coalescing deposits of a number of braided streams that flowed northwest across the lowland (Fyles 1990). In this depositional model, the inter-island channels would have to have been filled with sediment, and the 1200 km-long extent of the BF would thus have been a contiguous coastal plain (Fyles 1990; Figure 1.1). Fyles's hypothesis of a continuous coastal plain in the Pliocene echoes the patterns of Palaeogene provenance and sediment dispersal, which persisted through much of the Neogene, when the edge of the western CAA may also have been connected as a continuous coastal plain (Miall 1986; Figure 2.3).

If the BF was deposited in a short time period as one continuous braid plain, paleoenvironmental patterns would represent changes with latitude and continentality (i.e. spatial trends). For example, Fyles (1989) suggested that the Ellesmere Is. deposits are contemporaneous with but more continental than the remainder of the BF, as would be expected if the BF formerly infilled parts of the now inter-island channels and formed a contiguous landmass across the western CAA.

The hypothesized synchronicity of the BF deposition has interesting implications for how the sediment was mobilized, transported, and deposited on the coastal plain. The deposition of the BF would have required a significant volume of stored sediment to be

quickly eroded from the east and transported across the western CAA, which depends on the availability of source material. If the source material was resistant bedrock, it would have had to be previously weathered in order to be transported sufficiently quickly. This is consistent with the greater than 90% quartz composition of the BF sands and reworked Cretaceous to Ecocene palynomorphs (§ 2.2.3). The dominantly fluvial Eocene Eureka Sound Group, which is composed of mostly quartz-rich sands (Fyles 1990), lies to the east of the BF (Figure 1.1). It could have been quickly eroded from the landscape, providing a large volume of sediment in a short time. In addition, the partially unconsolidated Cretaceous Hassel and Isachsen Formations could also have supplied a significant volume of recycled quartz-rich sand. Thus, better chronology is needed to determine the time spanned by the deposition of the BF.

If the BF was a contiguous braid plain, what was the size of the associated drainage basin? What was the former extent of the deposit farther east (i.e. upstream) where it is presently eroded? What was the total volume of sediment deposited?

2.4 Hypothesis 2: The BF was deposited intermittently in space and time, as a sequence of independent coastal braid plains

Hypothesis 2 is that instead of occurring as one continuous braid plain, the BF was composed of independent braid plains that may represent separate Pliocene depositional events on isolated islands (the CAA channels may or may not have been present). Because the exact stratigraphic relationship between different localities of the BF is unclear, these may have been deposited at slightly different times, like other Miocene and Pleistocene unconsolidated fluvial deposits with abundant wood (§ 2.2.5).

According to this hypothesis, paleoenvironmental differences represent deposition at different stages of the climatic deterioration in the Pliocene (i.e. temporal tends). Matthews and Ovenden (1990) used floral comparisons to argue that the Prince Patrick Is. sediments are older than the Meighen Is. exposures. Based on this biostratigraphy, the Prince Patrick Is. beds would be either Pliocene or perhaps range from Miocene to Pliocene, demonstrating a younging trend northward; Devaney 1991). The BF on Banks Is. could be Early Pliocene in age (Fyles *et al.* 1994).

If the BF is indeed time-transgressive, this raises a new set of questions: how does it record changing conditions across time and space? How quickly were the different braid plains deposited? How are the different sites related? Were the channels between the islands ever filled with Pliocene sediment?

2.5 Hypothetical causes of deposition

What pre-conditions were necessary and what changes or events acted as triggers or causes for deposition of the BF across more than 1200 km? To what degree and in what ways was deposition of the BF influenced by a warm climate, which is documented by the fossil record? Similarly, did other phenomena such as eustatic and relative sea level, dynamic topography, tectonics, and glacial isostasy associated with Late Pliocene ice sheets influence deposition of the BF? What do past mechanisms of landscape change reveal about fundamental couplings in the Earth system, and about potential responses to future climate change?

The precise cause(s) of deposition cannot be determined without an accurate absolute chronology for the BF (Fyles 1990). For example, different causes of deposition would be implied by synchronous (i.e. tens of thousands of years) vs. diachronous (hundreds of thousands of years; Fyles *et al.* 1994) deposition, and by the precise timing of deposition (i.e. Mid Pliocene warm period vs. Late Pliocene).

Eustatic sea-level during the Pliocene was at times up to 20-25 m higher than today (Miller *et al.* 2005). If a single eustatic sea-level rise was the trigger for deposition of the BF, deposition would have been synchronous everywhere. Even with a slow rate of sediment delivery, the response time would have been rapid, as sedimentation responds to sea level change in 1000s of years or less (Syvitski and Milliman 2007). Rovere *et al.* (2014) showed that dynamic topography (long-wavelength topographic relief caused by mantle flow) played a significant role in the post-depositional displacement of Pliocene deposits across the globe, and this process could also have impacted the CAA. Uplift by dynamic topography would have been regional, simultaneously affecting most or all source areas of the BF, but occurring over a much longer time scale than sea level rise (100s of thousands of years; Conrad and Husson 2009). In contrast, uplift by lithospheric

tectonics and glacial isostasy (which would only be a relevant factor if there was ice in the CAA during the Pliocene) have more local effects; since the provenance of BF sediment varies among the different exposures (e.g. Mackenzie Mountains, Victoria, and Axel Heiberg highlands; Fyles 1990, Fyles *et al.* 1994; Figure 1.1), different source areas would have been affected at different times. However, tectonics would have acted on longer time scales (deposition within 100s of thousands of years) compared to glacial isostasy (less than 10s of thousands of years; Miller *et al.* 2005). Furthermore, climate change could have been either local or regional, resulting in either synchronous or diachronous effects across the CAA during the Pliocene, and could have affected rates of deposition (10s vs. 100s of thousands of years). Since it is not known whether the BF was fully deposited during the Mid Pliocene warm period everywhere, or in part during the onset of northern hemisphere glaciations at the Plio-Pleistocene boundary, or during an early Pleistocene interglacial, its deposition cannot be evaluated in the context of myriad variables, such as sea-level, sea ice, and sea surface temperature, mean annual temperature, orbital forcing, or CO_2. Nor can the BF be considered in light of vegetation and ice sheet models, or events such as the opening of Bering Strait (Marincovich *et al.* 2001) and the closing of the Central American Seaway (Verhoeven 2011). Therefore, it is not possible to gain insight into which global and regional factors occasioned deposition of the BF without knowledge of its synchronicity across different islands, duration, and precise timing in a global context (Fyles 1990).

2.6 Hypothetical consequences of deposition

If deposition of the Beaufort Fm. was synchronous, it may have significantly transformed the Canadian Arctic landscape in the Pliocene, covering the area between of the channels between the present day islands of the CAA and creating a contiguous coastal plain (of course, this assumes that the channels were present in some form prior to deposition). Similarly, it is possible that high rates of sedimentation associated with deposition of the BF instigated a significant northwestward extension of the continental shelf and a concomitant expansion of the coastline. Possible effects of these types of changes in paleogeography include more continental climate and vegetation in the high

Canadian Arctic, altered regional albedo, altered moisture supply to ice sheets on Greenland, and changed ocean circulation. As well, high rates of sedimentation on the shelf and slope would have likely instigated new rates and patterns of isostatic adjustments along the continental margin. In particular, a significant amount of freshwater input to the Labrador Sea currently comes through CAA, and bottom water formation in the north Atlantic has long been suspected as a trigger for drastic climate change (Matthiessen *et al.* 2009). Therefore, the deposition of the BF may have affected global climate through a decrease in freshwater delivery to the Labrador Sea.

2.7 Incision of the braid plain

If the BF was once a contiguous braid plain, significant dissection must have occurred, as it is now fragmented by the marine channels of the CAA. Fyles (1990) noted that the BF is not significantly displaced either laterally or vertically across these straits. This means that if the BF was once a contiguous braid plain, it has been incised rather than pulled apart. Incision may have occurred in response to a different set of regional and/or global variables or it may have been related to deposition. For example, if a sediment pulse was the main mechanism facilitating deposition of the BF, it is possible that a subsequent decrease in sediment supply initiated incision.

Several of the Earth system changes and events that happened during the Pliocene could have contributed to the incision through the BF by one of two mechanisms (or a combination of both): (1) drop in relative sea-level and subsequent river incision, and (2) new or renewed vertical motion caused by regional tectonics or mantle dynamics. A drop in relative sea-level could have been achieved by (a) a drop in eustatic sea-level, (b) uplift due to isostatic rebound after Pliocene continental or regional glaciation, or (c) uplift due to dynamic topography, or (d) a combination of these. Fortier and Morley (1956), Pelletier (1966), and Trettin (1989) interpreted the inter-island channels of the CAA to be a drowned drainage network (although no highland is present where these authors postulate there is a major drainage divide). Pelletier (1966) further used the lithological and structural control on channel location (e.g. some fiords coincide with linear belts of relatively weak rock types, or with Eurekan structural elements) to argue

that rivers caused the initial erosion. Additionally, the well-preserved, uniform, gentle slope of the regional BF upper sediment surface (Fyles 1990) resembles a peneplain (Harrison and Brent 2006; Figure 2.4) that is dipping seaward. Thus, several authors have assumed that changes in eustatic sea level were the primary controls for the deposition and abandonment of late Cenozoic fluvial deposits (e.g. Brigham-Grette and Carter 1992; Figure 2.1). Eustatic sea-level was approximately 20-25 m higher than today during the Mid Pliocene warm period (Miller *et al.* 2005), and would have dropped during colder periods of the Pliocene (e.g. cold 'M2' event at 3.2 Ma; Raymo *et al*. 2011) and during the glacial periods of the Pleistocene. This magnitude of eustatic sea-level change is not sufficient to explain the present-day depth of the channels (locally exceeding 500 m), nor their widths, which are too wide for river lengths of only a few hundred kilometers (England 1987). Therefore, the channels are interpreted to have been widened and over-deepened by glacial erosion during the Pleistocene (Pelletier 1966).

Evidence for a tectonic control on the CAA channels is sparse. The islands of the CAA seem to fit together in terms of geology and shape (Gregory 1913). England (1987) shows that diabase dikes and normal faults form conjugate sets paralleling Greely Fiord. Seismic studies have demonstrated the presence of normal faults crosscutting Miocene sediments offshore, but faults crossing Pliocene sediments are rare (McNeil et al. 2001), and no seismic profiles that have been collected across the channels show faults in recent sediment (Mosher 2012). Bounding faults may have been eroded, which would mean that the cliffs defining the channels are fault line scarps (Miall 1984). Thus, only indirect evidence is available to suggest that the channels were formed by grabens (fractured rock beneath them, parallel cliffed coastlines, cross-cutting of the regional drainage; England 1987). Furthermore, some of the channels have curves not consistent with formation by faults (Pelletier 1966). There is also no evidence for a major pan-Arctic tectonic event in the Neogene or Quaternary (Trettin 1989). The channels of the CAA could have tectonically initiated during the Neogene, and may have been infilled until

they were excavated by ice sheets to their present-day configuration. Thus, the formation of channels may relate to Mesozoic or Paleogene tectonic activity.

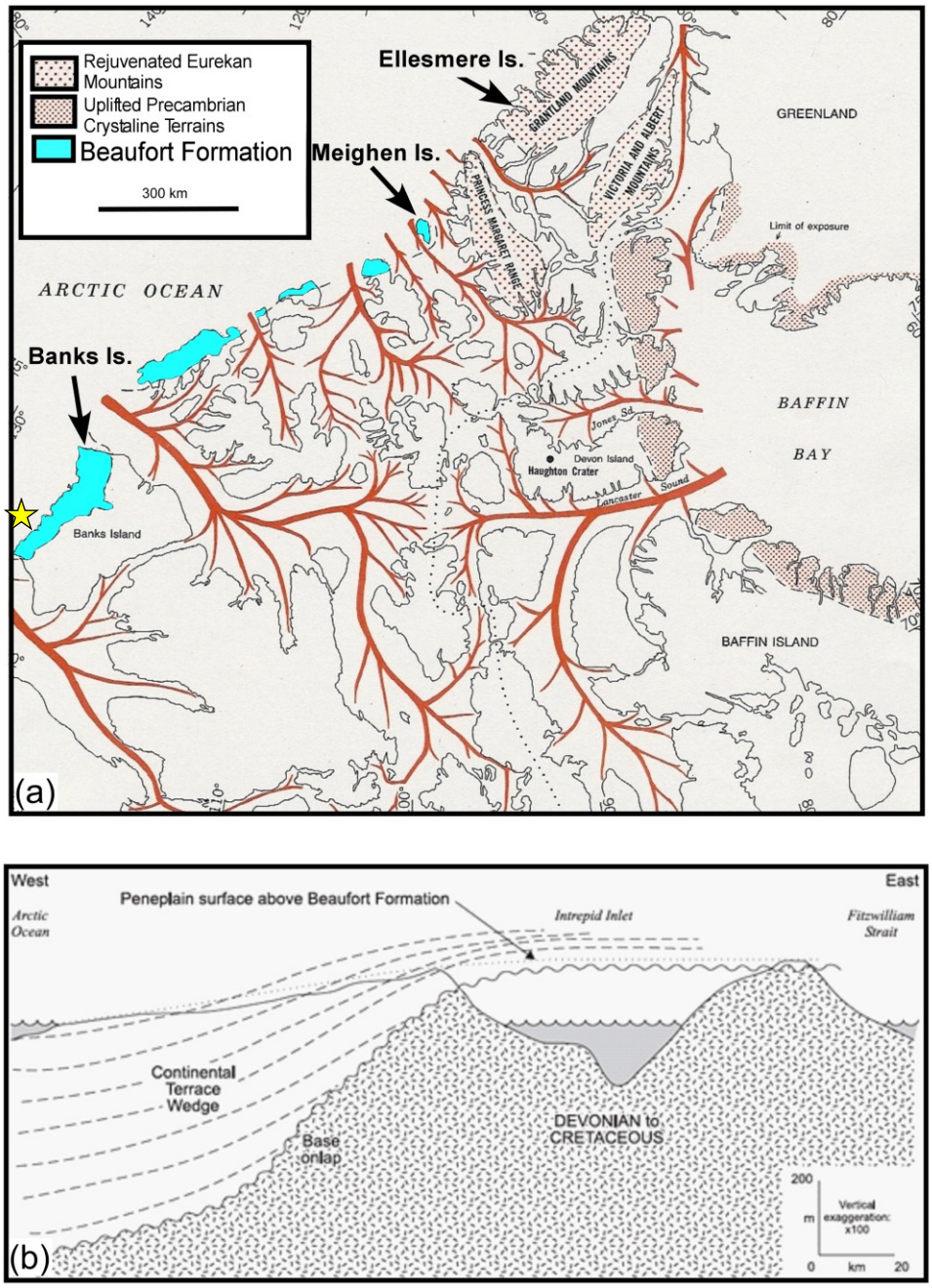

Figure 2.4 – Illustrations of base-level control on the incision of the CAA. (a) The hypothesis that the CAA was incised by streams was illustrated by Pelletier with this depiction of a drowned drainage network (1966). Ballast Brook is indicated by the yellow star. (b) The top of the BF may constitute part of a peneplain (Figure from Harrison and Brent 2006).

Alternatively, sediment availability may have been affected due to changes in ice cover, vegetation, or the more direct effects of climate change. Did vegetation, sea ice albedo, and changes in ocean circulation through the CAA cause feedbacks that accelerated landscape changes? Is it possible that incision contributed to the termination of the boreal forest by greatly diminishing the summer warmth of the previously contiguous landmass (England 1987)? These questions cannot be explored further without precise chronology. The incision events of different BF exposures must be dated and correlated in order to test for different mechanisms of incision. Precisely dating the incision events will also constrain the rates of processes involved, clarify their geographic reach, and place them in the context of multiple global time series (i.e. sea-level and climate).

2.8 Short-term objective: Banks Is.

Despite the recommendation of Prince Patrick Is. as the type locality for the BF, Devaney (1991) reported that the poor quality and paucity of BF exposures on Prince Patrick Is. severely limited the study. At that site, sections were no more than 34 m thick, required laborious excavation with a shovel, were prone to slumping, and included many colluvium- and till-covered sites. Likewise, the Meighen Is. exposure is a maximum of 30 m high (Fyles *et al*. 1991). Ballast Brook is an optimal site for better characterizing the BF, because it presents one of the best exposures of the BF and underlying Miocene sediments, including more than 10 km of continuous lateral exposure along the modern Ballast Brook, and cliff sections up to 84 m in height (Fyles *et al.* 1994). Additionally, Ballast Brook provides an ideal location to further characterize the BF sedimentology and fossil record because (1) it is the southernmost exposure of the BF, (2) the general stratigraphy has already been established by earlier studies (Hills 1969, Fyles *et al.* 1994), (3) an abundance of paleoenvironmental research has been conducted, which lends context to new observations, and (4) it is located within 10 km of M'Clure Strait and may contain a record of its age and size. In addition, the high exposures provide a good location for testing the TCN burial dating method (see Chapter 5).

Chapter 3 : Study Area and Previous Work

3.1 Introduction

Chapter 2 demonstrated how the present chronological constraints on the deposition and incision of the Beaufort Formation (BF) are insufficient to address a number of hypotheses, and that Ballast Brook is the most appropriate location for further study of the BF. This chapter discusses the history of work done on the BF at Ballast Brook and the present state of knowledge of the sedimentology, organics, and age of the BF at this locality. This chapter also discusses unresolved issues specific to Ballast Brook, and thus provides context for the present research.

3.2 History of research at Ballast Brook

Hills (1969, 1970) and Kuc and Hills (1971) were the first to thoroughly describe the stratigraphy at Ballast Brook. They recognized two units differing in mineralogy and degree of wood alteration and separated by an unconformity (Hills 1969). Both units were assigned to the BF, until Fyles (1990) suggested that only the upper unit properly belongs in the BF, as defined at the type section on Prince Patrick Is. Fyles *et al.* (1994) formally divided the sediments into the BF (upper 80 m) and BBF (lower 40m) based on differences in sedimentology, mineralogy, and plant fossil composition and preservation. By the early 1990s, several brief facies descriptions for the BF on Banks and Meighen Is. had been published, but most of the studies on the BF were focused on the unique and exquisitely preserved paleoenvironmental records (e.g., Matthews and Ovenden 1990). The most recent studies at Ballast Brook have focused on woody debris lenses, wood anatomy, and biomass (Murphy 2006, Mendell 2006, Williams *et al.* 2008). The only vertebrate biostratigraphic indicator known to have been recovered from the Ballast Brook region is a mammoth (left tibia shaft fragment of most likely *Mammuthus primigenius*) which was collected near the top of the Ballast Brook Bluff by L.V. Hills in 1976, stratigraphically above, and therefore assumed to be younger than, the BF (Harrington 2005).

Although the BF strata are exposed at a number of localities on Banks Is., Ballast Brook is the most studied in terms of sedimentology, stratigraphy, and paleoecology (Fyles 1990; Figure 1.1). Ballast Brook has received the most scientific scrutiny because here, the remaining record of the BF and BBF is up to 80 m thick, is well exposed, and is traceable for more than 10 km (Fyles *et al.* 1994; Figure 3.1). Thorsteinsson and Tozer (1962) could only distinguish the *in-situ* BF from reworked material in northwestern Banks Is. Even at Ballast Brook, the BF is capped by thin, glaciogenic sediments (including till and glaciofluvial sand and gravel) which exhibit varying degrees of glaciotectonic deformation and all imply some degree of erosion of the uppermost BF (French 1972, Vincent 1983, Harington 2005, England *et al.* 2009).

Although Ballast Brook is one of the best studied BF sites, previous research has not produced a conclusive chronostratigraphy (e.g detailed subdivision of the BF into several units), nor robust chronostratigraphic correlations with other exposures of the BF. Because the stratigraphy has already been generally established by earlier work, this is an appropriate location to further refine the stratigraphy (e.g., by trying to identify subunits).

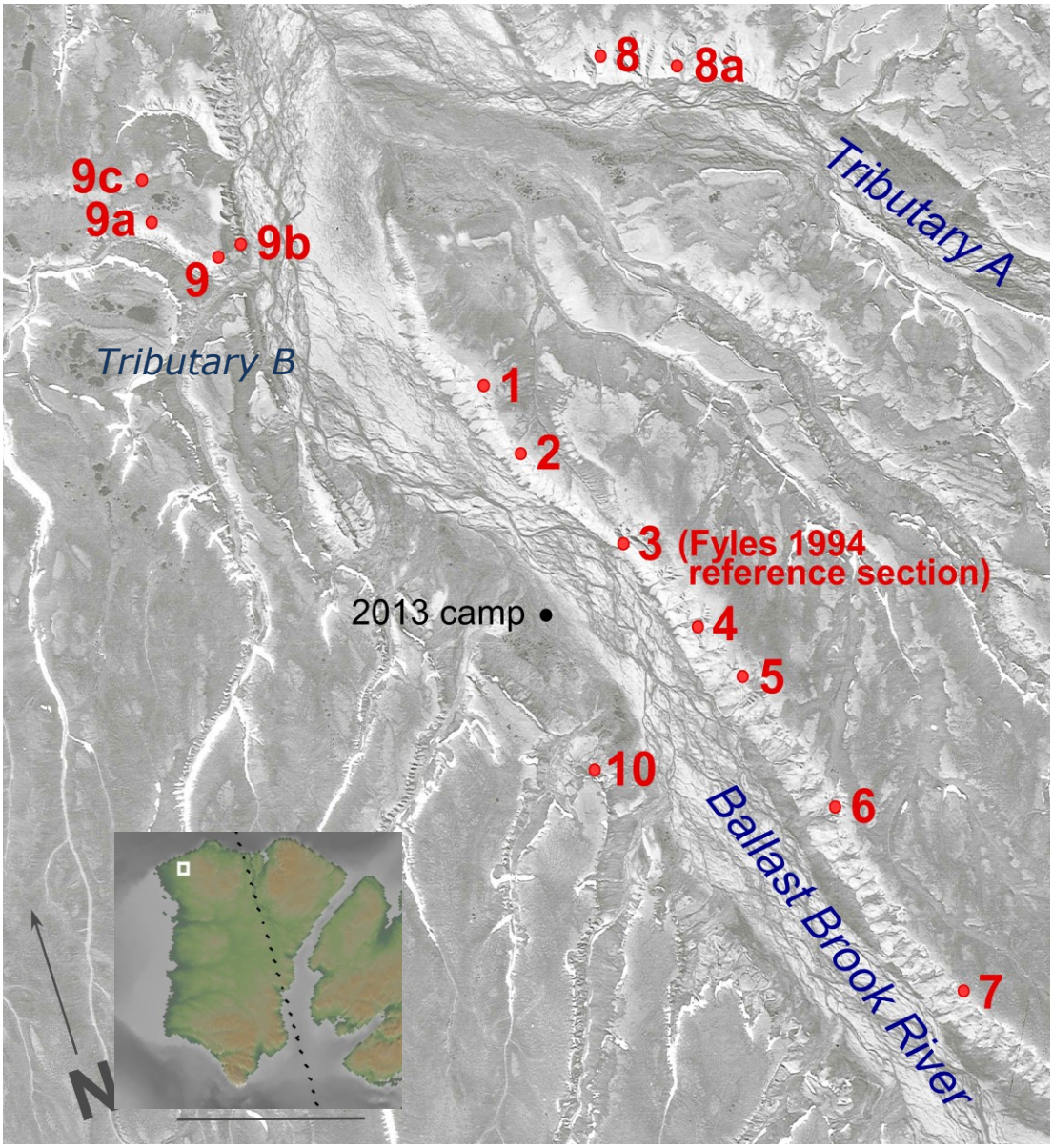

Figure 3.1 – Map of the Ballast Brook field area. Location is shown in inset map. Sample locations along the Ballast Brook, which is incised into the BF, expose the stratigraphy of the adjacent plateau over more than 10 km. Site numbering (1-10) is according to the most recent analysis by Fyles *et al.* (1994). Subdivision of site locations (9a, 9b, 9c and 8a) was adopted to record more precisely the location of measured sections of the present research. Sections 8a and 9b were studied in detail and sampled for TCN burial dating. Logs 1 and 2 both obtained at Section 9b. Due to a topographic ledge at Section 9, the upper 24 m of logs 1 and 2 were described at Section 9c. Section 9a is the site of Kuc and Hills' (1971) autochthonous peat. Camp location is at 74.349917°N, 123.18775°W. The base map is air photos # A17564 and A17564 from the National Air Photo Library (NRC).

3.3 Sedimentology and stratigraphy of the BF at Ballast Brook

3.3.1 Sedimentology and depositional environments

The BF at Ballast Brook consists of fluvial sand and gravel, in places interbedded with silt (including clayey silt; Figure 3.2). A reference section of the BF is located on the northeastern wall of the Ballast Brook valley (Section 3 in Figure 3.2; Fyles *et al.* 1994). At this site, much of the sand and gravel exhibit large-scale trough crossbedding, although some sand beds have tabular cross-stratification. Ripple cross-laminated and planar-laminated sand is less common. Gravel is a conspicuous component and ranges from beds dominated by pebbles and cobbles to sand containing isolated pebbles. Silt and clay beds are generally massive or have indistinct horizontal stratification, or alternating layers of sand and silt. Strata with silt and clay are common at the reference section and at Section 9 (Figure 3.1; Fyles *et al.* 1994).

Two fluvial depositional environments have been recognized at Ballast Brook: sandy-braided and gravelly-braided environments (meandering depositional environments have not been described on Banks Is.; Fyles *et al.* 1994). The sandy-braided deposits are dominated by cross-stratified to ripple cross-laminated medium- to coarse-grained sand with local pebble lenses at the base of channel scours (Fyles *et al.* 1994). The gravelly-braided deposits range from pebble to cobble gravels (Hills 1969), are clast-supported or matrix-supported, and characteristically horizontal or crossbedded (Fyles *et al.* 1994). They are characterized by abundant cut-and-fill structures, and were laid down in channels ranging from 2-3 m in depth and 5-20 m in width (Fyles *et al.* 1994). A similar sedimentary architecture was observed on Prince Patrick Is. by Devaney (1991), except that the sandy-braided deposits dominate at that locality, and that meandering stream facies were also described, with scroll bars, overbank deposits, and laterally accreted bars.

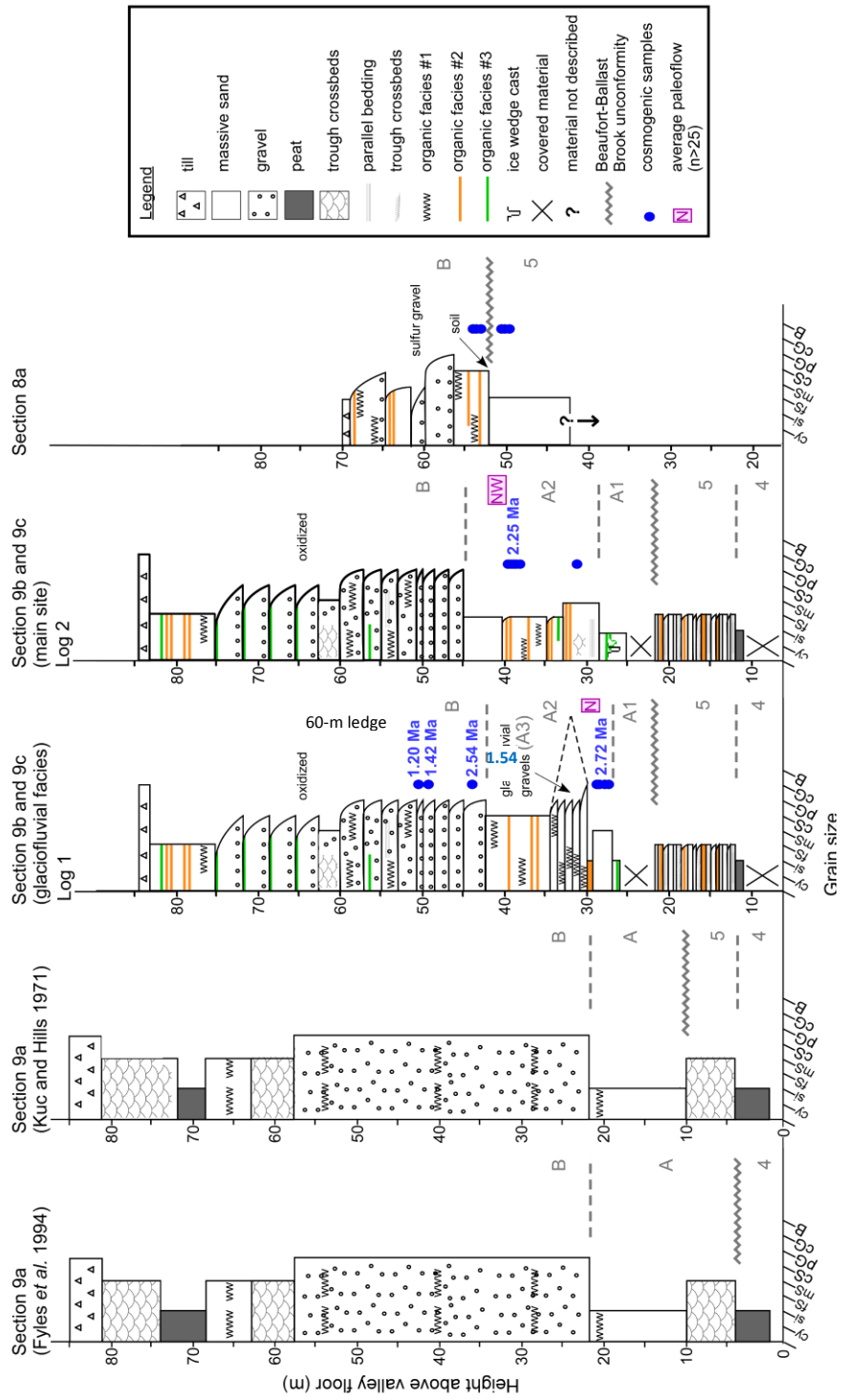

Figure 3.2 – Stratigraphic logs for three exposures of the BF at Ballast Brook. Refer to Chapter 4 for details of each section, including field photos. This study confirms the previously reported stratigraphy. The further subdivision of Unit A into Units A1, A2, and

A3 is informal and meant to provide context for the TCN chronology. Formation units are labelled in gray and burial ages are labelled in blue. Detailed description of the organic facies can be found in the text. The logs are aligned based on the height of the BBF-Unit 4 peat, a regional landmark. The precise height of the Unit 4 peat (or silty sand) at Section 8a was not recorded, so the Section 8a log is aligned based on the approximate height of the peat, using a dip of 6 m/km westward (Fyles *et al*. 1994). The dip of the peat is reflected by the lower height of the peat at Section 9a compared to Section 9b. The TCN results from bottom to top are: Lower A2 sample group, Upper A2 sample group, Sample 032, Sample 029, and Sample 030 (see Chapter 4).

The BF at Ballast Brook has been divided into two units, the lowermost 30 m, comprising medium- to coarse-grained sand, and the uppermost 30-40 m, consisting of pebble to cobble gravel interbedded with coarse- to medium-grained sand (Figure 3.2; Hills 1969, Fyles *et al.* 1994). These lower and upper units correspond to Units A and B of Fyles *et al.* (1994), respectively. Although Hills used different unit names, the more recent Fyles *et al.* (1994) convention is adopted here. The base of Unit A is characteristically lighter coloured than Unit B (Hills 1969); Fyles *et al.* (1994) describes it as a distinct, basal light coloured zone that thickens downstream (i.e. to the northwest). Part of Unit A is a characteristically cross-stratified channel fill that has an erosional contact with Unit B (Hills 1969). Although a number of uncompressed logs can be found, wood lenses are uncommon, and no cones were recovered by Hills and Ogilvie (1970). Unit B is also commonly cross-stratified, but it contains numerous lenses of uncompressed wood that are 0.3-1 m thick and 0.5-60 m long (Hills 1969).

3.3.2 The BF- BBF unconformity

Several lines of evidence suggest that a considerable time interval is represented by the angular unconformity between the BF and BBF, and that substantial erosion occurred: (1) the angular relationship between the inclined BBF strata and horizontal BF strata (Hills 1969, Fyles *et al.* 1994), (2) the contrast between the compressed and altered wood of the BBF and the uncompressed and unaltered wood of the BF (Hills 1969), which may indicate that there was a considerable load of overlying sediment that was removed by erosion prior to deposition of the BF (Fyles *et al.* 1994), and (3) differences between the plant taxa in the BBF (nearly 60% not found today in northern

regions and 10% are extinct, such as mid-Miocene floras from Asia), and in the BF (31% are non-native and 6% extinct; Matthews *et al*. unpublished data). This unconformity is potentially correlative to a Miocene Pliocene first-order regional-scale peneplain present in the Mackenzie River region (McNeil *et al.* 2001) and a similar unconformity identified in seismic data at the base of the Pliocene-Pleistocene Iperk Sequence on the adjacent Beaufort Sea Shelf (Blasco *et al.* 1990, McNeil *et al.* 2001).

There is debate about exactly where the unconformity resides in the Ballast Brook stratigraphy. Hills (1969) proposed that the unconformity was at the top of a sequence of ~20 m of fine grey sand overlying a prominent, 3-m thick peat (subsequently recognized as Unit 4 in Fyles *et al.* 1994). Fyles *et al.* (1994) differed in their interpretation and reassigned the fine grey sand to the BF, tentatively correlating it to Unit A at Section 3 (a reference section for the Ballast Brook Formation; Figure 3.2). The cross-stratified sand and silty-clay that make up the BBF-Unit 5 (~ 25 m thick) rest directly on the highly organic silt and autochthonous peat of the BBF-Unit 4. However, up-valley (southeast) from the reference section (Section 3), sediment immediately above the peat of Unit 4 is coarser and contains more prominent and abundant wood (Fyles *et al.* 1994). For example, at Section 4, gravel containing wood directly overlies the eroded upper surface of Unit 4 (Fyles *et al.* 1994). The Ballast Brook Formation beds dip 6 m/km toward the west (Fyles *et al.* 1994). A few kilometres southeast from Section 3, along the northeast side of the Ballast Brook valley (Figure 3.1), the basal unconformity of the BF crosscuts Unit 2 to 5 of the Ballast Brook Formation.

Thus, although the unconformity has been previously studied on a number of occasions, its exact location in the stratigraphy at Ballast Brook is still somewhat uncertain and must be resolved in order to develop a robust chronostratigraphy.

3.3.3 Lithologies, sediment source, and flow direction

Sand and gravel of the BF are predominantly quartz with some chert and shale also present. Sand in the BF may be slightly more quartz-rich (60% quartz, 30-35% chert, 5-10% others, mostly shale) than in the BBF (50% quartz, 35-40% chert, 10-15% others, mostly shale, Hills 1970). Hills (1970) states that throughout the BF, the quartz is

polycyclic (reworked), whereas the chert and shale are monocyclic. However, the presence of black and grey cherts in the Eureka Sound Group suggests that these may also have been reworked, even if this is not apparent from coatings on the grains. Gravel is up to 12 cm in diameter, sub-round to round, and consists of quartzite, chert, sandstone, and fine resistant sedimentary rock types. Dolomites are rare (Vincent 1990); igneous and metamorphic rocks are absent in most exposures (Fyles *et al.* 1994) but extremely rare in others (Vincent 1990). One occurrence of a quartzite boulder, measuring 1.5 m in diameter, has been documented (Fyles *et al.* 1994).

BF sediment was sourced from the east. Thorsteinsson and Tozer (1962) suggested that Proterozoic rocks on Victoria Is. and Upper Devonian strata on eastern Banks Is. were the source of much of the BF, based on the abundance of multicolored quartzite and chert clasts in the BF. Miall (1979) noted that the orange and brown chert of the BF and BBF contrast with the grey and black chert of the Eureka Sound Group, and that this transition is visible in numerous exploration wells. Fyles *et al.* (1994) proposed that channel orientation, cross-stratification, and mineralogy also indicate that this formation was derived from the east, and not, for instance, from the mountainous regions of the Yukon.

However, there are discrepancies in the paleoflow of the BF at Ballast Brook, which warrant resolution. Although paleoflow in the BF on Prince Patrick and Meighen Is. is generally stated as west and northwest (Thorsteinsson and Tozer 1961, Fyles 1990, Fyles *et al.* 1991), Fyles (1962) stated that the paleoflow direction of the BF at Ballast Brook is southwestward (roughly parallel to the west coast of Banks Is.). As well, Hills (1969) claimed that paleoflow is predominantly westward and southwestward in the upper part of his Unit G (corresponding to the upper Unit A and the Unit B of Fyles *et al.* 1994), whereas Vincent (1990) indicted that it is westward and northward.

3.4 Organics

3.4.1 Physical characteristics of the organics

As at other BF exposures, the BF at Ballast Brook contains remarkably unaltered, uncompressed wood, including water-worn sticks and fragments, but also non water-worn detrital trees with branches, roots and even some bark, and bedding-plane mats of fine plant material that have twigs with cones still attached (Fyles *et al.* 1994). Individual trees up to 80 cm in diameter, logs, and broken, water-worn pieces of wood lie parallel to bedding planes in sand and gravel, and less commonly in silt. Wood lenses are particularly common in trough-crossbedded sand and sandy gravel. There are three types of wood lenses (Murphy 2006). Type A lenses are underlain by a fining upward sediment sequence, and are composed of medium-sized woody debris. These lenses were likely debris jams, based on the size, poor sorting, and random orientation of the wood. Type B is underlain by uniform bedding, and contains only fine and well-sorted plant material. Type B lenses were likely deposited on shallow bars or banks. Lenses that do not correspond to Type A or B are classified as Type C. Articulated pieces of wood, trees with intact limbs, and remnants of bark lie alongside water worn pieces, so although all the plant material is water transported, some appears to have grown nearby (Fyles *et al.* 1994). Two autochthonous organic deposits have been found in the Ballast Brook area: the mossy sand studied by Kuc and Hills (1971) from Section 9a (Figure 3.1 and 3.2), and a partly cemented layer of peat near the top of the BF at Section 2 (Fyles *et al.* 1994).

3.4.2 Importance of the paleoenvironmental record

The organic material of the BF has been studied from pollen (Tozer and Thorsteinsson 1964, Hills 1975), cones (Hills 1969, Hills and Ogilvie 1970), plant macrofossils (Hills 1971, Matthews 1987, Matthews 1989, Matthews and Ovenden 1990), and moss (Hills and Ogilvie 1970, Kuc 1970, Kuc and Hills 1971, Hills and Klovan 1971). Some taxa were documented at Ballast Brook for the first time in North America, and many have paleoenvironmental and phytogeographic implications (Matthews

1989). Hills and Ogilvie (1970) described a new fossil spruce species (*Picea banksii*). Like similar records from other BF sites, the plant materials have a variety of associated insect fossils (Matthews 1974, 1976, 1977, Matthews and Telka 1997). Refining the absolute age of the BF at Ballast Brook would contribute to an improved Neogene biostratigraphy for the Arctic.

3.4.3 Paleoenvironmental comparisons

Similarities between fossil plant communities of the BF at Ballast Brook and the type section on Prince Patrick Is. have been demonstrated by a number of studies (Hills 1969, 1970, Hills and Matthews 1974, Matthews and Ovenden 1990). Both sites are indicative of a coniferous or boreal forest environment (Matthews and Ovenden 1990). Nearly all of the plant families from the BF at these localities have species that presently occur in northern Canada (Fyles *et al.* 1994). For example, *P. banksii* that grew on Banks Is. are relatives of modern *Picea* species*,* which grow in regions where mean July temperatures are 4-16°C (although 12-16°C is most favorable for growth), and where annual precipitation ranges from 500 to 1000 mm (Mendell 2006). The BF flora at Ballast Brook is similar to the modern Arctic treeline environment 600 km south of the study area, based on comparison with the forest composition near Inuvik, NT (Murphy 2006).

Early paleoecological studies assumed that the environmental requirements of extinct species and living counterparts were essentially the same, and thus, made attempts at identifying modern analogues for Pliocene environments (e.g., Roy and Hills 1972, Murphy 2006). Mendell (2006) compared tree ring widths to modern tree ring data. The annual growth of *Picea* suggested a mean annual temperature in the Pliocene at Ballast Brook of -4 to -6°C. Fyles *et al.* (1994) found evidence of extremely slow growth in Unit B, which is similar to growth rates of Pliocene fossil wood from Meighen Is. more than 900 km to the north. In addition, Murphy (2006) found that average ring thickness is larger for unworn wood. This may indicate that the climate was warmer at Ballast Brook than at sites farther up-drainage (i.e. to the east), although water availability may also have played a role in ring thickness (Murphy 2006).

3.5 Age of the BF at Ballast Brook

3.5.1 Comparison with Meighen Is.

As discussed in § 2.3.1, most of the dating techniques that were applied to the BF were restricted to the marine sediments on Meighen Is. or were relatively imprecise. The absence of interbedded marine sediments or of other suitable material for alternative chronometers rendered direct dating the BF at Ballast Brook unachievable. Biostratigraphy with respect to non-BF sites (see § 3.5.2 below) also placed constrains on the age, but these were too coarse to allow confident comparison of Ballast Brook with other BF locations. Thus, biostratigraphy between the BF on Ballast Brook with the BF on Meighen Is. was used to date the BF at Ballast Brook (Fyles *et al.* 1991).

Several studies recognized slight differences in plant microfossil assemblages between Ballast Brook and the type section at Mould Bay on Prince Patrick Is. and between Ballast Brook and the Gap Site on Meighen Is. In particular, the fossil assemblage on Meighen Is. represents a colder forest-tundra boundary environment, and is more depauperate than the coniferous forest flora on Banks Is. (Matthews and Ovenden 1990). For example, the warmer-climate taxon *Physalis* was found at Ballast Brook (in organic detritus draped over a 1-m diameter quartzite boulder at Section 2), but was not found at sites further north. These differences may be because the BF on Banks Is. is slightly older than sites further north, assuming that the climate changed sufficiently during the Pliocene and that species richness varied over time (Fyles *et al.* 1994). Alternatively, these differences may reflect contemporaneous regional variations in paleoclimate (e.g., due to latitude). Interestingly, the BF at Ballast Brook may have a greater abundance of older, rebedded fossils than the BF on Meighen Is. (Fyles *et al.* 1994), suggesting that the comparisons of inter-island assemblages may be more complicated than previously considered.

3.5.2 Biostratigraphic comparisons

The biostratigraphy of the BF at Ballast Brook has been developed using correlations to other circum-Arctic exposures of Neogene strata. The different lines of evidence for

biostratigraphic correlations are presented in this section. The BF flora at Ballast Brook lacks several distinctively mid-Miocene taxa which are present at both Alaskan and Russian sites. Fyles *et al.* (1994) suggested that this means that the BF is younger than Late Miocene, because these taxa have already become extinct in the Ballast Brook region. As well, a BF fossil beetle species (*Asaphidion* cf. *yukonense)* from the lower part of Section 9 is probably more primitive than one at Lost Chicken Mine (Fyles *et al.* 1994). If this is true, it implies that the lower part of the BF at Section 9 is older than the Lost Chicken site (Fyles *et al*. 1994), which was estimated to be 2.9 ± 0.4 Ma, based on tephrochronology (Matthews *et al.* 2003). Further, if, as proposed by Hills and Ogilvie (1970), the extinct *P. banksii* is an ancestor to modern species of *Picea*, then Roy and Hills (1972) argue that the BF cannot be younger than Early Pliocene, because the extant species *Picea glauca* was already in existence 5.7 million years ago. In addition, Fyles *et al.* (1994) writes that the presence of the fossil *Spirematospermum*, unless re-deposited, is consistent with a warmer climate (and therefore an Early Pliocene age) because it is a flowering plant. This interpretation assumes that floral assemblages reflect a general Mio Pliocene cooling trend (over several millions of years) rather than short-term Milankovitch climactic fluctuations (glacial cycles of 41 ka). Based on the same assumption, Fyles *et al.* (1994) states the BF at Ballast Brook is no younger than Early Pliocene if *Spirernato spermum wetzeleri* (ginger family) grew as far north as Banks Is. during deposition of the BF. Taking into account all biostratigraphic evidence, Fyles *et al.* (1994) concludes that the BF at Ballast Brook could represent an extended interval of time ranging from no older than earliest Pliocene (about 5 Ma) to no younger than Late Pliocene (about 3 Ma).

3.5.3 Paleomagnetic stratigraphy

Fyles *et al.* (1994) tried to establish a magnetostratigraphy at Ballast Brook, but found that the sediment is a very poor recorder of the paleomagnetic field, due to low magnetite concentrations and the overall dearth of thick sections of fine-grained sediments (which optimize the recording and measurement of detrital remanence). Tentatively, there appears to be a change from reversed polarity at the base of the BF,

to normal polarity in the middle, and reversed polarity towards the top, implying at least two reversals. However, the data are insufficient for robust correlations to the polarity time scale Figure 3.6 of Fyles *et al.* 1994). Similarly, the data provide no conclusive insight into the duration represented by the BF at Ballast Brook.

3.5.4 State of knowledge on the age of the BF at Ballast Brook

Although there is some disagreement on biostratigraphic interpretations, the BF on Banks Is. is believed to be Pliocene, and "perhaps slightly older, but unlikely younger" than the other exposures of the BF (Matthews and Ovenden 1990). Although Fyles *et al.* (1994) conclude that the BF is likely no older than earliest Pliocene (about 5 Ma), and no younger than Late Pliocene (about 3 Ma), Matthews (1989), states that the flora "provide little definite information on one of the most perplexing problems of the BF– its absolute age".

Chapter 4 : Field Methods and Results

4.1 Field methods

Fieldwork at Ballast Brook (Figure 1.1) was conducted for 30 days in July and August 2013. The fieldwork investigations had multiple objectives. The primary goal was to find suitable TCN burial dating sites to establish an absolute chronology for the Beaufort Formation (BF). The methods and results associated with TCN burial dating are discussed in Chapter 5. Another goal was to increase knowledge of the BF stratigraphy and sedimentology at Ballast Brook, in order to better understand how Ballast Brook differs from other more northern BF sites (e.g., texture, sorting, roundness, clast form, paleoflow, lithology, organic facies, periglacial features). In particular, it was essential to determine whether stratigraphic units can be found at this site, due to the superior exposure of the BF (more than 10 km of continuous exposure, more than 60 m vertically; Figure 3.1) compared to that of other sites.

All of the stratigraphic exposures described by Fyles *et al.* (1994) were revisited (Sections 1-10; Figure 3.2). Sections of the BF stratigraphy were described and measured at both Sites 8a and 9b, after having excavated thawed colluvium (Figure 3.2). Thicknesses were determined using measuring tapes and a Laser Technology Impulse laser rangefinder. The purpose of these measured sections was to provide context for the TCN measurements and add detail to a specific location of the BF and Ballast Brook. Hence, the base of the BF (where the TCN samples were collected) was described in more detail. Additionally, the sub-units identified in these measured sections may not be applicable across the entire Ballast Brook area.

In addition, six pebble counts of lithology (n=50) were performed, two at Section 9 (Unit A2 and Unit A3), one at Section 3 (lower Unit B), two in glaciofluvial gravels capping Section 3, and one from the modern Ballast Brook stream fill. Data for three clast shape analyses (n=25-45) were also collected, two at Section 9 (Unit A2 and Unit A3), and one at Section 3 (lower Unit B). Lastly, the paleoflow was measured whenever it was possible to do so accurately, resulting in 27 individual measurements at Sections 3

and 9 as well as four groups of measurements (n=25-45) at Section 9 (Unit A2 and Unit A3). The results of these investigations are described below.

4.2 Stratigraphic results

In the study area, the BF is incised by Ballast Brook, exposing the BF strata in gullies and large amphitheatres on both the eastern (continuous exposure for more than 10 km, Sections 1-7) and western (thickest exposure, ~80 m, Section 9b) sides of the river (Figure 3.1). Cliffs (strengthened by peat layers and modern permafrost) provide good access to the stratigraphy. The thickest sections received the greatest attention, owing to their higher probability for complete stratigraphy and to their better suitability for TCN burial dating. Section 8 is located on the northern side of a tributary to Ballast Brook (Tributary A; Figure 3.1). Although permafrost was not a major obstacle for excavation of the measured sections, slumping is conspicuous in some gullies, and in other gullies challenging to recognize and avoid. South of Sections 1-9 (Figure 3.1), the BF plateau is eroded at least partly by Pleistocene glaciers (Fyles 1962; Vincent 1982, 1983; England *et al*. 2009; Lakeman and England 2013).

The stratigraphic names and unit divisions used here are in accordance with the most recent analysis of the BF by Fyles *et al.* (1994). Field observations confirm the general stratigraphic framework proposed by Fyles *et al.* (1994) and their interpretations of sandy-gravelly braided river facies. However, new stratigraphic logs illustrated in Figure 3.2 summarize minor but important differences from the Hills (1969), Kuc and Hills (1971), and Fyles *et al.* (1994) records. Whereas the Hills (1969), Kuc and Hills (1971), and Fyles *et al.* (1994) logs are generalized summary logs for Section 9, the logs of the present study are composite measured sections for Sites 9b, 9c, and 8a. Differences for the studied sites include: (1) subdivision of Unit A of the BF into Units A1, A2, and A3, including an inferred glaciofluvial facies (Figure 3.2, Figure 4.1c; § 4.1.1 and 4.2.2), (2) new descriptions of three types of organic facies (Figure 4.4; § 4.1.3), (3) reinterpretation of the stratigraphic position of the unconformity between the BBF and BF (Figure 3.2; § 4.1.4), (4) new recognition of recurring layers of red-stained sand and concretions throughout the field area (Figure 4.5a; § 4.2.5), and (5) new observations of

a shift in paleoflow direction between the bottom and top of the BF (Figure 4.5b; § 4.2.6).

4.2.1 Composite measured section at Section 9b

The most detailed stratigraphic descriptions were performed at Section 9 (Figure 3.1, Figure 4.1). Two logs were measured at Section 9 in order to adequately characterize the apparent facies variability in the lower strata of the BF (Figure 3.2). Due to a topographic ledge 60 m above valley floor at Section 9, the lower 60 m of logs 1 and 2 are from Section 9b, and the upper 24 m are from Section 9c. Section 9 generally coarsens upward, excluding the uppermost ~10 m of fine sands. Logs 1 and 2 are jointly described below.

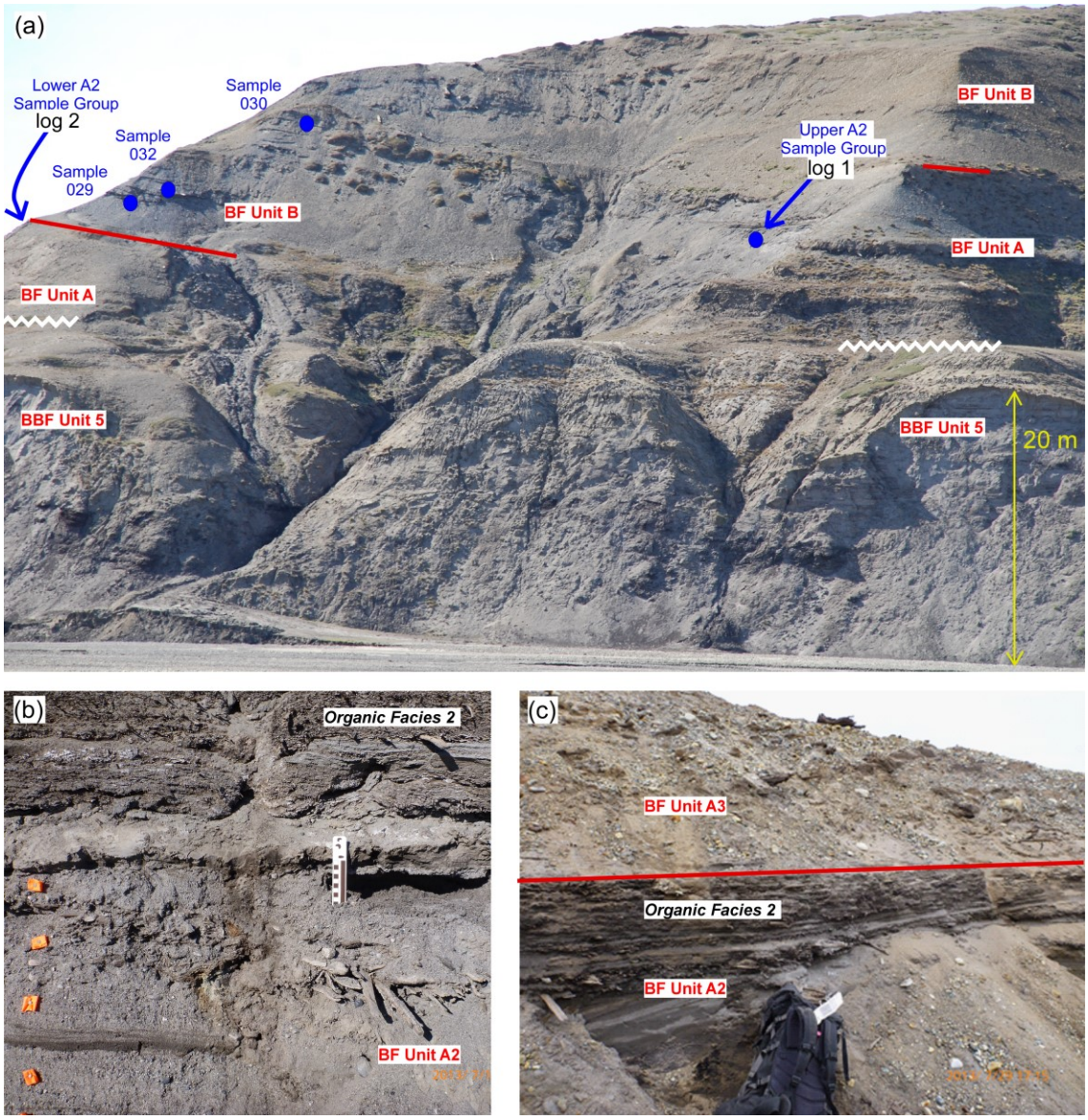

Figure 4.1– Field photos of Section 9. (a) Position and vertical extent of the BBF and BF at the Section 9 bluff, which is facing north-east. The BBF-BF unconformity is at the slope break shown by the white zigzag line (approximately 20 m above the modern river bed at the base of the photo). Beds in Units A2 and Unit B appear to dip northward (to the right of the photo), and shallow northward (measurements not available). Although small channels are present throughout the BF, the dip of some beds appears to be traceable over small distances (~10 m) in the photo. The Lower A2 sample group was obtained behind the visible face, as indicated by the curved arrow. The TCN sampling locations for the Upper A2 sample group and Samples 029, 032, and 030 are indicated by the blue circles. (b) TCN sampling in sand for the Upper A2 sample group, below a bed of organics (Organic facies 2 facies, see below § 4.2.3). (c) Poorly sorted, stained cobbles and sands of Unit A3 above a detritus layer (Organic facies 2 facies, see below § 4.2.3) are shown above the grey, fine- to coarse-grained sands of Unit A2 (below the detritus layer). See Appendix A for more field photos.

BBF-Unit 5

Although the fieldwork did not focus on the BBF, its uppermost sediments and upper contact were described. The uppermost part of the BBF, which overlies the BBF-Unit 4 peat, constitutes fine-grained, light-grey sand. This corresponds to the lower part of the BF-Unit A of Fyles *et al.* (1994; Figure 3.2). For reasons described in § 4.2.4, this package is interpreted as BBF-Unit 5 rather than BF-Unit A. The BBF-Unit 5 rests conformably above the Unit 4 peat. It is a succession of beds 30-50 cm thick, totalling ~ 10 m thickness in places, with varying concentrations of finely interbedded detrital organic matter. The sand itself is finely laminated, alternating between darker and lighter sands (60% quartz, 40% black chert, with other types of chert, garnet, and black undifferentiated grains). Some beds fine upward, but in many locations fining is subtle. Horizontal bedding and shallow-dipping crossbeds are present. In particular, crossbeds of alternate sand and organics (also observed at Section 3) may be a variation on the crossbedded organic facies observed in the BF on Meighen Is. (Davies *et al.* 2014).

The contact with the overlying BF is not well exposed at Section 9b. In places, the contact coincides with a prominent slope break above the BBF Unit 5 fine sands, but is typically covered by several meters of slumped coarse sand from the overlying BF (Figure 4.1; § 4.2.4). This contact is discussed in more detail in § 4.2.4.

BF-Unit A1

The lowest BF stratum at Section 9b is a 2-4 m thick silt and clay unit with minor sand, named Unit A1 (Figure 3.2). It is composed of interbedded tan silt, dark grey clay, and light-grey (outcropping in places as very white) very fine-grained sand, in 2-20 cm thick beds which are locally mottled. Organic beds classified as Organic facies 1 (see below § 4.2.3), are scattered throughout, as are layers of wood chips, which pinch and swell. Unit A1 is laterally variable: in places, it is dominated by very fine sand. In other places, it is composed of homogeneous clayey silt. Some iron concretions were also observed (§ 4.2.5). Despite the grain size variability, Unit A1 is laterally continuous over at least 50 m at section 9b. In one location, mottled clayey silt and very fine sand was observed in an irregular wedge-like shape, and may be an ice-wedge pseudomorph

(Figure 3.2, Figure 4.2). Since no marine shells have been reported in the clays, and no other analyses of the clays suggest a marine environment (Fyles *et al.* 1994), Unit A1 may represent a shallow meandering stream facies, with the silty units comprising crevasse splays, and the more clay-rich units representing laterally discontinuous oxbow lakes (Fyles *et al.* 1994). However, more detailed sedimentological analysis is required to refine this interpretation. Such a low-energy environment is consistent with the relatively flat regional unconformity upon which Unit A1 lies, and may be the result of a period of ponding after the deposition of the BBF.

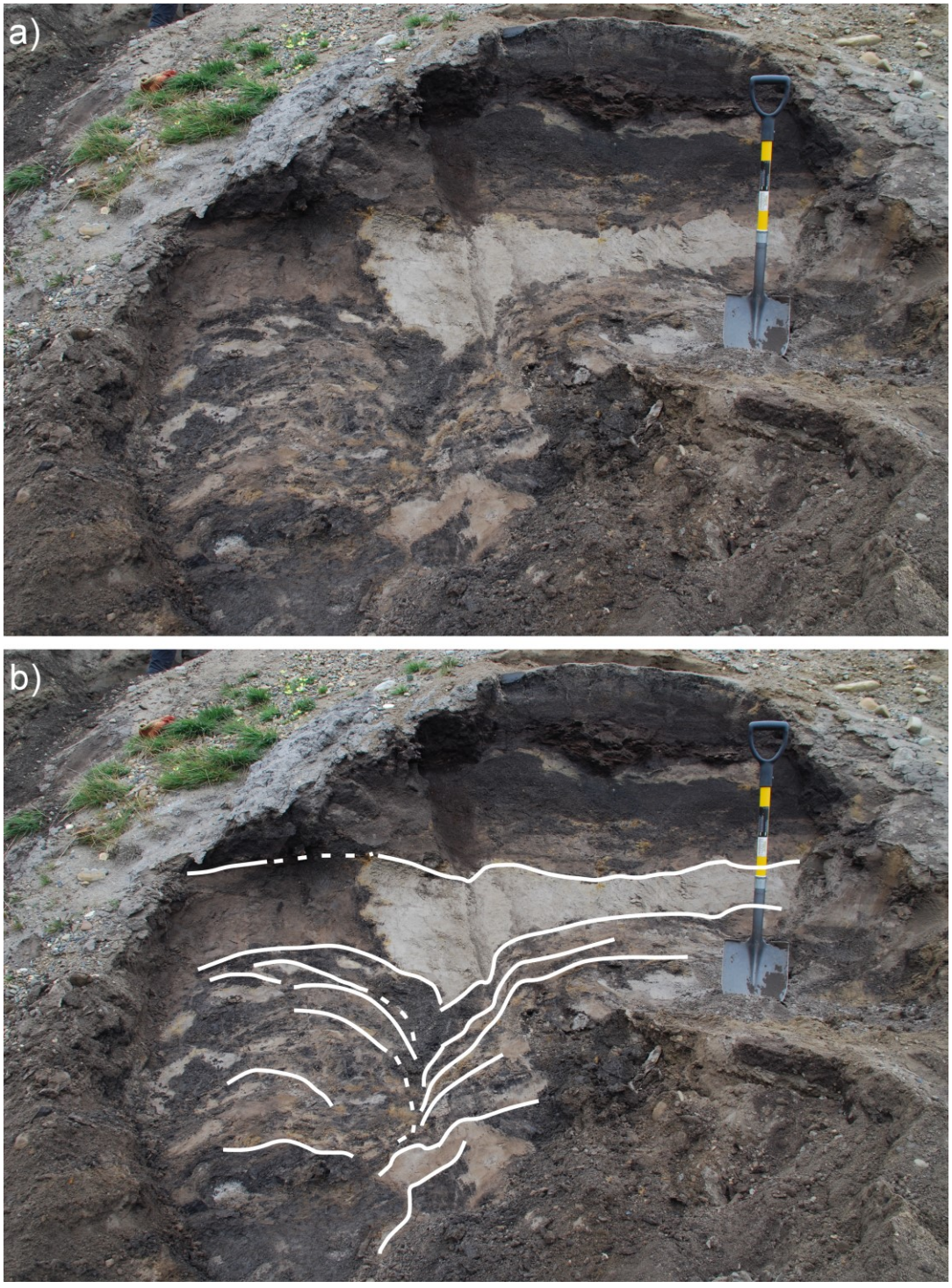

Figure 4.2 - Potential ice-wedge pseudomorph in Unit A1. Beds (1-20cm) of light grey fine sand, tan silt, and dark gray clay seem to form a wedge-like albeit distorted shape that is similar to an ice-wedge pseudomorph.

BF-Unit A2

The sand-dominated Unit A and gravel-dominated Unit B that were described by Hills (1969) and defined more precisely by Fyles *et al.* (1994) at Section 3 (supplementary reference section in Fyles *et al.* 1994) are also present at Section 9b (Figure 3.2, Figure 4.1). Unit A (renamed here Unit A2, ~15 m thick) is composed of fine to medium sand and organic material. The underlying contact with clayey silt of Unit A1 is erosional because it crosscuts underlying beds and constitutes an uneven, wavy surface. This light grey sand is found in horizontal beds or shallow-angle crossbeds. Unit A2 contains common, laterally extensive organic material classified as Organic facies 2 beds (see below § 4.2.3), almost always interbedded with fine sand. In some places, sandy interbeds predominate, and in other places, organic interbeds dominate, but sand is generally more abundant. Isolated cobble gravel lenses were observed and may represent channel lag deposits. Liesegang staining is uncommon but present. Unit A2 is interpreted to be a sand-dominated braided river environment, with rare gravel channel lags. The south side of a 20-m nested channel was excavated, including an angular relationship with underlying beds. The channel was immediately overlain by Organic facies 2 beds (bedded wood chips, see below § 4.2.3).

BF-Unit A3

A 4-5 m thick bed of poorly- to moderately-sorted coarse (cobble) gravel with distinctive yellow-blue staining was observed at Section 9b (here named Unit A3; Figure 4.1c). Clast shape analyses suggest the presence of more faceted and striated clasts than in Unit A2 (48% faceted clasts compared to 22%, and 4% striated clasts compared to 2%; n=50, two analyses in Unit A2 and A3 respectively), although insufficient sample size for the clast analysis of the other units precludes a statistical comparison. Observed striations are not likely caused by landsliding, since high-relief terrain is absent in the region. The gravel occurs in nested, narrow channels (less than 5 m depth) where graded bedding was not observed. The flow direction, determined from channel orientation and the alignment of 4-10 cm twigs and isolated logs immediately underlying the gravel is northward, which contrasts with the westward paleoflow in the rest of the lower BF (§

4.2.6). Unit A3 is interpreted as an ice-proximal, braided glaciofluvial deposit, based on the presence of striated clasts, the slightly poorer sorting compared to the overlying BF units, and the change in paleoflow direction. Lastly, Unit A3 may be equivalent to sulfur-coated gravels observed at Section 8, unless the staining in those gravels is related to the influence of modern or previous permafrost (§ 4.2.5).

Unit A3 occurs within the stratigraphic extent of Unit A2, within several meters of the potential ice-wedge pseudomorph in Unit A1 (Figure 3.2). Because the gravel was only observed at one location, was exposed on the confluence of Tributary B and Ballast Brook, and occurred at the same height as glaciofluvial terraces less than 1 km south of the exposure, it is possible that it was not part of the stratigraphy (i.e., a surficial deposit on the slope face). However, the preferred interpretation is that Unit 3A was in place. It could be traced for ~ 40 m (although it could not be traced further, a channel facies would be expected to show lateral variability). Furthermore, the gully in which the gravels were observed and described was freshly eroded by several meters at least, based on the steepness of slopes and the concave amphitheatre morphology (~ 40 m wide).

BF-Unit B

Unit B (~40 m thick) is dominated by moderately-sorted sandy gravel and organic matter that slightly coarsens upward, then fines upward. At the base of Unit B, a series of five fining upward cycles diminish in thickness from 2 m to 30 cm, and grade from pebble gravel to coarse sand with pebbles. The overlying 4 cycles (~2 m each) are slightly coarser (sandy pebble gravel), and mud rip-up clasts and wood are locally present. The individual fining upward packages are either composed of massive beds, or of thin (3 cm thick) beds which include organic interbeds. The uppermost part of Unit B constitutes 7-10 m of alternating trough crossbedded sand and massive sand, which was also reported by Kuc and Hills (1971) and Fyles *et al.* (1994; Figure 3.2). Some of these uppermost beds contain rare mud rip-up clasts, pebbles, and cobbles. Cobble and pebble lithology for Unit B is 30-50% quartzite, 25-60% chert, with the remainder consisting of sandstone, siltstone, and rare carbonates and ironstones. Toward the top of the unit, this matrix-

supported gravel is locally characterized by over-steepened crossbeds and deformed organic layers.

The first 64 m of the composite measured section in Figure 3.2 were measured and described at one site (Figure 4.1a; Section 9b in Figure 3.1), and the upper 20 m were measured and described at another site (with less than 1 km distance between the two sites; Section 9c in Figure 3.1). The upper 20 m in Figure 3.2 include four fining upward packages, which grade from coarse sand with pebbles to clay and Organic facies 3 (see below § 4.2.3). The uppermost 8 m constitutes horizontally-bedded fine sand with occasional interbeds of Organic facies 2 (see below § 4.2.3); this is similar to Unit A but lacks Organic facies 3 and gravel lags. It contains clayey-silt beds, associated with Organic facies 1 (see below § 4.2.3), but there are large zones of massive fine sand. The channels are broader than in underlying strata (bedding more horizontal), with the exception of one Organic facies 3 lens near the bottom (0.5 m-thick, laterally discontinuous lens of wood detritus; see below § 4.2.3). Unit B is interpreted to be a forested fluvial gravelly to sandy braided stream deposit.

Capping sediment

The capping sediment (averaging 1-2 m) is a massive, poorly sorted diamicton with a silty and sandy matrix and clasts sizes up to 1 m (Figure 3.2). In places, this diamicton is underlain by ~0.5 m of red, medium-grained, massive sand. The red staining appears to reflect iron-oxidation with hematite cementation. Contact with the underlying BF-Unit B strata is sharp and undulatory, with a relief of one or more metres. The diamicton is interpreted as a till on the basis of striated clasts (more than 5 %); this is consistent with previous studies on the glacial geology of northwestern Banks Is. (Vincent 1990, England *et al.* 2009; Lakeman and England 2013).

At the very top of the exposure is a cryic-entosol with a moderately-developed A-horizon (black) and weak B horizon (brown). Some clasts in the soil have vertically-oriented long axes, indicating cryoturbation. The soil is not uniformly thick, in part because the top of this unit is a hummocky till landscape, and in part because of surface erosion and solifluction across the dissected BF plateau. Oxidized sand crops out in

places and may constitute buried B-horizons; however, this was not studied in detail. No other evidence of buried soils was observed in the diamicton, but this does not preclude the possibility that the diamicton represents more than one glaciation. A Holocene peaty soil (up to several meters thick) was observed near Section 3.

Observations consistent with previously-mapped channel

Our observations may support Hills' (1969) description of a large channel, whose edge coincides with the location of Section 9. Observations consistent or contradictory with this mapped channel are explained below; the favoured interpretation is discussed in § 7.6.1. The northward dip of Units A2 and B, which shallows northward, is visible from afar (Figure 4.1). However, it was not identified while on the section, and as such, no measurements of dip were recorded. It is not possible to determine from the photo at which exact stratigraphic level the beds change dip (e.g., whether the base of Hills'(1969) channel would fall at the base of Unit A2, or within Unit A2 at the base of Unit A3). The northwestern paleoflow measured in Unit A2 is also consistent with Hills' (1969) observations. The presence of smaller nested channels within Unit A2 is consistent with the nearby edge of a larger channel; however, these are non-unique, as channels are abundant throughout the field area. Unit A1 is horizontally bedded and parallel to the underlying unconformity, suggesting that it is a distinct sediment package from the overlying sediment (i.e. potentially below the channel).

It was not possible to fully relocate Hills' (1969) channel. For example, the erosion of the BBF Unit 4 peat by the channel was not observed. Instead, the peat, which dips northwest, was observed to reach the valley floor ~50-100 m north of Section 9. To the south of Section 9, the BF is eroded, so the margin of the channel (i.e., juxtaposed beds of differing age and sedimentology) could not be observed. The other side of the channel (several kilometers north) also could not be relocated (although only a few hours were spent looking for it). Much of the supporting observations for Hills (1969) channel rely on the apparent inclination of the unit contacts at Section 9 (Figure 4.1a). Furthermore, paleoflow in Unit A3 was northward (see below § 4.2.6), and paleoflow throughout Ballast Brook (including at Section 9) was more northward in the upper BF.

This contradicts the westward paleoflow in Hill's (1969) channel, and may reflect the uncertainty associated with a low number of paleoflow measurements (discussed in § 4.2.6).

4.2.2 Measured section at Section 8

Section 8, on the north bank of Tributary A (Figure 3.1), exposes a thinner sequence of BF sediment than does Section 9b (Figure 3.2, Figure 4.3a). Unit A is entirely absent at this location (Figure 3.2, Figure 4.3a). Overall, the sediments coarsen upwards then fine again, as observed at Section 9b.

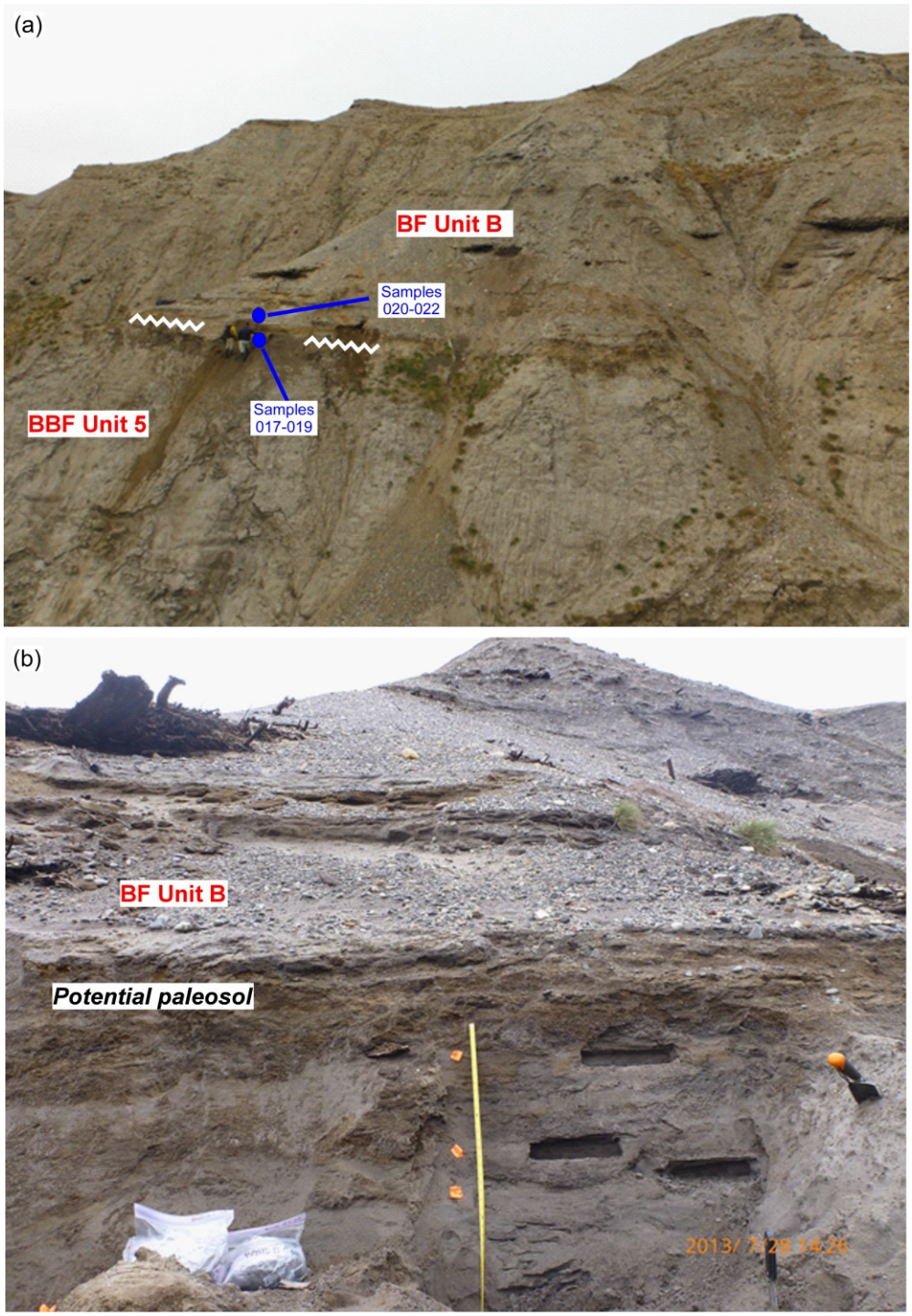

Figure 4.3 – Field photos of Section 8. (a) The sampling context for Section 8. The sample group which was analyzed is composed of Samples 020-022, above the unconformity. The unconformity coincides with the break in slope. The coarser sediment of the BF (Unit B) directly overlies the break in slope. (b) The lower oxidized soil zone (with samples 017-019 obtained below this zone). The unconformity would presumably be just above this soil.

Potential paleosol

At Section 8, there appears to be a paleosol straddling the regional unconformity (Figure 3.2, Figure 4.3b). A purple-black sandy silt (~3 cm thick) sharply overlies very fine to fine sand, which is parallel bedded and ripple cross-laminated, with some silt beds (3 cm thick). The purple-black sandy silt exhibits cohesion with blocky structure and may represent pedogenic structure in an organic-rich A-horizon. Below the purple-black horizon is a less than 1-m thick red to red-brown and yellow-brown sand, which may be a buried B-horizon. Above this is ~1 m of red, medium- to coarse-grained sand, which is trough crossbedded and has sparse woody detritus with rounded cross-sections. This may be another soil oxidation zone above the purple-black A-horizon.

Overlying this potential paleosol, there are 20 cm of massive brown silt, 40 cm of fining-upward, trough crossbedded fine- to medium-grained sand, and a cross-laminated dark grey-purple fine- to very fine-grained sand with green mottled silt. Altogether, the zone of reddened sand appears to top several topographic spurs in the gully, below a zone of uncompressed sticks in coarser brownish-red and tan BF sand (Figure 4.3a). Hence, this cemented oxidized zone forms a resistant layer that is apparent across the bluffs at Section 8.

BF-Unit B

The potential paleosol is overlain by ~5 m of coarse sand with granules, although the lower part of this package contains silty sand beds (Figure 3.2, Figure 4.3b). The sand is either massive, with planar laminations, or with low-angle crossbeds. It is tan to grey (more tan than higher in the section), although some beds appear reddened. This sand package also contains accumulations of Organic facies 2 (horizontal, planar, laminated rhythmites) and 3 (larger logs deposited in small channels; see below § 4.2.3).

Above this, the BF continues to coarsen upward, with a series of 2-m thick fining upward packages that include pebble gravel, coarse-, medium-, and fine-grained sand, and rare silt beds (Figure 3.2). Here, the sediment is light grey (compared to the tan colour lower in the section near the BBF-BF contact). The sand is either very well-sorted, or contains granules, pebbles and sometimes cobbles. Fine sand is commonly

interbedded with Organic facies 2 in horizontal, planar, laminated rhythmites (see below § 4.2.3). Coarse-grained sand forms trough crossbeds. The coarse-grained sands and gravels are interspersed with Organic facies 1 as lenses of wood that pinch and swell, typically located in small channels (~5 m wide; see below § 4.2.3). One fining-upward section is capped by a cliff-forming silt bed. Near the top, one *in-situ* layer of small (2-4 cm), red, sandy concretions was observed.

Above these Unit B braided stream sediments, a fine-grained, poorly-sorted, polymictic diamicton uniformly drapes the top of the cliff (Figure 3.2). This is likely the Pleistocene till also found at Section 9b (described by Vincent 1990, England *et al.* 2009; Lakeman and England 2013).

4.2.3 Organic facies

Organic beds with well-preserved woody detritus, which vary in their prevalence throughout the BF, mainly occur as one of three types that are distinguished based on the size and preservation of organic material and on associations with bounding clastic sediment (Figure 4.4).

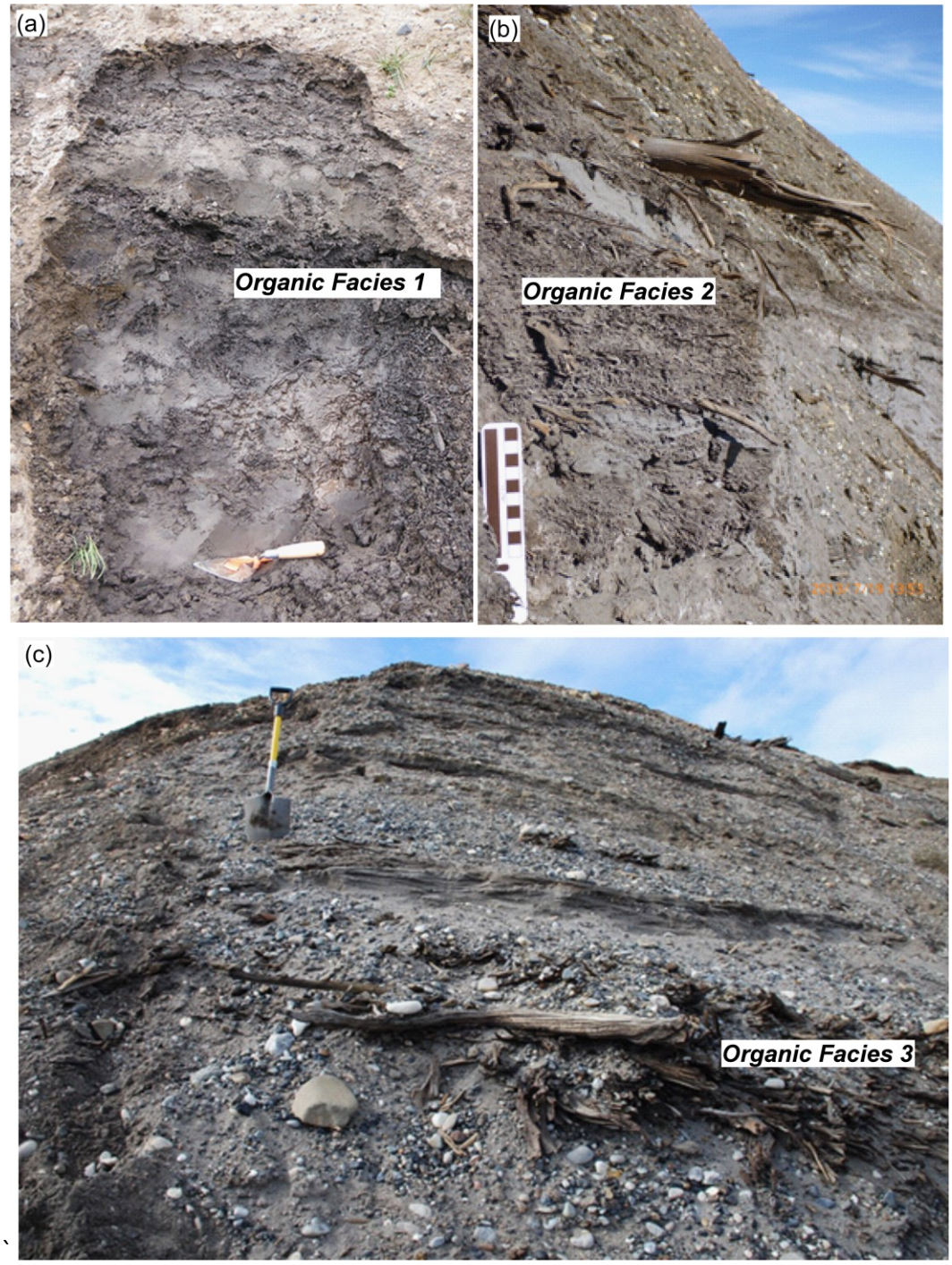

Figure 4.4 – Field photos of the organic facies. (a) Organic facies 1, composed of flattened wood flakes and leafy material, associated with clay and silt. (b) Organic facies 2, composed of rounded wood chips, interbedded with fine-grained, grey sand. The occasional twig and log can be found. (c) Organic facies 3, with larger logs and associated with coarser sediment and small channel fills. All photos are from Section 9. The orientation of wood chips in Organic facies 2 and of logs in Organic facies 3 were used for paleoflow measurements (see below § 4.2.6).

Organic facies 1 facies

Organic facies 1 ('Organic facies 1'; Figure 3.2; Figure 4.4a) constitutes wood flakes interbedded with silt and mud. The layers are thin flakes of wood that are pressed flat against each other, as well as amorphous organic matter (resembling 'coffee grounds'), filaments, twigs, and occasional wood chips with smoothed ends (less than 1 cm to several cm in length). The Organic facies 1 beds contain varying amounts of silt. Rare, larger pieces of wood (up to 25 cm in length) are concentrated in layers or dispersed throughout. No Organic facies 1 plants were found in growth position, and no roots were seen. Organic facies 1 is interpreted to be the cap of aggrading channels, based on the association with silt and mud, and the high concentration of amorphous and delicate organics in planar parallel bedding. Organic facies 1 is not horizontally extensive, because it is mostly associated with the clay and silt of Unit A1, which do not extend laterally over more than one or two meters.

Organic facies 2

The second type of organic facies ('Organic facies 2'; Figure 3.2; Figure 4.4b) is composed of laterally extensive (~ 20 m) beds of bark, indeterminate wood fragments, twigs, and pine cone fragments that range from flattened to fully rounded cross-sections, with diameters ranging from 1 to 5 cm, and 'coffee ground' organics. Organic facies 2 beds are commonly interbedded with fine, light-grey sand, and the organic beds themselves are sandy or silty. The interbeds are planar and parallel, typically 1-2 cm thick and rhythmic, over 1 to 2 m. Smaller packages of rhythmites may also accompany thicker beds of wood chips. Often, the clastic beds collectively (rather than in each interbed) fine upward from silty, fine-grained sand to fine- or medium-grained sand. The wood chips are generally parallel to each other, and parallel to occasional larger sticks. Organic facies 2 beds probably are the aggrading final stages of larger channels (~ 20 m wide), based on their occurrence above channels in the section.

Organic facies 3 facies

The third type of organic facies ('Organic facies 3'; Figure 4.4c) is composed of much larger logs, nested against one another, with a wider range of orientations than the wood chips in Organic facies 2 (Figure 3.2). These wood lenses are less laterally extensive than Organic facies 2; they typically taper off in less than 5 m and are irregular. The logs are often imbricated, split at the ends, and accompanied by minor amounts of smaller woody detritus. Unlike the other two types of organic facies, Organic facies 3 beds are not interbedded with clastic sediments, although they are usually associated with pebbly, coarse-grained sand with some cobbles. Organic facies 3 beds are interpreted to be the logs carried and deposited in small (less than 5 m) but energetic channels, perhaps as log jams.

Other organic material

The autochthonous peat described by Kuc and Hills (1971) in the BF was revisited. It is different than Organic facies 1-3 facies because it contains much more leaf matter, less wood, and less clastic material, and as a result, it appears more matted (Kuc and Hills 1971).

The only other observations of *in-situ* organic material at Ballast Brook were a cone delicately attached to a twig, a 10 cm-thick autochthonous peat, and a 2 m-tall stump in growth position. The cone was found approximately 25 m above the base of Section 9, on a bench marking the BBF-BF unconformity, and most likely part of the BF (Figure 3.2). The 10 cm-thick peat (horizontal extent less than 0.5 m) was located just south of Section 3 approximately half-way up the section (Figure 3.1). Individual moss stems were upright and very well-preserved. The thin layer of peat contained little to no clastic material. The upright stump was found near Section 2 (Figure 3.1) about half way up the section in a modern amphitheatre gully.

4.2.4 Unconformity

The location of the unconformity between the BBF and BF has been a point of debate in published literature (Hills 1969, Kuc and Hills 1971, Fyles *et al.* 1994). The

present work, based on observations at Section 8a and 9a (which were not as thoroughly described by Fyles *et al.* 1994), favours the original interpretation by Hills (1969) that the unconformity is above the BBF-Unit 5 package of light-grey fine-sands (Figure 3.2).

At Section 9, the contact between BBF-Unit 5 and the underlying peat is not erosional. The upper portion of the peat is mixed with clastic sediment, and the fine-grained sand package is rich in detrital organic layers. The contact is sharp, but does not cut down into the peat. In contrast, the contact between the BBF-Unit 5 and the BF-Unit A1 is sharp, including truncation of the underlying crossbedded sand (§ 4.2.1). It is undulatory, with relief up to 1 m, indicating erosion of the underlying sands. This preferred interpretation for the location of the unconformity at Section 9 also coincides with a subtle change in mineralogy (from 60% quartz and 40% chert in the BBF to 75% quartz and 25% chert in the BF; originally observed by Hills 1969), as well as a prominent slope break (Figure 3.2).

At Section 8, the preferred interpretation of the unconformity's stratigraphic location is also above the BBF-Unit 5 light-coloured fine-sand package (Figure 3.2, Figure 4.3a). Although the contact is not sharp at this site, this interpretation is supported by two observations. First, the potential contact is highly oxidized, with a dark organic horizon (approximately 15 cm) suggesting a soil zone (§ 4.2.2). Second, wood lenses change from altered (soft, friable to powdery), flattened wood (characteristic of the BBF) below this contact, to well-preserved, rounded wood (characteristic of the BF) above this contact. This change is visible on most slopes at Section 8, approximately 15-20 m below the top of the exposure (Figure 3.2), and also coincides with a slope break traceable across several gullies (for approximately 1 km).

At Sections 1-7 (Figure 3.2), the BBF-Unit 5 is absent (Fyles *et al.* 1994). Therefore, the unconformity is directly above the BBF 3-m thick peat (or above the silt at Section 3), and forms an erosional contact with the overlying BF sands. By extension, Fyles *et al.* (1994) inferred that the unconformity at Section 9 is also directly above the peat, and thus below the light-grey fine-sand package (Figure 3.2). At Section 8, they also define

the unconformity below this package, assigning it to the BF, and referring to the “basal white colour of the Beaufort Formation visible from afar”.

Therefore, despite remaining uncertainty, the new set of observations supports the original interpretation by Hills (1969) and Kuc and Hills (1971) that the unconformity is above the BBF- Unit 5. Thus, the white beds visible from afar (Fyles *et al.* 1994) are actually the uppermost BBF beds. It should be noted that, neither interpretation (i.e. Hills (1969) and Kuc and Hills (1971), or Fyles *et al*. (1994) has been confirmed by plant macrofossil analyses because the fine sands have insufficient organic material for adequate sample size (Fyles *et al.* 1994).

4.2.5 Concretions

Iron-oxidized sand beds with concretions cap topographic spurs near the top of the exposed BF across Ballast Brook valley (Figure 4.5a). At Section 3, separate occurrences are aligned at 310°. At Section 9a and 9b, an oxidized sand and concretion layer crops out for more than 1 km on topographic noses (Figure 3.2). Lastly, a single row of concretions (<5-10 cm) was found *in-situ* in grey sand ~10 m from the top of Section 8. All of these occurrences occur approximately 50 m above the valley floor of Ballast Brook.

The concretions are present primarily in coarse-grained, granular or pebbly sand (Figure 4.5a). The red colour implies that hematite is the primary cement. The cement could also be calcium carbonate; however, limestone or marble clasts are uncommon. The concretions are mostly spherical or oblate, and range in size from multiple sand grains to several decimetres. The concretions are associated with and observed to be in contact with iron-stained wood, cones, and peat, which is commonly lithified in compressed, oxidized blocks that resemble manufactured wood or aspenite. These iron-stained layers may be the **“**partly cemented layer of peat near the top of the Beaufort Formation at locality 2” mentioned by Fyles *et al.* (1994).

4.2.6 Paleoflow direction

Paleoflow was primarily to the northwest in the lower third of the BF, trending to north and northeast in the upper BF, as determined from 17 individual measurements and 4 groups of measurements (n=25-45), using the axes of channel troughs, the axes of trough crossbeds (Figure 4.5b), the orientation of small wood chips (approximately 2-5 cm) and isolated or imbricated straight sticks (10-30 cm long; Figure 4.4). There is some uncertainty in these paleoflow measurements because like elongated clasts forming a fabric, wood chips can be oriented parallel or transverse to flow; larger sticks can also form log jams and also be transverse to flow (Figure 4.6).

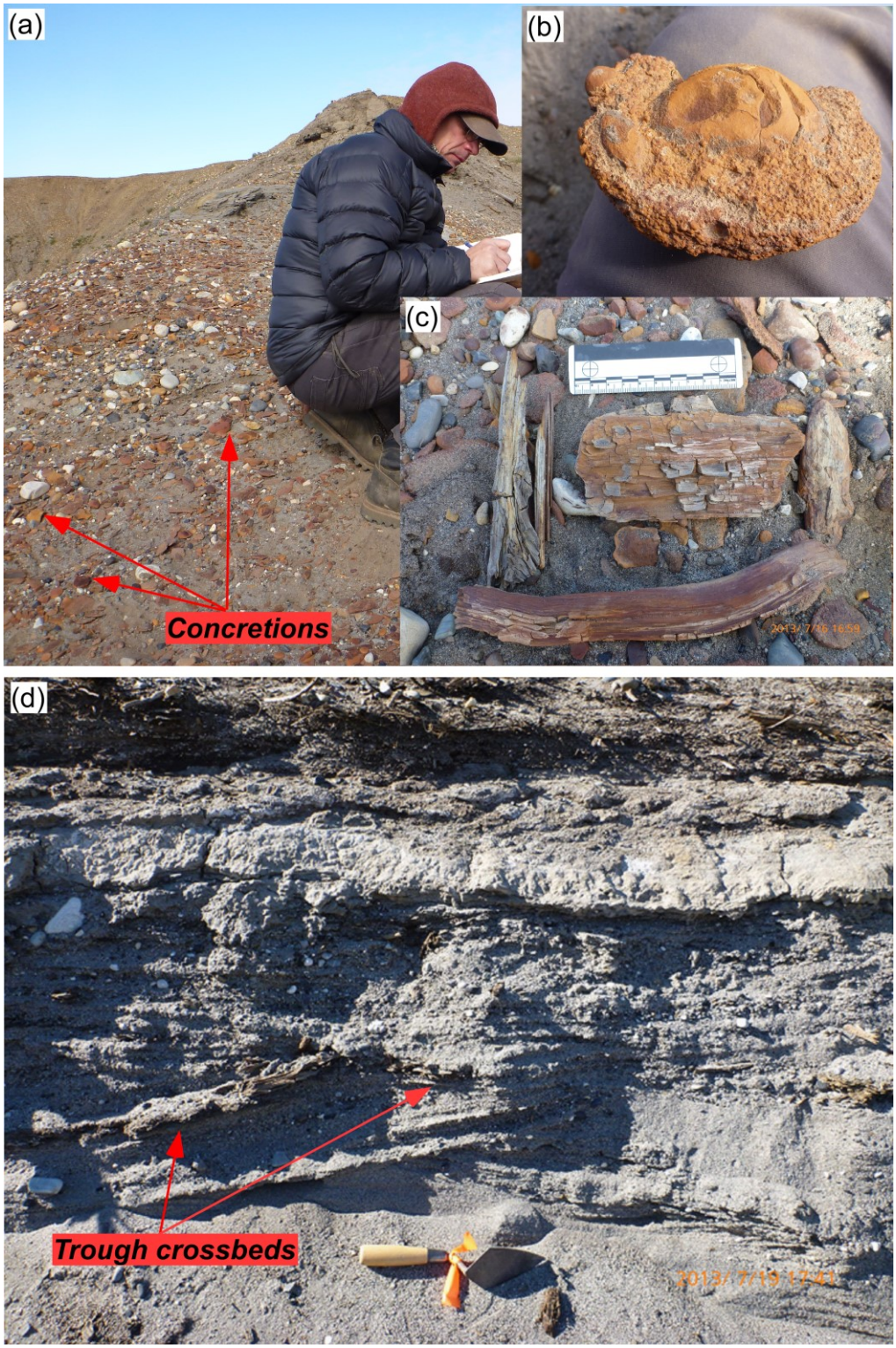

Figure 4.5 – Field photos of concretions and trough crossbeds. (a) Concretions on topographic noses at Section 3, often associated with oxidized wood and allochthonous peat. (b) Close up of concretion. (c) Associated red-stained organic material. (d) Trough crossbeds in a cut approximately normal to paleoflow.

The northwesterly flow direction in the lower BF was generally observed on the eastern wall of Ballast Brook, as well as at Sections 8 and 9 (Figure 3.2). For example, in Unit A2 at Section 9b, 19 measurements of the long axes of trough crossbeds (Figure 4.5b) yielded a direction of 320 ± 10° (2 σ), and twigs (3 cm long) in the woody detritus less than 1 m above this were oriented 320 ± 10° (2 σ; n=45; Figure 3.2). In contrast, measurements in trough crossbeds higher in Unit A2 and in Unit B were predominantly northerly. However, the measurements of flow directions were too variable be linked with a stratigraphic change. This is either because the change in paleoflow is gradual, exhibiting variability over a large range in elevation, or because the number of observations is insufficient to properly characterize the variability.

One exception to this general pattern is Unit A3, in the lower BF at Section 9b (Figure 3.2), which has a northern paleoflow (§ 4.2.1): woody detritus above gravel (Organic facies 2 twigs 4-10 cm; § 4.2.3) had an orientation of 000 ± 15° (2 σ; n=38), and isolated Organic facies 3 logs (§ 4.2.3) were oriented toward 005 ± 15° (2 σ; n= 34). Although paleoflow can vary due to channel bends, this may represent a more northerly transport of the glaciofluvial sediment in comparison to the rest of the BF.

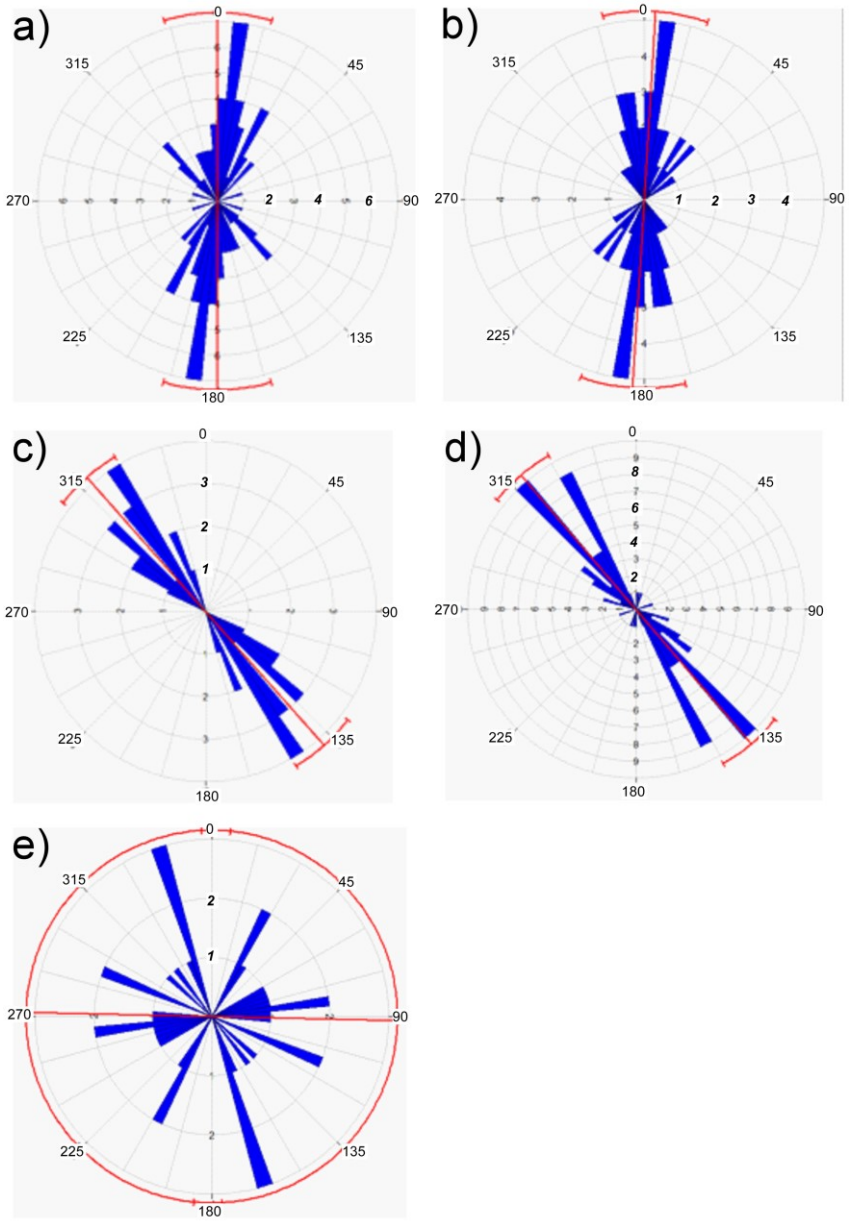

Figure 4.6 - Paleoflow measurements at Section 9. In these rose diagrams, azimuth direction is indicted by the labelled numbers external to each circle (unit = °), and the number of measurements are indicated by the labelled numbers within the circles (unit = counts). a) Measurements in the Organic 2 facies (~50 cm thick) immediately below Unit A3, from twigs 4-10 cm. b) Measurements from mainly isolated logs within the Unit A3 gravel . c)Measurements from trough cross beds in Unit A2 at the level of the Lower A2 sample group. d) Measurements in the Organic 2 facies above the Lower A2 sampling group, from in twigs >3 cm long. e) Measurements in Unit A2 and Unit B. These paleoflow measurements do not allow for a statistical comparison due to insufficient sample size (n= 25-45).

Chapter 5 : Methods and Results - Cosmogenic Nuclide Burial Dating

5.1 Cosmogenic burial dating methods

5.1.1 Method overview

The Beaufort Formation (BF) is too old to be dated using radiocarbon or optical luminescence techniques. Tephrochronology has been successfully applied to late Cenozoic sediments in Alaska and Yukon, where ash was in stratigraphically useful positions (Westgate *et al.* 1985). Previously applied dating methods have narrowed the possible age of the BF to between 3 and 5 Ma (e.g. using amino acid racemization on mollusc shells, comparisons of Sr isotopes in molluscs with a global marine time series, foraminifera and mollusc biostratigraphy; Fyles *et al.* 1991). Terrestrial cosmogenic nuclide (TCN) burial dating is a relatively new approach that has recently been successfully applied to Pliocene Arctic sediments (Rybczynski *et al.* 2013; Hidy *et al.* 2013). TCN burial dating has many advantages over previously applied methods, including offering absolute ages, the prospect of widespread applicability (i.e. only requirement is quartz sand; Gosse and Philips 2001), and total internal errors of approximately ± 0.5 Ma or less (1 σ; Hidy *et al.* 2013, Rybczynski *et al.* 2013)

This study has two primary goals for the use of TCN: i) calculating new TCN burial ages for the BF at Ballast Brook, and ii) calculating paleo-erosion rates of the BF source catchment. TCN burial dating is based on the production of the radionuclides ^{26}Al and ^{10}Be in quartz (Lal 1991, Nishiizumi *et al.* 1993, Gosse and Phillips 2001). Concentrations increase when the quartz is exposed to cosmic rays. When it is buried deeply (> 30 m of sediment for significant shielding from muons), concentrations diminish because the radioisotopes decay. The ^{26}Al:^{10}Be changes predictably with burial duration, because ^{26}Al and ^{10}Be have different half-lives (0.70 Ma and 1.37 Ma respectively; Nishiizumi 2004, Korschinek *et al.* 2010). Thus, the ratio of cosmogenic ^{26}Al:^{10}Be in the BF can be

measured to determine how long ago sampled sediment was deposited. Once the burial age is known, catchment-wide paleo-erosion rates can be calculated from the concentration of a single nuclide (i.e., ^{10}Be; Shaller *et al.* 2006, Hidy *et al.* 2013). ^{10}Be concentrations in buried fluvial sediment depend on the duration of time for which that sediment was exposed on the catchment (longer exposure for lower erosion rates; Lal 1991). TCN results did not allow for the use of the depth-profile isochron burial dating method, so although it was attempted, it is not described here in detail.

5.1.2 Sampling methods

Chapter 4 describes in detail the sedimentology and stratigraphy of two exposures at Ballast Brook. The measured sections at Sites 8 and 9 also provide context for TCN sampling. Initially, *in-situ* peat layers or soils (which may indicate prolonged exposure) were sought for 'depth profile' isochron burial dating (Balco and Rovey 2008); however, no *in-situ* peat or paleosol was found at Section 9b. Instead, five samples were collected from immediately below the thickest bed of Organic facies 2 in Unit A2, in hope that the thickness may have corresponded to thousands of years of exposure (log 1 in Figure 3.2). The samples were collected along a 1-m vertical profile, approximately 10 cm apart. A group of four additional samples (along a vertical profile with 10 cm spacing) was collected from Unit 2 sediments immediately underlying Unit A3 (glaciofluvial gravels in Figure 3.2). As well, 3 samples were collected along a vertical transect, measuring approximately 7 m in length and with meter-scale sample spacing, from the lower part of Unit B (Figure 3.2). At Section 8, two sample groups (3 samples each) were taken from above and below a soil that may represent the unconformity (§ 4.2.2; Figure 3.2).

Each sample consisted of 3-4 kg of quartz sand (ensuring sufficient mass for duplicate measurements if needed), and comprised no more than 5-7 vertical centimetres. At each sampling location, the latitude, longitude, elevation, and sample thickness (Appendix B) was precisely recorded to enable calculation of site-specific TCN production rates.

Chosen sampling locations satisfied cosmogenic burial dating requirements of deep sampling (> 30 m below the top of the stratigraphic exposures) and availability of

relatively coarse sand (250-350 μm). Deep sampling is necessary to reduce uncertainties in post-burial nuclide production from deeply penetrating muons (Granger and Muzikar 2001), and coarse sand is necessary for the sample preparation procedures (particularly the dissolution of 35% of the outer portion of each quartz grain to remove any meteoric ^{10}Be; Kohl and Nishizumi 1992, Gosse and Phillips 2001). Although the sediment immediately below the Miocene Ballast Brook Formation (BBF) Unit 4 peat was ideal for depth profile burial dating and sufficiently deep, it was deemed unsuitable for TCN burial dating because the grain size was too fine.

5.1.3 Sample preparation and analyses

Sample preparation was carried out at the Dalhousie Geochronology Centre (DGC). After rinsing with water and drying, a sufficient mass of 250-350 μm grains was obtained by sieving, and by crushing from 355-800 μm if there was insufficient mass from sieving. Quartz was then purified, using a combination of hand picking of magnetic grains, magnetic separation (Frantz Magnetic Separator), froth flotation, air abrasion, and selective chemical dissolution (e.g. HF with HNO_3 in hot, ultrasonic baths). After addition of ^{9}Be carrier (produced at DGC from a Ural Mountain phenacite; Carrier Be31 has 282 ±5 μg/mL Be, and ^{10}Be/^{9}Be typically below 5 x 10^{-16}, e.g. no counts in 300 s at > 10 μAmp) at Lawrence Livermore National Lab (LLNL; where the accelerator mass spectrometry was conducted), 95 -120 g of pure quartz was dissolved with trace-metal grade HF and Aqua Regia. Al carrier was not necessary because of sufficient native Al in the samples (determined with inductively coupled plasma optical emission spectrophotometry, ICP-OES, at DGC). The large sample masses were used because of the anticipated significant loss of the radionuclides due to prolonged decay (i.e. millions of years of burial). Fluoride was removed by repeated perchloric acid dissolutions and dry-downs. Next, Al and Be were isolated with anion chromatography (using 10 mL resins, due to the large sample masses), a pH-controlled precipitation (to remove unwanted cations), and two iterations of cation chromatography (the first to extract the majority of the Al, and the second to isolate Be from Ti). Before and after quartz digestion, aliquots were extracted and diluted for ICP-OES analysis of Al, Be, and Ti,

using the sequential dilution method. Lastly, $Al(OH)_3$ and $Be(OH)_2$ were precipitated with ultrapure ammonia gas, and ignited in a low-boron quartz vial, using a Bunsen flame. The resulting 0.3 mg of BeO and Al_2O_3 were mixed with ultrapure niobium, and packed into stainless steel cathodes.

^{26}Al:^{27}Al and ^{10}Be:^{9}Be were determined with Accelerator Mass Spectrometry (AMS) at LLNL. Process blank subtraction (1.60×10^5 ^{26}Al atoms, and 2.48×10^4 ^{10}Be atoms) averaged 3% of ^{26}Al, and 2% of ^{10}Be. The ^{26}Al concentration ranged from approximately 1.5×10^4 to 6.0×10^5 atoms g^{-1} and the ^{10}Be concentration ranged from approximately 9.5×10^3 to 1.6×10^4 atoms g^{-1}. Precision of the AMS measurements averaged 22% for ^{26}Al measurements and 3% for ^{10}Be measurements. Internal errors reflect 1) the AMS error, 2) the 2% error contributed by the sample preparation chemistry and the Be and Al elemental concentrations determined with ICP-OES, and 3) the error contributed by the uncertainty in the process blank subtraction (atoms g^{-1}), weighted for each sample. External errors reflect systematic and random errors contributed by, for instance, uncertainty in production rates at each sample, and the decay constant of ^{26}Al and ^{10}Be (Gosse and Phillips 2001).

5.1.4 Data reduction

The ^{10}Be and ^{26}Al concentrations are calculated from the ^{10}Be:^{9}Be and ^{26}Al:^{27}Al provided by LLNL-CAMS. Site-specific production rates are calculated based on latitude, longitude, elevation, and sample depth (Lifton *et al.* 2014), and used to obtain burial ages based on the following equation (Nishiizumi *et al.* 1991):

$$R_{26,10}(t) = \frac{N_{26}(t)}{N_{10}(t)} = \frac{P_{26}(0)\left(\lambda_{10} + \frac{\varepsilon}{\Lambda_{f,e}}\right)\left(1 - e^{\left[1 - e^{\left(-\lambda_{26} + \frac{\varepsilon}{\Lambda_{f,e}}\right)t}\right]}\right)}{P_{10}(0)\left(\lambda_{26} + \frac{\varepsilon}{\Lambda_{f,e}}\right)\left(1 - e^{\left[1 - e^{\left(-\lambda_{10} + \frac{\varepsilon}{\Lambda_{f,e}}\right)t}\right]}\right)}$$

where $R_{26.10}(t)$ is the ^{26}Al:^{10}Be ratio, $N_i(t)$ is the concentration of nuclide i (atoms g^{-1}), $P_i(0)$ is the production rate of nuclide i at the surface (atoms g^{-1} a^{-1}), λ_i is the decay constant for nuclide *i* (a^{-1}), ε is the mass erosion rate (g $cm^{-2}yr^{-1}$), $\Lambda_{f,e}$ is the effective

attenuation length (g cm^{-2}) for fast nucleons, and t is the exposure age (a). The equation guides the simplest interpretation of the results by assuming no post-burial (muonic) production and negligible inherited concentration from the catchment (i.e., production prior to burial).

Once the burial age is calculated, erosion rates for the catchment that sourced the BF are obtained from the ^{10}Be concentrations, given by Lal (1991):

$$\varepsilon = \left(\frac{P_{10}}{N_{10}} - \lambda_{10}\right) \cdot \frac{\Lambda_e}{\rho}$$

where ε is the catchment-wide erosion rate (cm a^{-1}), P_{10} is the average surface production rate of ^{10}Be over the entire catchment (atoms g^{-1} a^{-1}), N_{10} is the depositional ^{10}Be concentration (atoms g^{-1}), λ_{10} is the decay constant for ^{10}Be, Λ_e is the effective attenuation length of the cosmic flux near the Earth's surface (160 g cm^{-2}), and ρ is the mean density of the eroding material (2.0 g cm^{-3} for sediment).

5.2 Cosmogenic nuclide burial dating results

A total of 14 samples were analysed for ^{26}Al and ^{10}Be concentrations. The concentrations and simple burial ages are presented in Table 5.1. These concentrations are an order of magnitude lower than those for samples from Meighen Is. and Ellesmere Is. (on the order of 10^5 atoms of ^{26}Al instead of 10^6, and 10^4 atoms of ^{10}Be instead of 10^5; unpublished data). The number of counts detected (as low as 23 counts of ^{26}Al per 600s) resulted in high AMS counting errors, since the Poisson distribution is significantly controlled by $\frac{1}{\sqrt{n}}$ (Table 5.1). High masses, high Al, and the presence of chert also increased AMS errors because of low Al currents and ^{26}Al counts (see Appendix C). Sample BANKS-2013-C-025 from the Lower A2 Sample Group has been excluded on the basis of high AMS uncertainty (§ 5.1.3), compared to the other samples in the Lower A2 Sample Group (Table 5.1). No other outliers (concentrations >2 σ greater or lower than the average) were omitted from analysis.

Sample Group	Sample	Depth	^{10}Be Conc.	^{10}Be Conc. Error	^{26}Al Conc.	^{26}Al Conc. Error	^{26}Al:^{10}Be	^{26}Al:^{10}Be Error	Simple Burial Age	Age Pos. Error (1σ)	Age Neg. Error (1σ)
		(m)	(atoms g^{-1})	(atoms g^{-1})	(atoms g^{-1})	(atoms g^{-1})	(atoms/atoms)	(atoms/atoms)	(Ma)	(Ma)	(Ma)
Sec. 9 Lower A2	025	57.32	1.10 x10^{4}	507	3.26 x10^{4}	1.06 x10^{4}	2.94	0.97	1.73	1.64	0.42
	026	57.42	1.03 x10^{4}	412	1.78 x10^{4}	4.07 x10^{3}	1.72	0.40	2.85	0.71	0.37
	027	57.66	1.04 x10^{4}	427	2.12 x10^{4}	4.56 x10^{3}	2.03	0.44	2.50	0.63	0.36
	028	57.79	1.04 x10^{4}	398	1.91 x10^{4}	4.60 x10^{3}	1.84	0.45	2.73	0.74	0.41
	mean with 025	57.55	1.05 x10^{4}	215	2.00 x10^{4}	2.47 x10^{3}	1.92	0.24	2.11	0.18	0.28
	without 025	57.62	1.04 x10^{4}	238	1.93 x10^{4}	2.53 x10^{3}	1.85	0.25	2.72	0.34	0.24
Sec. 9 Upper A2	001	46.26	1.31 x10^{4}	450	4.06 x10^{4}	5.01 x10^{3}	3.09	0.40	1.64	0.32	0.23
	002	46.33	1.49 x10^{4}	767	2.53 x10^{4}	3.30 x10^{3}	1.70	0.24	2.86	0.37	0.23
	003	46.51	1.01 x10^{4}	492	3.87 x10^{4}	4.74 x10^{3}	3.83	0.50	1.18	0.29	0.26
	004	46.61	1.15 x10^{4}	555	3.80 x10^{4}	4.58 x10^{3}	3.31	0.43	1.48	0.30	0.25
	005	46.72	1.19 x10^{4}	461	3.42 x10^{4}	4.41 x10^{3}	2.87	0.39	1.80	0.29	0.28
	mean	46.48	1.20 x10^{4}	231	3.36 x10^{4}	1.91 x10^{3}	2.54	0.16	2.25	0.37	0.01
Sec. 9	032	44.05	1.24 x10^{4}	446	3.99 x10^{4}	7.64 x10^{3}	3.21	0.66	1.54	0.62	0.31
Sec. 9	029	39.30	1.46 x10^{4}	509	4.97 x10^{4}	8.10 x10^{3}	3.40	0.54	1.42	0.28	0.30
Sec. 9	030	37.05	1.62 x10^{4}	565	6.15 x10^{4}	3.81 x10^{3}	3.80	0.55	1.20	0.37	0.26
Sec. 8	020	16.20	1.03 x10^{4}	737	2.40 x10^{4}	8.23 x10^{3}	2.31	0.81	2.23	1.96	0.41
	021	16.66	9.61 x10^{3}	391	2.92 x10^{4}	4.73 x10^{3}	3.03	0.51	1.66	0.46	0.27
	022	16.94	9.61 x10^{3}	691	1.42 x10^{4}	1.02 x10^{4}	1.47	1.07	3.14	8.13	0.17
	mean	16.60	9.75 x10^{3}	309	2.60 x10^{4}	3.81 x10^{3}	2.64	0.40	2.35	0.28	0.19

Table 5.1 – TCN measurements and calculated simple burial ages for all samples at Sections 8 and 9. Sample 025 was omitted due to high AMS error, which is shown here as part of the ^{26}Al concentration error. Error weighted means are shown for each sample group in the grey rows. Depths measured from the top of the section, at 84 m for Section 9 and 70 m for Section 8 (Figure 3.2). For details on location and sample thicknesses and the chemistry and AMS data, see Appendix B and C.

5.2.1 Simple burial ages from individual samples

The ^{26}Al and ^{10}Be concentrations are reported in Table 5.1. Notably, when the modern sample depth (from the top of the section) is used to calculate *in-situ* (muonic) production of ^{26}Al and ^{10}Be since burial, none of the analysed samples plot within the allowable zone on a burial diagram (see below Figure 5.4). This means that using the present sample depth overestimates muonic production, indicating that the samples were buried to a greater depth for much of their burial history. Since the history of variable sample depth and muonic production is unknown (i.e., total erosion and thickness and timing of cover by Quaternary glacier ice are all uncertain), the sample ages were calculated without accounting for post-burial muonic production (i.e., by assuming simple burial conditions; Table 5.1). Simple burial ages range, in stratigraphic order, from 2.7 to 1.2 Ma, and constitute minimum estimates of the true burial age(s), because post-burial production is considered likely (as demonstrated below in § 6.3.3)

5.2.2 Trends at 1 m scale

Although the Lower A2 (and perhaps the Section 8) sample groups collected for depth profile isochron burial dating exhibit the expected decrease in ^{26}Al concentration, ^{10}Be concentration, ^{26}Al:^{10}Be with depth (Figure 5.1), none of the sample groups define a straight line on a ^{26}Al concentration -^{10}Be concentration plot, which is a requirement for their use in isochron burial dating (Balco and Rovey 2008; Figure 5.2). There is a linear relationship among the samples of the Lower A2 sample group (Figure 5.2a), but this relationship does not correspond to sampling depth (the decrease in concentration is not in stratigraphic order). Although there may be a higher concentration in the uppermost sample (which has high AMS errors, Appendix C) compared to the bottom three samples, the spread in concentrations is insufficient for defining the slope of an isochron, in part because the TCN concentrations are so low (Figure 5.3). Therefore, none of the depth profiles within the Lower A2, Upper A2, and Section 8 sample groups can be used for isochron burial dating.

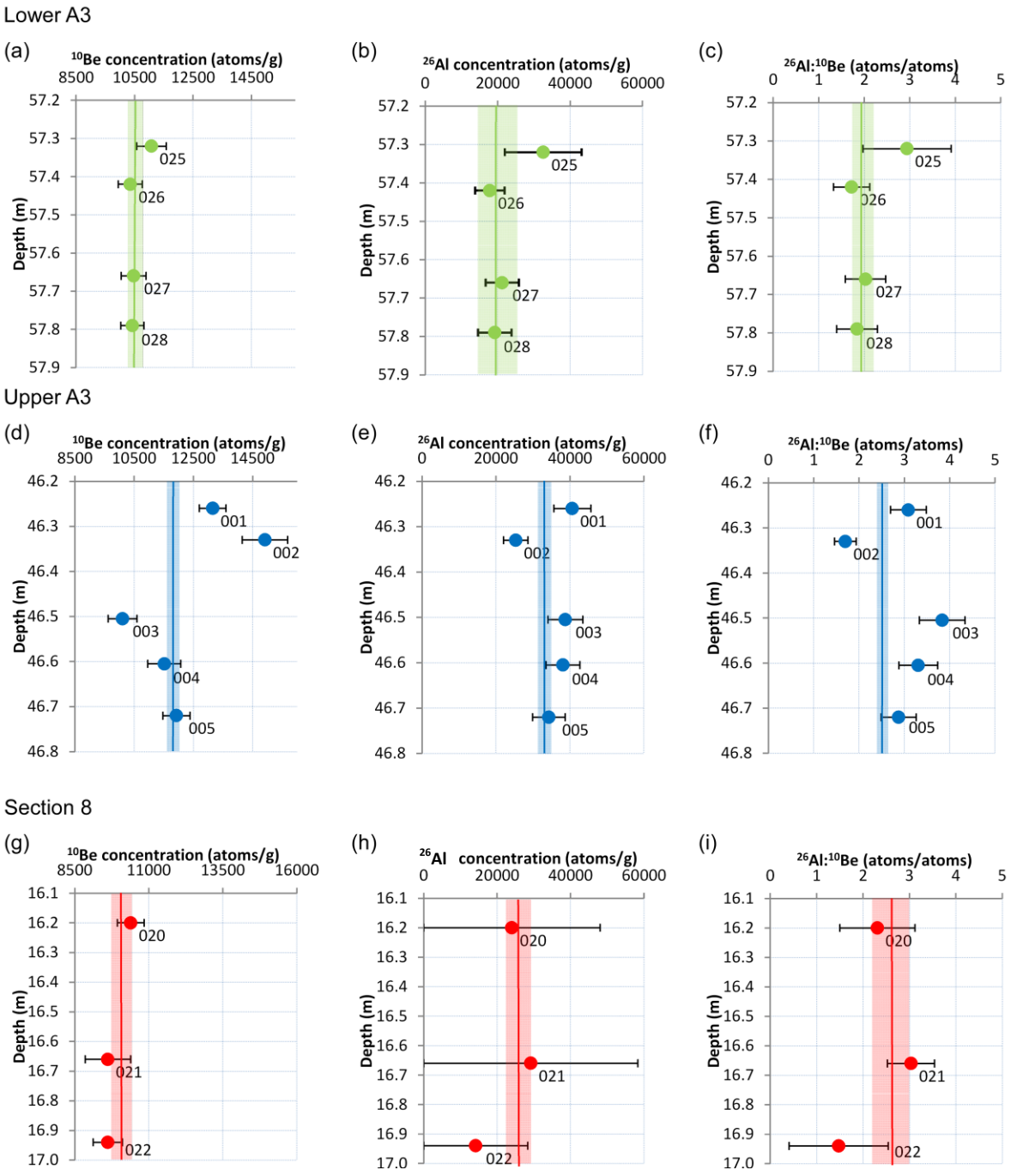

Figure 5.1 – ^{26}Al and ^{10}Be concentrations and ^{26}Al:^{10}Be with respect to depth for each sample group collected for depth profile isochron burial dating. Lower A2, shown in green (a-c), Upper A2, shown in blue (d-f) and Section 8 sample group, shown in red (g-i). The error-weighted mean concentrations of each sample group is depicted by the solid vertical line, and the 1 σ error is shown by the shaded vertical region.

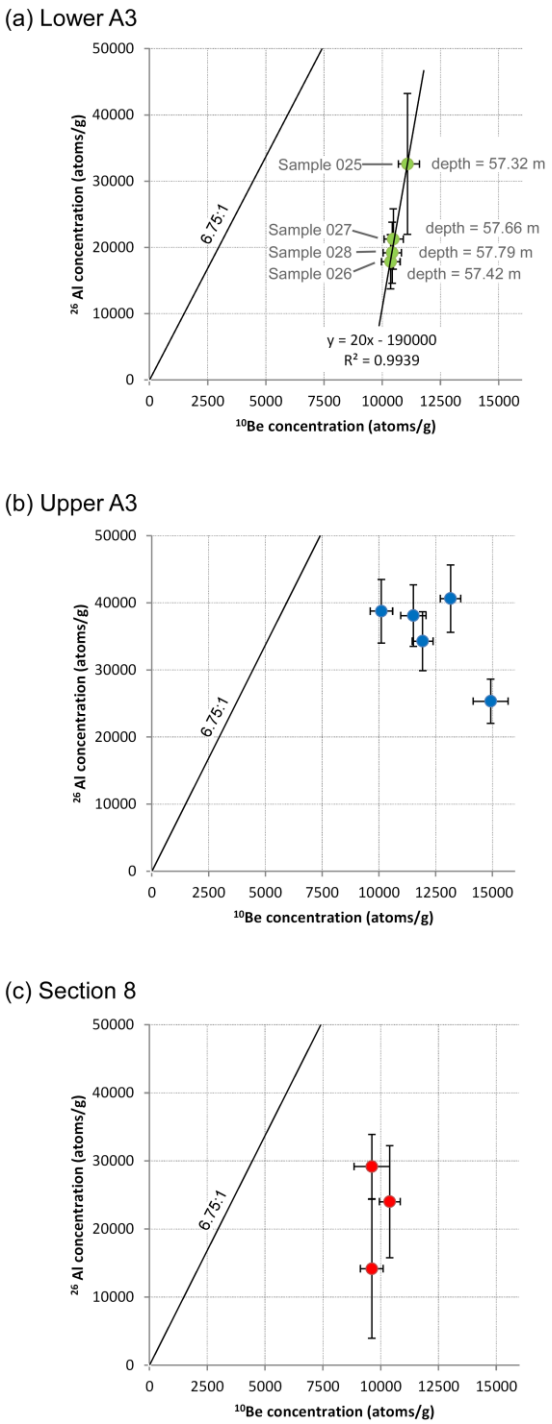

Figure 5.2 – ^{26}Al-^{10}Be isochron plots for each depth profile sample group. Isochron samples start on a line with a slope of 6.75 (the ^{26}Al: ^{10}Be production ratio); shallower samples have higher TCN concentrations. The slope between samples decreases over time, but the relationship between samples at different depths remains linear (Balco and Rovey 2008). Here, there is no linear relationship between samples that corresponds to stratigraphic depth.

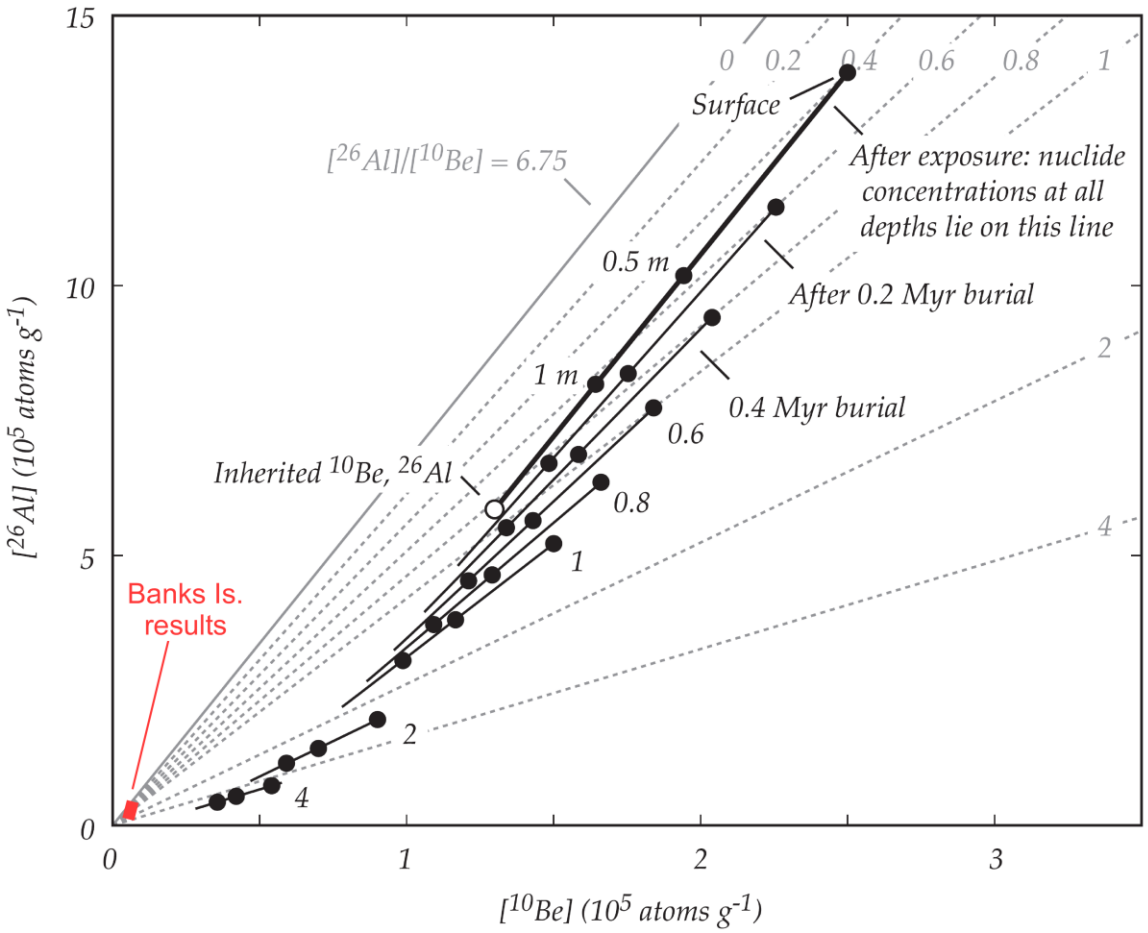

Figure 5.3 – Banks Is. results are plotted on an isochron plot to illustrate the low TCN concentrations of the Banks Is samples compared to typically published isochrons.

5.2.3 Trends at 20 m scale

While most applications of depth profile isochron dating have used 1 to 2 m depth profiles (Balco and Rovey 2008), if muonic production can be estimated, it is possible that nuclide concentrations and ratios for a vertical sampling profile spanning the stratigraphic exposure could be used to obtain a burial age for the complete sequence of BF sediments (as will be demonstrated in Chapter 6). This would require that the sediment was deposited and buried to sufficient depths sufficiently quickly for production during deposition and production during shallow burial to be considered negligible, and that the initial ratio for each sample was 6.75 at deposition (see below Chapter 6). Since each sample group obtained for isochron burial dating was collected vertically over less than 1 m, the samples in each group can be averaged to more precisely

represent the ^{26}Al and ^{10}Be concentrations at their respective depths. Thus, there are two groups of amalgamated samples at Section 9, and therefore 5 sets of ^{26}Al and ^{10}Be concentrations, over a depth range of approximately 20 m: the error-weighted average of the Lower A2 and Upper A2 sample groups, in addition to individual samples 032, 029, and 030 (Figure 3.2). These simple burial ages increase systematically with depth, as indicated on Figure 5.4. In fact, both ^{26}Al and ^{10}Be concentrations and ^{26}Al :^{10}Be decrease systematically with depth (Figure 5.5a, 5.5b). When these five samples are plotted on a burial diagram, they spread along an exposure line of approximately 5600 years (shown between 3 and 10 ka of pre-burial exposure, Figure 5.4).

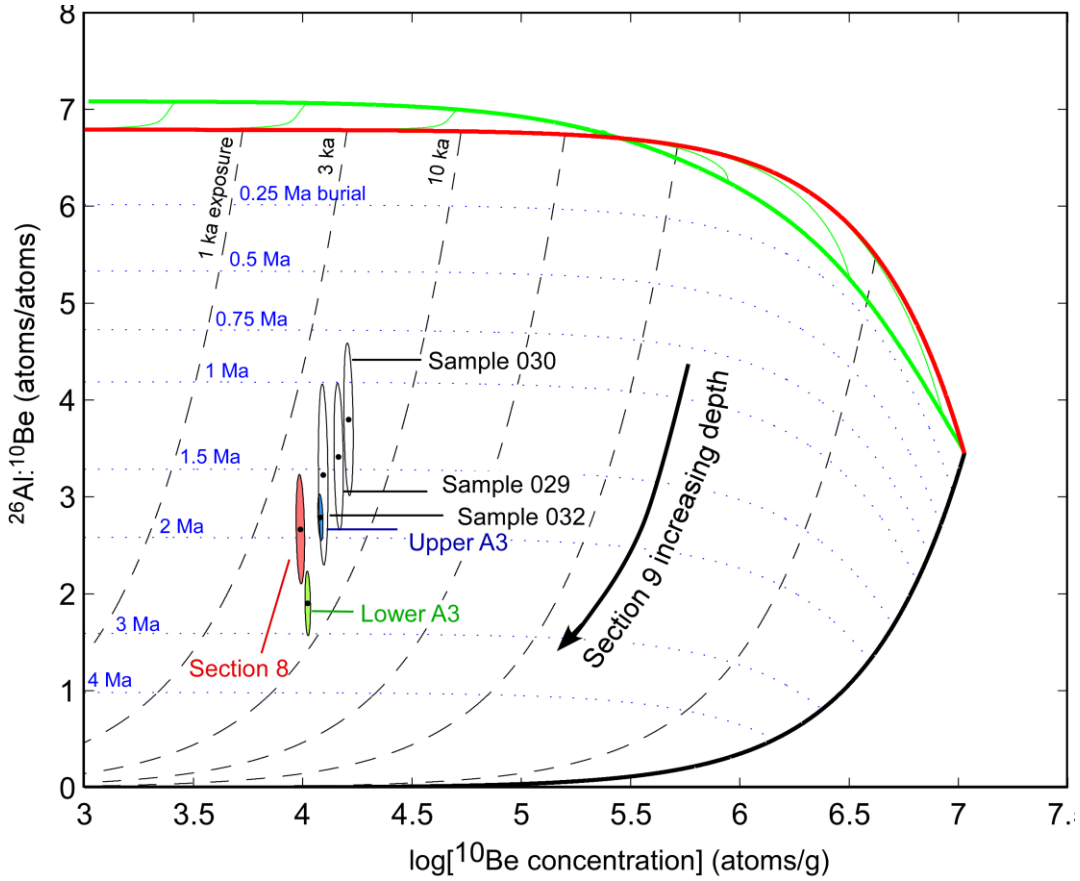

Figure 5.4 – ^{26}Al/^{10}Be vs. normalized ^{10}Be concentration burial plot, showing sample group averages (Lower A2, Upper A2, and Section 8) as well as individual measurements (Samples 032, 029, and 030). The data consistently indicate a minimum exposure duration of 5600 years prior to burial.

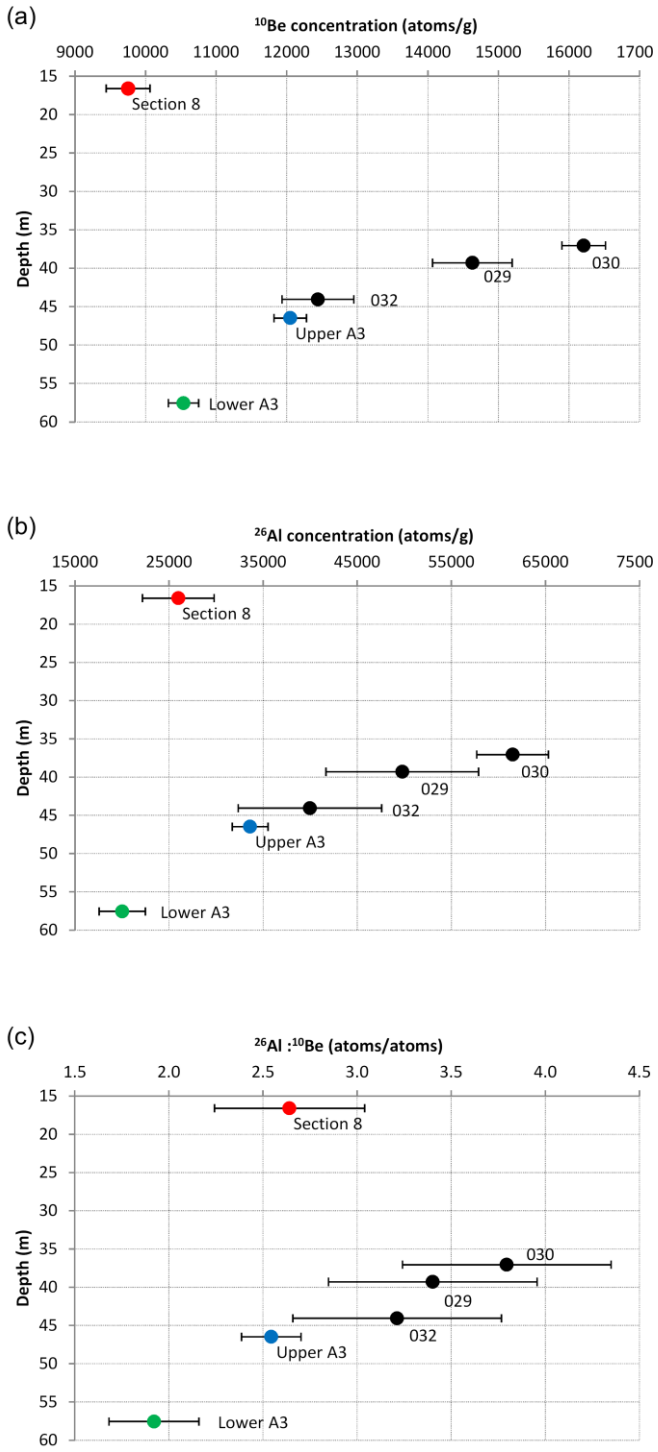

Figure 5.5 – Sample group averages (Lower A2, Upper A2, and Section 8) and individual measurements (Samples 032, 029, and 030) of ^{26}Al concentrations, ^{10}Be concentrations, and ^{26}Al:^{10}Be with respect to depth. The Section 9 data show systematic trends with depth, as indicated by the error-weighted linear fits. The Section 8 measurement is shown for comparison, but is not included in the calculation of these fits.

The results of the 20 m-scale amalgamated data can also be represented in ^{26}Al - ^{10}Be space (isochron plot), where they define a nearly linear fit with an equation of 8.0 ± 0.48 (1σ) ^{26}Al atoms/ ^{10}Be atoms (Figure 5.6). The linear fit does not pass through the origin, but rather has a large negative y-intercept of -63,000 ± 5,600 atoms ^{26}Al (1 σ). The cause of this trend is discussed in Chapter 6.

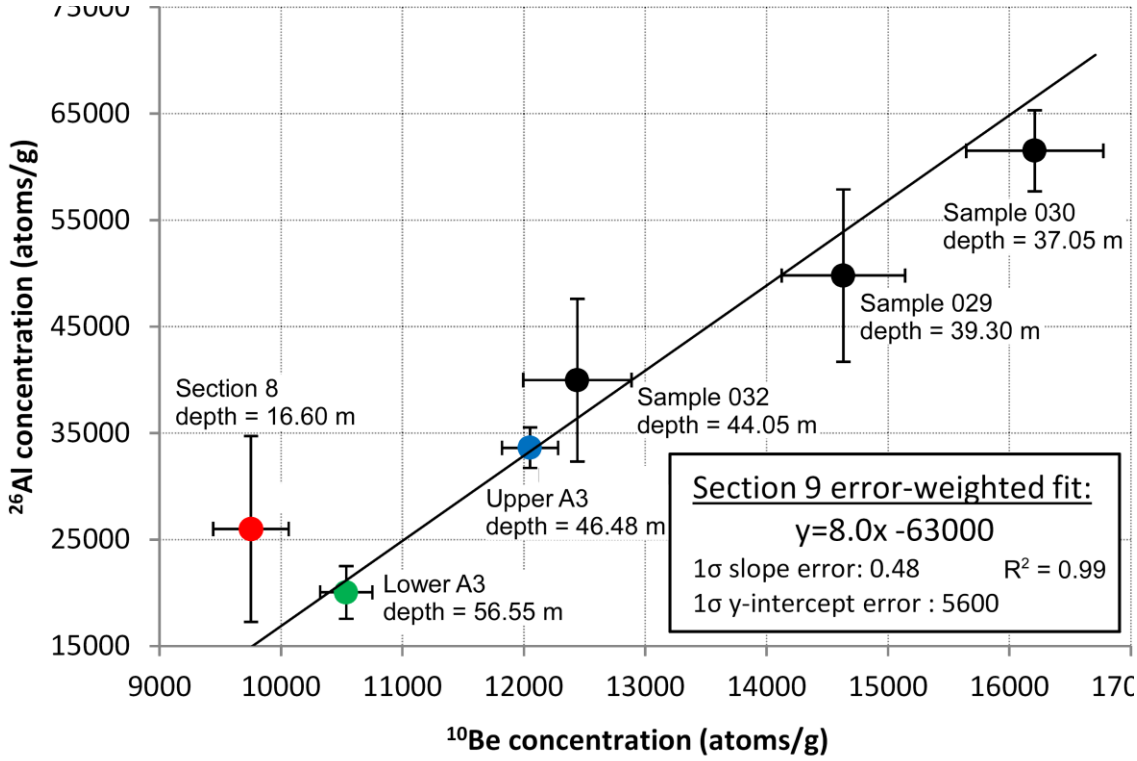

Figure 5.6 – Isochron plot for amalgamated concentrations (Lower A2, Upper A2, and Section 8) and individual measurements (Samples 032, 029, and 030) of ^{26}Al and ^{10}Be. The Section 9 data form a linear relationship, which also corresponds to changes in depth. The Section 8 measurement is shown for comparison, but is not included in the calculation of the linear fit.

5.2.4 Section 8

The average ^{26}Al and ^{10}Be concentration and ^{26}Al:^{10}Be for Section 8 do not align with the Section 9 linear relationships with depth (Figure 5.5); they fall outside the 2σ ranges of these fits. The Section 8 simple burial age also corresponds to a lower exposure age than the Section 9 samples at equivalent depth below the BF plateau (more to the left

on the ^{10}Be axis in Figure 5.4). Section 8 has a ^{26}Al concentration, ^{10}Be concentration, and ^{26}Al:^{10}Be ratio that are lower for their depth, relative to the Section 9 samples.

The cause of the TCN trends could be directly related to 1) depth below the regional BF plateau (i.e., if TCN production down through the top of the section is controlling the measured concentrations), 2) depth below other, lower ledges (i.e., if TCN production down through the top of more recent exposures is controlling the measured concentrations), or 3) stratigraphic height (i.e., if measured concentrations are related to depositional concentrations). Therefore, the Section 8 and 9 data are plotted using different reference frames. Figure 5.7 shows the Section 8 samples with the Section 9 samples plotted with depth below a prominent 60-m ledge at Section 9 (Figure 5.7a, 5.7b, 5.7c), and using the height above the BBF-BF unconformity for both Sections 8 and 9 (Figure 5.7d, 5.7e, 5.7f). The Section 8 data still does not align with the Section 9 relationships in these reference frames, although the closest alignment may be the increase in ^{26}Al:^{10}Be with height above the unconformity (Figure 5.7f).

5.3 Summary

None of the sample groups collected for depth profile isochron burial dating define a straight line on a ^{26}Al concentration -^{10}Be concentration plot, which is a requirement for their use for isochron burial dating. Since each sample group was collected vertically over less than 1 m, the samples in each group were amalgamated to more precisely represent the ^{26}Al and ^{10}Be inventories at their respective depths. The ^{26}Al and ^{10}Be concentrations and ^{26}Al :^{10}Be decrease systematically with depth (over the 20 m vertical span of the samples), and the simple burial ages increase systematically with depth, from 1.2 Ma to 2.7 Ma. When plotted on a burial diagram, the amalgamated samples spread along an exposure line of approximately 5600 years. The cause of these trends with depth is discussed in Chapter 6. The average ^{26}Al and ^{10}Be concentration and ^{26}Al:^{10}Be for Section 8 do not align with the Section 9 linear relationships with depth. Section 8 has a ^{26}Al concentration, ^{10}Be concentration, and ^{26}Al:^{10}Be ratio that are too low for their depth, relative to the Section 9 samples.

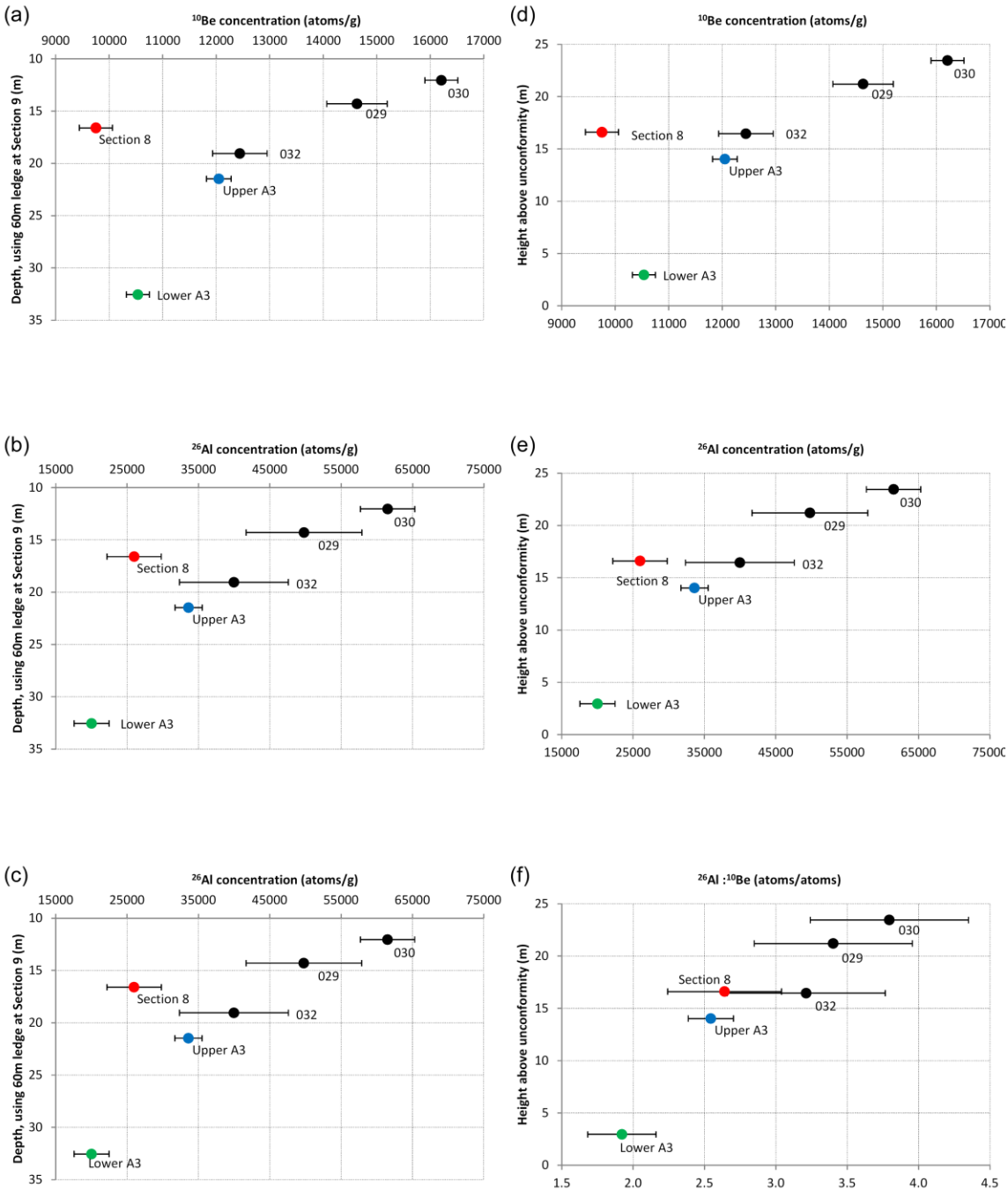

Figure 5.7 – ^{26}Al and ^{10}Be concentration plotted in different frames of reference. Section 8 and 9 ^{26}Al and ^{10}Be concentration and ^{26}Al:^{10}Be vs. depth below the 60 m ledge for Section 9 (Figure a, Figure b, Figure c) are shown. The same data are plotted using height above the BBF-BF unconformity for both Sections 8 and 9 (Figure d, Figure e, Figure f). The Section 8 datum does not align with the Section 9 linear relationship, except perhaps in Figure 8f. Error bars are 1σ.

Chapter 6 : Interpretation of Cosmogenic Nuclide Results

6.1 Introduction

Although studies by J. Fyles, L. Hills, J.V. Matthews and others suggest an Early Pliocene age for the Beaufort Formation (BF) at Ballast Brook, the simple burial ages obtained at Section 9 range between 2.7 and 1.2 Ma from bottom to top, and the simple burial age from Section 8 is 2.35 Ma. Thus, these results appear to contradict previous age estimates because the simple burial ages are younger (oldest age is only Late Pliocene). However, uncertainties with first-order assumptions in the simple burial dating method complicate attempts at assigning new absolute ages to the BF. For example, simple burial dating assumptions would be violated if production of TCN had occurred after burial.

Interpretation of the ^{26}Al and ^{10}Be concentrations in a given sample is fundamentally linked to assumptions about the exposure and burial history of that sample, because these dictate the duration of decay of the deposited TCN concentration and the amount of *in-situ* TCN production. Ages are obtained by accounting for decay that has occurred since deposition and by subtracting any *in-situ* production during burial (i.e. if the samples are not 100% shielded from muons).

In this chapter, several dating hypotheses regarding the timing of TCN production, the exposure and burial histories, and the age(s) of the samples are tested in order to test if the simple burial ages are accurate or if they are anomalously young. This chapter is focused on the Section 9 measurements, because the trends with depth obtained at that site can be used to test some of these hypotheses. The hypotheses are also tested using sedimentology, field geometry, and geological constraints on landscape processes (e.g., erosion rates). The resulting interpretation is then extended to the Section 8 samples, and paleo-erosion rates are calculated.

6.2 Production before burial

6.2.1 Hypothesis 1a: Trends are caused by differences in burial duration.

The simplest interpretation of the TCN measurements at Section 9 is that simple burial dating assumptions are not violated, and that the obtained simple burial ages are true ages (Hypothesis 1a, Table 6.1). Simple burial dating assumes that there is a period of exposure of source material in the catchment, during which TCN concentrations increase, followed by rapid transport, deposition, and an instantaneous and complete burial period, during which production halts, and TCN concentrations decay. There are no complications to the exposure and burial history, such as burial during transport or incomplete burial after deposition, and the initial (depositional) $^{26}Al:^{10}Be$ in all samples is assumed to be 6.75 (Granger and Muzikar 2001). If these assumptions are met, the $^{26}Al:^{10}Be$ reflects the duration of burial, since TCN concentrations decay from the time they are produced.

Simple burial dating assumptions	Timing of TCN production	Hypotheses	Implication for age(s) of Section 9 samples	Evidence in support or against hypotheses
Assumptions acceptable	Inherited – before burial – neutron and muon production	1a) Trends are caused by differences in burial duration.	The samples range in age from 1.2-2.7 Ma.	– required constant rate of deposition over 1.2 Ma unlikely – required depositional rate of 20 m of sediment over 1.5 Ma unlikely – slow average deposition rate is violation of simple burial assumptions
Assumptions invalid		1b) Trends are caused by change in inheritance.	A maximum age of the entire section is 1.2 Ma.	– required uniform change in inherited TCN is unlikely – erosion and shielding cannot account for the measured trend in ^{26}Al:^{10}Be
	Syn-burial – during deposition of section – neutron and muon production	2a) Trends are caused by a syn-burial production.	The simple burial ages are closely-limiting minimum ages; their range is the true range in burial ages.	– required constant rate of deposition over 1.2 Ma unlikely – required depositional rate of 20 m of sediment over 1.5 Ma unlikely
		2b) Syn-burial production is a significant fraction of measured TCN.	The simple burial ages are closely-limiting minimum ages; entire section may or may not be one age.	– required slow depositional rate of 100 cm/ka is unlikely but not impossible
	Post-incision – after erosion from the modern river – neutron and muon production	3a) Trends are caused by post-incision production.	A minimum age of the entire section is 2.7 Ma.	– depth of sampling, local slope, and variations in shielding due to cliff geometry do not correlate with variations in TCN – parallel scarp retreat suggests that variation in cliff retreat rate is unlikely – post-incision production cannot account for the measured trend in ^{26}Al:^{10}Be
		3b) Post-incision production is a significant fraction of measured TCN.	The simple burial ages are closely-limiting minimum ages; entire section may or may not be one age.	– it is reasonable to assume that retreat rates are faster than 500 cm/ka, in which case post-incision production would be insignificant

Simple burial dating assumptions	Timing of TCN production	Hypotheses	Implication for age(s) of Section 9 samples	Evidence in support or against hypotheses
	Post-burial – after deposition of the full section but before erosion of the modern river – muon production	4a) Trends are caused by post-burial production.	A minimum age of the entire section is 2.7 Ma.	– the measured TCN trends are predicted by equations of post-burial muonic TCN production and decay
		4b) Post-burial production is a significant fraction of measured TCN.	The simple burial ages are minimum ages; entire section may or may not be one age.	– if post-burial production produced the measured TCN trends (Hypothesis 4a), it must be a significant fraction of measured TCN

Table 6.1 – Hypotheses for the interpretation of the measured TCN concentrations at Section 9. In particular, these hypotheses seek to explain the measured trends in ^{26}Al and ^{10}Be concentrations and ^{26}Al:^{10}Be with depth.

However, the sedimentology and TCN observations appear to be contrary to Hypothesis 1a. Firstly, the 11 TCN measurements at 5 depths provide a consistent change in simple burial ages with depth, suggesting a constant rate of deposition over 1.2 Ma (Figure 5.6). However, the time span of 1.3 Ma would include many Pleistocene and Pliocene glacial cycles, making it unlikely that the change in burial age with depth would be so consistent (Figure 5.4). Secondly, the depositional rate of 20 m of sediment over 1.5 Ma is unlikely. Sandy-gravelly braided river systems deposit at least a few meters of sediment every thousand years (Miall 1977), which means that less than 10 ka may explain the deposition of the 20 m between the bottommost and topmost samples at Section 9. For the ages to be correct, this implies that there must have been periods of erosion or prolonged periods of non-deposition between the samples, but there is neither stratigraphic nor TCN evidence observed to suggest that this is the case. No major hiatuses or paleosols were observed in the field at Section 9 between the samples. The only major changes in the section were the transition between the sand-dominated Unit A to the gravel-dominated Unit B, and the laterally discontinuous glaciofluvial gravel (Unit A2; Figure 3.2). Furthermore, TCN sample groups were obtained from below two of the most prominent surfaces in the section (Organic facies 2 beds), and neither of these exposure profiles indicate a detectable duration of exposure of the surface. This decreases the likelihood that long periods of negligible erosion are present in the stratigraphy (but masked as apparent bedding planes or concealed by colluvium cover). Lastly, the sedimentology and TCN data appear to be contrary to Hypothesis 1a because the slow average deposition rate is a violation of the simple burial assumption of instantaneous deep burial. If there were indeed erosion and non-deposition surfaces throughout the section, this would violate the simple burial dating assumption that the section was instantaneously buried deeply. Slow deposition would imply incomplete shielding and continued production after burial, making the simple burial ages minimum ages of varying degrees. For these reasons, *Hypothesis 1a is false, and the simple burial ages do not reflect the actual timing of deposition of the Section 9 sediments* (Table 6.1).

6.2.2 Hypothesis 1b: trends are caused by changes in inheritance.

Hypothesis 1b is that a systematic increase in inherited ^{26}Al and ^{10}Be concentrations and in inherited ^{26}Al:^{10}Be during the deposition of Section 9 is the cause of the measured decrease in ^{26}Al and ^{10}Be concentrations and ^{26}Al:^{10}Be with depth (Table 6.1). This violates the assumption of constant inherited concentrations and ratio of 6.75 in Hypothesis 1a. Hypothesis 1a and 1b are closely linked, because in both scenarios, the TCN concentration measured today was produced prior to burial (inherited). Although the assumptions of Hypothesis 1a and 1b about burial history are the same (no post-burial production), the assumptions about exposure history and inherited TCN concentrations differ.

Without independent chronology, the initial ^{26}Al:^{10}Be at the time of deposition cannot be determined. If the initial ^{26}Al:^{10}Be of a sample is actually lower than the assumed value of 6.75, the simple burial age calculation overestimates the sample's age by falsely assuming that it has decayed since deposition from 6.75 to its present ratio. Hence, Hypothesis 1b implies that the simple burial age of the shallowest Section 9 sample (1.2 Ma) is the most closely-limiting maximum estimate of the true burial age of the section. If the remaining samples were buried for the same duration, they would be less closely-limiting maximum estimates of this duration, since their initial depositional ^{26}Al:^{10}Be would be assumed to be lower than that of the shallowest sample.

A number of processes can cause variation in the inherited ^{26}Al and ^{10}Be concentrations, the inherited ^{26}Al:^{10}Be, or both. For example, TCN concentrations could increase if erosion rates of the catchment surface decrease over time. The measured Section 9 concentrations can be used to reconstruct a range in parent surface concentrations of 1.4×10^4 ^{10}Be atoms g^{-1} to 2.2×10^4 ^{10}Be atoms g^{-1} (using 1.2 Ma of burial, and assuming no TCN production during transport). This would require a change in erosion rates from 115 cm/ka to 75 cm/ka (assuming the parent surface concentrations were at equilibrium with erosion). Alternatively, a shift in sediment provenance could also cause a change in inherited TCN concentrations. Tectonic and climatic (and glacial) changes can affect catchment characteristics (including size and

geometry), or cause rivers to incise into different sediment sequences with varying susceptibility to erosion. Tectonics and climate also influence vegetation and snow cover, although this shielding cannot likely explain more than a 10% change in TCN production unless there was a rainforest (Gosse and Philips 2001; Plug *et al.* 2007), for which there is no evidence. Hidy *et al.* (2013) demonstrated how changes in climate and landscape processes can influence inherited TCN concentrations. Until this system is better characterized (and modelled), these proposed mechanisms remain speculative.

However, there are important issues regarding how these mechanisms explain the measured trends. For example, the 11 TCN measurements at 5 depths provide a uniform change in TCN concentrations and ratios at Section 9, as demonstrated by the small 1σ error of the slope (isochron plot; Figure 5.6). This change (from 1.04 $x10^4$ to 1.62 $x10^4$ ^{10}Be atoms/g and 1.93 $x10^4$ to 6.15 $x10^4$ ^{26}Al atoms/g; Table 5.1) occurs over 20 m and over several changes in sedimentology, including the apparent transition from a glaciofluvial gravel (Unit A2, Figure 3.2). It is improbable that episodic changes in erosion, sediment source, or shielding would cause such a uniform change in inherited TCN, especially considering the variation in sedimentology. Furthermore, although erosion and shielding can account for variations in concentrations, they cannot account for the observed decrease in *ratio* with depth in the deposit: higher erosion rates and more shielding would cause a raise in the ^{26}Al:^{10}Be, causing a slight increase in ratio with depth. *For these reasons, Hypothesis 1b is reasonably falsified and the measured TCN trends are not caused by systematic variations in inheritance* (Table 6.1).

6.3 Production after burial

Both Hypotheses 1a and 1b assume that the measured TCN concentrations are derived entirely from exposure prior to burial, and that the measured concentrations therefore reflect decay that has occurred since that time. This requires burial to have been sufficiently deep for the sediment to have been completely shielded from further TCN production. However, there are three ways in which incomplete shielding could have occurred at this site, and these are deemed likely (Figure 6.1).

First, simple burial dating assumes that both the sampled section and a sufficient thickness above the section are instantaneously deposited, thus completely shielding the sampled depths from TCN production instantly after burial. However, if accumulation of sediment at the site is not instantaneous, TCN production continues in the sediment while it is only partially shielded (*syn-burial production;* Granger *et al.* 2013; Figure 6.1 inset). This pathway of TCN production is named syn-burial rather than syn-depositional because syn-burial production can occur in a given bed long after deposition of that bed (during deposition of the remainder of the section). Syn-burial production is problematic for two reasons: (i) at any given stratigraphic level, it occurs after the burial event targeted for dating, and (ii) with partial shielding, the TCN production rate and mechanism (fast neutrons, slow negative muons, fast muons) will vary with depth and time, changing the ^{26}Al:^{10}Be in each sample. The importance of this syn-burial production on the measured TCN concentrations at Section 9 depends on the burial rate.

Second, at present, the sampled stratigraphic exposures are exposed to cosmic rays. Incision of the BF by the Ballast Brook (and by earlier, abandoned, westward-draining Pleistocene (?) drainage systems), has generated the steep valley sides in the study area. This has caused first order tributary gullies along the river valley walls, including v-shaped tributary gullies along the main valley. Present-day TCN production is occurring on these retreating slope surfaces (*post-incision production;* Figure 6.1). The importance of this post-incision production on the measured TCN inventory at Section 9 depends on the timing of the incision and the rate of slope erosion.

Third, after deposition of the BF, but prior to its incision, the burial depth may have been insufficient to preclude significant muonic production (Figure 6.1). Although deep muonic production is typically considered insignificant, the low muonic production rates of ^{10}Be and ^{26}Al are significant when considered in light of the unusually low TCN concentrations at Section 9 (in the range of 10^5 atoms g^{-1} ^{26}Al and 10^4 atoms g^{-1} ^{10}Be). The importance of this *post-burial production* on the measured TCN concentrations depends on the sample depth throughout its burial history. For the purpose of this

paper, the term post-burial production will be used to indicate production that occurred after deposition of the entire stratigraphy at Section 9 but before incision (and, hence, before post-incision TCN production). The TCN production pathways are not presented chronologically, in order to simplify discussion by addressing the hypotheses with a process of elimination.

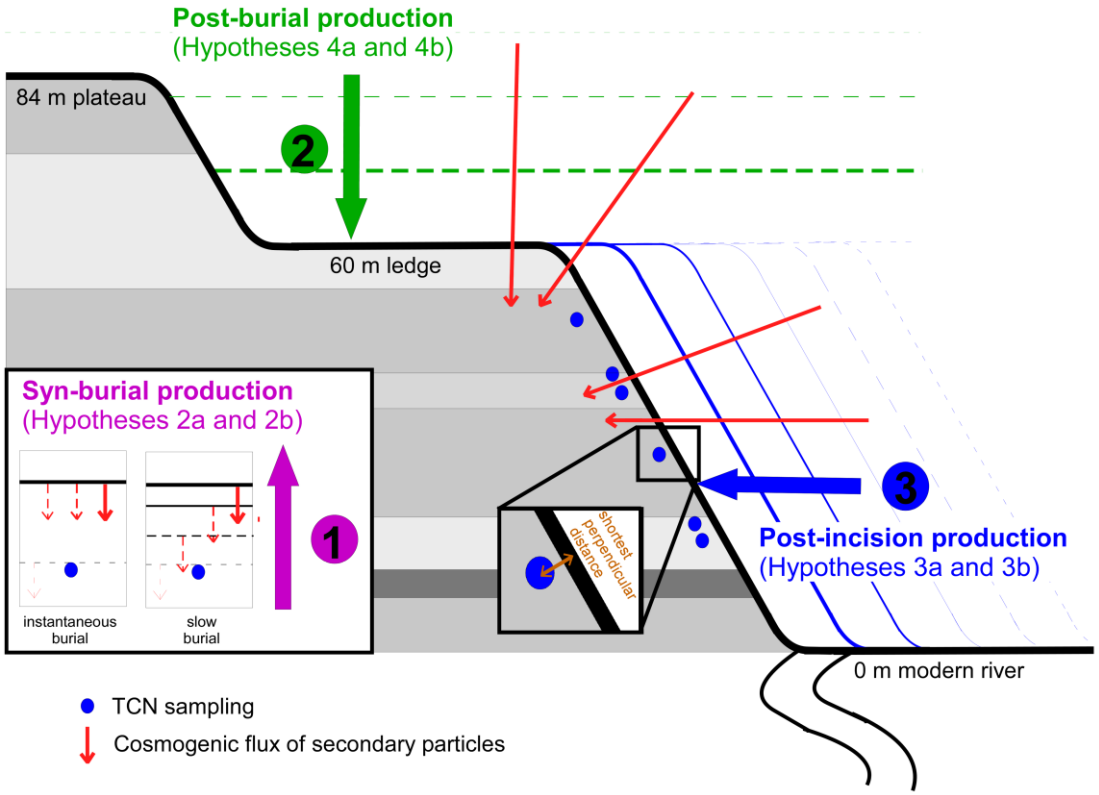

Figure 6.1 – The different pathways of post-burial TCN production in the BF at Ballast Brook. TCN samples were obtained below the 60-m ledge at Section 9b. The upper 24 m of logs 1 and 2 (from the 60-m ledge to the 84-m plateau) were described at Section 9c.

Thus, the measured TCN concentrations may have been influenced by one or several sources of production after burial: *syn-burial production, post-incision production,* and *post-burial production*. Given the low measured TCN concentrations, it is even possible that a significant fraction - or all - of the TCN in the measured samples were produced after burial. If one ascribes the measured TCN concentrations (in their entirety) to post-burial muonic production, then simple burial ages, which are calculated

under the false assumption that all production was inherited prior to burial, are rendered minimum estimates of the timing of burial.

6.3.1 Hypothesis 2a and 2b: Syn-burial production

Hypothesis 2a states that syn-burial production accounts for the measured trend in apparent ages (Table 6.1). Hypotheses 1a and 2a both rely on varying durations of decay (i.e., burial age) to cause the measured TCN trends, but they differ with respect to the timing of TCN production. In Hypothesis 1a, the TCN is produced prior to burial (in the catchment, during fast transport, or *in-situ*). In Hypothesis 2a, the TCN are produced during a slow, *in-situ* increase in burial depth. While Hypothesis 1a implied that the obtained simple burial ages are true burial ages, Hypothesis 2a implies that they are only minimum estimates. Because syn-burial production occurs syndepositionally, much before post-incision and post-burial production, Hypothesis 2a implies that the simple burial ages are more closely-limiting minimum ages than they would be if post-incision and post-burial production occurred. *The above discussion regarding the average depositional rate and the presence of hiatuses concluded that variations in burial age are not likely the cause of variations in observed TCN trends, and like for Hypothesis 1a, this makes it unlikely for Hypothesis 2a to be true.*

Hypothesis 2b states that post-burial production that occurs after sediment is partially shielded, during burial of the section (syn-burial), is a significant fraction of the measured TCN concentrations (Table 6.1; Figure 6.1 inset). If the burial rate was constant, all samples would have received the same amount of syn-burial production. The faster the burial rate, the less the syn-burial production the samples received (since they are exposed to TCN production for a shorter time). The magnitude of syn-burial production can be calculated for different rates of deposition, in order to determine the rates at which syn-burial production is significant. For both ^{26}Al and ^{10}Be, depositional rates of 1000 cm/ka and faster result in muon-produced ^{26}Al and ^{10}Be concentrations that are less than the 1σ measurement errors for the Section 9 samples. For both nuclides, a depositional rate of approximately 100 cm/ka or less is required for the magnitude of syn-burial production to be measurable at Section 9. Furthermore, these

initial concentrations decay with burial, so the older the burial age of Section 9, the slower the depositional rate needs to be for the syn-burial production to be analytically distinguishable from other TCN in the sample. As discussed earlier (§ 6.3.1), a slow depositional rate of 100 cm/ka is unlikely (but not impossible), based on 1) estimated deposition rates for sandy-gravelly braided environments (Miall, 1979), 2) the apparent paucity of hiatuses in the stratigraphy, based on sedimentological observations, 3) lack of TCN profile concentrations indicating long periods of exposure under the most conspicuous potential exposure surfaces. *This suggests that Hypothesis 2b is likely not true and that syn-burial production is likely not an important component of measured TCN concentration.*

6.3.2 Hypothesis 3a and 3b: Post-incision production

Hypothesis 3a states that the measured trends in ^{26}Al and ^{10}Be concentrations and ^{26}Al:^{10}Be of the Section 9 samples are the result of exposure to post-incision production, with variable shielding either spatially (up section) or temporally (as the modern valley side retreats). Systematic variation in shielding may be due to: (1) sampling distance from the slope, (2) cliff morphology, and (3) erosion rates. Each of these mechanisms is addressed below.

The Balco *et al.* (2013) complex geometry shielding calculator was used to calculate the shielding factor for various sampling distances from the slope and for different slope angles. The calculator creates a shape file of the sample site, simulates a neutron and muon flux with different angles and energies, and integrates resulting path lengths using a Monte Carlo approach. The sampling distance from the slope at Section 9 was measured perpendicular to the surface which was removed by hand before collecting the sample (inset, Figure 6.1). Figure 6.2 demonstrates that the shielding factor is very sensitive to sampling distance from the slope, and that the degree of sensitivity depends on the angle of the slope. However, in order for this mechanism to explain the measured TCN trends, the sampling distance from the slope or the slope angle would need to vary systematically with depth, and the slopes would need to be retreating very slowly.

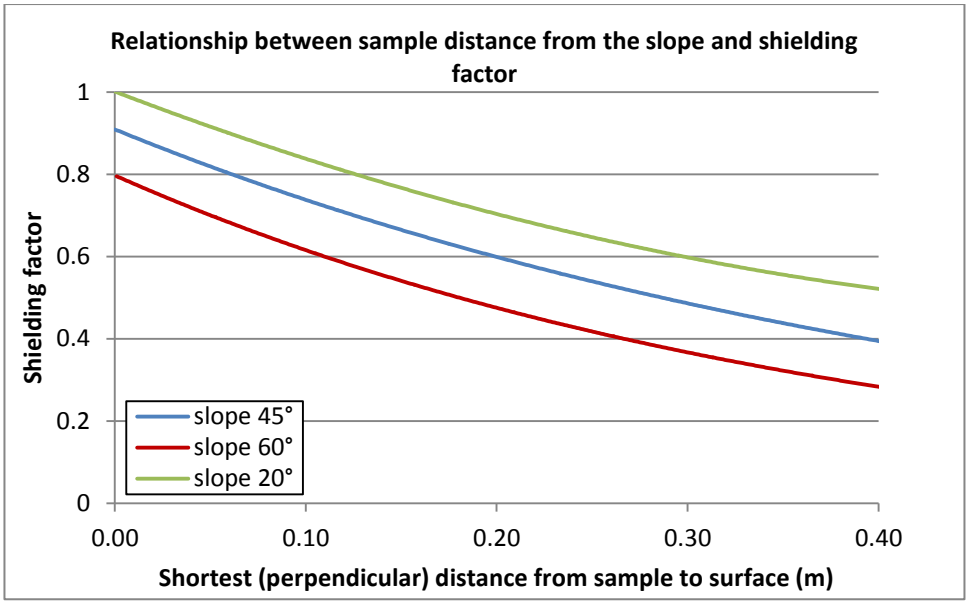

Figure 6.2 – Shielding factor vs. sample distance from the slope. The relationship between sampling distance from the slope and shielding factor was calculated using the Balco *et al*. (2013) shielding calculator. The dimensionless shielding factor is the ratio of the production rate at a shielded site to the production rate at an identical unshielded site. A shielding factor of 0 means that the sediment is fully shielded. This shows that the shielding factor decreases as sample distance from the slope increases. Steeper slopes also cause more shielding than shallower slopes.

A systematic change in sampling distance from the slope could have caused a systematic change in shielding. This could have occurred unintentionally (e.g., as a result of systematic changes due to permafrost, changes related to sedimentology, time allotted to sampling, etc.). However, after careful consideration of field photographs, it was confirmed that the distance from the slope of sampling did not systematically vary with depth: the Lower A2 group samples ranged from 10-30 cm sampling distances from the slope; the Upper A2 group samples ranged from 10-50 cm sampling distances from the slope; Sample 029 was at a sampling distance from the slope of approximately 30 cm; Sample 030 was at a sampling distance from the slope of approximately 5 cm; and from memory, the sampling distance from the slope of Sample 032 was approximately the same as Sample 030.

The wider (~100 m) cliff geometry was also reconstructed from field photos to identify potential systematic variations in shielding. For example, samples farther inside

gullies were more shielded than those on the spurs between gullies. Furthermore, the valley wall is eroded at the intersection of Tributary A with the main channel (Figure 3.1), so samples closer to this confluence are less shielded than samples farther down the length of the cliff. If these differences in shielding had significantly impacted TCN concentrations, the Lower A2 sample group would have the highest TCN concentrations because it was sampled from a ridge, close to the confluence of Tributary A with Ballast Brook. On the contrary, this sample group has the lowest TCN concentrations. Therefore, this is not a determinant of the measured TCN concentrations. Samples obtained higher in the section and closer to the 60 m ledge are also less shielded because they are currently more exposed to neutrons and muons that penetrate from the top of the section (Figure 6.1). However, the Balco shielding calculator was used to demonstrate that the shielding factor is not affected by the distance to this ledge. Thus, variations in cliff geometry do not control the measured TCN concentrations.

Lastly, samples obtained from shallower slopes are also less shielded than those obtained from steeper slopes, owing to a foreshortening effect of the primarily vertical cosmic ray flux. The Balco shielding calculator can be used to demonstrate that the shielding factor is sensitive to slope (Figure 6.3). The local slope of each sampling location at Section 9 was reconstructed from field photos, and it was demonstrated that while there is considerable variation in slope, there is no systematic steepening with depth.

The reason that modern shielding based on current morphology does not correlate to measured TCN concentrations may be that the present shape of the cliff is not representative of its shape for the last few thousand years. However, based on the current undercutting of the Section 9 cliff by the modern main Ballast Brook channel, parallel scarp retreat is the most likely mechanism of erosion. This would be consistent with constant retreat rates with depth.

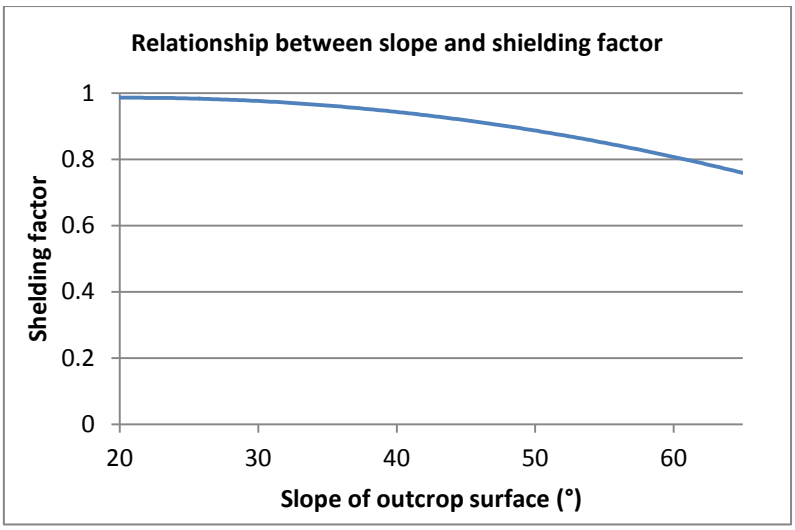

Figure 6.3 – Shielding factor vs. surface slope. Steeper slopes cause more shielding than shallower slopes. This relationship is also visible from Figure 6.2.

Lastly, none of these mechanisms involving variation in post-incision production with depth can explain the observed trend of decreasing $^{26}Al:^{10}Be$ with depth. On the contrary, higher shielding coefficients imply a higher fraction of muonic production, and thus a higher $^{26}Al:^{10}Be$. *For these reasons, it is unlikely that Hypothesis 3a is true, and that post-incision production is the cause of the measured TCN concentrations trends at Section 9.*

Hypothesis 3b states that post-incision production is a significant fraction of the measured TCN concentrations (Table 5.1). Calculation of the muonic TCN production using the current geomorphology reveals that this overestimates the true muonic TCN production, because all samples plot below the allowable zone on a burial plot (i.e., white zone in Figure 5.6). This means that the present morphology is not an adequate representation of Section 9's burial depth throughout most of its burial history. Since post-incision production is the most recent type of production after burial, a given amount of post-incision production has a greater effect of making the simple burial ages minimum ages than does earlier production (Figure 6.4).

Hypothesis 3b was tested by calculating TCN concentrations for different onset times of post-incision production, and for different retreat rates of the escarpment. The

Balco *et al*. (2013) shielding calculator was used to construct an equation for the shielding factor as a function of horizontal distance from the escarpment edge. Shielding factors were repeatedly calculated at different horizontal distances, using a density of 2.0 g/cm^3, and these outputs were combined to create an erosion rate *versus* concentration curve (Figure 6.4). The calculator does not include muonic production, so muonic production was incorporated in a simple way by using the same shielding function as neutrons, but with an attenuation length of 1500 g/cm^2 instead of 208 g/cm^2. Separate erosion rate *versus* concentration curves were calculated for slopes of 20°, 30°, 45°, and 60°. The equations for these curves were then used to calculate TCN concentrations under different cliff retreat scenarios (Figure 6.5).

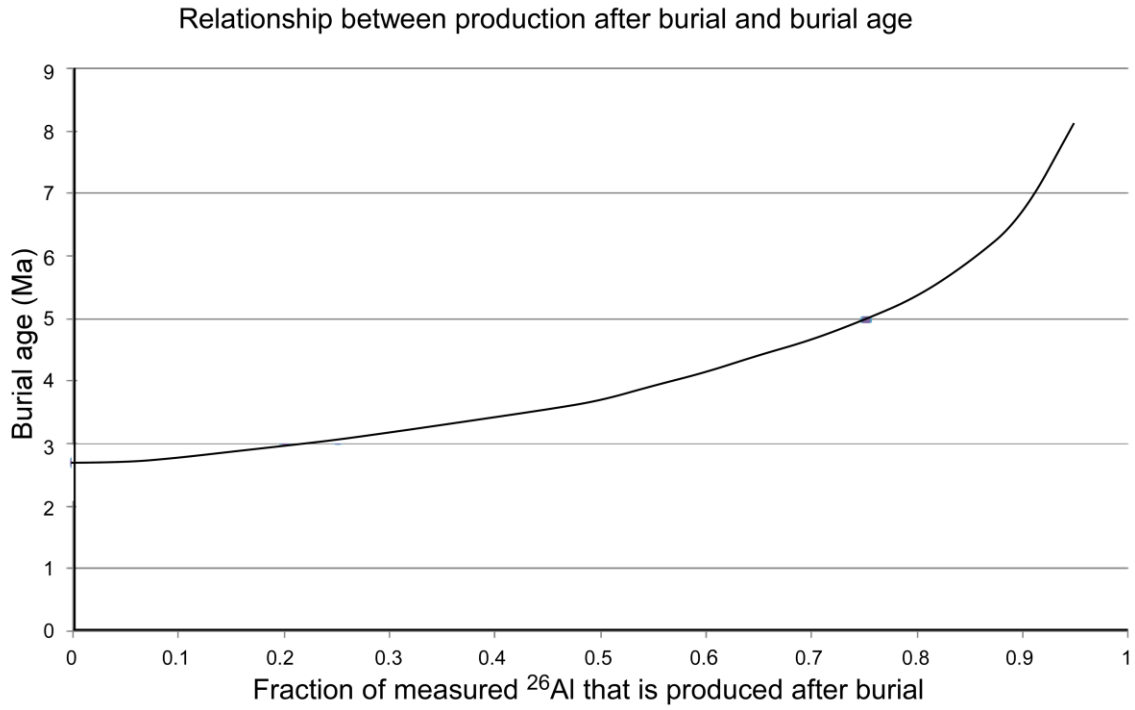

Figure 6.4 – Graph of burial age vs. fraction of post-burial ^{26}Al. If more of the measured ^{26}Al concentration was caused by recent ^{26}Al production, the ^{26}Al:^{10}Be of the decayed inheritance is lower, and the true burial age is older. The individual points represent individual calculations of the burial age, after removing different fractions of the measured ^{26}Al. No simple fits accurately characterize this relationship, so the calculations were left as individual points.

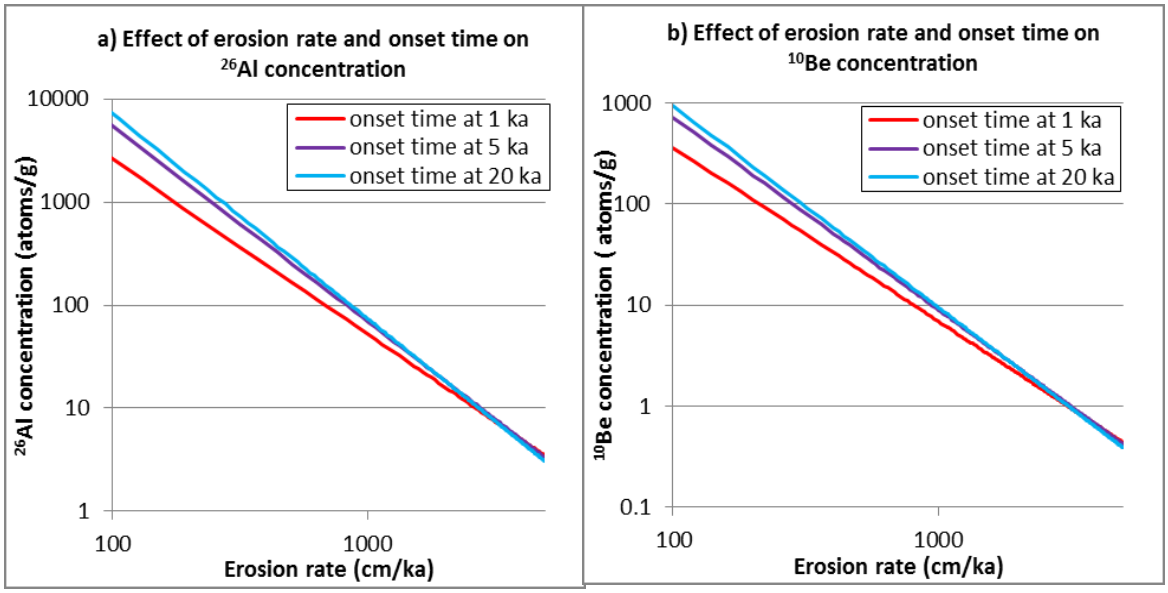

Figure 6.5 – Log-log plots of the effect of erosion rate and timing of incision on TCN concentration. a) ^{26}Al. b) ^{10}Be. Lower slope retreat rates lead to higher TCN concentrations. The onset of slope retreat also has an effect on TCN concentration, but only within the order of magnitude determined by the erosion rate.

The retreat rate determines the order of magnitude of TCN concentration buildup during escarpment retreat (Figure 6.5). An earlier onset time of parallel scarp retreat can double the TCN concentrations, but only for low retreat rates (less than 500 cm/ka). Likewise, escarpment retreat rates have a larger effect on TCN concentrations if the onset of post-incision production is recent. Despite the lesser importance of onset time for TCN concentrations, it cannot be ignored as a variable, or the ^{26}Al and ^{10}Be concentrations would not agree. This is because the onset time of parallel scarp retreat has a greater effect on ^{26}Al, due to the higher rate of ^{26}Al production by deep muonic production.

The retreat rate of the Section 9 cliff, composed of unconsolidated sand and gravel, is probably controlled by the Ballast Brook channel position and permafrost thaw. Section 9 is currently being undercut by the modern river, and this has likely accelerated the rate of scarp retreat. For these reasons, it is reasonable to assume that retreat rate of Section 9 is faster than 500 cm/ka. *Thus, regardless of when the modern Ballast Brook started to incise into the sediments, this provides evidence against Hypothesis 3b, and*

suggests that the TCN concentration buildup due to post-incision production is negligible for both ^{26}Al and ^{10}Be (less than measurement error).

6.3.3 Hypothesis 4a and 4b: Post-burial production

Hypothesis 4a states that the measured trends in ^{26}Al concentration, ^{10}Be concentration, and ^{26}Al:^{10}Be are caused by decreasing muonic production with depth (Table 6.1). In other words, the trends in concentrations with depth are potentially a product of muonic production along a depth profile. Hypothesis 4b states that post-burial production is a significant fraction of the measured TCN concentrations, and is thus a corollary of Hypothesis 4a.

The fundamental equations of TCN production and decay can be used to calculate the theoretical time-evolution of muogenic TCN concentrations at various depths, given any arbitrary erosion rate (Appendix D). The calculations in Appendix D demonstrate that the measured trends in ^{26}Al concentration, ^{10}Be concentration, and ^{26}Al:^{10}Be can be entirely obtained by muonic production, for certain combinations of depth range, erosion rate, and exposure time. For example, if erosion is less than 10 cm/ka, the measured trends can be explained with as little as 1 Ma of exposure to muonic production, at the present depths of the Section 9 samples. Greater values of erosion homogenize the concentrations with depth, so a small erosion rate is required to explain the steepness of the measured gradient. If the samples were deeper than their present depths (i.e., only recently exhumed or shielded by ice during glaciations), the erosion rate would need to be even lower (e.g., for 25 m depth above the shallowest sample, the erosion rate could not be more than 2-3 cm/ka). Similarly, the measured change in ^{26}Al:^{10}Be with depth can be explained entirely by muonic production, as long as erosion is no greater than 20 cm/ka and exposure has occurred for at least 0.4 Ma. Since these values are within the timeframe, depth-range, and range of erosion rates plausible for the plateau surface at Section 9, muogenic TCN is a likely cause of the measured trends in ^{26}Al concentration, ^{10}Be concentration, and ^{26}Al:^{10}Be. In fact, these calculations demonstrate that there are a range of scenarios for which the observed trends *should*

be present. This provides a mechanism for Hypothesis 4a (i.e., for post-burial muonic production to produce the measured TCN trends), and by extension, Hypothesis 4b.

However, no combination of a burial time, a constant erosion rate, and an unchanging depth can explain *both* the trends in concentration and the trends in ratios. This is because depth and erosion rate have changed over time (i.e., glacial cover, erosion down from surrounding plateau, etc.), and the trends in concentration and trends in ratios respond differently to changes in depth and erosion (i.e., they decay at different rates). Thus, the measured TCN trends place constraints on the exposure age at Section 9 (i.e., antiquity of the plateau surface), "effective depths" of the samples (production-rate and time-weighted average depth of the sample during its exposure), and "effective erosion rate" of Section 9 (production-rate and time-weighted average erosion rate of the section during its exposure; § 6.5), but cannot be used to solve for an absolute exposure age, depth, or erosion rate.

In conclusion, the precise depth-history scenario (i.e., involving a single combination of duration of exposure to muons, plateau erosion rate, and sample depth over time) that theoretically accounts for the measured trends in muogenic ^{26}Al concentration, ^{10}Be concentration, and ^{26}Al:^{10}Be ratio is unknown. However, the observed trends can separately be explained by a calculated range of values of erosion, depth, and exposure time. *Therefore, Hypothesis 4b and 4a are the most likely interpretation for the Section 9 samples, and are the basis for the age estimate used hereafter (§ 6.5.1).*

6.4 Age Interpretation

6.4.1 Section 9

The identification of post-burial production as the likely cause of the differences in ^{26}Al and ^{10}Be concentration between different samples leads to certain conclusions regarding the age of the BF at Section 9. Firstly, samples at different depths are inferred to have been all deposited at the same time, but the shallower samples have more post-burial production. Secondly, the low measured ^{26}Al:^{10}Be (ranging from 1.85 to 3.80 atoms/atoms) requires the inheritance to have decayed (i.e., ^{26}Al:^{10}Be to have lowered),

because the production ^{26}Al:^{10}Be ranges between 6.7 -8.2 atoms ^{26}Al /atoms ^{10}Be (from the surface to a depth of 10000 g cm^{-2}). However, although the differences in TCN concentration between samples are caused by post-burial production, it is unknown what fraction of the measured TCN of the bottom sample is due to post-burial production (and therefore what fraction represents the decayed inheritance). This means that the deepest sample (2.72 Ma, Lower A2 sample group) is the most closely-limiting minimum estimate of the true burial age of the section. This age has a total analytical uncertainty at 1σ of $^{+0.34}/_{-0.24}$ Ma, and represents the best minimum estimate of the age of the BF at Ballast Brook.

The most probable burial ages of the BF at Ballast Brook can also be computed (Figure 6.6). The lowest measured ^{26}Al and ^{10}Be provide a maximum estimate of the inherited TCN concentration that remains in the measured TCN concentration today. A probability distribution function of burial ages was produced by randomly sampling below these constraints on inheritance (Figure 6.6a). However, this histogram is only statistically relevant if it is equally likely for the ^{26}Al and ^{10}Be to lie anywhere within the allowable range. In other words, the probabilities do not reflect process, but rather the fraction of the input range in inheritance that results in a given age. Figure 6.6b shows the combinations of inherited ^{26}Al and ^{10}Be that yield ages older than 2.72 Ma.

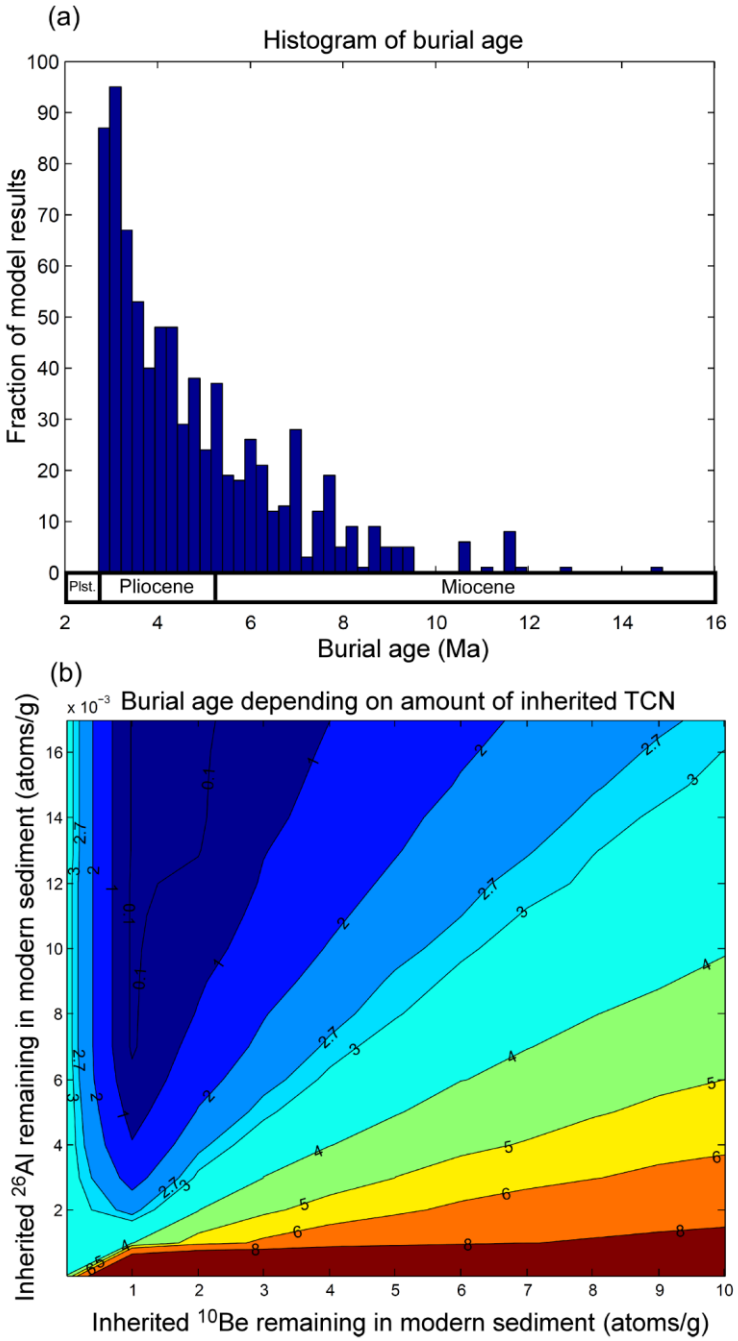

Figure 6.6 – Impact of inherited TCN on simple burial age. a) Histogram of possible ages for the BF. This histogram was produced by randomly varying possible values of inherited TCN concentration that remains in the measured TCN concentration today, and calculating corresponding burial ages. Therefore, a “higher number of results” means that a larger fraction of the allowable range of inherited TCN concentration

corresponds to that burial age. The total number of runs is 803. The location of the peak is probably a function of the low number of runs; if many more runs had been attempted, the distribution may have had a maximum fraction at the youngest age permitted. b) Combinations of inherited 26Al and 10Be concentration that remains in the measured TCN concentration today that correspond to burial ages of 0.1, 1, 2, 2.7, 3, 4, 5, 6, 7 and 8 Ma.

6.4.2 Section 8

If the interpretation that measured TCN concentrations at Ballast Brook are a function of (1) post-burial muonic production and (2) inherited production holds true for Section 8, a minimum age of 2.4 Ma is obtained. However, although post-burial muonic production depends on depth (as well as age and erosion rate), the average ^{26}Al concentration, ^{10}Be concentration and ^{26}Al:^{10}Be for Section 8 do not correspond to the TCN concentrations at Section 9 for a similar depth (Figure 5.7), and do not align with the Section 9 linear relationship on the isochron plot (Figure 5.6). They fall outside the 2 σ ranges of these fits. Section 8 has ^{26}Al concentration, ^{10}Be concentration, and ^{26}Al:^{10}Be that are lower for their depth, relative to the Section 9 samples.

It is necessary to consider that Sections 8 and 9, which are several kilometers apart (Figure 3.2) may differ in their initial depositional concentration, syn-depositional production, post-incision production, and post-depositional production. Although differences in inherited concentrations between Section 8 and 9 cannot be ruled out, the constant inheritance across 20 m of stratigraphy at Section 9 suggests that inherited concentrations may be similar at adjacent sites as well (Walther's Law). Furthermore, Sections 8 and 9 have similar ^{26}Al:^{10}Be, and lie on an exposure line in a burial plot (Figure 5.6), suggesting similar depositional concentrations. A difference in depositional rate between Sections 8 and 9 (syn-burial production) will not affect the measured TCN concentrations (§ 6.3.1). Similarly, although Section 8 and 9 appear to have a different style of erosion due to the position of the modern river channel near Section 9 (i.e., with Section 8 undergoing gully incision and Section 9 experiencing parallel scarp retreat, as confirmed by examination of the sections on air photos), the difference in post-incision

production will not affect the measured TCN concentration (§ 6.3.2). Lastly, Sections 8 and 9 could have experienced a different depth-history (and therefore different post-burial muonic production, which was shown to be a significant fraction of the measured TCN concentrations at Section 9). However, the similar height of the exposures along the Ballast Brook (60 m ledge at Section 9, 62.5 m cliff at Section 8, and 64 m at Section 3), which correspond to the height of the surrounding plateau, suggest that neither of these localities has experienced significantly different regional erosion. Therefore, it is likely that Section 8 and 9 have experienced similar post-burial muonic production, and a minimum age of 2.35 Ma is assumed for Section 8.

Sections 8 and 9 are probably representative for the rest of the BF at Ballast Brook, based on the broad similarity of the sedimentology across Ballast Brook exposures and the similarity of the TCN measurements at Section 8 and 9. Although the minimum age of Section 8 (2.35 Ma) is younger than the minimum age of Section 9 (2.72 Ma), the depth of sediment above the Section 8 samples was much shallower than above Section 9 samples (Table 5.1), which makes the Section 8 minimum age less closely-limiting. Hence, the Section 9 minimum age is adopted for the BF at Ballast Brook.

6.4.3 Maximum age

An important assumption of TCN burial dating is that depositional TCN has an initial $^{26}Al:^{10}Be$ of 6.75. If the initial $^{26}Al:^{10}Be$ in BF sediment was depressed due to temporary burial of sediment prior to final deposition at Ballast Brook, calculated simple burial ages would constitute maximum-limiting ages. In the case of the BF at Ballast Brook, this would make the final estimates maximum estimates of minimum-limiting ages. However, the low variability in TCN at Section 9 (after accounting for post-burial muonic production which caused the trend with depth) 9 suggests that the inheritance concentration was constant overall or so low that its variability is inconsequential. The fact that all the Section 9 samples lie on an exposure line in a burial plot (Figure 5.6) also suggests similar depositional concentrations. It is curious that the Upper A2 sample group had much more internal variation than the Lower A2 sample group or Samples 032, 029, and 030 (Figure 5.4), as though there is more variation in inheritance at this

level. In conclusion, since several measures suggest that the samples have constant inheritance, the samples are considered not to have had depressed initial ratios (and even if they had it can be demonstrated that it would be inconsequential).

6.5 *In-situ* muonic exposure history

The measured trends in concentrations and ratios at Section 9 cannot be explained with one single scenario (constant *in-situ* erosion, and depth), which confirms that Section 9 has experienced changing conditions of *in-situ* erosion and depth over time (e.g., episodic erosion, glacial cover; § 6.3.3). In a simple way (ignoring changes in conditions over time), the trend in concentrations and the trend in ratios can provide some information on *in-situ* erosion and depth, because post-burial production can only explain each respective trend under certain conditions.

The exposure to muons at Section 9 likely started in the Pleistocene or earlier, because the trend in ^{10}Be with depth requires at least 0.7 Ma to develop, and the trend in ^{26}Al with depth requires at least 1.4 Ma to develop. This is later than the minimum simple burial age, suggesting that erosion happened after deposition of the BF at Ballast Brook. This agrees with the step-wise erosion visible from the 84-m surrounding plateau to the 60-m ledge at Section 9.

Additionally, the trend in ^{10}Be with depth cannot be explained if the depth above the shallowest sample (Sample 030; depth at which post-burial TCN production occurred) was greater than 25 m or ever less than 10 m. This suggests that the depth of the section during most of its exposure to muons was between 10 and 25 m, which also agrees with the height of the 60-m ledge (note that Figure 3.2 considers the stratigraphy up to the 84-m plateau). This is consistent with the fact that the data plot in the forbidden zone of the burial plot at modern depths, since this means that the thickness of the modern section must have been greater for much of its history. Lastly, the trend in ^{26}Al:^{10}Be with depth requires a maximum *in-situ* erosion rate of 20-30 cm/ka (if erosion rate is higher, the steepness of the trend cannot be produced by post-burial muonic TCN production).

Thus, the measured TCN trends at Section 9: 1) suggest Pleistocene erosion after initial burial, 2) constrain the depth above the shallowest sample to 10-25 m, which corresponds to the height of the 60-m ledge, 3) constrain maximum *in-situ* erosion rate to 20-30 cm/ka. In contrast, the data cannot constrain the time of the Ballast Brook incision or rate of cliff retreat, because the TCN concentrations are largely unaffected by post-incision production.

6.6 Paleo-erosion rates

The TCN concentrations can be used to reconstruct paleo-erosion rates for the catchment that sourced the BF. These calculations assume that no TCN production occurred during the transport of the sediment and that the parent surface concentrations were at equilibrium with erosion in a steadily eroding catchment. The catchment-wide production rate used was that of Ballast Brook at Section 9. This is a slight underestimation of true production rates for the BF sediment source region because the surface of the catchment is higher than the sample locations at Section 9. However, considering the low relief (less than 200-300 m) of Banks and Victoria Is., the likely source of the BF at Ballast Brook (Fyles *et al*. 1994), this is considered a close approximation.

The paleo-erosion rate calculated for Section 9 using ^{26}Al is $178\ ^{+27}/_{-21}$ cm/ka, and using ^{10}Be is 86±2 cm/ka. The paleo-erosion rate calculated for Section 8 using ^{26}Al is 133±2 cm/ka, and using ^{10}Be is 92±3 cm/ka. The ^{26}Al concentrations yield higher erosion rates and more variation in erosion rates than do the ^{10}Be concentrations because the paleo-erosion rate calculation assumed that there is no post-burial production, and more ^{26}Al is produced during post-burial production than is ^{10}Be.

Post-burial production raises the ^{26}Al and ^{10}Be concentrations, and ^{26}Al:^{10}Be of samples. This causes samples to shift upward on a burial plot (e.g., Figure 5.6), thus crossing exposure lines. Therefore, the depositional concentration is underestimated, and the paleo-erosion rate overestimated. The most closely-limiting maximum estimate of the paleo-erosion rate is the ^{10}Be estimate (86±2 cm/ka for Section 9).

A lower limit on catchment-wide paleo-erosion can be obtained by assuming that the BF is not Miocene (i.e., older than 5.33 Ma), which is a reasonable assumption based on plant macrofossils (Matthews and Ovenden 1990). The combinations of decayed inherited ^{26}Al and ^{10}Be that correspond to a Miocene age (greater than 5.33 Ma) are summarized in Figure 6.6b. The highest concentration of ^{10}Be that will produce this age is $10x10^3$ atoms ^{10}Be. This ^{10}Be concentration, decayed by 5.33 Ma, produces a lower limit on paleo-erosion rate of 49±1 cm/ka. Thus, the paleo-erosion rate can be constrained to 49-86 cm/ka. This paleo-erosion rate is higher than the *in-situ* maximum erosion rate of 20-30 cm/ka (§ 6.5).

6.7 Conclusion

In this Chapter, various hypotheses about the sources of TCN production and age of the BF were tested, in an effort to reconcile the young simple burial ages obtained in Chapter 5 with the older ages previously inferred from plant macrofossil evidence (Fyles *et al.* 1994; § 3.5). Syn-burial production and post-incision production were shown to be insignificant to TCN burial age calculations, and post-burial production was proven to be a valid mechanism for the observed trends in concentration and ratios with depth. Based on this, a minimum age of 2.72 Ma was obtained for the BF at Ballast Brook, as well as a paleo-erosion rate of 49-86 cm/ka for the catchment that sourced the BF.

Chapter 7 : Discussion

7.1 Characterization of the BF stratigraphy

The present research has resulted in a slightly revised interpretation of the depositional environments of the BF at Ballast Brook. New observations (paleoflow, organic facies, concretions, potential ice-wedge pseudomorph) have helped better characterize the sedimentology of the BF at Ballast Brook. This enables better comparisons of the stratigraphy among different BF exposures, and contributes to a better understanding of the late Cenozoic development and incision of a formerly extensive coastal plain.

7.1.1 Depositional environments of the BF and subdivision of the stratigraphy

Lower energy fluvial facies at the base of the BF on Banks Is.

One of the objectives of this research was to determine whether there are any distinct changes in the sedimentology or stratigraphy at Ballast Brook that that could be mapped regionally and correlated to other BF exposures. The description of clayey silt (and local silty clay) at the base of the BF at Ballast Brook indicates a former, low-energy environment, such as a floodplain, which followed the erosion that generated the unconformity. Owing to the inferred low relief of the braid plain, if there was ponding in one area, there was likely ponding along more of the coastal plain. Although the Fyles *et al.* (1994) reference section for the BF has a sandy base (Figure 9 in Fyles *et al.* 1994), Fyles *et al.* (1994) suggested that at other locations, the thin organic clay overlying the BBF-Unit 4 peat represent substantial intervals of floodplain pond sedimentation in the fluvial system. To reflect the importance of the distinct grain size of this silt and clay unit, the BF-Unit A1 was distinguished from the remainder of BF-Unit A at Ballast Brook (Figure 3.2).

Several of the other BF localities across the CAA also have fine-grained facies, and transition from a lower energy depositional environment to a braided river environment through a coarsening upward trend, although not necessarily at the base of the BF. The BF on Prince Patrick Is. locally contains a clay and silt unit (interpreted as overbank

suspension deposits; Facies E in Devaney 1991). This mud is relatively pure (sand-free, almost no visible woody detritus) although its lateral extent is uncertain. On Ellesmere Is., the BF-contemporaneous Fyles Leaf Bed section has parallel, finely-laminated silt and fine sand interpreted as a small subaqueous fan, overlain by shallow crossbedded leafy sand beds that gradually (more than 40 m) coarsen upwards and transition to a cobble braided stream facies (Rybczynski *et al.* 2013). The laterally extensive (discontinuous over more than 500 m, averaging more than 1 m thick) peat and clay at the Beaver Pond site (Rybczynski *et al.* 2013) also indicates a low-energy environment, but the basal contact of the High Terrace Sediments at this site was not exposed. Lastly, the BF exposed at Meighen Is. contains one or possibly multiple marine clay and silt units bedded between sandy fluvial sediment. The mud beds are interpreted to represent a shallow marine delta and estuarine environment (Fyles *et al.* 1991; Gosse, unpublished data).

However, these fine-grained units cannot be confidently correlated across the BF sites. While it appears that a general coarsening upwards towards a higher energy fluvial system is recorded in all of these (most comprehensively studied) BF sites, these transitions may be caused by different controls at each site. For instance, Ballast Brook may be the only BF locality that experienced a period of floodplain ponding immediately after the regional erosion event indicated by the unconformity.

Glacial facies at the base of the BF on Banks Is.

Despite some uncertainty (§ 4.2.1), the favoured interpretation is that the Unit A3 glaciofluvial gravel is in place. This interpretation rests primarily on the TCN concentrations, which are indistinguishable after accounting for differences due to muonic production (§ 6.3.3), and is consistent with the lateral extent of the gravel (~ 40 m) and apparent recent erosion of the exposed surface (§ 4.2.1).

Although the depositional environment of the BF has previously been described as a sandy-and gravelly-braided fluvial system, with occasional meandering stream facies (Fyles 1990), the new observation of ice-proximal glaciofluvial gravel (Unit A3; Figure 3.2) suggests that the BF on Banks Is. fortuitously records a Pliocene terrestrial proglacial

environment. The gravel is also consistent with the observation of a potential ice-wedge pseudomorph stratigraphically a few meters below (in Unit A1; Figure 3.2). This adds to the complexity of Pliocene landscape and paleoenvironmental changes recorded by the BF. Although the glaciofluvial gravel is thin (up to 5 m) and not necessarily representative of the rest of the BF, it indicates that the BF was deposited in part due to glacial processes. Furthermore, the glacial facies has obvious paleoclimatological implications that contribute to other records of the Arctic Pliocene paleoenvironment (i.e., plant assemblages, paleofauna, ice-wedge pseudomorphs, and numerous temperature and precipitation proxies; Matthews and Ovenden 1990, Tedford and Harington 2003, Ballantyne *et al.* 2010, Csank *et al.* 2011, Rybczynski *et al.* 2013).

7.1.2 Other characterizations of the BF on Banks Is.

Slight shift in paleoflow on Banks Is. not described at other sites

Although the present research has generally confirmed the northwestern to northern paleoflow direction previously described for the BF on Banks Is. (e.g., Hills 1969, Fyles 1990; § 3.3), a change in paleoflow within the BF was observed at different exposures along Ballast Brook (northwestward near the base, and northward near the top; § 3.3), which has not been previously reported on Banks Is. or at other sites of the BF (the uncertainty of this result is reported in § 4.2.6). This may indicate a change in general flow direction at the Ballast Brook locality, although the shift could not be linked with any particular stratigraphic change (because the change in paleoflow was transitional or because the number of observations is insufficient to properly characterize the variability). With further verification, the shift could potentially provide insight for changes in contemporaneous regional topography (i.e., the incision of wide channels between the islands of the archipelago; see below, § 7.5).

Classification of organics on Banks Is. and comparison to other sites

The diversity and quality of preservation of flora and faunal material have been a key interest for the extensive research on the BF, as demonstrated by a number of studies entirely on the organics (e.g., Matthews and Fyles 2000, Hutchison and

Harington 2002, Tedford and Harington 2003; § 2.3.2). The organics have been studied extensively in terms of plant assemblages (e.g., Matthews and Ovenden 1990, Matthews and Fyles 2000), temperature proxies (e.g., Ballantyne *et al.* 2010), and vertebrate fossils (e.g., Rybczynski *et al.* 2013). There has also been interest in terms of the spatial relationship of organics to the braid plain (e.g., Devaney 1991), and whether the Pliocene organic-rich deposits are different from Pleistocene organic-rich deposits such as super interglacials (Matthews *et al.* 1989). Murphy (2006) described three types of wood lenses in the BF at Ballast Brook, in terms of internal structure (e.g. presence of beds, dip of the beds within the lens), size, gradual or sudden tapering, and symmetry.

The present research has built on the previous work by dividing the BF organics into three facies. There is no clear correlation with Murphy (2006)'s classification of organic-bearing sediment lenses. Murphy (2006)'s study was restricted to 8 lenses on the eastern side of Ballast Brook, including anomalous lenses that were not consistent with the proposed classification. The present research is applicable for sections on both the eastern and western sides of Ballast Brook (e.g., Sections 8 and 9), and focuses on the characteristics of the organics and their association with adjoining clastic facies, rather than on the geometry of lenses.

This new classification has revealed that with only a few exceptions, all occurrences of organic material in the BF at Ballast Brook are allochthonous (Fyles *et al.* 1994). The organics were transported various distances before deposition. Organic facies 1 (wood flakes interbedded with silt and mud) probably represents the low-energy cap of abandoned channels. Organic facies 2 beds (horizontally extensive flat beds of rounded wood fragments, interbedded with fine-grained light-grey sands) probably are the aggrading final stages of larger channels (~ 20 m wide). Organic facies 3 beds (jammed logs) are interpreted to be the logs carried and deposited in small (less than 5 m) but energetic channels (i.e. log jams).

However, a few isolated autochthonous organics were also present. The only observations at Ballast Brook that indicate little or no transportation were a cone delicately attached to a twig, two sub-metre thick autochthonous mossy peats, and an

upright stump. These findings are similar to those of other BF localities. On Prince Patrick Is., no autochthonous organic material was observed (Devaney 1991). Either a forested watershed may have been providing material to a poorly vegetated braid plain, or the braid plain was vegetated, but highly efficient at reworking root traces, paleosols, and *in-situ* plant material, (since these were absent from the examined sections; Devaney 1991). The presence of thick mats of moss, which look *in-situ* but are likely allochthonous, suggest that the vegetation source was at least nearby (Devaney 1991). This may also be the case for the detrital layers (Organics 1-3) at Ballast Brook. In contrast, on Meighen Is., two layers of autochthonous mossy peat (although they have different colour and fossil content), with well-preserved wood that still contains bark, were observed at the top of Unit 3 (Fyles *et al*. 1991).

Iron concretions in the Beaufort Formation appear to have formed in-situ

Iron concretions were found and described at Sections 3 and 8. No previously published accounts of the BF mention iron concretions, and Hills (1969) specifically indicates that he observed no concretions in the BF at Ballast Brook despite their occurrence in the Eureka Sound Group nearby. It is unclear by what process the concretions form (how long they required to form and at what depth; Vogt 1990). Reworking of concretions from the Eureka Sound Group to explain all observed concretions is unlikely because, in places, the concretions are present within 10-100 cm thick red-beds and attached to cemented plant material which would not have been eroded from the Eureka Sound Group. Instead, the concretions are likely diagenetically formed where groundwater conditions are favourable for redox reactions (Vogt 1990). They may occur in periglacial aquitards in the BF, or in organic zones, where groundwater flow would be slowed. There seems to be a close association of the observed concretions and hematite cementation with organics.

Ice-wedge pseudomorphs on Banks and Ellesmere Is.

The potential ice-wedge pseudomorph in Unit A1 at Section 9 is important because it provides evidence of permafrost during deposition of the lower BF. The potential

pseudomorph was found at the very base of the BF, perhaps suggesting that the period of sedimentation immediately above the unconformity was a cold period. If its formation occurred on a forested landscape (which is not necessary depending on how far the organics were transported) this would indicate that the Banks Is. boreal forest was coincident with at least discontinuous permafrost conditions. This is important because the extent of permafrost during the warm conditions of the Pliocene is not evident. While northern Alaska may have been too warm for permafrost at 2.48 Ma (Brigham-Grette and Carter 1992), permafrost was present in Russian sites by 3.5-3.0 Ma (Anisimov *et al.* 2002).

The presence of permafrost in the BF on Banks Is. is also particularly interesting given the presence of ice-wedge pseudomorphs in other occurrences of the BF. The Fyles Leaf Bed site records the only other known occurrence of fossil ice-wedge pseudomorphs in the BF and related sediments, and the northernmost dated evidence of Pliocene permafrost (Rybczynski *et al.* 2013). The presence of a potential ice-wedge pseudomorph as far south as Banks Is. may also warrant a reconsideration of the ice-wedge pseudomorphs in the BF sediment on Prince Patrick Is., which could not be differentiated from modern pseudomorphs (Devaney 1991).

7.2 The BF on Banks Is. is Pliocene

TCN burial dating of the BF at Ballast Brook confirms, with a completely independent method, previous estimates of the age of the BF at Ballast Brook using plant macro- and microfossils, biostratigraphy, and correlation with Meighen Is. that the BF is not Pleistocene in age (§ 3.7). The technique yielded a minimum age of 2.72 $^{+0.34}/_{-0.24}$ (1σ) Ma. Although the estimate falls within 1σ error into the Plio-Pleistocene boundary (2.588 Ma; Cohen *et al.* 2014), it is unlikely that the BF at Ballast Brook is Pleistocene because the age is a minimum. Since plant macrofossils also suggest that a Miocene age is highly unlikely (Fyles *et al.* 1990), the BF at Ballast Brook was likely deposited during the Pliocene.

TCN burial dating was unable to further refine the age of the BF to greater precision. There are still two possibilities regarding the age of the BF at Ballast Brook: (1) 2.72

$^{+0.34}/_{-0.24}$ (1σ) Ma is a close minimum-limiting age, and the BF at Ballast Brook was deposited during the Plio-Pleistocene transition, after the BF on Meighen Is. (3.3 $^{+0.19}/_{-0.22}$ (1σ) Ma), at the Beaver Pond site (3.4 $^{+0.6}/_{-0.4}$ (1σ) Ma), and at the Fyles Leaf Bed site ($3.7^{+1.0}/_{-0.7}$ (1σ) Ma; Figure 1.1), or (2) 2.72 $^{+0.34}/_{-0.24}$ (1σ) Ma is not a close minimum-limiting age, and the BF was deposited earlier in the Pliocene (e.g., possibly during the Mid Pliocene warm period; Rybczynski *et al.* 2013), and may be the same age as the BF at other localities. The minimum age obtained with TCN burial dating does not allow a differentiation between these two scenarios. Biostratigraphic interpretations that the BF is older than 3 Ma (§ 3.5.2) suggest that the TCN age is not closely limiting. The implications for these two scenarios have already been explored: implications for the continuity of the braid plain (§ 2.3.1 and 2.5), explaining variations in paleoenvironmental records (§ 2.1.4), the extent of the braid plain (§ 2.1.3), the time span represented by the deposit (§ 2.1.4), the causes of deposition (§ 2.1.5), the consequences of deposition on pan-Arctic climate and ocean circulation (§ 2.1.6), and the causes of incision of the braid plain (§ 2.1.7).

7.3 Catchment-wide paleo-erosion rates

Because the BF is a thick sequence marking a significant phase of Pliocene coastal plain aggradation, it offers an opportunity to contribute to the study of how Pliocene erosion rates compare to Pleistocene and modern erosion rates. At the Plio-Pleistocene transition and the onset of NHG (Figure 7.1), different lines of research have shown that global sediment flux may have increased, decreased, or remained the same (e.g., Molnar 2004, Syvitski and Milliman 2007, Willenbring and von Blanckenburg 2010). In the western Canadian Arctic, rapid erosion contributed to the greater than 3 km-thick, Plio–Pleistocene Iperk Formation and a 23-fold increase in sedimentation rates relative to the Early and Middle Miocene (McNeil *et al.* 2001, § 2.1). Measurements of the BF paleo-erosion rate will help understand how sediment flux changed in the latest Neogene.

The maximum erosion rate estimate for the paleo-catchment (likely on Banks and Victoria Is. based on provenance; § 2.2.3), ranging from 49-86 ± 2 cm/ka) suggests a relatively high sediment flux for this part of the CAA (§ 6.6). This high catchment-wide

paleo-erosion rate is consistent with the findings that the samples spanning 20 m at Section 9 are the same age (the TCN concentrations are indistinguishable after accounting for differences due to muonic production; § 6.3.3). The 49-86 ± 2 cm/ka rate is much higher than modern global averages of 4-7 cm/ka obtained from river load data (Willenbring and von Blanckenburg). Late Quaternary bedrock erosion rates on the dissected plateaus of the eastern Canadian Arctic are extremely slow (0.1-0.7 cm/ka, Margreth 2015; Marquette 2004), perhaps mainly because that area has been weathered little during Quaternary interglacials, or more likely, that the eastern Arctic has been subjected to a much greater magnitude of glacial erosion since the Late Pliocene (Staiger *et al.* 2006). Erosion rates obtained for the Texas Coastal Plain, which may constitute an analogue for the BF coastal plain, are also much lower than 49-86 ± 2 cm/ka (maximum of 5 cm/ka; Hidy *et al.* 2010).

The BF catchment-wide erosion rate may be higher than these erosion rates because the availability of sand from sand-rich relatively unconsolidated sources (e.g., Eocene Eureka Sound Group, Cretaceous Hassel and Isachsen Formations) was nearly unlimited. The deposition of such a large (part of the 3-km Iperk Formation offshore) and quick (49-86 ± 2 cm/ka) erosion event would have required a readily accessible source of unconsolidated sediment, because the erodibility of unconsolidated sediment compared to consolidated rocks differs by a factor of seven (Schaller *et al.* 2006). For example, changing climate in the Pliocene (e.g., thawing permafrost, increased precipitation) may have suddenly made the widespread, unconsolidated Eureka Sound Group (along with other parent sources) available for transport. This scenario agrees with the lower post-depositional *in-situ* erosion rates obtained at Section 9 (10-20 cm/ka), which suggest that Pleistocene *in-situ* erosion rates (of the BF plateau surface) were much lower than Pliocene erosion rates on the catchment that sourced the BF. If transport ability then dropped, this may have been linked to the subsequent incision of the BF. This suggests a transport-limited depositional system. In contrast, in the bedrock-dominated eastern Canadian Arctic, deposition was sediment-limited. In the eastern Canadian Arctic, large deposition events would require more weathering of

bedrock to produce regolith, rather than mobilization of stored unconsolidated sediment. Similarily, a stripping event may have produced the Upper White Channel Gravel (minimum erosion rate 25 cm/ka; Gosse *et al.*, in prep.).

Thus, the catchment-wide paleo-erosion rate and *in-situ* erosion rate obtained by the present research enable a regional interpretation of sediment storage, transport, and deposition. However, although these processes were likely linked to Pliocene climate changes, these links remain conceptual, especially without precise chronology (several hypotheses are presented in § 2.1.5). This study provides one of the only Arctic estimates of Pliocene-Pleistocene erosion rates (Flowers *et al.* 2006 over the past 1000 Ma, Staiger *et al.* 2006 over the past 3.5 Ma, Hidy *et al.* 2013 over the past 2.6 Ma).

7.4 Earliest terrestrial evidence of glaciers on Banks Island

7.4.1 Glaciation styles possible considering the glaciofluvial gravel on Banks Is.

Although the glaciofluvial sediment described on Banks Is. was thin and limited in lateral extent (Figure 3.2), the presence of striated cobbles indicates the presence of penecontemporaneous, active subglacial abrasion within the catchment, which requires warm-based ice. Warm-based ice is caused by thicker ice (i.e., an ice sheet that traps geothermal heat) or by frictional heat generated by rapid ice flow due to ice streams or converging ice in regions of high relief (Staiger 2006). The latter can be ruled out because of low relief on Banks Is. (~ 300 m, up to 1000 m). Banks Is. could have had its own ice cap. A useful analogue may be the Meighen Is. ice cap because it is at the same elevation as Banks Is. (approximately 200 m above sea level; Koerner *et al.* 1977), although it is presently cold-based. It seems that the presence of an ice sheet would be the simplest explanation for the necessary warm-based conditions. Ice sheet growth or expansion onto Banks Island is plausible considering Pliocene paleoclimate records. Further, the western CAA was likely a contiguous coastal plain at this time and, hence, the deep modern channels would not have been present to direct ice-flow. If the

observed glaciofluvial sediment is the product of a Pliocene continental glaciation (i.e., a Pliocene LIS) it has a number of implications, which are explored below.

7.4.2 Oldest continental glaciation age in the Canadian Arctic

It is widely acknowledged that several major continental glacial advances occurred on Greenland and Antarctica before the Pleistocene (Lisiecki and Raymo 2005). According to North Atlantic (Kleiven *et al.* 2002) and Lomonosov Ridge (Moran *et al*. 2006) IRD records, the Greenland Ice Sheet first appeared at ~3.3-3.2 Ma. This coincides with the M2 Pliocene Glacial (3.305-3.285 Ma), which is documented by a drop in global $\delta^{18}O$ records (Lisieki and Raymo 2005; Figure 7.1a) and which witnessed low Arctic summer temperatures (inferred from vegetation composition; Brigham Grette *et al.* 2013). Based on marine oxygen isotope records, Mudelsee and Raymo (2005) suggested that the Greenland Ice Sheet may have appeared as early as 3.6 Ma (Figure 7.1e), and proposed that a steady increase in global ice volume started at that time (Figure 7.1e).

However, some of the Pliocene glaciations did not have ice outside of Greenland and Antarctica. For example, drilling from the Ross Sea suggests that most of the M2 $\delta^{18}O$ anomaly can be attributed to ice advance in Antarctica (McKay *et al.* 2012). The M2 was perhaps the failed onset of northern hemisphere glaciations (De Schepper *et al.* 2013). Warmer Arctic summers in the Lake El'gygytgyn record during the Pliocene would be unlikely if ice was present in the Arctic, and are therefore consistent with Pliocene glaciations being restricted to the Antarctic (Brigham-Grette *et al.* 2013). High latitude winter insolation was also elevated in the Pliocene, peaking between 3.5 and 4 Ma (Rybczynski *et al.* 2013, Figure 7.1b).

At some point, there was a temperature threshold whereby northern hemisphere ice sheets arose (referred to as the onset of Northern Hemisphere Glaciation, NHG; De Schepper *et al.* 2013). The amplitude of fluctuations in global sea level increased shortly before or at the Plio-Pleistocene boundary, as demonstrated from $\delta^{18}O$ from benthic and planktonic foraminifera (Lisiecki and Raymo 2005; Figure 7.1a). Ice rafted debris from the North Pacific and oxygen isotope data also reveal global glacial expansions at 2.7 Ma (Haug *et al.* 1999, Figure 7.1d) and 2.5 Ma (Shackleton *et al.* 1984; Figure 7.1e). A

compilation of ice rafted debris records from the North Atlantic and Nordic seas dates the expansion of ice sheets in northern Europe at 2.75 Ma (Kleiven *et al.* 2002; Figure 7.1d). The transition in both opal and magnetic susceptibility from core 882 in the northern Pacific also shows a transition at 2.7 Ma, indicating cooling of water temperatures and the occurrence of ice rafted debris, respectively (Haug *et al.* 1999, Figure 7.1d).

However, it is unclear exactly when the transition to northern hemisphere glaciations occurred, due to the nature of $\delta^{18}O$ records and ice rafted debris records. Although eustatic equivalent changes in sea level give an indication of global ice volume (Lisiecki and Raymo 2005), they do not indicate where the ice was located (small increases of ice volume in Greenland and Antarctica could explain them). Similarly, ice-rafted debris, which is widespread in the Late Pliocene and early Pleistocene marine sediments (Haug *et al*. 2005) gives an indication of timing, but does not provide a measure of glacier type or size (local alpine systems with tidewater outlet glaciers could produce them), and interpretation is complicated by the potential transport of IRD by sea ice (Stickley *et al.* 2007, Polyak *et al.* 2013). Terrestrial records are the only evidence that truly indicate ice-sheet extent, but dating terrestrial records of early glaciation is difficult because later glaciations often obscure or remove earlier evidence (Gibbons *et al.* 1984). Terrestrial ages help constrain ice-sheet models by placing physical constraints on ice sheet geometry, to understand how glaciations respond to CO_2 concentrations and polar temperatures. CO_2 and temperature proxies have been studied in the BF on Ellesmere Is. (e.g. Ballantyne *et al.* 2010). The glacial sediments in the BF at Ballast Brook are particularly important because of their terrestrial nature.

The BF glaciation age is comparable to several previously published terrestrial ages for ice sheet extent. The oldest date bearing on the earliest evidence of the Pleistocene LIS is from burial dating of tills in Missouri is 2.4 Ma (Balco and Rovey 2010; Figure 7.1g). The oldest date constraining the first occurrence of continental glaciation in the Canadian Cordillera (first CIS) is 2.64 $^{+0.20}/_{-0.18}$ (1σ) Ma (Hidy *et al.* 2013; Figure 7.1g). These ages are just slightly younger than the ages for the CIS of Harris *et al.* (1994) and

Duk-Rodkin *et al.* (2004; Figure 7.1g). Gao *et al.* (2012) argue that a 3.5 Ma ice sheet was present in the James Bay Lowland, suggesting continental glaciation in the mid-latitudes during the Mid Pliocene. The 2.72 $^{+0.34}/_{-0.24}$ (1σ) Ma minimum age for the presence of glacier ice on Banks Is. provides the oldest date for glaciation (albeit of unknown scale and origin) in the Canadian Arctic (within error of the age for the CIS in the Yukon). Considering the 1 σ uncertainty, the age from Banks Island may support the results of Hidy *et al.* (2013).

Until more precise ages are available for the Banks Is. glaciofluvial gravel, it will not be possible to determine the precise age of the associated glaciation. The Banks Is. age is a minimum age, which means that glacier ice may have been present on Banks Is. even earlier than the Pliocene-Pleistocene transition. Depending on whether or not the age is a closely-limiting minimum age, an ice sheet may have been present on Banks Is. in the Late Pliocene (i.e., marine isotope stage G6 at 2.72 Ma), or Mid Pliocene (perhaps the M2 event at 3.30 Ma or the MG6 event at 4.5 Ma; Lisiecki and Raymo 2005, De Schepper *et al.* 2013), although biostratigraphic interpretations suggest that the BF is older than 3 Ma (§ 3.5.2). Thus, the glacial sediments in the BF at Ballast Brook provide the earliest estimate of continental glaciation in the Canadian Arctic. The glacial facies on Banks Is. may be correlative to a documented increase in precipitation and onset in cold winter temperatures in the Lake El'gygytgyn record, Siberia, which occurred at 2.73 Ma. These changes are consistent with preliminary model simulations showing the climatic impact of NHG (Brigham-Grette *et al.* 2013; Figure 7.1f).

.

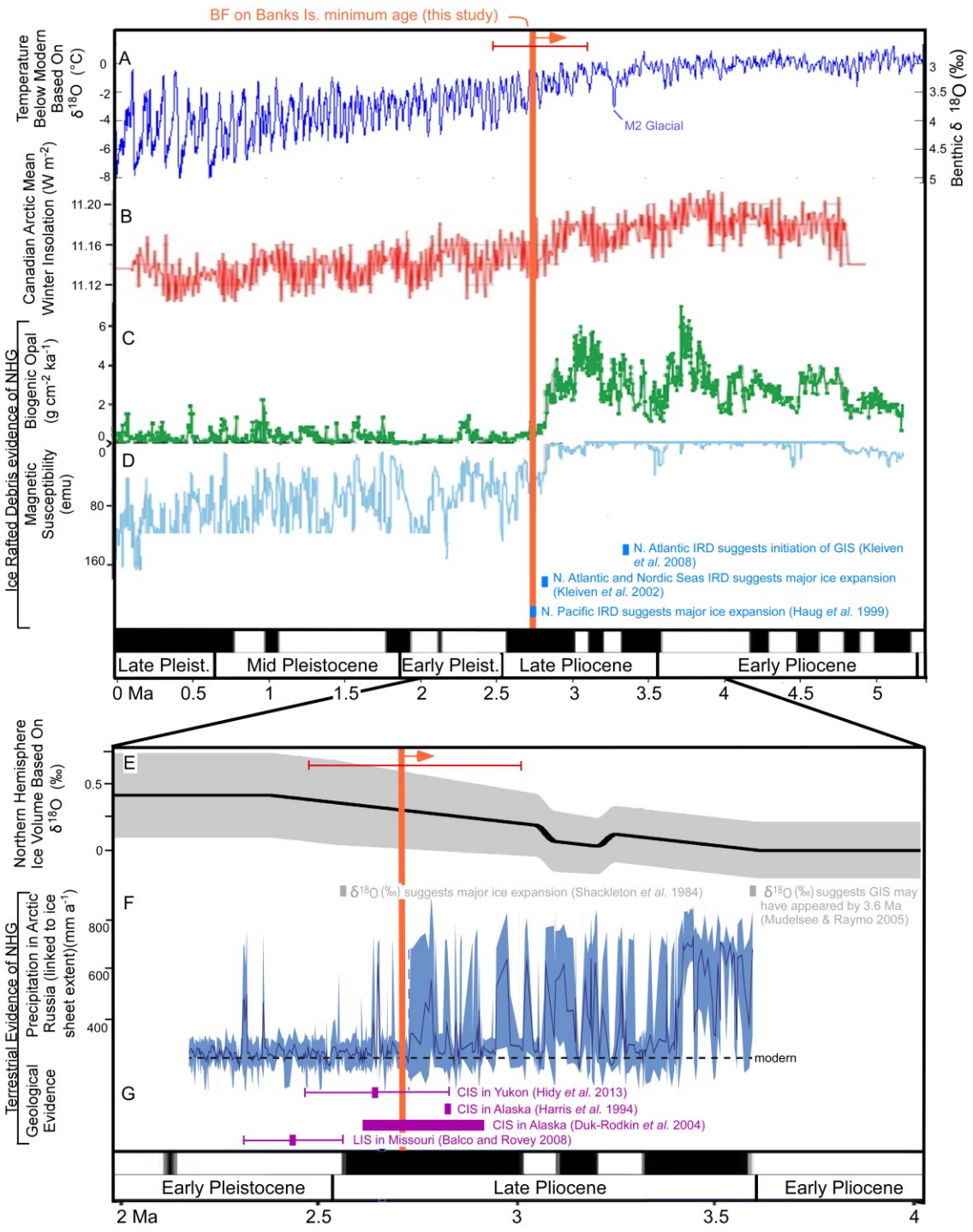

Figure 7.1 – Evidence of Pliocene glaciation. A) Temperature record for the Pliocene, based on a compilation of benthic and planktonic δ18O (Lisiecki and Raymo 2005). The M2 interglacial is indicated at 3.305-3.285 Ma. B) Mean winter isolation for the Canadian Arctic (78°N; Rybczynski *et al*. 2013). C and D) Biogenic opal and magnetic susceptibility for ODP site 882 in the Northern Pacific (Haug *et al*. 1999). Threshold ice rafted debris

(IRD) events are also indicated, such as the onset of the Greenland Ice Sheet (GIS). E) Schematic view of the increase in global ice volume, based on a compilation of globally distributed benthic and planktonic $\delta^{18}O$ (Mudelsee and Raymo 2005). Threshold events in $\delta^{18}O$ are also indicated. F) Annual precipitation at Lake El'gygytgyn (Arctic Russia). The drop at 2.7 Ma is consistent with preliminary models showing the climatic impact of large ice sheets (Brigham-Grette *et al*. 2013). G) Geologic evidence for the presence of the Cordilleran Ice sheet (CIS) and Laurentide Ice Sheet (LIS). Error bars are indicated at 1σ. Timescale from Cohen *et al.* (2014).

7.5 Making sense of the Pliocene paleoenvironmental records

One issue regarding reconstructions of the Pliocene paleoenvironment has been that it is hard to differentiate whether records of warm temperatures reflect interglacial conditions or overall warm Pliocene conditions. For example, Csank *et al.* (2013) suggested that since the Bylot Is. forest deposit and the Kap København deposit represent warm interglacial periods during the overall cool Plio-Pleistocene, other Arctic forest records (i.e., Pliocene records of the BF) may also capture a snapshot of interglacial conditions, rather than the average Pliocene climate. Therefore, they may not be suitable records to study long-term Pliocene cooling. The main barrier to identifying whether the deposits record interglacial periods or average conditions is that the deposits are spatially and temporally isolated from each other.

At Ballast Brook, both glacial and warm conditions may be juxtaposed at one site. It is reasonable to assume that the glaciofluvial gravel (BF-Unit A3) was deposited during a glacial period. Although striated clasts can be deposited by rivers reworking till, the contrast of the BF-Unit A3 clast size, sorting, colour from sediment immediately above and below the gravel, and the presence of striations only within BF-Unit A3 (not in the sediment immediately above or below the gravel), suggests that the BF-Unit A3 is outwash (§ 7.1.1). In contrast, the abundance of wood in the sediment above the outwash (BF-Unit A2 and BF-Unit B), which includes organic beds with very little clastic matter and the autochthonous peat of Kuc and Hills (1971) at Section 9a (Figure 3.1), suggests that it records warm conditions. Therefore, both glacial and warm conditions are present at Section 9, as could be confirmed by detailed paleoenvironmental proxy analyses.

As a result, Section 9 is an appropriate location for higher-precision dating of both the cold-climate and warm-climate sediments. Unfortunately, although the TCN results suggest one depositional event and a single age for the 20 m of Section 9, glacial cycles (41 ka in the Pliocene) are within error of this age ($^{+340}/_{-240}$ ka 1σ). Therefore, Section 9 would therefore be an ideal target for higher-resolution chronology (although no currently known methods can achieve the required precision for the Pliocene).

7.6 Insight into the most recent inception of the M'Clure Strait

7.6.1 Hills' (1969) channel

Hills (1969) mapped a large (~3 km width) Pliocene channel with an axis parallel to the northern coast of Banks Is. (Figure 7.2). Surficial maps by French (1972) and Vincent (1990) also indicate reworked BF in this zone. According to Hills' (1969) observations, Section 9 falls on the southern edge of this channel (Figure 7.2).

The apparent northern dip of Unit A2 and Unit B at Section 9 is consistent with Hills' (1969) observations, suggesting that these units are part of the channel fill (§ 4.2.1). The northward dip shallows towards the north, and eventually becomes horizontal, over lateral distances northward of hundreds of metres (inferred from field photographs; Unit G of Hills 1969, Figure 7.2). In, contrast the thin but laterally extensive exposure of Unit A1 is horizontally bedded and parallel to the underlying unconformity, suggesting that it is a distinct sediment package from the overlying, hypothesized channel fill. The presence of a larger channel is also consistent with the observation of nested channels (although channels are common throughout the field area; § 4.2.1).

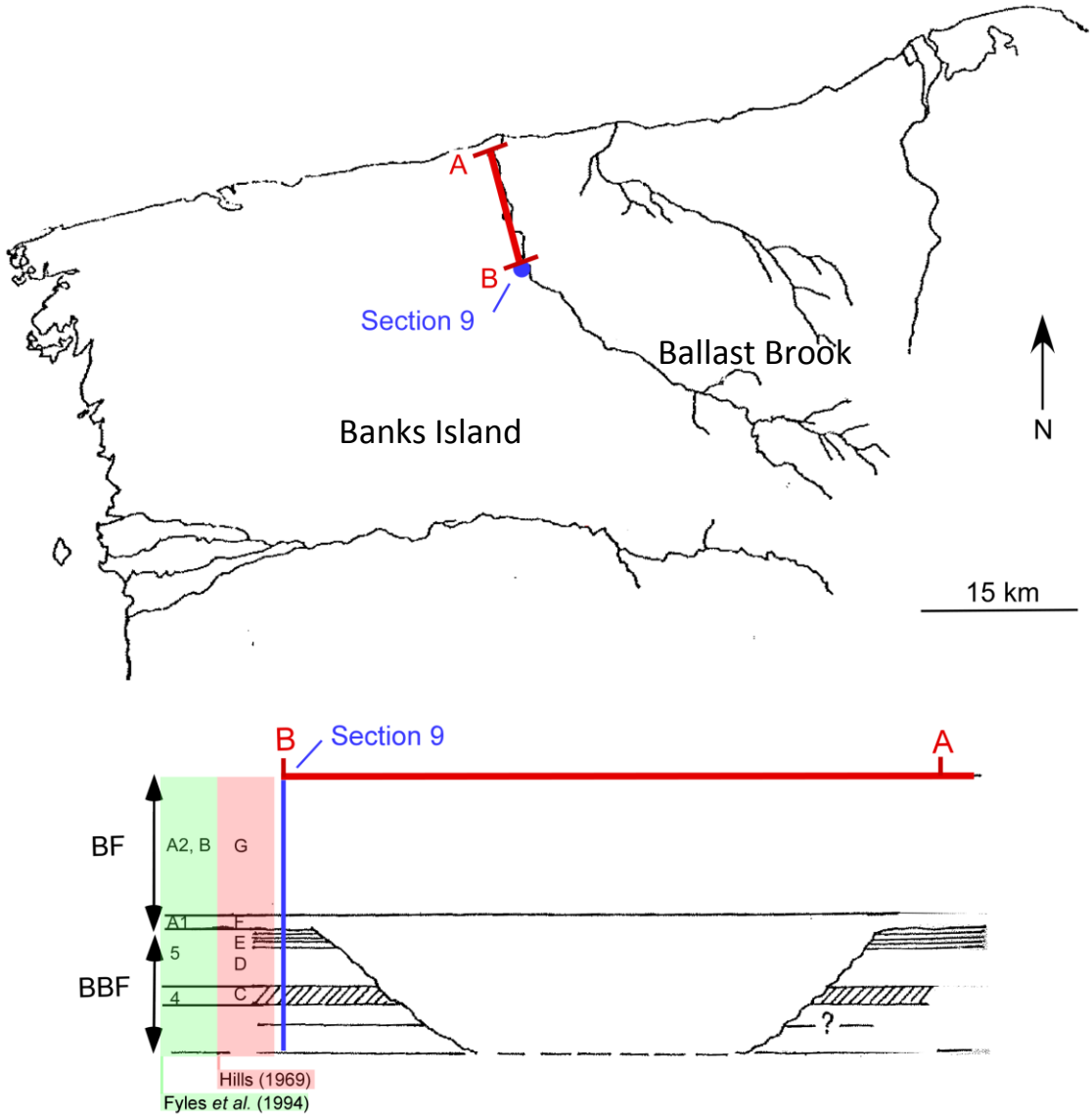

Figure 7.2 – Cross-section through Hills' (1969) Pliocene channel. The cross-section runs along the Ballast Brook exposures of the Beaufort Formation (BF) and Ballast Brook Formation (BBF). Units A-G refer to Hills' (1969) notation of BBF and BF units.

The channel may either be Pleistocene or Pliocene. Hills (1969) ascribed the channel to the Pliocene BF. However, Hills' (1969) channel is parallel to smaller Pleistocene glacial drainage channels on northwest Banks Island (e.g., French 1972). The glaciofluvial gravel, which Hills (1969) did not describe, could indicate a Pleistocene cut and fill within the BF. The Pleistocene channel fill would be very similar to the Pliocene BF because it would be composed of reworked BF. Pleistocene interglacial conditions may have been

sufficiently warm to explain the growth of the Kuc and Hills (1971) autochthonous peat (e.g., fossil forest present in Pleistocene interglacial deposits on Bylot Is.; Csank *et al.* 2013). However, there are a number of problems with a literal interpretation of the simple burial ages (ranging in stratigraphic order from 2.7 to 1.4 Ma; § 6.2.1). According to the TCN chronology, Section 9, and therefore Hills' (1969) channel, is Pliocene (§ 6.5.1). Therefore, at some time in the Pliocene, a large channel ran parallel to the modern northern coast of Banks Is. and parallel to M'Clure Strait.

The formation of Hills' (1969) channel may have required a drop in eustatic sea level (corresponding to global glaciation). The proximity to the ocean (no more than ~ 100 km away in the Pliocene, based on the location of the shelf edge; Figure 3.1) and the absence of tectonic activity in the Pliocene (§ 2.5) suggest that a eustatic sea-level drop would have been necessary to incise the flat coastal plain. Therefore, the presence of a Pliocene channel may be another an indication of Pliocene glaciation. This would be consistent with the presence of a glaciofluvial gravel near the base of the channel and the occurrence of a potential ice-wedge pseudomorph at a similar stratigraphic level as the gravel (Figure 3.2).

7.6.2 Implications of the channel for the opening of the M'Clure Strait

The Pliocene age of this large channel has a number of implications. Since the channel is parallel to the northern coast of Banks Is. (several kilometers wide, but less than 10 km from the current coast; Hills 1969), M'Clure Strait could not have been as wide in the Pliocene as it is currently. If M'Clure Strait was open, Hills' channel would have run north toward it (unless it was not blocked by glacier ice in the strait). The potential shift to a northerly paleoflow in the upper third of the BF at Section 9 (§ 4.2.6) may be an indication of the inception of M'Clure Strait during the later stages of BF deposition at Ballast Brook. This shift in paleoflow probably occurred where the dip of BF-Unit B shallows; however, the change in dip is difficult to identify from the photographs (§ 4.2.1). A contradiction arises if the shift in paleoflow (from north-westward to northward) occurs within the extent of Hill's (1969) channel, because the

channel has a westward paleoflow. This may also be due to an issue with the paleoflow data (§ 4.2.1).

7.7 Future TCN work

7.7.1 TCN at Ballast Brook

This research has established the potential for future TCN dating at Ballast Brook, both in terms of what can and what cannot be completed. There are several tasks that can be attempted. First, the Section 9 muon exposure profile could be revisited with a Monte Carlo simulation. At present, there are too many unknowns at Section 9 (e.g., changes in sample shielding over time, erosion rate, inheritance, etc.) to precisely constrain the chronology, but these variables could be tested with a model in the same way that Margreth (2015) built a Monte-Carlo model to interpret the timing of last plucking and establish episodic erosion rates on a surface with exposure history > 1 Ma (Margreth 2015). Depending on the degrees of freedom of the data, this may result in some constraints on the maximum age of the BF at Ballast Brook, as well as on the depth history at that site. Maximum ages would allow for a refinement of the paleo-erosion rates (which are currently overestimated). Second, samples have been obtained from the BF at Section 3 and below the soil at Section 8, and can be used to obtain a minimum age with cosmogenic $^{26}Al/^{10}Be$ burial dating. Third, samples from the BBF at Sections 3 and 9 have been obtained, and can also be dated, using cosmogenic $^{21}Ne/^{10}Be$. This would date the BBF-BF unconformity, a regional first-order unconformity representing a significant period of regional erosion (McNeil *et al.* 2001), and would give context to previous work conducted on the BBF organics (e.g., Matthews and Ovenden 1990). The ^{21}Ne concentrations would also help characterize the exposure history of the sediment prior to deposition at Ballast Brook, and may help the interpretation of the ^{26}Al and ^{10}Be measured in the BF at Ballast Brook. Lastly, *in-situ* ^{14}C can be measured in any of the collected samples, to better characterize modern TCN production (>50 ka), and perhaps also help the interpretation of the ^{26}Al and ^{10}Be measured in the BF at Ballast Brook. The

samples necessary for the ^{21}Ne and ^{14}C analyses have already been obtained, and some are already partly processed.

This research has also identified the limitations of TCN burial dating of the BF at Ballast Brook. Since no suitable paleosols or peats for depth-profile isochron burial dating could be found, this is not a strategy to attempt again at this site. However, a grain-size isochron approach may be possible in coarser deposits at depths greater than 30 m. Additionally, since TCN inheritance was found to be very low, and post-depositional production therefore relatively significant, only minimum ages can be obtained. It is now known that absolute ages cannot be obtained with TCN dating of the sand at BF at Ballast Brook, although a Monte Carlo model may provide further insight to reduce the total uncertainty and provide a most probable age

7.7.2 Future work for the BF in general

The principal remaining issue is still the chronology of the BF. Therefore, future work at other localities of the BF should focus on finding sites where TCN concentrations can be interpreted more easily, to obtain an absolute age for the BF. Banks Is. may be the only site with the challenge of low inheritance concentrations, since Meighen and Ellesmere Is. had 5-7 times higher TCN concentrations. Therefore, targeting other islands for TCN dating may be more fruitful than continuing investigations on Banks Is.

Chapter 8 : Conclusion

A long-term objective of this research is to establish a chronostratigraphy for the Beaufort Formation (BF) and to piece together a better interpretation of the development and incision of a once-extensive western coastal plain on the shores of the Beaufort Sea in the CAA. One of the main short-term objectives of the present thesis that contributes to this long-term objective was to further characterize the BF stratigraphy at Ballast Brook and identify variations in sedimentation among different BF localities (e.g., changes in depositional environments, evidence for separate depositional events; Figure 1.2).

A number of outcomes of the present research helped attain this short-term objective. The sandy lower unit of the BF identified by Hills (1969), Kuc and Hills (1972) and Fyles *et al.* (1994) was subdivided at Section 9 into Units A1, A2, and A3. Units A1, A2, and A3 were not all observed at other sections at Ballast Brook, and therefore may only represent the local stratigraphy at Section 9. Nevertheless, the subdivision of Unit A provides the stratigraphic framework upon which to base and interpret the TCN chronology. Unit A1 was defined separately from the rest of Unit A to highlight a lower energy fluvial facies on the unconformity at the base of the BF on Banks Is., which may represent a period of floodplain ponding immediately after the regional erosion event. The limited but laterally extensive exposure of Unit A1, generally horizontally bedded and apparently parallel to the contact above the BBF, suggests that it is a distinct sediment package from the overlying Unit A2. Unit A2 marks the base of the braided stream fill of a 3 km-wide channel, first described by Hills (1969). It coarsens upward, as has been observed at other BF sites. Unit A3 was separated from the rest of Unit A to differentiate a newly observed glaciofluvial gravel. Although the depositional environment of the BF has previously been described as entirely sandy- and gravelly-braided fluvial deposits, with some meandering stream facies (Fyles 1990), this gravel suggests that the BF on Banks Is. records a Pliocene terrestrial glacial environment (see implications below). In addition to the subdivision of Unit A at Section 9, the BF organics

were categorized into three facies (based on the size and preservation of organic material and association with clastic sediment), iron concretions were found and described, and a potential ice-wedge pseudomorph in Unit A1 was shown to provide evidence of permafrost approximately contemporaneous with the glaciofluvial gravels. The latter suggests that the period of sedimentation immediately above the unconformity was a cold period.

A second short-term objective of this research was to test the usability of the TCN method in new geologic scenarios (Figure 1.2). The field investigations revealed that the BF at Ballast Brook is a poor candidate for isochron burial dating, because it does not contain long exposure surfaces that were deeply buried, and underlain by medium- to coarse-grained sand. In addition, the measured TCN concentrations at Ballast Brook were an order of magnitude lower than TCN concentrations at other BF or BF-equivalent sites (i.e., Meighen and Ellesmere Is.), probably because of a low depositional concentration. This changed the assumptions of simple burial dating that could be made at this locality. For example, post-burial production could not be ignored as it could be on Meighen Is. (Gosse, unpublished data), and in fact caused measurable trends of decreasing ^{26}Al and ^{10}Be over the 20 m of Section 9. Thus, the present research demonstrated that simple burial dating can be used to obtain a minimum burial age for the BF at Ballast Brook, and that a Bayesian most probable age may be attainable with further modelling. The conditions for the usability of TCN at this site apply to other locations with similar geologic variables (i.e., low inheritance, high relative post-depositional production, and unknown post-burial shielding).

Another short-term objective of this research was to refine the BF chronology (Figure 1.2). TCN burial dating of the BF at Ballast Brook yielded a minimum age of 2.72 $^{+0.34}/_{-0.24}$ (1σ) Ma. This suggests, with a completely independent method, that the BF at Ballast Brook is not Pleistocene in age; this is consistent with previous estimates (using plant macro- and microfossils, biostratigraphy, and correlation with Meighen Is.). The

minimum age does not exclude the possibility that the BF was deposited at the Plio-Pleistocene climate transition, like the Upper White Channel Gravel in the Yukon (Hidy *et al.* 2013), although Biostratigraphic interpretations that the BF is older than 3 Ma (§ 3.5.2) suggest that the TCN age is not closely limiting.

The BF at Ballast Brook gives the earliest terrestrial evidence of ice in the Canadian Arctic Archipelago, based on (1) the presence of a glaciofluvial gravel, (2) the association of the gravel with a large (glacial?) channel, and (3) the occurrence of a potential ice-wedge pseudomorph at a similar stratigraphic level as the glaciofluvial gravel. Although the glaciofluvial sediment described on Banks Is. was thin and not very extensive (Figure 3.2), the presence of striations requires warm-based ice, and an ice sheet is the most likely explanation for this basal thermal regime. Thus, the dating of the BF at Ballast Brook provides the oldest evidence of an ice sheet in the Canadian Arctic, and the age is comparable to or older than several previously published terrestrial ages for ice sheet extent (i.e., oldest date for the LIS based the dating of tills in Missouri is 2.4 Ma, and the oldest date for the CIS from the Yukon is 2.64 $^{+0.20}/_{-0.18}$ (1σ) Ma; Balco and Rovey 2010, Hidy *et al.* 2013). The Banks Is. age is a minimum age, which means that thick ice may have been present on Banks Is. even earlier. This is an important outcome of this research because it is unclear exactly when the transition to northern hemisphere glaciations occurred; terrestrial ages help constrain ice-sheet models by placing physical constraints on ice sheet geometry.

A related short-term objective of the present research was to obtain paleo-erosion rates for the catchment that sourced the BF (Figure 1.2). The maximum erosion rate estimate obtained for the paleo-catchment (49-86 ± 2 cm/ka) suggests a high sediment flux for this part of the CAA. This estimate agrees with the finding that the samples spanning 20 m at Section 9 are of the same age (the TCN concentrations are indistinguishable after differences due to muonic production are removed). This also agrees with the fact that, like BF at other localities, the BF at Ballast Brook does not appear to have been deposited in several, distinct events. The deposition of such a large (up to >3 km offshore) and quick (49-86 ± 2 cm/ka) event would have required a readily

available source of unconsolidated sediment. This is consistent with the presence of the nearly unlimited unconsolidated Eureka Sound Group to the east. Thus, the catchment-wide paleo-erosion rate obtained by the present research (one of the only Arctic estimates of Late Cenozoic erosion rates) enables a bigger-picture interpretation of sediment storage, transport, and deposition in the Pliocene.

The last short-term objective of the present research was to gain insight into the most recent inception of M'Clure Strait (Figure 1.2). The presence of a 3 km-wide Pliocene channel (noted previously, Hills 1969) parallel to the present northern coast of Banks Is. suggests that M'Clure Strait could not have been as wide in the Pliocene as it is currently. Although the present research has generally confirmed the northwestern to northern paleoflow direction previously described for the BF on Banks Is. (e.g., Hills 1969, Fyles 1990; § 3.4), a change in paleoflow within the BF was observed at different exposures along the Ballast Brook (paleoflow is towards the northwest near the bottom, and towards the north near the top, § 3.4), which has not been previously reported on Banks Is. or at other sites of the BF. If this shift to a more northern paleoflow represents a change in the general flow direction during later stages of BF deposition at Ballast Brook, it likely dates the inception of M'Clure Strait (minimum age of 2.72 Ma).

The present research has a number of implications for other fields of study. Offshore-onshore stratigraphic correlations are aided by the further characterization of BF stratigraphy at Ballast Brook and identification of variations in sedimentation among different BF localities. Additionally, the fast maximum paleo-erosion rates obtained for the BF, which were tenuously linked to the unconsolidated sediment source of the BF, demonstrate threshold changes in sediment flux (potentially associated with major climatic changes) that are interesting for the study of landscape evolution. New evidence for glaciation at Ballast Brook provides new constraints for Pliocene paleoclimate and ice-sheet modelling, while the dating of the inception of the M'Clure Strait has crucial implications for paleoceanography (i.e., the flux of water through the

CAA to the Labrador Sea). Further paleontology and biostratigraphy research is enabled by the confirmation, with an independent method, of a Pliocene age for the BF.

References

Anisimov, O.A., Shiklomanov, N.I., and Nelson, F.E. (2002). Variability of seasonal thaw depth in permafrost regions: a stochastic modeling approach. *Ecological Modelling*, *153*(3), 217-227.

Asudeh, I., Forsyth, R., Stephenson, R., Embry, A., Jackson, H.R., and White, D. (1989). Crustal structure of the Canadian polar margin: results of the 1985 seismic refraction survey. *Canadian Journal of Earth Sciences*, *25*(5), 853-866.

Balco, G. (2013). Simple computer code for estimating cosmic-ray shielding by oddly shaped objects. *Quaternary Geochronology*, *22*, 175-182.

Balco, G., and Rovey, C.W. (2008). An isochron method for cosmogenic-nuclide dating of buried soils and sediments. *American Journal of Science*, *308*(10), 1083-1114.

Ballantyne, A., Rybczynski, N., Baker, P., Harington, C., and White, D. (2006). Pliocene Arctic temperature constraints from the growth rings and isotopic composition of fossil larch. *Palaeogeography, Palaeoclimatology, Palaeoecology*, *242*(3), 188-200.

Ballantyne, A.P., Greenwood, D.R., Sinninghe Damste, J.S., Csank, A.Z., Eberle, J.J., and Rybczynski, N. (2010). Significantly warmer Arctic surface temperatures during the Pliocene indicated by multiple independent proxies. *Geology*, *38*(7), 603-606.

Barendregt, R., J.V. Jr.Matthews, J. G. Fyles, L. Maricovich, V. Behan-Pelletier, J. Brigham-Grette, L. E. Ovenden, E. Brouwers (1997). Biostratigraphy, Age and the Paleoenvironment of The Pliocene Beaufort Formation on Meighen Island, Canadian Arctic Archipelago.

Bennike, N.A., M. Bak, C. Israelson, P. Konradi, J. Matthiessen, A. Witkowski (2002). A multi-proxy study of Pliocene sediments from Ile de France, North-East Greenland. *Palaeogeography, Palaeoclimatology, Palaeoecology*, *186*, 1-23.

Blasco S., G.F., P. R. Hill, M. J. O'connor and J. Brigham-Grette (1990). The late Neogene and Quaternary stratigraphy of the Canadian Beaufort Continental Shelf. In: *The Arctic Ocean region*, edited by A. Grantz, L.J., Geological Society of America, Boulder, Colorado.

Brigham-Grette, J., Carter, L.D. (1992). Pliocene Marine Transgressions of Northern Alaska: Circumarctic Correlations and Paleoclimatic Interpretations. *Arctic*, *45*(1), 74-89.

Brigham-Grette, J., *et al*. (2013). Pliocene warmth, polar amplification, and stepped Pleistocene cooling recorded in NE Arctic Russia. *Science*, *340*(6139), 1421-1427.

Church, M., and Ryder, J.M. (1972). Paraglacial Sedimentation: A Consideration of Fluvial Processes Conditioned by Gkciation. *Geological Society of America Bulletin*, *83*, 3059-3072.

Clague, J.J. (1976). Quadra Sand and its relation to the late Wisconsin glaciation of southwest British Columbia. *Canadian Journal of Earth Sciences*, *13*.

Cohen, K.M., Gibbard, P.L., Fan, J.X. (2014). The ICS International Chronostratigraphic Chart. International Commission on Stratigraphy, 199-204 pp.

Conrad, C.P., and Husson, L. (2009). Influence of dynamic topography on sea level and its rate of change. *Lithosphere*, *1*(2), 110-120.

Craig, B.G., and Fyles, J.G. (1965). Quaternary of Arctic Canada. . In: *Anthropogen Period in Arctic and Subarctic*, Scientific Research Institute of the Geology of the Arctic.

Csank, A.Z., Fortier, D., and Leavitt, S.W. (2013). Annually resolved temperature reconstructions from a Late Pliocene–early Pleistocene polar forest on Bylot Island, Canada. *Palaeogeography, Palaeoclimatology, Palaeoecology*, *369*, 313-322.

Csank, A.Z., Patterson, W.P., Eglington, B.M., Rybczynski, N., and Basinger, J.F. (2011). Climate variability in the Early Pliocene Arctic: Annually resolved evidence from stable isotope values of sub-fossil wood, Ellesmere Island, Canada. *Palaeogeography, Palaeoclimatology, Palaeoecology*, *308*(3-4), 339-349.

Csank, A.Z., Tripati, A.K., Patterson, W.P., Eagle, R.A., Rybczynski, N., Ballantyne, A.P., and Eiler, J.M. (2011). Estimates of Arctic land surface temperatures during the Early Pliocene from two novel proxies. *Earth and Planetary Science Letters*, *304*(3-4), 291-299.

Davies, N.S., Gosse, J.C., and Rybczynski, N. (2014). Crossbedded Woody Debris From A Pliocene Forested River System In the High Arctic: Beaufort Formation, Meighen Island, Canada. *Journal of Sedimentary Research*, *84*(1), 19-25.

Dawson, M.R., and Harington, C.R. (2007). *Boreameryx*, an unusual new artiodactyl (Mammalia) from the Pliocene of Arctic Canada and endemism in Arctic fossil mammals. *Canadian Journal of Earth Sciences*, *44*(5), 585-592.

De Schepper, S., Groeneveld, J., Naafs, B. D. A., Van Renterghem, C., Hennissen, J., Head, M. J., & Fabian, K. (2013). Northern Hemisphere glaciation during the globally warm early Late Pliocene. *PloS one*, *8*(12), e81508.

Devaney, J.R. (1991). Clastic Sedimentology of the Beaufort Formation, Prince Patrick Island, Canadian Arctic Islands: Late Tertiary Sandy Braided River Deposits with Woody Debris Beds. *Arctic*, *44*(3), 206-216.

Duk-Rodkin, A., Froese, D.G., Weber, F., Enkin, R., Smith, R., Zazula, G.D., Waters, P. and Klassen, R. (2004). Timing and extent of Plio-Pleistocene glaciations in north-western Canada and east-central Alaska. In: *Quaternary Glaciations - Extent and Chrology Part II*, edited by Ehlers, J., and Gibbard, P.L., pp. 313-345.

Dyke, A., Andrews, J., Clark, P., England, J., Miller, G., Shaw, J., and Veillette, J. (2002). The Laurentide and Innuitian ice sheets during the last glacial maximum. *Quaternary Science Reviews*, *21*(1), 9-31.

Elias, S.A., and Matthews Jr, J.V. (2002). Arctic North American seasonal temperatures from the latest Miocene to the Early Pleistocene, based on mutual climatic range analysis of fossil beetle assemblages. *Canadian Journal of Earth Sciences*, *39*(6), 911-920.

England, J. (1987). Glaciation and the evolution of the Canadian high arctic landscape. *Geology*, *15*, 419-424.

England, J.H., Furze, M.F.A., and Doupé, J.P. (2009). Revision of the NW Laurentide Ice Sheet: implications for paleoclimate, the northeast extremity of Beringia, and Arctic Ocean sedimentation. *Quaternary Science Reviews*, *28*(17), 1573-1596.

Evans, D.J., England, J.H., La Farge, C., Coulthard, R.D., Lakeman, T.R., and Vaughan, J.M. (2014). Quaternary geology of the Duck Hawk Bluffs, southwest Banks Island, Arctic Canada: a re-investigation of a critical terrestrial type locality for glacial and interglacial events bordering the Arctic Ocean. *Quaternary Science Reviews*, *91*, 82-123.

Feyling-Hanssen, R.W., Funder, S., and Petersen, K.S. (1983). The Lodin Elv Formation; a Plio-Pleistocene occurrence in Greenland. *Bulletin of the Geological Society of Denmark*, *31*(3-4), 81-106.

Flowers, R.M., Bowring, S.A., and Reiners, P.W. (2006). Low long-term erosion rates and extreme continental stability documented by ancient (U-Th)/He dates. *Geology*, *34*(11), 925-928.

Fortier, Y. 0. and Morley, L.W. (1956). Geological unity of the Arctic Islands. *Transactions of the Royal Society of Canada*, *3*(50), 3.

French, H.M. (1972). The proglacial drainage of northwest Banks Island. *The Muskox*.

Funder, S., Bocher, J., Israelson, C., Petersen, K.S., and Simonarson, L.A. Late Pliocene Greenland - The Kap Kobenhavn Formation in Northern Greenland. *Bulletin of the Geological Society of Denmark*, 117-134.

Fyles, J.G. (1962). Physiography. *In: Banks, Victoria and Stefansson islands, Arctic Archipelago.* Geological Survey of Canada, pp. 8-17.

Fyles, J.G. (1989). High terrace sediments, probably of Neogene age, west central Ellesmere Island, Northwest Territories. Geological Survey of Canada. pp. 101-104.

Fyles, J.G. (1990). Beaufort Formation (Late Tertiary) as Seen from Prince Patrick Island, Arctic Canada. *Arctic*, *43*(4), 393-403.

Fyles, J.G., Hills, L.V., Matthews, J.V., Barendregt, R., Baker, J., Irving, E., and Jette, H. (1994). Ballast Brook and Beaufort Formations (Late Tertiary) on Northern Banks Island, Arctic Canada. *Quaternary International*, *22/23*, 141-171.

Fyles, J.G., Marincovich, L., Jr., Matthews, J.V.J., and Barendregt, R. (1991). Unique mollusc find in the Beaufort Formation (Pliocene) on Meighen Island, Arctic

Canada. *Current Research, Geological Survey of Canada, Paper 91-1B*, *Part B*, 105-112.

Fyles, J.G., Mcneil, D.H., Matthews, J.V., Barendregt, R.W., Marincovich, Jr., L., Brouwers, E., Bednarski, J., Brigham-Grette, J., Ovenden, L.E., Miller, K.G., Baker, J., and Irving, E. (1998). Geology of Hvitland Beds (Late Pliocene), White Point Lowland, Ellesmere Island, Northwest Territories. *Geological Survey of Canada Bulletin*(512), 35.

Gao, C., Mcandrews, J.H., Wang, X., Menzies, J., Turton, C.L., Wood, B.D., Pei, J., and Kodors, C. (2012). Glaciation of North America in the James Bay Lowland, Canada, 3.5 Ma. *Geology*, *40*(11), 975-978.

Gibbard, P. L., and Head, M. J. (2009). The definition of the Quaternary system/era and the Pleistocene series/epoch. *Quaternaire. Revue de l'Association française pour l'étude du Quaternaire*, *20*(2), 125-133.

Gibbons, A.B., Megeath, J.D., and Pierce, K.L. (1984). Probability of moraine survival in a succession of glacial advances. *Geology*, *12*(6), 327-330.

Gosse, J.C., and Phillips, F.M. (2001). Terrestrial in situ cosmogenic nuclides: theory and application. *Quaternary Science Reviews*, *20*(14), 1475-1560.

Gosse, J.C., Hidy, A., Froese, D., Bond J. (in prep). A geologically-buffered climate-controlled global erosion system, *Nature Geoscience*.

Granger, D.E., and Muzikar, P.F. (2001). Dating sediment burial with in situ-produced cosmogenic nuclides: theory, techniques, and limitations. *Earth and Planetary Science Letters*, *188*(1-2), 269-281.

Granger, D.E., Lifton, N.A., and Willenbring, J.K. (2013). A cosmic trip: 25 years of cosmogenic nuclides in geology. *Geological Society of America Bulletin*, *125*(9-10), 1379-1402.

Gregory, J.W. (1913). *The nature and origin of fiords.* J. Murray, London, 542 pp.

Harrington, C.R. (2005). The Eastern Limit of Beringia: Mammoth Remains from Banks and Melville Islands, Northwest Territories. *Arctic*, *58*(4), 361-369.

Harris, S.A. (1994). Chronostratigraphy of glaciations and permafrost episodes in the Cordillera of western North America. *Progress in Physical Geography*, *18*(3), 366-395.

Harrison, J. C., Brent, T. A., and Oakey, G. N. (2006). Bedrock geology of the Nares Strait region of Arctic Canada and Greenland, with explanatory text and GIS content. *Geological Survey of Canada, Open File*, *5278.*

Harrison, J.C., Mayr, U., Mcneil, D.H., Sweet, A.R., Mcintyre, D.J., Eberle, J.J., Harington, C.R., Chalmers, J.A., Dam, G., and Nohr-Hansen, H. (1999). Correlation of Cenozoic sequences of the Canadian Arctic region and Greenland; implications for the tectonic history of northern North America. *Bulletin of Canadian Petroleum Geology*, *47*(3), 223-254.

Haug, H.H., *Et al*. (2005). North Pacific seasonality and the glaciation of North America 2.7 million years ago. *Nature*, *433*, 821-825.

Haywood, A.M., Dowsett, H.J., Valdes, P.J., Lunt, D.J., Francis, J.E., and Sellwood, B.W. (2009). Introduction. Pliocene climate, processes and problems. *Philosophical transactions. Series A, Mathematical, physical, and engineering sciences*, *367*(1886), 3-17.

Heer, O., Cramer, K.E., Nordenskiöld, A.E., and Schröter, C. (1868). *Flora fossilis arctica: Die fossile flora der polarländer*, J. Wurster & comp.

Helwig, J., Kumar, N., Emmet, P., and Dinkelman, M.G. (2011). Regional seismic interpretation of crustal framework, Canadian Arctic passive margin, Beaufort Sea, with comments on petroleum potential. *Geological Society, London, Memoirs*, *35*(1), 527-543.

Hidy, A.J., Gosse, J.C., Froese, D.G., Bond, J.D., and Rood, D.H. (2013). A latest Pliocene age for the earliest and most extensive Cordilleran Ice Sheet in northwestern Canada. *Quaternary Science Reviews*, *61*, 77-84.

Hidy, A.J., Gosse, J.C., Pederson, J.L., Mattern, J.P., and Finkel, R.C. (2010). A geologically constrained Monte Carlo approach to modeling exposure ages from profiles of

cosmogenic nuclides: An example from Lees Ferry, Arizona. *Geochemistry Geophysics* Geosystems, 11, Q0AA10.

Hills, L.V. (1969). Beaufort Formation, northeastern Banks Island, District of Franklin, Geological Survey of Canada Part A, p. 204-207.

Hills, L.V. (1970). Stratigraphy of Beaufort Formation Along Western Margin Canadian Arctic Islands. American Association of Petroleum geologists Bulletin: 54:2486 (abstract).

Hills, L.V. (1971). Paleoclimatic interpretation of the Beaufort flora (Late Tertiary), Banks Island, Arctic Canada. *American Journal of Botany*, *58*(5).

Hills, L.V. (1975). Late Tertiary floras arctic Canada: An interpretation.

Hills, L.V., and Ogilvie, R.T. (1970). *Picea banksii* n. sp. Beaufort Formation (Tertiary), northwestern Banks Island, Arctic Canada. *Canadian Journal of Botany*, *48*, 457-464.

Hills. L.V., K., J.E. and Sweet, A.R. (1974). *Juglans eocinerean*. sp., Beaufort Formation (Tertiary) southwestern Banks Island, Arctic Canada. *Canadian Journal of Botany*, *52*, 65-90.

Hodgson, D.A., and Vincent, J.-S. (1984). A 10,000 yr BP extensive ice shelf over Viscount Melville Sound, Arctic Canada. *Quaternary Research*, *22*(1), 18-30.

Houseknecht, D.W., and Bird, K.J. (2011). Chapter 34 Geology and petroleum potential of the rifted margins of the Canada Basin. *Geological Society, London, Memoirs*, *35*(1), 509-526.

Hutchison, J.H., and Harington, C.R. (2002). A peculiar new fossil shrew (Lipotyphla, Soricidae) from the High Arctic of Canada. *Canadian Journal of Earth Sciences*, *39*(4), 439-443.

James, N.P., and Dalrymple, R.W. (2010). *Facies models*, Geological Association of Canada.

Kleiven, H.F., Jansen, E., Fronval, T., and Smith, T. (2002). Intensification of Northern Hemisphere glaciations in the circum Atlantic region (3.5–2.4 Ma)–ice-rafted

detritus evidence. *Palaeogeography, Palaeoclimatology, Palaeoecology*, *184*(3), 213-223.

Koerner, R.M. (1977). Ice thickness measurements and their implications with respect to past and present ice volumes in the Canadian High Arctic ice caps. *Canadian Journal of Earth Sciences*, *14*(12), 2697-2705.

Korschinek, G., Bergmaier, A., Faestermann, T., Gerstmann, U.C., Knie, K., Rugel, G., Wallner, A., Dillmann, I., Dollinger, G., and Von Gostomski, C.L. (2010). A new value for the half-life of 10 Be by heavy-ion elastic recoil detection and liquid scintillation counting. *Nuclear Instruments and Methods in Physics Research Section B: Beam Interactions with Materials and Atoms*, *268*(2), 187-191.

Kuc, M. (1970). Vascular plants from some localities in the western and northern parts of the Canadian Arctic Archipelago. *Canadian Journal of Botany*, *48*, 1931-1938.

Kuc, M., and Hills, L.V. (1971). Fossil mosses, Beaufort Formation (Tertiary), Northwestern Banks Island, Western Canada Arctic. *Canadian Journal of Botany*, *49*, 1089-1094.

Lakeman, T.R., and England, J.H. (2013). Late Wisconsinan glaciation and postglacial relative sea-level change on western Banks Island, Canadian Arctic Archipelago. *Quaternary Research*, *80*(1), 99-112.

Lal, D. (1991). Cosmic ray labeling of erosion surfaces: in situ nuclide production rates and erosion models. *Earth and Planetary Science Letters*, *104*(2-4), 424-439.

Lifton, N., Sato, T., and Dunai, T.J. (2014). Scaling in situ cosmogenic nuclide production rates using analytical approximations to atmospheric cosmic-ray fluxes. *Earth and Planetary Science Letters*, *386*, 149-160.

Lisiecki, L.E., and Raymo, M.E. (2005). A Pliocene-Pleistocene stack of 57 globally distributed benthic δ18O records. *Paleoceanography*, *20*(1), PA1003.

M'Clure, R.J.L.M., and Osborn, S. (1865). *The Discovery of the North-west Passage by HMS" Investigator,": Capt. R. M'Clure, During the Years, 1850, 1851, 1852, 1853, 1854*, W. Blackwood and sons.

Marincovich, L., and Gladenkov, A.Y. (2001). New evidence for the age of Bering Strait. *Quaternary Science Reviews*, *20*(1), 329-335.

Matthews Jr, J.V. (1976). Evolution of the subgenus Cyphelophorus (Genus Helophorus, Hydrophilidae, Coleoptera): description of two new fossil species and discussion of Helophorus tuberculatus Gyll. *Canadian Journal of Zoology*, *54*(5), 652-673.

Matthews Jr, J.V. (1977). Tertiary Coleoptera Fossils from the North American Arctic. *The Coleopterists Bulletin*, *31*(4), 297-308.

Matthews Jr, J.V. (1987). Plant macrofossils from the Neogene Beaufort Formation on Banks and Meighen Islands, District of Franklin*,* 73-87 pp, Geological Survey of Canada.

Matthews Jr., J.V., and Ovenden, L.E. (1990). Late Tertiary Plant Macrofossils from Localities in Arctic/Subarctic North America: A Review of the Data. *Arctic*, *43*(4), 364-392.

Matthews, J.V. (1989). New information on the flora and age of the Beaufort Formation, Arctic Archipelago, and related Tertiary deposits in Alaska. *Geological Survey of Canada, Current Research Part D, Paper*, 105-111.

Matthews, J.V., Jr., and Fyles, J.G. (2000). Late Tertiary plant and arthropod fossils from the High Terrace Sediments on the Fosheim Peninsula of Ellesmere Island (Northwest Territories, District of Franklin, Canada). Geological Survey of Canada. pp. 295-317.

Matthews, J.V., Telka, A. (1997). Insect fossils from the Yukon. In: Danks, H.V., Downes, J.A., (Eds)., Insects of the Yukon. Ottawa, Canada. Biological Survey of Canada (Terrestrial Arthropods), 911-962.

Matthews, J.V., Westgate, J.A., Ovenden, L., Carter, L.D., and Fouch, T. (2003). Stratigraphy, fossils, and age of sediments at the upper pit of the Lost Chicken gold mine: new information on the Late Pliocene environment of east central Alaska. *Quaternary Research*, *60*(1), 9-18.

Matthiessen, J., Knies, J., Vogt, C., and Stein, R. (2009). Pliocene palaeoceanography of the Arctic Ocean and subarctic seas. *Philosophical Transactions of the Royal Society A: Mathematical, Physical and Engineering Sciences*, *367*(1886), 21-48.

Margreth, A. (2015). Climate sensitivities of polythermal ice sheet, ice cap, and alpine ice dynamics and related episodic erosion on Cumberland Peninsula, Baffin Island, Nunavut. Doctoral Thesis, 441 pp.

Mckay, R., Naish, T., Carter, L., Riesselman, C., Dunbar, R., Sjunneskog, C., Winter, D., Sangiorgi, F., Warren, C., and Pagani, M. (2012). Antarctic and Southern Ocean influences on Late Pliocene global cooling. *Proceedings of the National Academy of Sciences*, *109*(17), 6423-6428.

McNeil, D.H. (1990). Tertiary marine events of the Beaufort-Mackenzie Basin and correlation of Oligocene to Pliocene marine outcrops in arctic North America. *Arctic 43*(4), 301-313.

McNeil, D.H., Duk-Rodkin, A., Dixon, J., Dietrich, J.R., White, J.M., Miller, K.G., and Issler, D.R. (2001). Sequence stratigraphy, biotic change, 87Sr/86Sr record, paleoclimatic history, and sedimentation rate change across a regional late Cenozoic unconformity in Arctic Canada. *Canadian Journal of Earth Sciences*, *38*(2), 309-331.

Mecham, G.F. (1855). Travelling Journal of Lieut. G.F. Mecham. In: *Further Papers relative to the Recent Arctic Expedition in Search of Sir John Franklin and the crews of H.M.S" Erebus" and "Terror."*, edited, pp. 499-540, H.M. Stationery Office, London.

Mendell, E.K. (2006). Using Fossil Trees to Estimate Paleoclimate of Banks Island, Arctic Canada and the Effects of Modern Climate Change on the Arctic. In: *19th Annual Keck Symposium.*

Miall, A. D. (1984). Sedimentation and tectonics of a diffuse plate boundary: the Canadian Arctic Islands from 80 Ma BP to the present. *Tectonophysics*, *107*(3), 261-277.

Miall, A.D. (1977). A Review of the Braided-River Depositional Environment. *Earth Science Reviews*, *13*, 1-62.

Miall, A.D. (1986). The Eureka Sound Group (Upper Cretaceous-Oligocene), Canadian Arctic Islands. *Bulletin of Canadian Petroleum Geology*, *34*(2), 240-270.

Miller, G.H., *et al*. (2010). Temperature and precipitation history of the Arctic. *Quaternary Science Reviews*, *29*(15-16), 1679-1715.

Molnar, P. (2004). Late Cenozoic increase in accumulation rates of terrestrial sediment: how might climate change have affected erosion rates? *Annual Review of Earth Planetary Science*, *32*, 67-89.

Moran, K., *et al*. (2006). The Cenozoic palaeoenvironment of the Arctic Ocean. *Nature*, *441*(7093), 601-605.

Mosher, D.C., Shimeld, J., Hutchinson, D., Lebedeva-Ivanova, N., and Chapman, C.B. (2012). Submarine landslides in arctic sedimentation: Canada Basin. In: *Submarine Mass Movements and Their Consequences*, edited, pp. 147-157, Springer.

Mudelsee, M., and Raymo, M.E. (2005). Slow dynamics of the Northern Hemisphere glaciation. *Paleoceanography*, *20*(4), PA4022.

Murphy, J. (2006). Woody Debris Lenses: Paleoenvironmental Archives. Paper presented at 19th Annual Keck Symposium.

Nishiizumi, K., Kohl, C.P., Arnold, J.R., Dorn, R., Klein, I., Fink, D., Middleton, R., and Lal, D. (1993). Role of in situ cosmogenic nuclides 10Be and 26Al in the study of diverse geomorphic processes. *Earth Surface Processes and Landforms*, *18*(5), 407-425.

Nishiizumi, K., Kohl, C.P., Shoemaker, E.M., Arnold, J.R., Klein, J., Fink, D., and Middleton, R. (1991). In-situ 10 Be-26 Al exposure ages at meteor Crater, Arizona. *Geochimica et Cosmochimica Acta*, *55*(9), 2699-2703.

Pagani, M., Liu, Z., Lariviere, J., and Ravelo, A.C. (2010). High Earth-system climate sensitivity determined from Pliocene carbon dioxide concentrations. *Nature Geoscience*, *3*(1), 27-30.

Pelletier, B.R. 1966. Development of Submarine Physiography in the Canadian Arctic and its Relation to Crustal Movements, Bedford Institute of Oceanography.

Plug, L.J., Gosse, J.C., Mcintosh, J.J., and Bigley, R. (2007). Attenuation of cosmic ray flux in temperate forest. *Journal of Geophysical Research-Earth Surface*, *112*(F2).

Polyak, L., Best, K.M., Crawford, K.A., Council, E.A., and St-Onge, G. (2013). Quaternary history of sea ice in the western Arctic Ocean based on foraminifera. *Quaternary Science Reviews*, *79*, 145-156.

Polyak, L., *et al*. (2010). History of sea ice in the Arctic. *Quaternary Science Reviews*, *29*(15-16), 1757-1778.

Raymo, M.E., Mitrovica, J.X., O'leary, M.J., Deconto, R.M., and Hearty, P.L. (2011). Departures from eustasy in Pliocene sea-level records. *Nature Geoscience*, *4*(5), 328-332.

Roulet, N.T. (2000). Peatlands, carbon storage, greenhouse gases, and the Kyoto protocol: prospects and significance for Canada. *Wetlands*, *20*(4), 605-615.

Rovere, A., Raymo, M.E., Mitrovica, J.X., Hearty, P.J., O'leary, M.J., and Inglis, J.D. (2014). The Mid Pliocene sea-level conundrum: Glacial isostasy, eustasy and dynamic topography. *Earth and Planetary Science Letters*, *387*, 27-33.

Roy, S.K., and Hills, L.V. (1972). Fossil woods from the Beaufort Formation (Tertiary), northwestern Banks Island, Canada. *Canadian Journal of Botany*, *50*, 2637-2648.

Rybczynski, N., Gosse, J.C., Harington, C.R., Wogelius, R.A., Hidy, A.J., and Buckley, M. (2013). Mid Pliocene warm-period deposits in the High Arctic yield insight into camel evolution. *Nature communications*, *4*, 1550, 10.1038.

Schaller, M., and Ehlers, T.A. (2006). Limits to quantifying climate driven changes in denudation rates with cosmogenic radionuclides. *Earth and Planetary Science Letters*, *248*(1-2), 153-167.

Staiger, J.W., Gosse, J., Little, E.C., Utting, D.J., Finkel, R., Johnson, J.V., and Fastook, J. (2006). Glacial erosion and sediment dispersion from detrital cosmogenic nuclide analyses of till. *Quaternary Geochronology*, *1*(1), 29-42.

Stickley, C.E., St John, K., Koç, N., Jordan, R.W., Passchier, S., Pearce, R.B., and Kearns, L.E. (2009). Evidence for middle Eocene Arctic sea ice from diatoms and ice-rafted debris. *Nature*, *460*(7253), 376-379.

Stocker, T.F., Qin, D., Plattner, G.K., Tignor, M., Allen, S.K., Boschung, J., Nauels, A., Xia, Y., Bex, B., and Midgley, B.M. (2013). IPCC, 2013: climate change 2013: the physical

science basis. Contribution of working group I to the fifth assessment report of the intergovernmental panel on climate change.

Stokes, C.R., and Tarasov, L. (2010). Ice streaming in the Laurentide Ice Sheet: A first comparison between data-calibrated numerical model output and geological evidence. *Geophysical Research Letters*, *37*(1) 10.1029.

Syvitski, J.P.M., and Milliman, J.D. (2007). Geology, geography, and humans battle for dominance over the delivery of fluvial sediment to the coastal ocean. *The Journal of Geology*, *115*(1), 1-19.

Tedford, R.H., Harington, R. (2003). An Arctic mammal fauna from the Early Pliocene of North America. *Nature*, *425*, 388-390.

Thorsteinsson, R., and E.T. Tozer (1961). Banks, Victoria, and Stefansson Islands, District of Franklin, Northwest Territories, Geological Survey of Canada.

Thorsteinsson, R., and Tozer, E.T. (1962). Banks, Victoria and Steffanson Islands, Arctic Archipelago, Geological Survey of Canada, p. 85 pp.

Tozer, E.T. (1956). Geological reconnaissance, Prince Patrick, Eglinton, and western Melville islands, Arctic Archipelago, Northwest Territories. Geological Survey of Canada. p. 32.

Tozer, E.T., and Thorsteinsson, R. (1964). Western Queen Elizabeth Islands, Arctic Archipelago., Geological Survey of Canada., p. 242.

Trettin, H.P. (1989). *The Arctic Islands*, Geological Society of America.

Trettin, H.P., Okulitch, A.V., Harrison, J.C., Brent, T.A., Fox, F.G., Packard, J.J., Smith, G.P., and Zolnai, A.I. (1991). Silurian–Early Carboniferous deformational phases and associated metamorphism and plutonism, Arctic Islands. *Geology of the Innuitian Orogen and Arctic Platform of Canada and Greenland: Geological Survey of Canada, Geology of Canada*, *3*, 293-341.

Vaughan, J.M., England, J.H., and Evans, D.J.A. (2014). Glaciotectonic deformation and reinterpretation of the Worth Point stratigraphic sequence: Banks Island, NT, Canada. *Quaternary Science Reviews*, *91*, 124-145.

Verhoeven, K., Louwye, S., Eiríksson, J., and De Schepper, S. (2011). A new age model for the Pliocene–Pleistocene Tjörnes section on Iceland: its implication for the timing of North Atlantic–Pacific palaeoceanographic pathways. *Palaeogeography, Palaeoclimatology, Palaeoecology*, *309*(1), 33-52.

Vincent, J-S. (1982). The Quaternary history of banks island, NWT, Canada. *Géographie physique et Quaternaire*, *36*(1-2), 209-232.

Vincent, J-S. (1983). La geologie du Quaternaire et la geomorphologie de l'ile Banks, Arctique canadien, Commission Geologique du Canada, p. 118.

Vincent, J-S. (1990). Late Tertiary and early Pleistocene deposits and history of Banks island, southwestern Canadian arctic Archipelago. *Arctic*, 339-363.

Westgate, J.A., Walter, R.C., Pearce, G.W., and Gorton, M.P. (1985). Distribution, stratigraphy, petrochemistry, and palaeomagnetism of the late Pleistocene Old Crow tephra in Alaska and the Yukon. *Canadian Journal of Earth Sciences*, *22*(6), 893-906.

Willenbring, J.K., and Von Blanckenburg, F. (2010). Long-term stability of global erosion rates and weathering during late-Cenozoic cooling. *Nature*, *465*(7295), 211-214.

Williams, C.J., Mendell, E.K., Murphy, J., Court, W.M., Johnson, A.H., and Richter, S.L. (2008). Paleoenvironmental reconstruction of a Middle Miocene forest from the western Canadian Arctic. *Palaeogeography, Palaeoclimatology, Palaeoecology*, *261*(1-2), 160-176.

Appendix A : Field Photos and Measurements

Sections 1-7 (exposure on Eastern side of Ballast Brook)

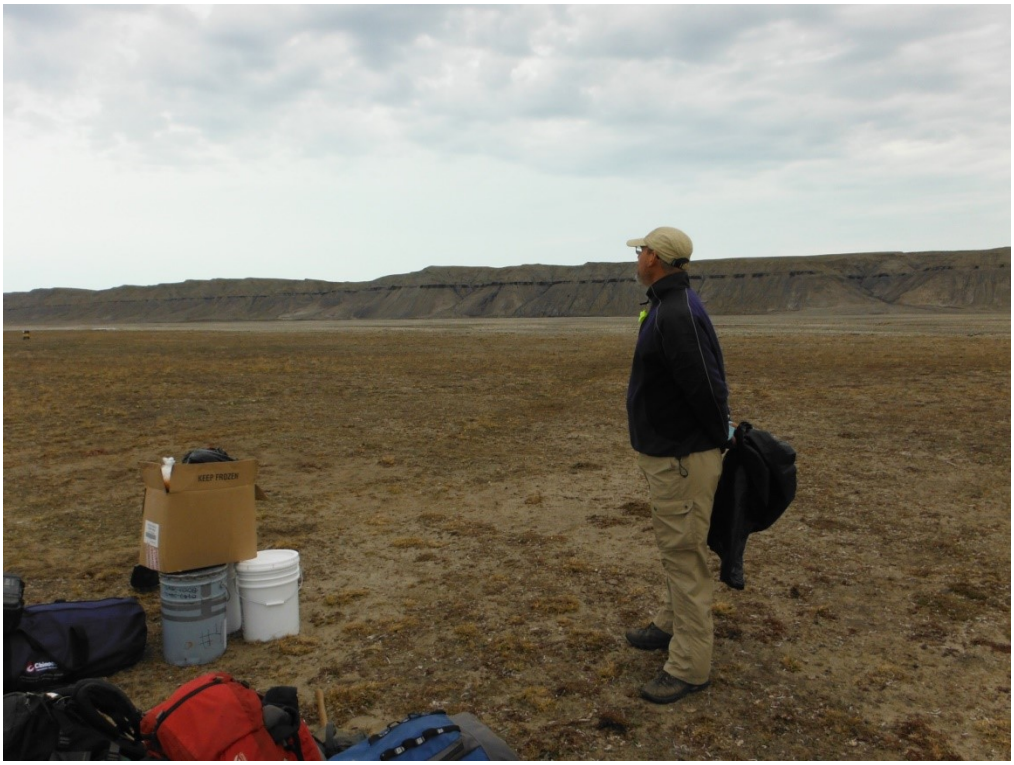

Figure 1 – BBF-Unit 4 peat on the eastern side of Ballast Brook.

Figure 2 – BBF-Unit 4 peat.

Figure 3 – Organic facies 2.

Figure 4 – Upper BF.

Figure 5 – Organic facies 3

Figure 6 –Charred wood.

Figure 7 – Wood, potentially beaver-cut.

Figure 8 – Stump possibly in growth position.

Figure 9 - Sampling BBF-Unit 4 peat.

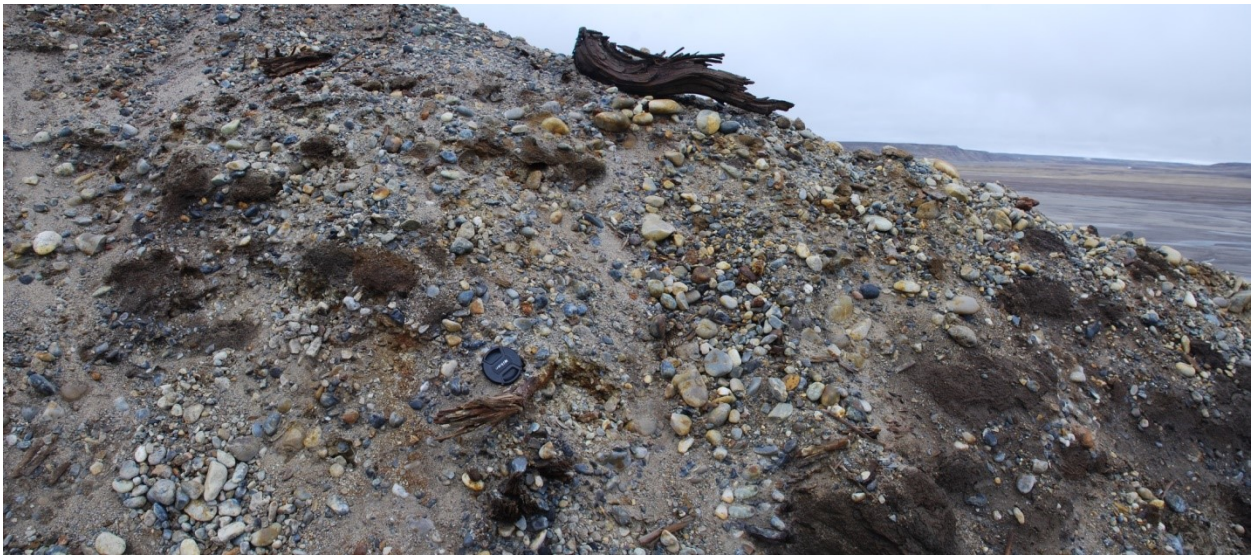

Figure 10 - Layer of iron concretions.

Figure 11- Tinted wood associated with concretion layers.

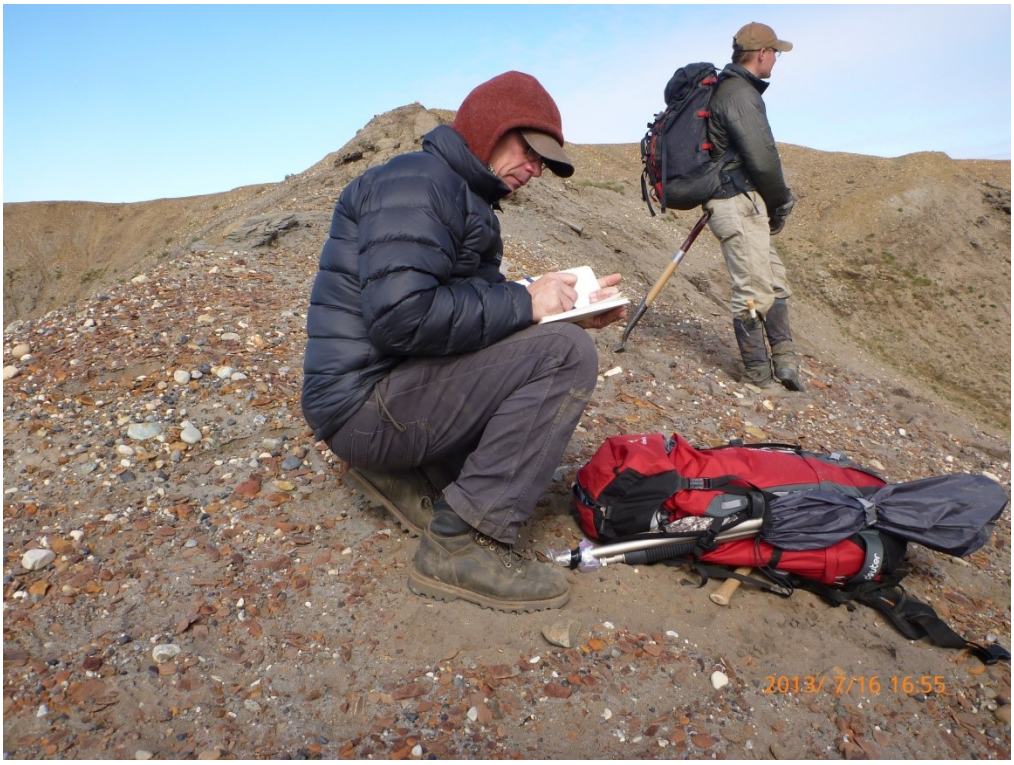

Figure 12 - Iron concretions.

Figure 13 - Iron concretions, associated with plant material.

Figure 14 - Quartize boulder, previously described by Fyles et al. (1994). The boulder has moved downward several meters since it was first observed in-situ.

Figure 15 – Quartzite boulder (different from Fyles et al. 1994 boulder)

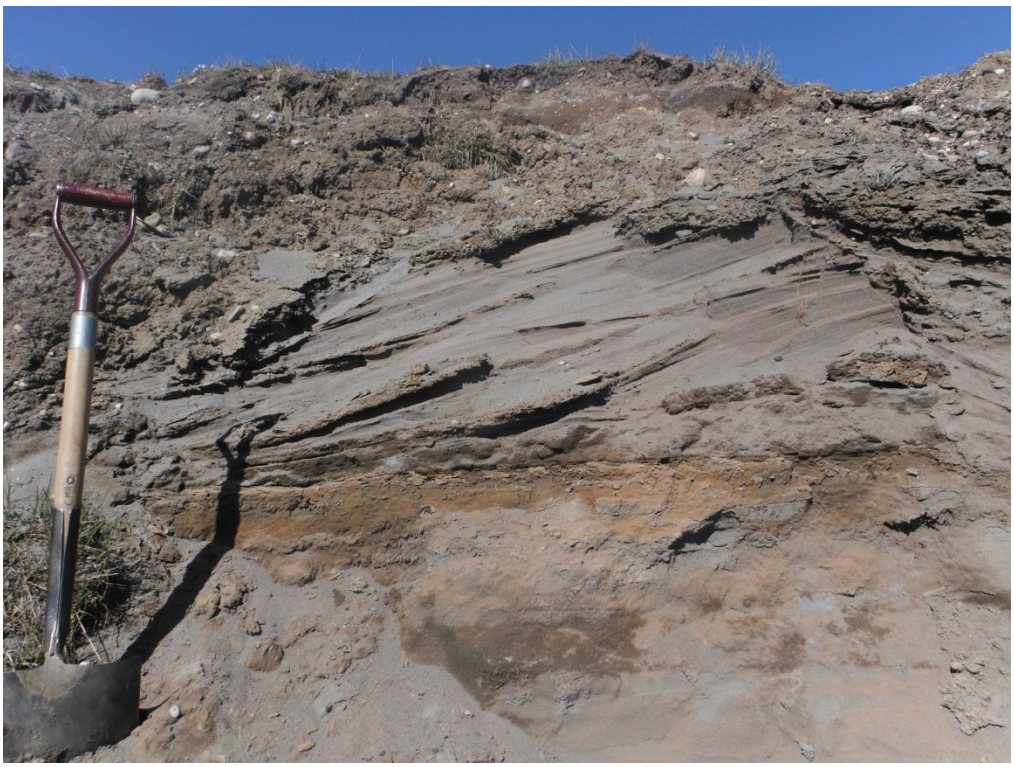

Figure 16 - Crossbedded sand and organics at the top of the BF.

Figure 17 - Potential holocene peat.

Figure 18 - Glaciofluvial cap at the top of Section 3.

Figure 19 - Glaciofluvial cap at the top of Section 3.

Section 9

Figure 20 - Section 9b.

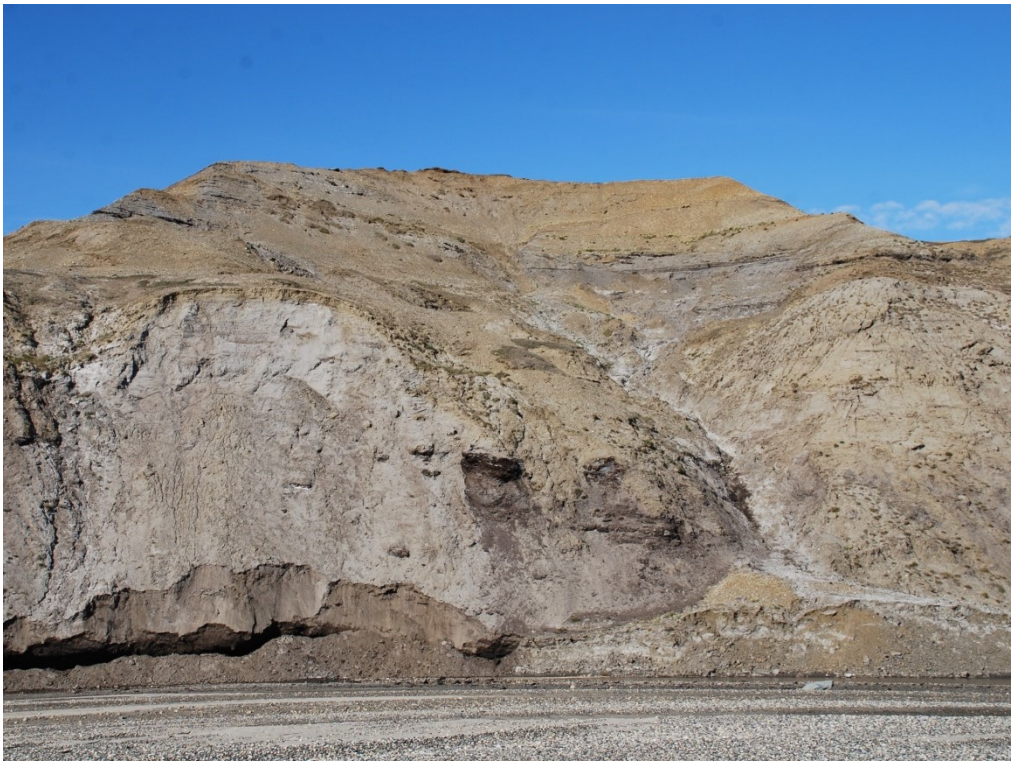

Figure 21 - Section 9b.

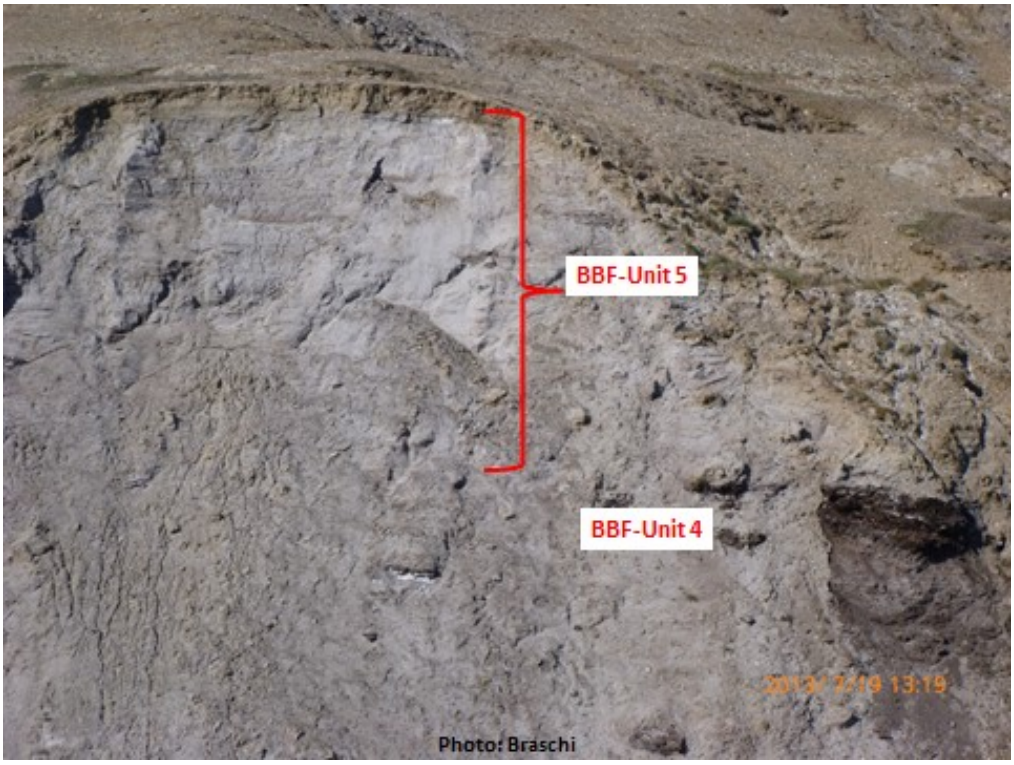

Figure 22 - Upper BBF; measured section at site 9a.

Figure 23 - BBF-Unit 5.

Figure 24 - Crossbedded wood chips in BBF-Unit 5.

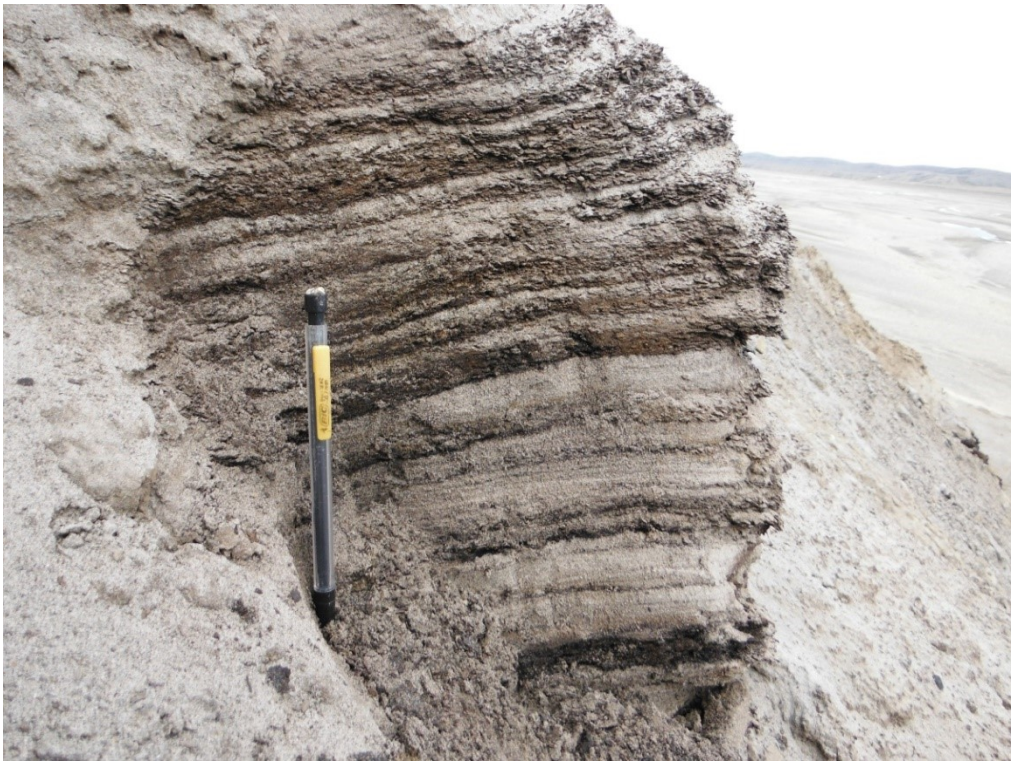

Figure 25 - Crossbedded wood chips in BBF-Unit 5.

Figure 26 - Break in slope above BBF-Unit 5.

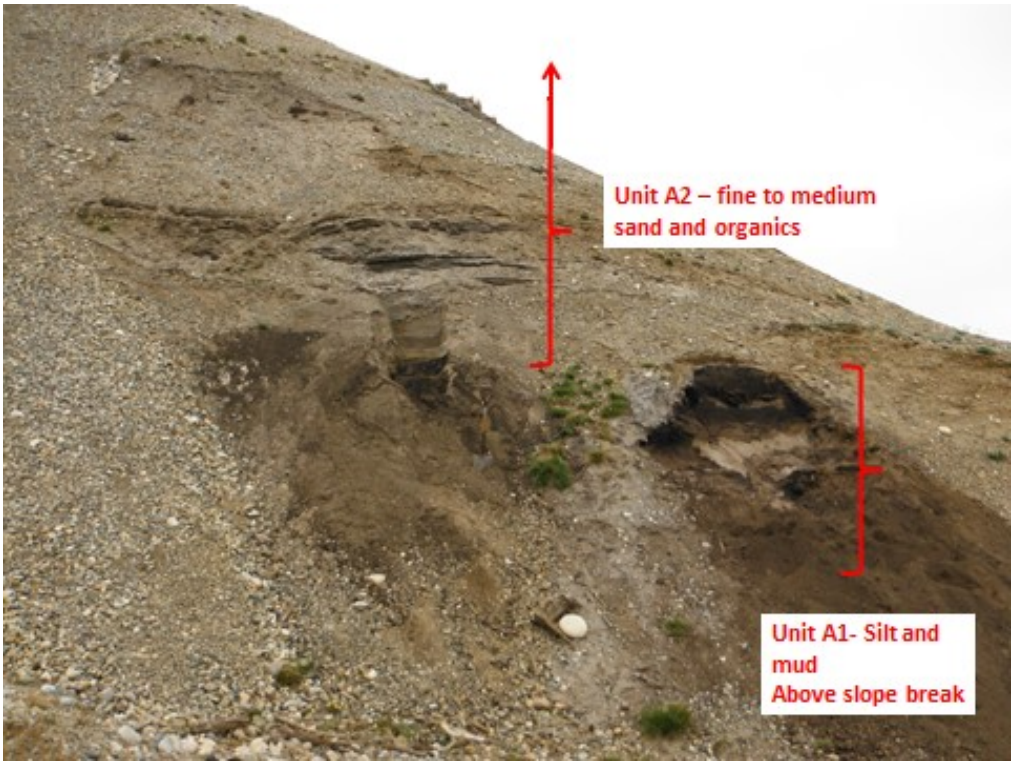

Figure 27 - Unit A1 and A2.

Figure 28 - Potential ice-wedge pseudomorph in Unit A1.

Figure 29 - Clay and silt in Unit A1, with Organic facies 1.

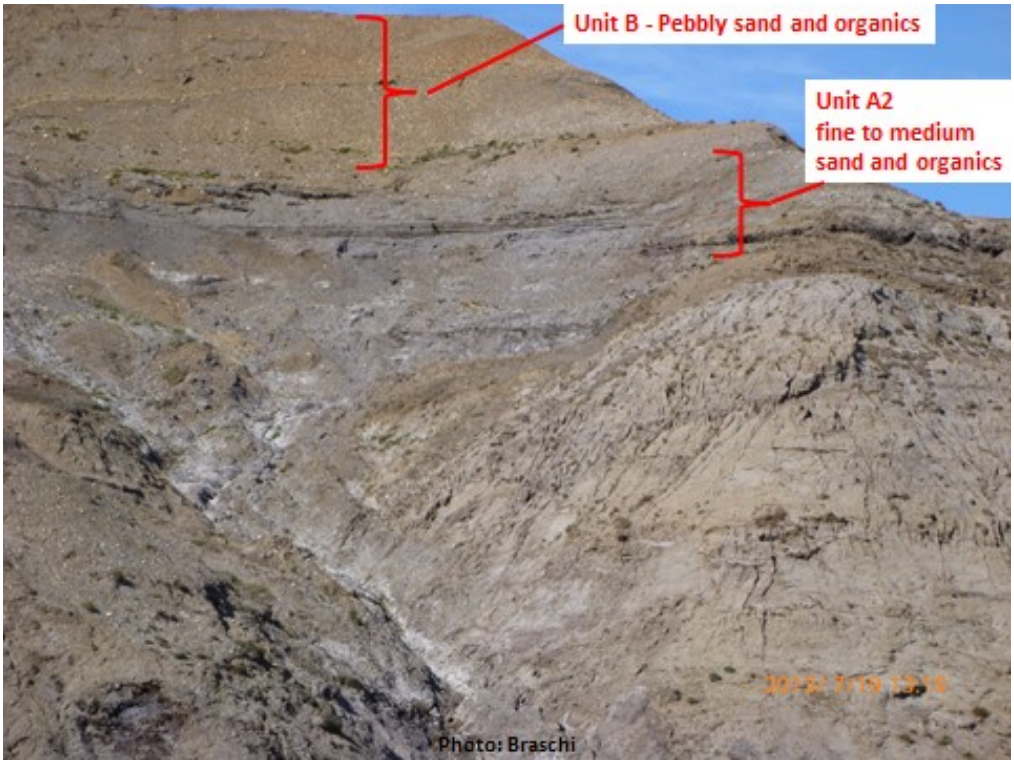

Figure 30 - Unit A2 and Unit B.

Figure 31 - Fining-upward and thining-upward beds in Unit B, with Organic facies 3.

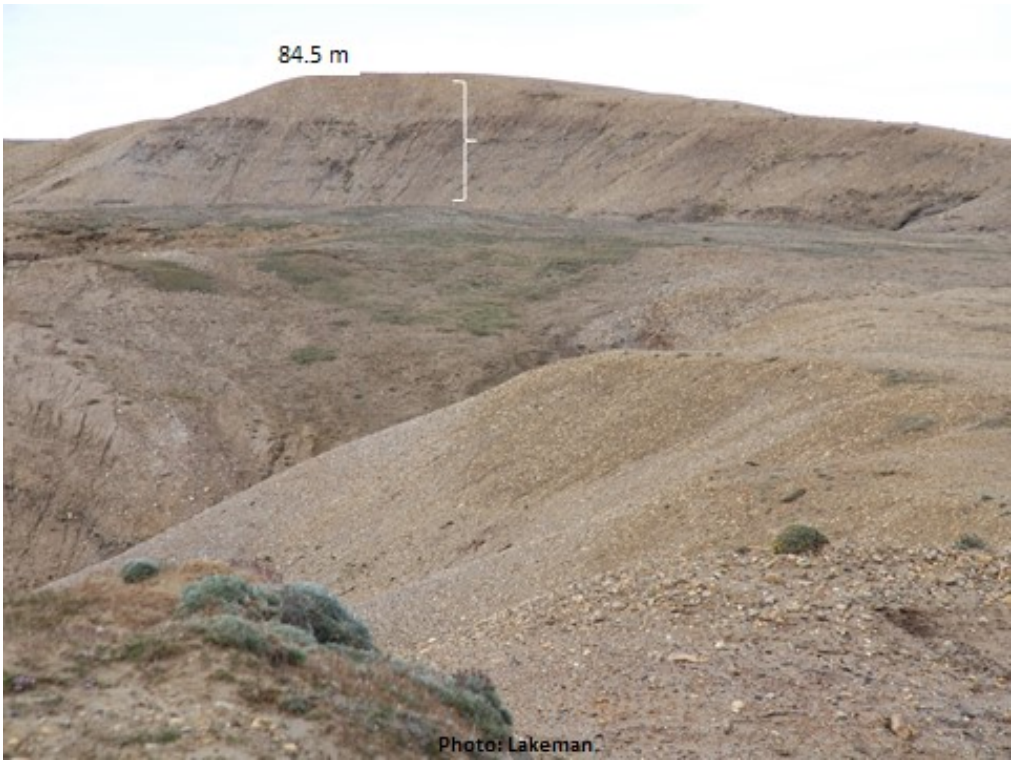

Figure 32 - Site 9c. White bracket indicates where upper 24 m of Logs 1 and 2 of Section 9 were described.

Figure 33 - TCN Sampling for Banks-13-C-016.

Figure 34 - Nested cahannel in Unit A2 of Section 9a, and sampling site for sample group Upper A2.

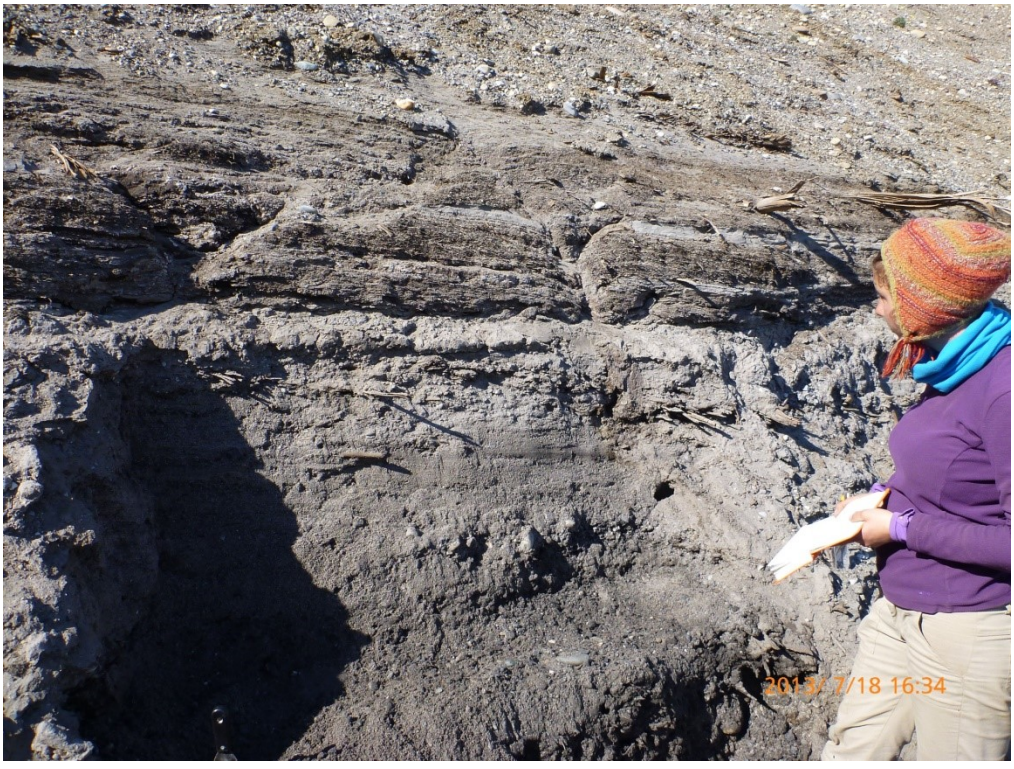

Figure 35 - Upper A2 sampling location.

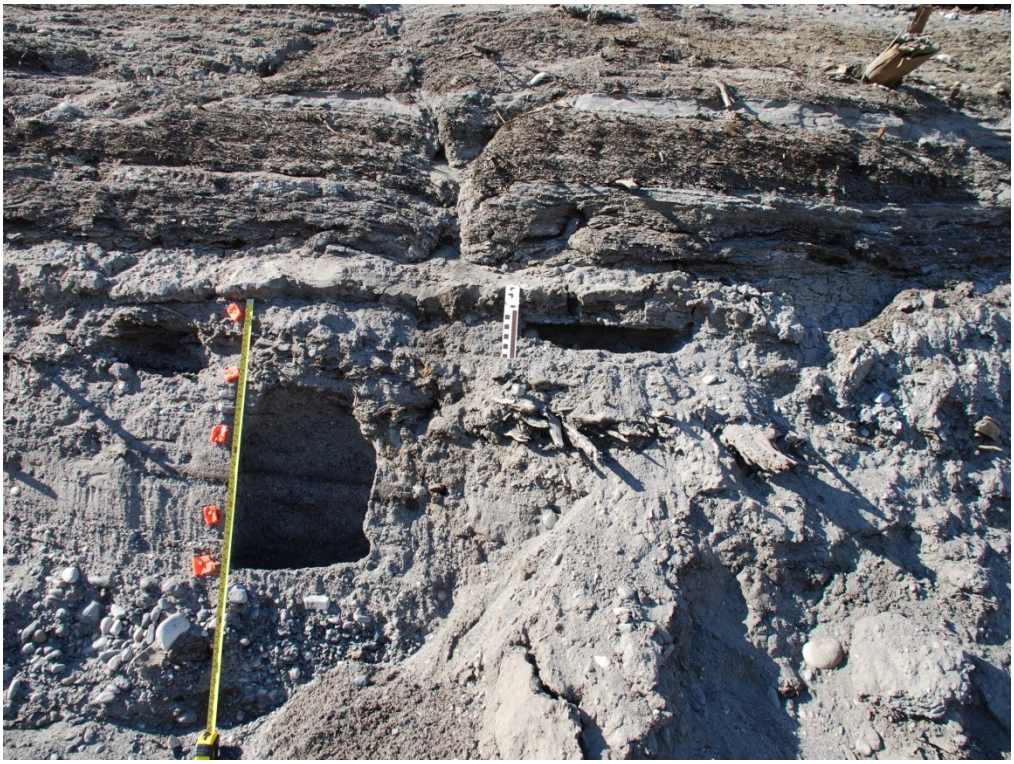

Figure 36 - Upper A2 sampling, overlain by Organic facies 2.

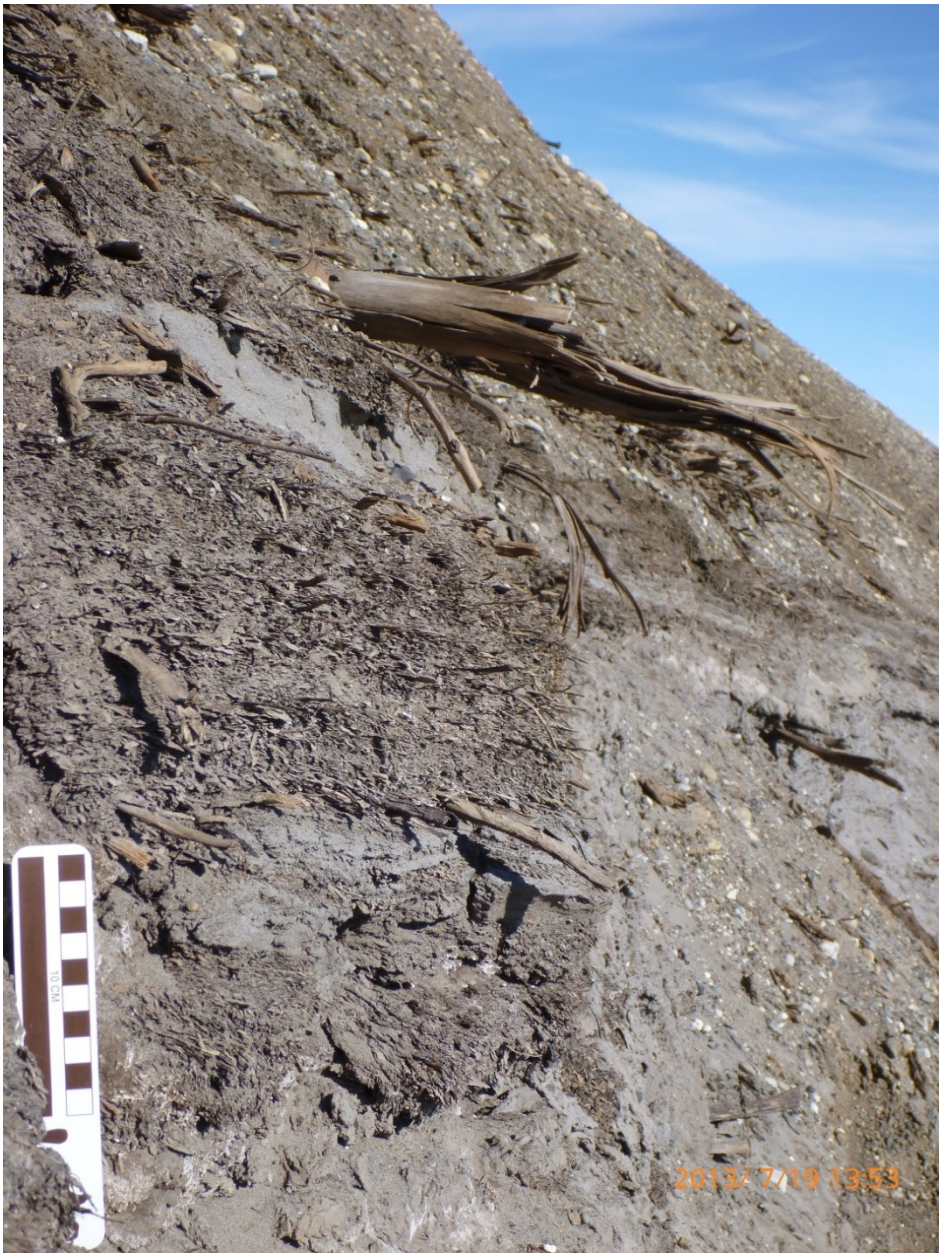

Figure 37 - Organic facies 2.

Figure 38 - Organic facies 2.

Figure 39 - Capping sediment at 60-m ledge of Section 9b.

Figure 40 - Striated stone found in sediment capping Section 9b.

Figure 41 – Unit A3, Log 2, Section 9b.

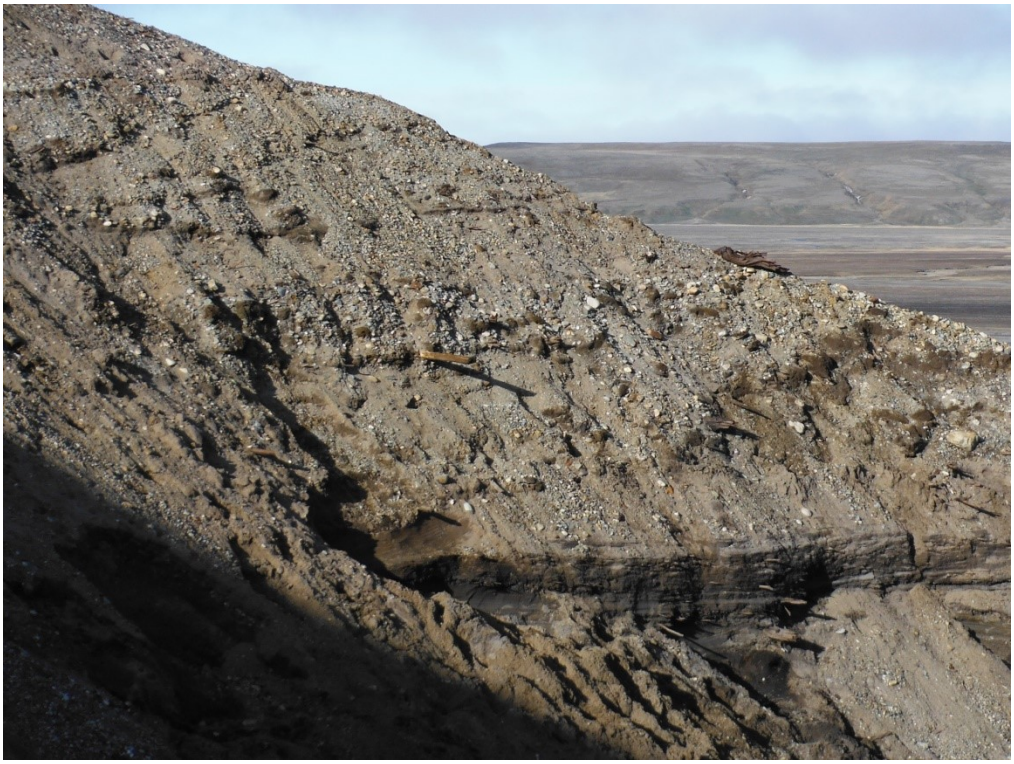

Figure 42 - Unit A3, log 2, Section 9b.

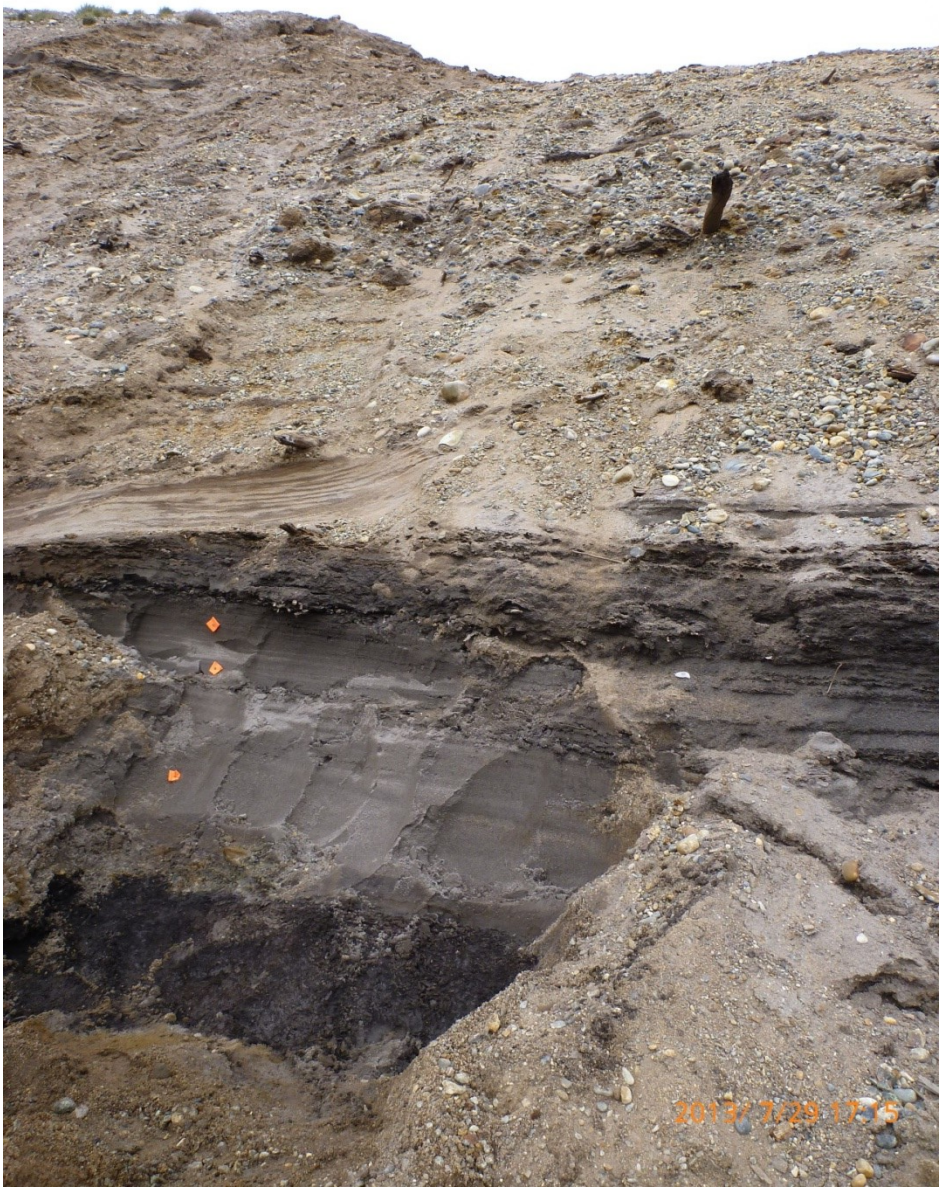

Figure 43 - Sampling below Unit A3.

Figure 44 - Backside of Section 9, likely the location of Section 9b.

Figure 45 - Autochthonous peat previously described by Kuc and Hills (1971) at Section 9b.

Figure 46 - Kuc and Hills (1971) peat at Section 9b.

Figure 47 - Kuc and Hills (1971) peat at Section 9b.

Figure 48 - Kuc and Hills (1971) peat.

Figure 49 - Bone fragment found at Section 9b.

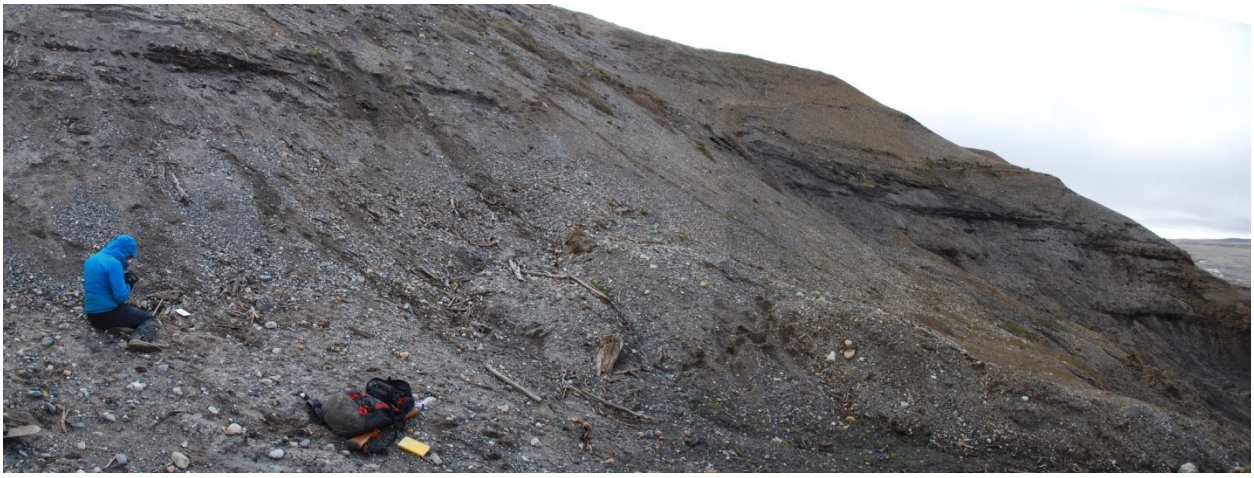

Figure 50 – Site where bone fragment was found (see Figure 49) at Section 9b.

Section 8

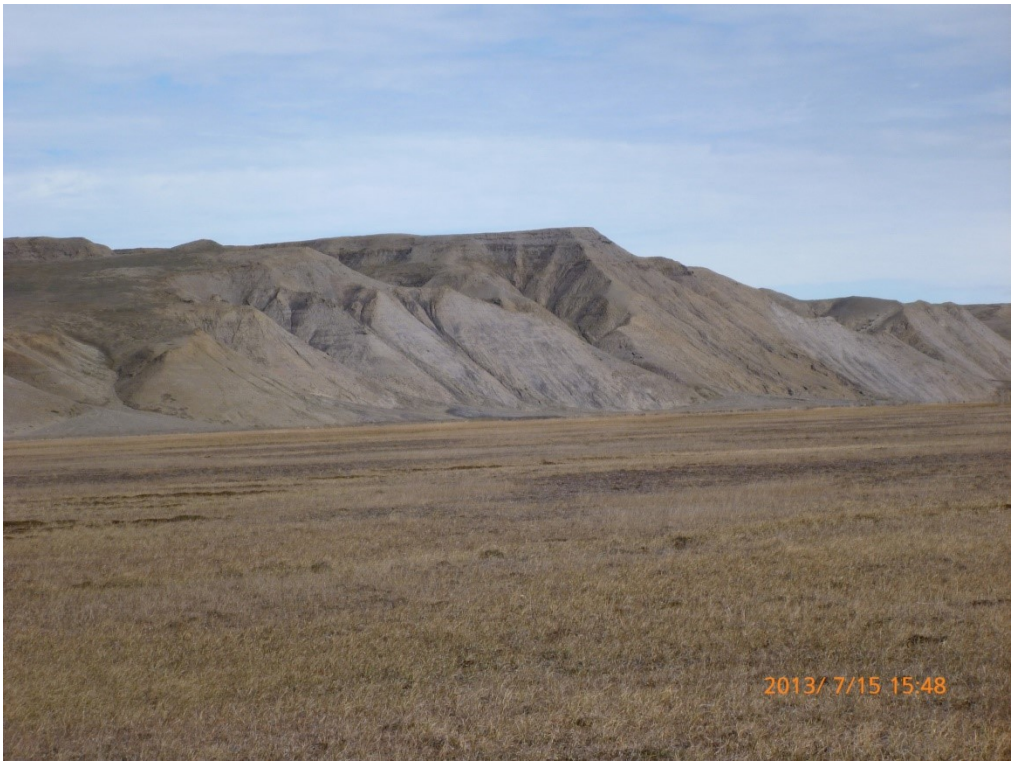

Figure 51 - Section 8 from afar

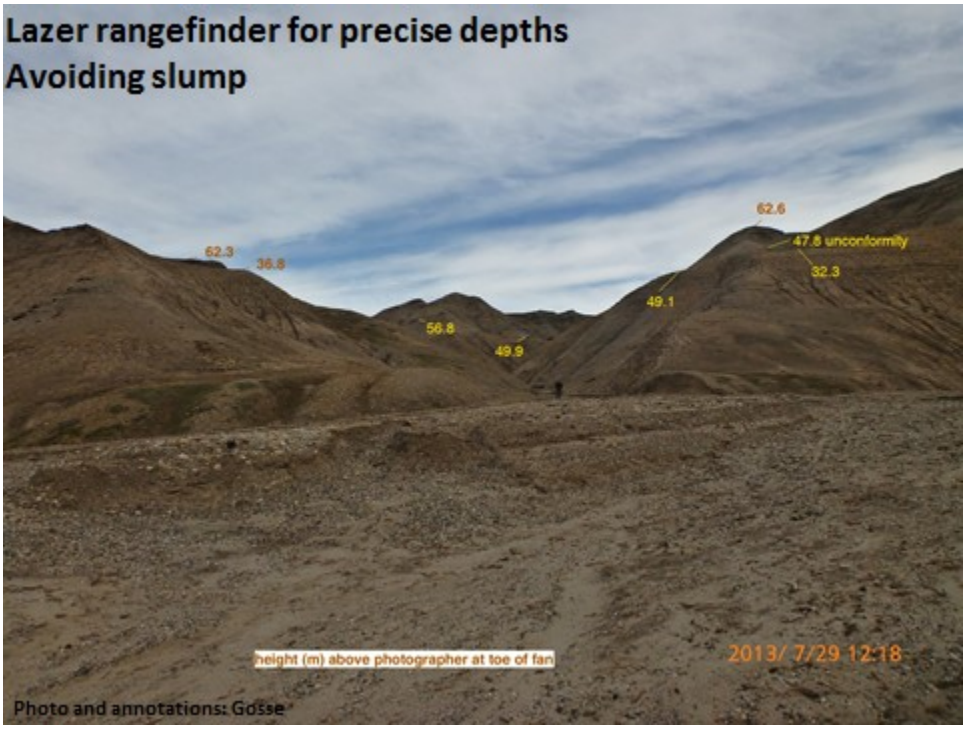

Figure 52 - Laser rangefinder heights at Section 8.

Figure 53 - Sampling at Section 8.

Figure 54 - Potential sampling above sampling at Section 8.

Figure 55 - Oxidized sands at Section 8, in the BBF.

Figure 56 - Organic facies 1, and sampling of logs for tree ring analysis.

Figure 57 - Sampling at Section 8.

Figure 58 - Section 8 sampling location.

Figure 59 - Detritus layer.

Appendix B : List of Samples

Samples collected in the field

Sample	Type	Unit	Section (Fyles *et al.* 1994)
Banks-13-C-001	TCN isochron	BF	9
Banks-13-C-002	TCN isochron	BF	9
Banks-13-C-003	TCN isochron	BF	9
Banks-13-C-004	TCN isochron	BF	9
Banks-13-C-005	TCN isochron	BF	9
Banks-13-E-006	ziplock woody peat	BF	9
Banks-13-E-007	ziplock woody peat	BF	9
Banks-13-E-008	ziplock woody peat	BF	9
Banks-13-E-009	ziplock woody peat	BF	8
Banks-13-E-010	ziplock woody peat	BF	8
Banks-13-E-011	ziplock woody peat	BF	8
Banks-13-P-012	white leg fragment	BF or Quaternary	West of 9
Banks-13-P-013	Fe-stained leg fragment	BF	West of 9
Banks-13-P-014	bone fragment	On fan surface (BF or Quaternary)	North of 3
Banks-13-E-015	peat tub	BBF Unit 4	9
Banks-13-C-016	burial TCN	BF	8
Banks-13-C-017	TCN isochron	BF?	8
Banks-13-C-018	TCN isochron	BF?	8
Banks-13-C-019	TCN isochron	BF?	8
Banks-13-C-020	TCN isochron	BF?	8
Banks-13-C-021	TCN isochron	BF?	8
Banks-13-C-022	TCN isochron	BF?	8
Banks-13-P-023	bone fragment	BF or Quaternary	3
Banks-13-E-024	thin organic-rich layer above soil	BF?	8
Banks-13-C-025	TCN isochron	BF	9
Banks-13-C-026	TCN isochron	BF	9
Banks-13-C-027	TCN isochron	BF	9
Banks-13-C-028	TCN isochron	BF	9
Banks-13-C-029	burial TCN	BF	9
Banks-13-C-030	burial TCN	BF	9
Banks-13-C-031	burial TCN	BF	9
Banks-13-C-032	burial TCN	BF	9
Banks-13-E-033	wood disk	BF	8
Banks-13-E-034	wood disk	BF	8

Sample	Type	Unit	Section (Fyles *et al.* 1994)
Banks-13-E-035	wood disk	BF	8
Banks-13-E-036	wood disk	BF	8
Banks-13-E-037	wood disk	BF	9
Banks-13-E-038	wood disk	BF	9
Banks-13-E-039	wood disk	BF	9
Banks-13-E-040	wood disk	BF	8
Banks-13-E-041	wood disk	BF	8
Banks-13-E-042	wood disk	BF	8
Banks-13-E-043	peat in rubbermaid box	BBF Unit 4	< 3
Banks-13-E-044	wood disk	BF	< 3
Banks-13-E-045	wood disk	BF	< 3
Banks-13-E-046	wood disk	BF	< 3
Banks-13-E-047	wood disk	BF	< 3
Banks-13-E-048	wood disk	BF	< 3
Banks-13-E-049	wood disk	BF	< 3
Banks-13-E-050	wood disk	BF	< 3
Banks-13-E-051	wood disk	BF	< 3
Banks-13-C-052	TCN or U-Pb	BBF Unit 5?	south of section 3
Banks-13-C-053	TCN or U-Pb	BBF Unit 5?	south of section 3
Banks-13-E-054	wood disk	middle BF	south of section 3
Banks-13-C-055	U-Pb detrital	BBF	south of section 3
Banks-13-C-056	U-Pb detrital	BBF	south of section 3
Banks-13-C-057	U-Pb detrital	BBF	south of section 3
Banks-13-C-058	U-Pb detrital	BBF	south of section 3
Banks-13-C-059	Recent sediment flux (TCN)	modern stream	south of section 3
Banks-13-E-060	wood disk	BF	2 (near Fyles' Boulder)
Banks-13-E-061	bone fragment	/	9
Banks-13-E-062	wood disk	lower mid BF	2
Banks-13-E-063	wood disk	upper BF	2
Banks-13-E-064	wood disk	lower mid BF	2

Table 1 - Samples obtained during 2013 fieldwork to Ballast Brook, NW Banks Is.

Appendix C : Data Tables

AMS raw data

AMS ID	AL 13161	AL 13162	AL 13163	AL 13164	AL 13165	AL 13175	AL 13176	AL 13177	AL 13178	AL 13179	AL 13180	AL 13181	AL 13182	AL 13183	AL 13184
Field ID (Banks-13-C-XXX)	001	002	003	004	005	blank	020	021	022	025	026	027	028	029	030
CNEF ID	JG 2986	JG 2987	JG 2988	JG 2989	JG 2990	JG 2914	JG 2995	JG 2996	JG 2997	JG 2998	JG 2999	JG 3000	JG 3001	JG 3002	JG 3003
which set of standards (1st, 2nd, etc)	1	1	1	1	1	3	3	3	3	4	4	4	4	4	4
max time (e.g. 600s)	600	600	600	600	600										
	600	600	600	600	600										
	600	600	600	600	600										
Ratio (counts/nC)	0.000038	0.000029	0.000029	0.000039	0.000024	1.41E-06	8.40E-06	0.000018	6.02E-06	2.00E-04	4.78E-06	5.80E-06	7.94E-06	1.70E-05	2.10E-05
	0.000029	0.000026	0.000031	0.000027	0.000025	3.32E-06	0.000024	0.000029	1.36E-06	0.000015	8.33E-06	6.84E-06	7.73E-06		
	0.00029	0.00029	0.000025	0.000033	0.000021	2. 70E-06	0.000021	0.000021	0.000011	6.67E-06	9.95E-06	8.07E-06	6.72E-06		
	0.00032			halted (currrent low)											
AVERAGE	0.00016925	0.000115	2.83333E-05	0.000033	2.33333E-05	0.000002473	0.000017801	2.26667E-05	6.12567E-06	7.38913E-05	7.68667E-06	0.000006905	7.46467E-06	0.000017	0.000021
ave current	1.417289	1.601014	1.323474	1.583648	1.536944	1.185457	1.388	1.4834	1.6623	1.49	1.741	1.723	1.6788	1.36	1.444
	0.986662	1.26068	1.495327	0.983492	1.415108	1.0046	0.7515	0.8728	1.2243	1.137	1.6	1.9486	1.29		
	0.565802	0.974685	1.34058	1.170695	1.699799	0.618	0.568	0.974	1.186	0.998852	1.17	1.85			
	0.5728	41													

AMS ID	AL 13161	AL 13162	AL 13163	AL 13164	AL 13165	AL 13175	AL 13176	AL 13177	AL 13178	AL 13179	AL 13180	AL 13181	AL 13182	AL 13183	AL 13184
Field ID (Banks-13-C-XXX)	001	002	003	004	005	blank	020	021	022	025	026	027	028	029	030
CNEF ID	JG 2986	JG 2987	JG 2988	JG 2989	JG 2990	JG 2914	JG 2995	JG 2996	JG 2997	JG 2998	JG 2999	JG 3000	JG 3001	JG 3002	JG 3003
Primary nC	5102.2422	5763.6543	4764.5073	5701.1362	5533.001	4267	4998	5340	5984	5371	6270	6204	6042	4923	5199
	35551.9785	4538.4521	5383.1816	3540.5713	5094.3882	3616	2705	3142	4407	4092	5763	7015	4656		
	2036.8868	3508.8689	4831.4009	4214.5054	6119.2773	2226	2045	3506	4272	3595	4222	6690	3571		
	2062.2317														
Gated events (counts)	32	28	23	37	22	1	7	16	6	18	5	6	8	14	18
	17	20	28	16	21	2	11	15	1	10	8	8	6		
	10	17	20	23	21	1	7	12	8	4	7	9	4		
	11														
analysed events (counts)	267	269	197	269	165	322	260	211	190	1011	188	157	152	214	229
	242	292	135	284	218	380	312	243	275	1092	301	256	263		
	282	262	324	252	286	707	270	279	267	736	136	207	188		
	284														
LiveTime (less than or equal to 1)	1	1	1	1	1	1	1	1	1	1	1	1	1		
	1	1	1	1	1	1	1	1	1	1	1	1	1		
	1	1	1	1	1	1	1	1	1	1	1	1	1		
STDEV ratio (btw runs)	12.64	5.46	11.49	17.96	9.47	39.43	12.14								

Table 2 - Raw AMS data for ^{26}Al (not available for ^{10}Be)

Name	Ident	Pri. Average			
JG2986	AL13161	1.42	0.99	0.57	0.57
JG2987	AL13162	1.60	1.26	0.97	
JG2988	AL13163	1.32	1.50	1.34	
JG2989	AL13164	1.58	0.98	1.17	
JG2990	AL13165	1.54	1.42	1.70	
JG2995	AL13176	1.39	0.75	0.57	0.57
JG2996	AL13177	1.48	0.87	0.97	
JG2997	AL13178	1.66	1.22	1.19	1.11
JG2998	AL13179	1.49	1.14	1.00	
JG2999	AL13180	1.74	1.60	1.17	0.56
JG3000	AL13181	1.72	1.95	1.86	
JG3001	AL13182	1.68	1.29	0.99	
JG3002	AL13183	1.37	1.45	1.29	
JG3003	AL13184	1.44	1.43	1.64	
JG3005	AL13185	1.66	1.86	1.88	
AVERAGE		1.54	1.31	1.22	
KNSTD10650	AL13221	1.58	1.42	1.28	0.71
KNSTD10650	AL13222	1.51	1.47	0.76	0.62
KNSTD30960	AL13226	1.41	1.38	1.21	1.18
KNSTD30960	AL13227	1.27	1.28	1.30	1.06
KNSTD30960	AL13228	1.53	1.30	1.24	1.07
KNSTD30960	AL13229	1.53	1.40	1.38	1.40
KNSTD30960	AL13230	1.22	1.06	1.13	1.16
KNSTD30960	AL13231	1.24	1.17	1.21	1.17
KNSTD30960	AL13232	1.06	1.06	1.12	1.08
KNSTD30960	AL13233	1.29	1.19	1.17	1.11
KNSTD4694	AL13219	0.80	1.23	1.00	0.94
KNSTD4694	AL13220	1.12	1.28	1.30	0.87
KNSTD480	AL13130	0.53	0.67	0.54	0.53
KNSTD480	AL13211	0.78	0.58	0.49	0.48
KNSTD74440	AL13159	0.74			
KNSTD74440	AL13243	1.32	1.33	1.25	1.40

Table 3 – ^{26}Al AMS current

Sample	ID	Current (microA)					
JG2986	BE36533	15.3	10.5	8.3			
JG2987	BE36534	11.7	9.8	8.2	6.8		
JG2988	BE36535	10.3	5.6	1.4			
JG2989	BE36536	9.9	9.1	8.4	6.6		
JG2990	BE36537	13.7	11.9	10.9	8.9		
JG2995	BE36548	11.8	8.8	7.1	3.2		
JG2996	BE36549	11.5	8.4	8.0			
JG2997	BE36550	13.9	7.9	5.3	2.9		
JG2998	BE36551	13.4	10.3	8.6			
JG2999	BE36552	14.7	11.7	9.8	7.9		
JG3000	BE36553	13.1	10.2	8.4			
JG3001	BE36554	13.4	10.1	6.7	4.2		
JG3002	BE36555	8.9	8.3	7.1			
JG3003	BE36556	14.2	7.6	4.2			
JG3005	BE36557	10.3	9.9	8.6			
	average	12.4	9.3	7.4			
KNSTD 1032	BE36593	15.3	17.4	16.6	15.7	14.7	13.8
KNSTD 1032	BE36594	13.1	14.3	13.5	14.1	13.4	13.6
KNSTD 3110	BE36599	19.5	19.8	19.3	18.6	18.1	17.6
KNSTD 3110	BE36600	20.9	20.1	19.9	19.0	19.1	18.4
KNSTD 3110	BE36601	20.0	18.0	18.1	18.3	18.0	16.9
KNSTD 3110	BE36602	19.9	18.2	18.0	17.4	18.0	18.7
KNSTD 3110	BE36603	20.2	20.1	19.6	20.3	19.7	18.5
KNSTD 3110	BE36604	20.1	18.5	19.1	19.1	19.1	17.4
KNSTD 3110	BE36605	20.2	19.8	19.2	20.7	19.5	
KNSTD 3110	BE36606	21.7	18.3	19.7	17.6	17.4	17.3
KNSTD 3110	BE36607	20.0	18.1	17.8	17.9	17.2	17.1
KNSTD 3110	BE36608	19.0	18.6	14.3	7.3	6.1	
KNSTD 549	BE36499	19.1	18.7	19.4	18.9	17.8	17.3
KNSTD 549	BE36500	18.7	17.7	17.5	17.2	16.8	17.5
KNSTD 9422	BE36616	20.6	20.1	20.2	19.6	18.4	18.5
KNSTD 9422	BE36617	21.6	18.4	18.3	18.3	17.9	17.5

Table 4 - ^{10}Be AMS currents.

AMS standard-corrected output

						26Al/27Al RATIO		26Al/27Al RATIO		26Al/27Al RATIO		
								(SAMPLE BKGD)		(CORR. FOR BKGD)		
NAME	CAMS#	runs	r_to_rstd	interror	exterror	Al_ratio1	ratio_err1	bkgd_ratio	bkgd_error	RATIO	ERROR	
KNSTD 30960	AL 13226	13	1.00724	0.0052767	0.0053314	3.118E-11	1.651E-13			3.118E-11	1.651E-13	1.007
KNSTD 30960	AL 13227	12	1.01539	0.0057751	0.0082884	3.144E-11	2.566E-13			3.144E-11	2.566E-13	1.015
KNSTD 30960	AL 13228	10	1.012247	0.0063311	0.0118561	3.134E-11	3.671E-13			3.134E-11	3.671E-13	1.012
KNSTD 30960	AL 13229	7	1.000256	0.0081744	0.013602	3.097E-11	4.211E-13			3.097E-11	4.211E-13	1.000
KNSTD 30960	AL 13230	7	0.9751397	0.007518	0.0093047	3.019E-11	2.881E-13			3.019E-11	2.881E-13	0.975
KNSTD 30960	AL 13231	8	0.9910667	0.0065667	0.0086301	3.068E-11	2.672E-13			3.068E-11	2.672E-13	0.991
KNSTD 30960	AL 13232	9	0.9930769	0.0064451	0.0081012	3.075E-11	2.508E-13			3.075E-11	2.508E-13	0.993
KNSTD 30960	AL 13233	10	0.979811	0.0064213	0.0073394	3.033E-11	2.272E-13			3.033E-11	2.272E-13	0.980
KNSTD 74440	AL 13159	1	2. 453082	0.0502722	0	7.595E-11	1.556E-12			7.595E-11	1.556E-12	1.020
KNSTD 480	AL 13130	9	0.0161827	0.0004429	0.0003713	5.010E-13	1.371E-14			5.010E-13	1.371E-14	1.004
KNSTD 480	AL 13211	6	0.0159747	0.0005543	0.0008966	4.946E-13	2.776E-14			4.946E-13	2.776E-14	0.991
KNSTD 4694	AL 13219	9	0.1533965	0.0017186	0.0019231	4.749E-12	5.954E-14			4.749E-12	5.954E-14	1.012
KNSTD 4694	AL 13220	6	0.1494878	0.0021188	0.0020245	4.628E-12	6.560E-14			4.628E-12	6.560E-14	0.986
KNSTD 10650	AL 13221	8	0.3446527	0.0026012	0.0026544	1.067E-11	8.218E-14			1.067E-11	8.218E-14	1.002
KNSTD 10650	AL 13222	4	0.3454791	0.0040358	0.0040952	1.070E-11	1.268E-13			1.070E-11	1.268E-13	1.004

						26Al/27Al RATIO		26Al/27Al RATIO		26Al/27Al RATIO		
								(SAMPLE BKGD)		(CORR. FOR BKGD)		
KNSTD 74440	AL 13243	9	2.401382	0.0133804	0.0174639	7.435E-11	5.407E-13			7.435E-11	5.407E-13	0.999
JG2986	AL 13161	4	0.0011818	0.0001423	0.0000731	**3.659E-14**	**4.406E-15**	2.45E-15	1.32E-15	3.414E-14	4.598E-15	
JG2987	AL 13162	3	0.00102	0.0001268	0.0000374	**3.158E-14**	**3.926E-15**	2.45E-15	1.32E-15	2.913E-14	4.140E-15	
JG2988	AL 13163	3	0.0010239	0.0001221	0.0000621	**3.170E-14**	**3.780E-15**	2.45E-15	1.32E-15	2.925E-14	4.003E-15	
JG2989	AL 13164	3	0.001202	0.0001395	0.000125	**3.721E-14**	**4.319E-15**	2.45E-15	1.32E-15	3.477E-14	4.515E-15	
JG2990	AL 13165	3	0.0008288	0.0001039	0.000041	**2.566E-14**	**3.217E-15**	2.45E-15	1.32E-15	2.321E-14	3.475E-15	
JG2995	AL 13176	4	0.0004836	0.0000973	0.000164	**1.497E-14**	**5.077E-15**	1.13E-15	1.13E-15	1.385E-14	5.201E-15	
JG2996	AL 13177	3	0.0008022	0.0001245	0.0001278	**2.484E-14**	**3.957E-15**	1.13E-15	1.13E-15	2.371E-14	4.114E-15	
JG2997	AL 13178	4	0.000146	0.0000425	0.000105	**4.520E-15**	**3.251E-15**	1.13E-15	1.13E-15	≤ 6.88E-15		
JG2998	AL 13179	3	0.0004752	0.0000924	0.0001539	**1.471E-14**	**4.765E-15**	1.13E-15	1.13E-15	1.359E-14	4.896E-15	
JG2999	AL 13180	4	0.0002568	0.0000574	0.0000485	**7.951E-15**	**1.777E-15**	1.13E-15	1.13E-15	6.824E-15	2.104E-15	
JG3000	AL 13181	3	0.0002643	0.0000557	0.0000287	**8.183E-15**	**1.724E-15**	1.13E-15	1.13E-15	7.056E-15	2.060E-15	
JG3001	AL13182	3	0.0002921	0.000069	0.0000121	**9.043E-15**	**2.136E-15**	1.13E-15	1.13E-15	7.916E-15	2.415E-15	
JG3002	AL13183	3	0.0006941	0.0001051	0.0000353	**2.149E-14**	**3.254E-15**	1.13E-15	1.13E-15	2.036E-14	3.444E-15	
JG3003	AL13184	3	0.0007399	0.0001035	0.0000908	**2.291E-14**	**3.204E-15**	1.13E-15	1.13E-15	2.178E-14	3.397E-15	
JG3005	AL13185	3	0.0008144	0.0000993	0.0001636	**2.521E-14**	**5.065E-15**	1.13E-15	1.13E-15	2.409E-14	5.189E-15	

Table 5 - ^{26}Al AMS data. Standard used for normalization: KNSTD 30960 (K. Nishiizumi); 26/27 ratio for standard =0.00000000003096.

							10Be/9Be RATIO		10Be/9Be RATIO		10Be/9Be RATIO		
							(CORRECTED FOR BORON)		(SAMPLE BKGD)		(CORR. FOR BKGDS)		
SAMPLE NAME	CAMS #	runs	r_to_rstd	interror	exterror	Truefrac	BE_ratio1	ratio_err1	bkgd_ratio	bkgd_error	RATIO	ERROR	
KNSTD 3110	BE 36599	12	0.9840179	0.0044545	0.0033465	0.9999	2.804E-12	1.270E-14			2.804E-12	1.27E-14	0.984
KNSTD 3110	BE 36600	12	0.998969	0.0046206	0.0073322	0.9999	2.847E-12	2.090E-14			2.847E-12	2.09E-14	0.999
KNSTD 3110	BE 36601	12	1.000124	0.0046422	0.0062273	0.9999	2.850E-12	1.775E-14			2.850E-12	1.77E-14	1.000
KNSTD 3110	BE 36602	11	0.9952118	0.0047422	0.0044287	0.9999	2.836E-12	1.352E-14			2.836E-12	1.35E-14	0.995
KNSTD 3110	BE 36603	12	0.9974622	0.004789	0.0095369	0.9999	2.843E-12	2.718E-14			2.843E-12	2.72E-14	0.997
KNSTD 3110	BE 36604	9	1.023702	0.0059344	0.0075777	0.99991	2.918E-12	2.160E-14			2.918E-12	2.16E-14	1.024
KNSTD 3110	BE 36605	5	1.030035	0.0097143	0.0168803	0.9999	2.936E-12	4.811E-14			2.936E-12	4.81E-14	1.030
KNSTD 3110	BE 36608	1	0.9951774	0.0274616	0	0.99985	2.836E-12	7.827E-14			2.836E-12	7.83E-14	0.995
KNSTD 3110	BE 36606	12	0.9825481	0.0045975	0.0052588	0.99989	2.800E-12	1.499E-14			2.800E-12	1.50E-14	0.983
KNSTD 3110	BE 36607	12	1.011651	0.0046357	0.0053454	0.9999	2.883E-12	1.523E-14			2.883E-12	1.52E-14	1.012
KNSTD 549	BE 36499	11	0.1802642	0.0017504	0.0012359	0.99973	5.138E-13	4.989E-15			5.138E-13	4.99E-15	0.960
KNSTD 549	BE 36500	9	0.1864977	0.0020336	0.0023162	0.9997	5.315E-13	6.601E-15			5.315E-13	6.60E-15	0.993
KNSTD 1032	BE 36593	12	0.3381847	0.0022712	0.0020526	0.99979	9.638E-13	6.473E-15			9.638E-13	6.47E-15	0.992
KNSTD 1032	BE 36594	9	0.349936	0.0027885	0.0027354	0.99984	9.973E-13	7.947E-15			9.973E-13	7.95E-15	1.026
KNSTD 9422	BE 36616	9	3.021311	0.0120839	0.0167797	0.99991	8.611E-12	4.782E-14			8.611E-12	4.78E-14	1.006
KNSTD 9422	BE 36617	7	3.068832	0.0151696	0.0201317	0.99991	8.746E-12	5.738E-14			8.746E-12	5.74E-14	1.022

							10Be/9Be RATIO		10Be/9Be RATIO		10Be/9Be RATIO		
							(CORRECTED FOR BORON)		(SAMPLE BKGD)		(CORR. FOR BKGDS)		
JG2986	BE 36533	3	0.0325529	0.0007445	0.0002367	0.99185	9.278E-14	2.122E-15	1.43E-15	1.43E-15	9.134E-14	2.56E-15	
JG2987	BE 36534	4	0.0302103	0.0006884	0.0013333	0.9863	8.610E-14	3.800E-15	1.43E-15	1.43E-15	8.466E-14	4.06E-15	
JG2988	BE 36535	2	0.0255606	0.0009504	0.0010107	0.98393	7.285E-14	2.880E-15	1.43E-15	1.43E-15	7.141E-14	3.21E-15	
JG2989	BE 36536	4	0.0224852	0.0006105	0.0008386	0.96781	6.408E-14	2.390E-15	1.43E-15	1.43E-15	6.265E-14	2.78E-15	
JG2990	BE 36537	4	0.0293082	0.0006132	0.000824	0.98333	8.353E-14	2.348E-15	1.43E-15	1.43E-15	8.209E-14	2.75E-15	
JG2995	BE 36548	4	0.0165496	0.0005516	0.0009958	0.97891	4.717E-14	2.838E-15	1.36E-15	4.91E-16	4.581E-14	2.88E-15	
JG2996	BE 36549	3	0.0251177	0.0007195	0.000685	0.99286	7.159E-14	2.051E-15	1.36E-15	4.91E-16	7.023E-14	2.11E-15	
JG2997	BE 36550	3	0.0248912	0.0007254	0.0016396	0.99653	7.094E-14	4.673E-15	1.36E-15	4.91E-16	6.958E-14	4.70E-15	
JG2998	BE 36551	3	0.0190408	0.0005827	0.0004636	0.99078	5.427E-14	1.661E-15	1.36E-15	4.91E-16	5.291E-14	1.73E-15	
JG2999	BE 36552	4	0.0236776	0.0005571	0.0006249	0.9942	6.748E-14	1.781E-15	1.36E-15	4.91E-16	6.612E-14	1.85E-15	
JG3000	BE 36553	3	0.0258891	0.0006872	0.0007577	0.99577	7.378E-14	2.159E-15	1.36E-15	4.91E-16	7.242E-14	2.21E-15	
JG3001	BE 36554	4	0.0257658	0.0006559	0.0006462	0.99402	7.343E-14	1.869E-15	1.36E-15	4.91E-16	7.207E-14	1.93E-15	
JG3002	BE 36555	3	0.0383859	0.0009554	0.0006296	0.99564	1.094E-13	2.723E-15	1.36E-15	4.91E-16	1.080E-13	2.77E-15	
JG3003	BE 36556	3	0.0368666	0.0009109	0.0006144	0.997	1.051E-13	2.596E-15	1.36E-15	4.91E-16	1.037E-13	2.64E-15	
JG3005	BE 36557	3	0.0324019	0.0008066	0.0005538	0.99511	9.235E-14	2.299E-15	1.36E-15	4.91E-16	9.099E-14	2.35E-15	

Table 6- ^{10}Be AMS results. Standard used for normalization: 07KNSTD3110 (K. Nishiizumi); 10/9 ratio for standard = 2.85E-12. Boron correction factor =(0.8±0.1)x10^-4.

ICP Results

CNEF ID	100 mL volume	Concentration	Take from 100 mL volume	Take from 100 mL volume	Dry out and Re-dissolve 2%HNO3 12 mL	Concentration of 12 mL volume	Take from 12 mL volume	Take from 12 mL aloquot	Bring up to 10mL	Concentration of 10mL volume	measured ICP concentration	concentration	total 27Al in sample
	(mL)	**(g quartz/mL)**	**(mL)**	**(g quartz)**	**(mL)**	**(g quartz/mL)**	**(mL)**	**(g quartz)**	**(mL)**	**(g quartz/mL)**	**(ug 27Al/mL)**	**(ug 27Al/ g quartz)**	**(ug 27Al)**
2986	100	1.169918	4.8557	5.680770833	11.7916	0.481764208	4.0971	1.973836136	10.8251	0.182338836	9.38	51.42276249	6016.041545
2987	100	0.942768	5.0474	4.758527203	12.1632	0.391223297	4.0456	1.582732969	10.0894	0.156870871	6.02	38.35957529	3616.418008
2988	100	1.18902	5.0213	5.970426126	12.2889	0.485838938	3.9883	1.937671437	10.7537	0.180186488	10.21	56.68072068	6739.45105
2989	100	0.908984	4.9845	4.530830748	12.704	0.356645997	4.0527	1.445379233	10.6613	0.135572513	6.51	47.98489893	4361.750537
2990	100	1.163488	5.0959	5.929018499	12.5617	0.471991729	4.2061	1.985244441	10.5202	0.188707858	11.75	62.2526628	7243.022613
2995	100	0.720232	4.8715	3.508610188	12.0896	0.290217227	4.2183	1.224223329	10.4598	0.117040797	9.19	78.52019894	5655.275992
2996	100	1.202275	4.8614	5.844739685	11.5795	0.504748883	4.1878	2.113787377	10.7993	0.195733739	10.77	55.03462702	6616.675619
2997	100	1.20908	4.8771	5.896804068	11.5877	0.508884772	3.973	2.021799198	10.5699	0.191278933	29.38	153.5886161	18570.0924
2998	100	0.787809	4.787	3.771241683	11.9559	0.315429343	4.2455	1.339155276	10.6768	0.125426652	13.22	105.418318	8304.949969

CNEF ID	100 mL volume	Concentration	Take from 100 mL volume	Take from 100 mL volume	Dry out and Re-dissolve 2%HNO3 12 mL	Concentration of 12 mL volume	Take from 12 mL volume	Take from 12 mL aloquot	Bring up to 10mL	Concentration of 10mL volume	measured ICP concentration	concentration	total 27Al in sample
	(mL)	**(g quartz/mL)**	**(mL)**	**(g quartz)**	**(mL)**	**(g quartz/mL)**	**(mL)**	**(g quartz)**	**(mL)**	**(g quartz/mL)**	**(ug 27Al/mL)**	**(ug 27Al/ g quartz)**	**(ug 27Al)**
2999	100	1.055518	5.0337	5.313160957	11.1365	0.477094326	4.0354	1.925266441	10.5	0.183358709	20.00	109.0496336	11510.38512
3000	100	1.143547	4.8228	5.515098472	11.832	0.46611718	3.9667	1.848947017	10.5377	0.175460206	21.76	124.0433208	14184.93673
3001	100	1.149089	4.8439	5.566072207	12.1672	0.457465334	4.2876	1.961428364	10.4569	0.187572642	19.13	102.0111449	11721.98845
3002	100	1.208558	4.8551	5.867669946	12.4321	0.471977377	4.1518	1.959555673	10.7303	0.182618908	19.46	106.5523107	12877.46475
3003	100	1.053238	4.8114	5.067549313	11.7769	0.43029569	4.1379	1.780520536	10.732	0.165907616	20.45	123.2868859	12985.04331
3005	100	1.201068	4.7163	5.664597008	12.2918	0.460843571	4.2399	1.953930658	10.5155	0.185814337	13.64	73.39745814	8815.533826

Table 7 - ICP results.

Data reduction

Al Carrier Mass in blank	Al Carrier ID	27Al Carrier Conc	Al Carrier Density	27Al in carrier in blank	27Al in carrier in blank	26Al/27Al (not bkgd corr) blank	26Al/27Al (not bkgd corr) error	26 atoms in blank	26 atoms in blank error	blank error	Al AMS ID	27 Al in total sample	27 Al in total sample	26Al/27Al AMS (not blk corr)	26Al/27Al AMS (not blk corr) 1σ error	1σ AMS error	26 atoms not 'process' corrected	26 atom process correct e
(g)	(txt)	(µg/mL)	(g/mL)	(µg 27Al)	(atoms)	(26Al/27Al)	(26Al/27Al)	(atoms)	(atoms)	frac	(txt)	g	atoms	(26Al/27Al)	(26Al/27Al)	(%)	(atoms)	(atoms)
0.2	Al carrier	1000	1.013	197.43		2.500E-15	2.000E-16				BE1234			3.33E-13	2.22E-15	2.7%		
2.9633	AL13098	1000	1.010	2933.96	6.55E+19	2.45E-15	1.32E-15	1.60E+05	8.61E+04	0.54	AL13161	0.000000000	0.0000E+00	3.659E-14	4.406E-15	0.1204	0.0000E+00	-1.601E+05
2.9633	AL13098	1000	1.010	2933.96	6.55E+19	2.45E-15	1.32E-15	1.60E+05	8.61E+04	0.54	AL13162	0.000000000	0.0000E+00	3.158E-14	3.926E-15	0.1243	0.0000E+00	-1.601E+05
2.9633	AL13098	1000	1.010	2933.96	6.55E+19	2.45E-15	1.32E-15	1.60E+05	8.61E+04	0.54	AL13163	0.000000000	0.0000E+00	3.170E-14	3.780E-15	0.1192	0.0000E+00	-1.601E+05
2.9633	AL13098	1000	1.010	2933.96	6.55E+19	2.45E-15	1.32E-15	1.60E+05	8.61E+04	0.54	AL13164	0.000000000	0.0000E+00	3.721E-14	4.319E-15	0.1161	0.0000E+00	-1.601E+05
2.9633	AL13098	1000	1.010	2933.96	6.55E+19	2.45E-15	1.32E-15	1.60E+05	8.61E+04	0.54	AL13165	0.000000000	0.0000E+00	2.566E-14	3.217E-15	0.1254	0.0000E+00	-1.601E+05
2.9633	AL13098	1000	1.010	2933.96	6.55E+19	2.45E-15	1.32E-15	1.60E+05	8.61E+04	0.54	AL13176	0.000000000	0.0000E+00	1.497E-14	5.077E-15	0.3391	0.0000E+00	-1.601E+05
2.9633	AL13098	1000	1.010	2933.96	6.55E+19	2.45E-15	1.32E-15	1.60E+05	8.61E+04	0.54	AL13177	0.000000000	0.0000E+00	2.484E-14	3.957E-15	0.1593	0.0000E+00	-1.601E+05
2.9633	AL13098	1000	1.010	2933.96	6.55E+19	2.45E-15	1.32E-15	1.60E+05	8.61E+04	0.54	AL13178	0.000000000	0.0000E+00	4.520E-15	3.251E-15	0.7192	0.0000E+00	-1.601E+05

Al Carrier Mass in blank	Al Carrier ID	27Al Carrier Conc	Al Carrier Density	27Al in carrier in blank	27Al in carrier in blank	26Al/27Al (not bkgd corr) blank	26Al/27Al (not bkgd corr) error	26 atoms in blank	26 atoms in blank error	blank error	Al AMS ID	27 Al in total sample	27 Al in total sample	26Al/27Al AMS (not blk corr)	26Al/27Al AMS (not blk corr) 1σ error	1 AMS error	26 atoms not 'process' corrected	26 atom process correct e
(g)	(txt)	(g/mL)	(g/mL)	(g 27Al)	(atoms)	(26Al/27Al)	(26Al/27Al)	(atoms)	(atoms)	frac	(txt)	g	atoms	(26Al/27Al)	(26Al/27Al)	(%)	(atoms)	(atoms)
0.2	Al carrier	1000	1.013	197.43		2.500E-15	2.000E-16				BE1234			3.33E-13	2.22E-15	2.7%		
2.9633	AL13098	1000	1.010	2933.96	6.55E+19	2.45E-15	1.32E-15	1.60E+05	8.61E+04	0.54	AL13179	0.000000000	0.0000E+00	1.471E-14	4.765E-15	0.3239	0.0000E+00	-1.601E+05
2.9633	AL13098	1000	1.010	2933.96	6.55E+19	2.45E-15	1.32E-15	1.60E+05	8.61E+04	0.54	AL13180	0.000000000	0.0000E+00	7.951E-15	1.777E-15	0.2235	0.0000E+00	-1.601E+05
2.9633	AL13098	1000	1.010	2933.96	6.55E+19	2.45E-15	1.32E-15	1.60E+05	8.61E+04	0.54	AL13181	0.000000000	0.0000E+00	8.183E-15	1.724E-15	0.2107	0.0000E+00	-1.601E+05
2.9633	AL13098	1000	1.010	2933.96	6.55E+19	2.45E-15	1.32E-15	1.60E+05	8.61E+04	0.54	AL13182	0.000000000	0.0000E+00	9.043E-15	2.136E-15	0.2362	0.0000E+00	-1.601E+05
2.9633	AL13098	1000	1.010	2933.96	6.55E+19	2.45E-15	1.32E-15	1.60E+05	8.61E+04	0.54	AL13183	0.000000000	0.0000E+00	2.149E-14	3.254E-15	0.1514	0.0000E+00	-1.601E+05
2.9633	AL13098	1000	1.010	2933.96	6.55E+19	2.45E-15	1.32E-15	1.60E+05	8.61E+04	0.54	AL13184	0.000000000	0.0000E+00	2.29073E-14	3.204E-15	0.1399	0.0000E+00	-1.601E+05
2.9633	AL13098	1000	1.010	2933.96	6.55E+19	2.45E-15	1.32E-15	1.60E+05	8.61E+04	0.54	AL13185	0.000000000	0.0000E+00	2.52138E-14	5.065E-15	0.2009	0.0000E+00	-1.601E+05

Table 8 - ^{26}Al AMS data reduction. ^{27}Al measured by ICP-OES.

Be Carrier Mass	Carrier ID	Be Carrier conc	Be Carrier density	9Be added through carrier	Be AMS ID	10Be/9Be blank boronc orr	10Be/9Be blank error	blank error	10Be atoms in blank	10Be atoms in blank error	10Be/9Be AMS boronc orr	10Be/9Be AMS 1σ error	1σ AMS error	measured 10Be atoms	10Be atoms blnk corr	blank error	Total AMS error
(g)	(txt)	(μg/mL)	(g/mL)	(atoms 9Be)	(txt)	(10Be/9Be)	(10Be/9Be)	frac	(atoms)	(atoms)	(10Be/9Be)	(10Be/9Be)	frac	(atoms)	(atoms)	frac	frac
0.2	Becarrier	1000	1.013		BE1234	4.00E-15	4.00E-16				5.00E-13	9.00E-15	1.1%	78678929.4	78223012.13	0.001554625	0.023
0.9061	Be Carrier B31 Sept 28, 2012 285ug/ml	282	1.013	1.686E+19	BE36533	1.43E-15	1.43E-15	0.995	2.477E+04	2.465E+04	9.27758E-14	2.122E-15	0.02	1.564E+06	1.539E+06	0.016	0.03
0.8939	Be Carrier B31 Sept 28, 2012 285ug/ml	282	1.013	1.663E+19	BE36534	1.43E-15	1.43E-15	0.995	2.477E+04	2.465E+04	8.60994E-14	3.8E-15	0.04	1.432E+06	1.407E+06	0.017	0.05
0.9052	Be Carrier B31 Sept 28, 2012 285ug/ml	282	1.013	1.684E+19	BE36535	1.43E-15	1.43E-15	0.995	2.477E+04	2.465E+04	7.28477E-14	2.88E-15	0.04	1.227E+06	1.202E+06	0.020	0.05
0.8991	Be Carrier B31 Sept 28, 2012 285ug/ml	282	1.013	1.673E+19	BE36536	1.43E-15	1.43E-15	0.995	2.477E+04	2.465E+04	6.40828E-14	2.39E-15	0.04	1.072E+06	1.047E+06	0.023	0.05
0.9091	Be Carrier B31 Sept 28, 2012 285ug/ml	282	1.013	1.691E+19	BE36537	1.43E-15	1.43E-15	0.995	2.477E+04	2.465E+04	8.35284E-14	2.348E-15	0.03	1.413E+06	1.388E+06	0.017	0.04
0.8811	Be Carrier B31 Sept 28, 2012 285ug/ml	282	1.013	1.639E+19	BE36548	1.43E-15	1.43E-15	0.995	2.477E+04	2.465E+04	4.71664E-14	2.838E-15	0.06	7.731E+05	7.483E+05	0.032	0.07
0.8869	Be Carrier B31 Sept 28, 2012 285ug/ml	282	1.013	1.650E+19	BE36549	1.43E-15	1.43E-15	0.995	2.477E+04	2.465E+04	7.15854E-14	2.051E-15	0.03	1.181E+06	1.156E+06	0.021	0.04
0.8998	Be Carrier B31 Sept 28, 2012 285ug/ml	282	1.013	1.674E+19	BE36550	1.43E-15	1.43E-15	0.995	2.477E+04	2.465E+04	7.09E-14	4.67E-15	0.07	1.187E+06	1.163E+06	0.021	0.07
0.8894	Be Carrier B31 Sept 28, 2012 285ug/ml	282	1.013	1.654E+19	BE36551	1.43E-15	1.43E-15	0.995	2.477E+04	2.465E+04	5.42663E-14	1.661E-15	0.03	8.978E+05	8.730E+05	0.027	0.05
0.8906	Be Carrier B31 Sept 28, 2012 285ug/ml	282	1.013	1.657E+19	BE36552	1.43E-15	1.43E-15	0.995	2.477E+04	2.465E+04	6.74812E-14	1.781E-15	0.03	1.118E+06	1.093E+06	0.022	0.04
0.8906	Be Carrier B31 Sept 28, 2012 285ug/ml	282	1.013	1.657E+19	BE36553	1.43E-15	1.43E-15	0.995	2.477E+04	2.465E+04	7.37839E-14	2.159E-15	0.03	1.222E+06	1.198E+06	0.020	0.04
0.8951	Be Carrier B31 Sept 28, 2012 285ug/ml	282	1.013	1.665E+19	BE36554	1.43E-15	1.43E-15	0.995	2.477E+04	2.465E+04	7.34325E-14	1.869E-15	0.03	1.223E+06	1.198E+06	0.020	0.04
0.8811	Be Carrier B31 Sept 28, 2012 285ug/ml	282	1.013	1.639E+19	BE36555	1.43E-15	1.43E-15	0.995	2.477E+04	2.465E+04	1.094E-13	2.723E-15	0.02	1.793E+06	1.768E+06	0.014	0.03

Be Carrier Mass	Carrier ID	Be Carrier conc	Be Carrier density	9Be added through carrier	Be AMS ID	10Be/9Be blank boronc orr	10Be/9Be blank error	blank error	10Be atoms in blank	10Be atoms in blank error	10Be/9Be AMS boronc orr	10Be/9Be AMS 1σ error	1σ AMS error	measured 10Be atoms	10Be atoms blnk corr	blank error	Total AMS error
(g)	(txt)	(μg/mL)	(g/mL)	(atoms 9Be)	(txt)	(10Be/9Be)	(10Be/9Be)	frac	(atoms)	(atoms)	(10Be/9Be)	(10Be/9Be)	frac	(atoms)	(atoms)	frac	frac
0.2	Becarrier	1000	1.013		BE1234	4.00E-15	4.00E-16				5.00E-13	9.00E-15	1.1%	78678929.4	78223012.13	0.00155 4625	0.023
0.8861	Be Carrier B31 Sept 28, 2012 285ug/ml	282	1.013	1.648E+19	BE36556	1.43E-15	1.43E-15	0.995	2.477E+04	2.465E+04	1.0507E-13	2.596E-15	0.02	1.732E+06	1.707E+06	0.014	0.03
0.8843	Be Carrier B31 Sept 28, 2012 285ug/ml	282	1.013	1.645E+19	BE36557	1.43E-15	1.43E-15	0.995	2.477E+04	2.465E+04	9.23454E-14	2.299E-15	0.02	1.519E+06	1.494E+06	0.016	0.04

Table 9 - ^{10}Be AMS data reduction.

Concerns with the data

Sample Group	Sample	Sediment Characteristics*	Quartz separation	Mass (g) if <100	Wet Chemistry	AMS (spreadsheet, word notes)	Results	Burial age calculation (max probability estimated from Figure 12)
Lower A2	025 (top)	• S, mica-rich, grey	• mostly 250-355, some 150-250 (only sed)	72	-	• Al current <ave (down to 1) • Al error >ave (47%)	not an outlier >2σ	0.016 (< average of 0.03)
	026	• m-fS, grey • aggregates	• mostly 250-355, some 150-250 (only sed)	-	-	-	not an outlier >2σ	0.025 (< average of 0.03)
	027	• mS, grey, mica-rich • aggregates	• mostly 250-355, some 150-250 (only sed)	-	• cont. ptte: 2.0 ml gel, little pinkish • ppte on cap	-	not an outlier >2σ	0.027 (< average of 0.03)
	028 (bottom)	• mS, dusty, mica-rich, grey	• mostly 250-355, some 150-250 (only sed)	79	-	-	not an outlier >2σ	0.024 (< average of 0.03)
Upper A2	001 (top)	• cS, salt and pepper (s&p)	• 255-850 (mix of crushed and sed.)	-	-	• Al current <ave (down to 0.6)	not an outlier >2σ	0.012 (< average of 0.03)
	002	• cS, granules, pebbles, s&p - grey	• 255-850 (mix of crushed and sed.)	94	-	• Be error >ave (4.4%)	not an outlier >2σ	0.045
	003	• cS, grey	• 255-850 (mix of crushed and sed.)	-	-	• Be current < ave • Be error >ave (4%)	not an outlier >2σ	0.045
	004	• cS, rare pebbles, grey	• 255-850 (mix of crushed and sed.)	91	-	-	not an outlier >2σ	0.023 (< average of 0.03)
	005 (bottom)	• NA	• 255-850 (mix of crushed and sed.)	-	-	-	not an outlier >2σ	0.045
Section 9 remainder	030 (37m depth)	• mS, grey-brown, dusty	• 250-355 sed • low purity	-	-	• Be current < ave	not an outlier >2σ	0.014 (< average of 0.03)

Sample Group	Sample	Sediment Characteristics*	Quartz separation	Mass (g) if <100	Wet Chemistry	AMS (spreadsheet, word notes)	Results	Burial age calculation (max probability estimated from Figure 12)
	029 (39.3 m)	• cS, pebbles and cobbles grey-s&p •	• 250-355, only sed • low purity	-	• ppte on cap	• Be current < ave	not an outlier >2σ	0.037
	032 (44 m)	• NA	• 500-850 crushed • med. purity	-	-	-	not an outlier >2σ	4.5E-3 (< average of 0.03)
Section 8	020 (top)	• mS, rusty-brown, dusty	• 150-355 (crushed and sed)	-	-	• Al current <ave (down to 0.6) • Al error >ave (54%) • Be error >ave (6%)	not an outlier >2σ	0.04
	021	• S, rusty, dusty	• 250-355 (sed)	-	-	• Al current <ave (down to 0.6)	not an outlier >2σ	0.045
	022 (bottom)	• S, orange	• 250-355 (crushed and sed)	-	• controlled ppte: 1.5 ml pptt large, whiter (centrifuged)	• Al error MUCH >ave (72%) • Be current < ave • Be error >ave (6.6%)	not an outlier >2σ	0.03

Table 10 - Confidence in the results.

Appendix D : Matlab codes

Code available upon request. Matlab R2013B used.

Burial Age Calculation

```
function burialplot_LSD(data, muontype, sample, sigma, plotbanana,
consts)


%This function creates a muon inclusive burial plot for a
%sample-specific location and depth assuming a simple surface buildup
and
%burial history.
%
%INPUTS:
%data = name of ascii file with nine columns of data (e.g. 'data.txt'):
%   column 1 is the depth of burial for each sample; (cm)
%   column 2 is the average density of material above each sample;
(g/cc)
%   column 3 is the decimal latitude of each sample (used in buildup
model
%   for production)
%   column 4 is the dicmal longitude of each sample (used in buildup
model
%   for production)
%   column 5 is the elevation of each sample site; (m)
%   column 6 is measured [10Be]; (atoms/g)
%   column 7 is the 1 sigma error in [10Be]; (atoms/g)
%   column 8 is measured [26Al]; (atoms/g)
%   column 9 is the 1 sigma error in [26Al]; (atoms/g)
%
%muontype = deep muon scheme to use; surface buildup model uses Lifton
et
%al. (2013), but this  parameter refers to the scheme used at depth. If
=
%0, there is no deep muon production; if = 1 Lifton (2013) is used at
depth
```

```
%(estimate from J. Stone, pers. comm.); if = 2 Heisinger (2002) is used
at
%depth.
%
%sample = the row number of the sample you wish to plot; all samples
will
%plot regardless, however, because of muons, the plot is structurally
%different at different depths and will therefore only be accurate for
the
%sample specified here unless 1) all sample depths are identical or 2)
muon
%production is not included (muontype = 0)
%
%sigma = specifies the sigma confidence for the error ellipse
%
%plotbananna = if true, will also plot the banana window
%
%consts = a matlab structure containing constants used in the LSD
scaling
%model. This structure is loaded in the startup.m file.
%
%
%A. Hidy
%%%%%%%%%%%%%%%%%%%%%%%%%%%%%%%%%%%%%%%%%%%%%%%%%%%%%%%%%%%%%%%%%%%%%%%
%%%
%%%%%%%%%%%%%%%%%%%%%%%%%%%%%%%%%%%%%%%%%%%%%%%%%%%%%%%%%%%%%%%%%%%%%%%
%%%

%load data

burial_data = load(data);

depths = burial_data(:,1);
densities = burial_data(:,2);
lats = burial_data(:,3);
longs = burial_data(:,4);
elevs = burial_data(:,5);
```

```
Be_concs = burial_data(:,6);
Be_errs = burial_data(:,7);
Al_concs = burial_data(:,8);
Al_errs = burial_data(:,9);
ratios = Al_concs./Be_concs;


%decay constants (1/s)

Be10_lambda = log(2)/1387000; %Korschinek et al. (2010)
Al26_lambda = log(2)/705000; %Nishiizumi (2004)


%neutron attenuation length (g/cm^2)

neutron_atten = 160; %Follows Balco et al. (2008); see Gosse and
Phillips (2001)

%spallogenic production (atoms/g/a)

refspalprod = 4.48; %Value from Balco et al. (2008); 4.96/1.106 to
reflect recalibration of Nishiizumi et al. (2007)
ratio_init = 6.75; %Follows Balco et al. (2008); 6.1/1.106 to reflect
recalibration of Nishiizumi et al. (2007)


%Get LSD scaling factors

maxage = 30000; %age over which to integrate production rates

LSD10 = LSD(lats(sample),longs(sample),elevs(sample),1,maxage,-1,10);
LSD26 = LSD(lats(sample),longs(sample),elevs(sample),1,maxage,-1,26);


agegrid = 0:1:maxage;
```

```
%average spallogenic surface production rate over age range

Be10_spalsurf =
mean(refspalprod.*interpolate(LSD10.tv,LSD10.Be,agegrid));
Al26_spalsurf =
mean(refspalprod.*ratio_init.*interpolate(LSD26.tv,LSD26.Al,agegrid));


%average total muogenic surface production rate over age range

meanRC = mean(interpolate(LSD10.tv,LSD10.Rc,agegrid));
meanSPhi = mean(interpolate(LSD10.tv,LSD10.SPhi,agegrid));

Be10_musurf =
P_mu_totalLSD(0,LSD10.pressure,meanRC,meanSPhi,consts,10,'no');
Al26_musurf =
P_mu_totalLSD(0,LSD10.pressure,meanRC,meanSPhi,consts,26,'no');



%muonic production at depth

if muontype == 0 %no muon production
    Be10_mudepth = 0;
    Al26_mudepth = 0;
else if muontype == 1 %Use LSD rates based on
        Be10_mudepth =
P_mu_totalLSD(depths(sample)*densities(sample),LSD10.pressure,meanRC,mea
nSPhi,consts,10,'no');
        Al26_mudepth =
P_mu_totalLSD(depths(sample)*densities(sample),LSD10.pressure,meanRC,mea
nSPhi,consts,26,'no');
    else if muontype == 2
```

```
            Be10_mudepth =
muonproduction_heisinger(depths(sample)*densities(sample),elevs(sample),
1);
            Al26_mudepth =
muonproduction_heisinger(depths(sample)*densities(sample),elevs(sample),
0);
        end
    end
end


%override buildup production rates here (for example, to assume basin-
wide
%production rate for source)

     Be10_spalbuildup = Be10_spalsurf;
     Al26_spalbuildup = Al26_spalsurf;
     Be10_mubuildup = Be10_musurf;
     Al26_mubuildup = Al26_musurf;


%rock density used during buildup phase (g/cc)

r_density = 2.0;


%simple buildup model with no erosion

    %buildup due to exposure at surface; assumes no inheritance

    function Be10_conc_buildup = Be10_buildup(t_exposure)
        Be10spall_buildup = (Be10_spalbuildup/Be10_lambda)*(1-exp(-
Be10_lambda*t_exposure));
        Be10muon_buildup = (Be10_mubuildup/Be10_lambda)*(1-exp(-
Be10_lambda*t_exposure));
        Be10_conc_buildup = Be10spall_buildup + Be10muon_buildup;
```

```
    end

    function Al26_conc_buildup = Al26_buildup(t_exposure)
        Al26spall_buildup = (Al26_spalbuildup/Al26_lambda)*(1-exp(-
Al26_lambda*t_exposure));
        Al26muon_buildup = (Al26_mubuildup/Al26_lambda)*(1-exp(-
Al26_lambda*t_exposure));
        Al26_conc_buildup = Al26spall_buildup + Al26muon_buildup;
    end

    %burial production; assume buildup is inheritance

    function Be10_conc_burial = Be10_burial(t_exposure, t_burial)
        Be10spall_burial = (Be10_spalsurf/Be10_lambda)*exp(-
depths(sample)*densities(sample)/neutron_atten)*(1-exp(-
Be10_lambda*t_burial));
        Be10muon_burial = (Be10_mudepth/Be10_lambda)*(1-exp(-
Be10_lambda*t_burial));
        Be10inheritance = Be10_buildup(t_exposure)*exp(-
Be10_lambda*t_burial);
        Be10_conc_burial = Be10spall_burial + Be10muon_burial +
Be10inheritance;
    end

    function Al26_conc_burial = Al26_burial(t_exposure, t_burial)
        Al26spall_burial = (Al26_spalsurf/Al26_lambda)*exp(-
depths(sample)*densities(sample)/neutron_atten)*(1-exp(-
Al26_lambda*t_burial));
        Al26muon_burial = (Al26_mudepth/Al26_lambda)*(1-exp(-
Al26_lambda*t_burial));
        Al26inheritance = Al26_buildup(t_exposure)*exp(-
Al26_lambda*t_burial);
        Al26_conc_burial = Al26spall_burial + Al26muon_burial +
Al26inheritance;
    end

%simple buildup model with erosion
```

```
    %new lambda term spallation

    function Be10lambda = Be10_elambda(erate)

        Be10lambda = Be10_lambda + erate*r_density/neutron_atten;
    end

    function Al26lambda = Al26_elambda(erate)

        Al26lambda = Al26_lambda + erate*r_density/neutron_atten;
    end

    %need effective lambda for muons; dominated by spall, so use rough
    %estimate of 1500 (this value doesn't matter much since it only is
used
    %for plotting the banana

    effective_muon_atten = 1500;

    function Be10lambdamu = Be10_elambdamu(erate)

        Be10lambdamu = Be10_lambda +
erate*r_density/effective_muon_atten;
    end

    function Al26lambdamu = Al26_elambdamu(erate)

        Al26lambdamu = Al26_lambda +
erate*r_density/effective_muon_atten;
    end

    %buildup due to exposure at surface; assumes no inheritance

    function eBe10_conc_buildup = eBe10_buildup(t_exposure, erate)
```

```
        Be10spall_buildup = (Be10_spalbuildup./Be10_elambda(erate)).*(1-
exp(-Be10_elambda(erate).*t_exposure));
        Be10muon_buildup = (Be10_mubuildup./Be10_elambdamu(erate)).*(1-
exp(-Be10_elambdamu(erate).*t_exposure));
        eBe10_conc_buildup = Be10spall_buildup + Be10muon_buildup;
    end

    function eAl26_conc_buildup = eAl26_buildup(t_exposure, erate)
        Al26spall_buildup = (Al26_spalbuildup./Al26_elambda(erate)).*(1-
exp(-Al26_elambda(erate).*t_exposure));
        Al26muon_buildup = (Al26_mubuildup./Al26_elambdamu(erate)).*(1-
exp(-Al26_elambdamu(erate).*t_exposure));
        eAl26_conc_buildup = Al26spall_buildup + Al26muon_buildup;
    end

%Plotting parameters
%%%%%%%%%%%%%%%%%%%%%%%%%%%%%%%%%%%%%%%%%%%%%%%%%%%%%%%%%%%%%%%%%%%%%%%%%%%%
%%%
%%%%%%%%%%%%%%%%%%%%%%%%%%%%%%%%%%%%%%%%%%%%%%%%%%%%%%%%%%%%%%%%%%%%%%%%%%%%
%%%

%define axis for plot
plot_axis = [3 7.5 0 8]; %x-axis, y-axis

%Define locations of contours on burial plot, in years
%n1 = [100000 500000 1000000 2000000 3000000 4000000 60000000 8000000];
%burial contours
%n1 = [50000 100000 250000 500000 750000 1000000 1500000 2000000 3000000
4000000 6000000];
n1 = [250000 500000 750000 1000000 1500000 2000000 3000000 4000000];
n2 = [1000 3000 10000 30000 100000 1000000]; %exposure contours

%erosion rate contours for erosion banana, cm/a
n3 = [200 50 10  2  0.5 0.1  0.0100]/1000;
```

```
%Create grids for plot contours
texp = 1:100:20000000;
tbur = 1:100:20000000;
eeros = 0:0.001/1000:500/1000;



figure
hold on
box on
axis(plot_axis);
xlabel('log[^{10}Be] (atoms g^{-1})');
ylabel('^{26}Al/^{10}Be');
title('Burial Plot');

%Plot error ellipses and mean values for sample concentrations
plot(log10(Be_concs),ratios,'k.');

for k = 1:numel(Be_concs)

ellipse_generic(Be_concs(k),Be_errs(k),Al_concs(k),Al_errs(k),sigma);
end



%burial contours
for k = 1:numel(n1)

plot(log10(Be10_burial(texp,n1(k))),Al26_burial(texp,n1(k))./Be10_burial
(texp,n1(k)),'b:');
end



%exposure contours
for k = 1:numel(n2)

plot(log10(Be10_burial(n2(k),tbur)),Al26_burial(n2(k),tbur)./Be10_burial
(n2(k),tbur),'k--');
```

```
end


%surface curve for zero erosion
plot(log10(Be10_burial(texp,0)),Al26_burial(texp,0)./Be10_burial(texp,0)
,'r-','linewidth',2);


%burial path starting at zero-erosion surface saturation (lower plot
%boundary)
plot(log10(Be10_burial(100000000,tbur)),Al26_burial(100000000,tbur)./Be1
0_burial(100000000,tbur),'k-','linewidth',2);


%include erosion banana?
if nargin < 5
    return
end

plot(log10(eBe10_buildup(10000000,eeros)),
eAl26_buildup(10000000,eeros)./eBe10_buildup(10000000,eeros),'g-
','linewidth',2);
plot(log10(Be10_burial(texp,0)),Al26_burial(texp,0)./Be10_burial(texp,0)
,'r-','linewidth',2);
for k = 1:numel(n3)
    plot(log10(eBe10_buildup(texp,n3(k))),
eAl26_buildup(texp,n3(k))./eBe10_buildup(texp,n3(k)),'g-');

plot(log10(Be10_burial(texp,0)),Al26_burial(texp,0)./Be10_burial(texp,0)
,'r-','linewidth',2);
end


%depth curve for zero erosion
```

```
function Be10_conc_buildupA = Be10_buildupA(t_exposure)
        Be10spall_buildup = (Be10_spalsurf/Be10_lambda)*(1-exp(-
Be10_lambda*t_exposure))*exp(-depths(sample)*densities(sample)/160);
        Be10muon_buildup = (Be10_mudepth/Be10_lambda)*(1-exp(-
Be10_lambda*t_exposure));
        Be10_conc_buildupA = Be10spall_buildup + Be10muon_buildup;
    end

    function Al26_conc_buildupA = Al26_buildupA(t_exposure)
        Al26spall_buildup = (Al26_spalsurf/Al26_lambda)*(1-exp(-
Al26_lambda*t_exposure))*exp(-depths(sample)*densities(sample)/160);
        Al26muon_buildup = (Al26_mudepth/Al26_lambda)*(1-exp(-
Al26_lambda*t_exposure));
        Al26_conc_buildupA = Al26spall_buildup + Al26muon_buildup;
    end

plot(log10(Be10_buildupA(texp)),Al26_buildupA(texp)./Be10_buildupA(texp)
,'r-','linewidth',2);

return
% %plot play (for multi-depth)
%     function Be10_conc_buildupA = Be10_buildupA(t_exposure,newdepth)
%         Be10spall_buildup = (Be10_spalprodrate/Be10_lambda)*(1-exp(-
Be10_lambda*t_exposure))*exp(-newdepth*densities(sample)/160);
%         Be10muon_buildup =
(muonproduction_generic(newdepth*densities(sample),elevs(sample),1)/2/Be
10_lambda)*(1-exp(-Be10_lambda*t_exposure));
%         Be10_conc_buildupA = Be10spall_buildup + Be10muon_buildup;
%     end
%
%     function Al26_conc_buildupA = Al26_buildupA(t_exposure,newdepth)
%         Al26spall_buildup = (Al26_spalprodrate/Al26_lambda)*(1-exp(-
Al26_lambda*t_exposure))*exp(-newdepth*densities(sample)/160);
%         Al26muon_buildup =
(muonproduction_generic(newdepth*densities(sample),elevs(sample),0)/2/Al
26_lambda)*(1-exp(-Al26_lambda*t_exposure));
```

```
%         Al26_conc_buildupA = Al26spall_buildup + Al26muon_buildup;
%     end
%
%
%
%     function Be10_conc_burialA = Be10_burialA(t_exposure, t_burial,
newdepth)
%         Be10_muonprodrateA =
muonproduction_generic(newdepth*densities(sample),elevs(sample),1)/2;
%         Be10spall_burial = (Be10_spalprodrate/Be10_lambda)*exp(-
newdepth*densities(sample)/neutron_atten)*(1-exp(-
Be10_lambda*t_burial));
%         Be10muon_burial = (Be10_muonprodrateA/Be10_lambda)*(1-exp(-
Be10_lambda*t_burial));
%         Be10inheritance = Be10_buildupA(t_exposure,newdepth)*exp(-
Be10_lambda*t_burial);
%         Be10_conc_burialA = Be10spall_burial + Be10muon_burial +
Be10inheritance;
%     end
%
%     function Al26_conc_burialA = Al26_burialA(t_exposure, t_burial,
newdepth)
%         Al26_muonprodrateA =
muonproduction_generic(newdepth*densities(sample),elevs(sample),0)/2;
%         Al26spall_burial = (Al26_spalprodrate/Al26_lambda)*exp(-
newdepth*densities(sample)/neutron_atten)*(1-exp(-
Al26_lambda*t_burial));
%         Al26muon_burial = (Al26_muonprodrateA/Al26_lambda)*(1-exp(-
Al26_lambda*t_burial));
%         Al26inheritance = Al26_buildupA(t_exposure, newdepth)*exp(-
Al26_lambda*t_burial);
%         Al26_conc_burialA = Al26spall_burial + Al26muon_burial +
Al26inheritance;
%     end
%
%
%      function Be10_complex = Be10complex(t_exposure,t_burial,newdepth)
```

```
%          Be10spall_buildup =  (Be10_spalprodrate/Be10_lambda)*(1-exp(-
Be10_lambda*t_exposure));
%          Be10muon_buildup =
(muonproduction_generic(0,elevs(sample),1)/Be10_lambda)*(1-exp(-
Be10_lambda*t_exposure));
%          Be10_conc_buildup = Be10spall_buildup + Be10muon_buildup;
%
%          Be10_muonprodrateA =
muonproduction_generic(newdepth*densities(sample),elevs(sample),1)/2;
%          Be10spall_burial = (Be10_spalprodrate/Be10_lambda)*exp(-
newdepth*densities(sample)/neutron_atten)*(1-exp(-
Be10_lambda*t_burial));
%          Be10muon_burial = (Be10_muonprodrateA/Be10_lambda)*(1-exp(-
Be10_lambda*t_burial));
%          Be10inheritance = Be10_conc_buildup*exp(-
Be10_lambda*t_burial);
%          Be10_complex = Be10spall_burial + Be10muon_burial +
Be10inheritance;
%      end
%
%     function Al26_complex = Al26complex(t_exposure,t_burial,newdepth)
%         Al26spall_buildup = (Al26_spalprodrate/Al26_lambda)*(1-exp(-
Al26_lambda*t_exposure));
%         Al26muon_buildup =
(muonproduction_generic(0,elevs(sample),0)/Al26_lambda)*(1-exp(-
Al26_lambda*t_exposure));
%         Al26_conc_buildup = Al26spall_buildup + Al26muon_buildup;
%
%         Al26_muonprodrateA =
muonproduction_generic(newdepth*densities(sample),elevs(sample),0)/2;
%         Al26spall_burial = (Al26_spalprodrate/Al26_lambda)*exp(-
newdepth*densities(sample)/neutron_atten)*(1-exp(-
Al26_lambda*t_burial));
%         Al26muon_burial = (Al26_muonprodrateA/Al26_lambda)*(1-exp(-
Al26_lambda*t_burial));
%         Al26inheritance = Al26_conc_buildup*exp(-
Al26_lambda*t_burial);
```

```
%         Al26_complex = Al26spall_burial + Al26muon_burial +
Al26inheritance;
%     end
%
%
%
plot(log10(Be10_buildupA(texp,depths(sample))),Al26_buildupA(texp,depths
(sample))./Be10_buildupA(texp,depths(sample)),'r-','linewidth',2);
%
%
% n4 = [400 500 1000];
% depthfit = 1:5:8000;
% epos1 = 150000;
% epos2 = 20000;
%
%
%plot(log10(Be10_burialA(10000000000,0,depthfit)),Al26_burialA(100000000
00,0,depthfit)./Be10_burialA(10000000000,0,depthfit),'b-
','linewidth',2);
%
% % for k = 1:numel(n4)
% %
plot(log10(Be10_burialA(10000000000,0,n4(k))),Al26_burialA(10000000000,0
,n4(k))./Be10_burialA(10000000000,0,n4(k)),'k.','linewidth',4);
% %
plot(log10(Be10complex(epos1,tbur,n4(k))),Al26complex(epos1,tbur,n4(k)).
/Be10complex(epos1,tbur,n4(k)),'k--');
% %
plot(log10(Be10complex(epos2,tbur,n4(k))),Al26complex(epos2,tbur,n4(k)).
/Be10complex(epos2,tbur,n4(k)),'k--');
% % end




end
```

Syndepositional production

```
%function syndep(muontype, sigma, consts, t_exposure, erate, thickness)
muontype=1;
sigma=1;
erate=0;

%input
lat = 74.349917;
long = -123.18775;
elev = 50;
density = 2;



%%%%%%%%%%%%%%%%%%%%%%%%%%%%%%%%%%%%%%%%%%%%%%%%%%%%%%%%%%%%%%%%%%%%%%%%%%%%%%%
%%%
% calculate buildup at the surface
t_exposure=10000;

%decay constants (1/s)
Be10_lambda = log(2)/1387000; %Korschinek et al. (2010)
Al26_lambda = log(2)/705000; %Nishiizumi (2004)

%neutron attenuation length (g/cm^2)
neutron_atten = 160; %Follows Balco et al. (2008); see Gosse and
Phillips (2001)

%spallogenic production (atoms/g/a)
refspalprod = 4.48; %Value from Balco et al. (2008); 4.96/1.106 to
reflect recalibration of Nishiizumi et al. (2007)
ratio_init = 6.75; %Follows Balco et al. (2008); 6.1/1.106 to reflect
recalibration of Nishiizumi et al. (2007)

%Get LSD scaling factors
maxage = 100000; %age over which to integrate production rates
LSD10 = LSD(lat,long,elev,1,maxage,-1,10);
LSD26 = LSD(lat,long,elev,1,maxage,-1,26);
```

```
agegrid = 0:1:maxage;

%average spallogenic surface production rate over age range
Be10_spalsurf =
mean(refspalprod.*interpolate(LSD10.tv,LSD10.Be,agegrid));
Al26_spalsurf =
mean(refspalprod.*ratio_init.*interpolate(LSD26.tv,LSD26.Al,agegrid));

%average total muogenic surface production rate over age range
meanRC = mean(interpolate(LSD10.tv,LSD10.Rc,agegrid));
meanSPhi = mean(interpolate(LSD10.tv,LSD10.SPhi,agegrid));
Be10_musurf =
P_mu_totalLSD(0,LSD10.pressure,meanRC,meanSPhi,consts,10,'no');
Al26_musurf =
P_mu_totalLSD(0,LSD10.pressure,meanRC,meanSPhi,consts,26,'no');

% %muonic production at depth
Be10_mudepth = 0; % (deleted code)
Al26_mudepth = 0;

%override buildup production rates here (for example, to assume basin-
wide
%production rate for source)
Be10_spalbuildup = Be10_spalsurf;
Al26_spalbuildup = Al26_spalsurf;
Be10_mubuildup = Be10_musurf;
Al26_mubuildup = Al26_musurf;

%rock density used during buildup phase (g/cc)
r_density = 2.0;

%simple buildup model with no erosion

%buildup due to exposure at surface; assumes no inheritance

    %function Be10_conc_buildup = Be10_buildup(t_exposure)
```

```
        Be10spall_buildup = (Be10_spalbuildup/Be10_lambda)*(1-exp(-
Be10_lambda*t_exposure));
        Be10muon_buildup = (Be10_mubuildup/Be10_lambda)*(1-exp(-
Be10_lambda*t_exposure));
        Be10_conc_buildup = Be10spall_buildup + Be10muon_buildup;
    %end

    %function Al26_conc_buildup = Al26_buildup(t_exposure)
        Al26spall_buildup = (Al26_spalbuildup/Al26_lambda)*(1-exp(-
Al26_lambda*t_exposure));
        Al26muon_buildup = (Al26_mubuildup/Al26_lambda)*(1-exp(-
Al26_lambda*t_exposure));
        Al26_conc_buildup = Al26spall_buildup + Al26muon_buildup;
    %end

 Be10_conc_burial = 0; % (deleted code)
 Al26_conc_burial = 0;

%buildup due to exposure at surface; assumes no inheritance
Be10lambdamu = Be10_lambda; %because no erosion (deleted code, see
original code syndep.m)
Al26lambdamu = Al26_lambda;
   % function eBe10_conc_buildup = eBe10_buildup(t_exposure, erate)
        Be10spall_buildup = (Be10_spalbuildup./Be10_lambda).*(1-exp(-
Be10_lambda.*t_exposure));
        Be10muon_buildup = (Be10_mubuildup./Be10lambdamu).*(1-exp(-
Be10lambdamu.*t_exposure));
        Be10_conc_buildup = Be10spall_buildup + Be10muon_buildup;
   % end

   % function eAl26_conc_buildup = eAl26_buildup(t_exposure, erate)
        Al26spall_buildup = (Al26_spalbuildup./Al26_lambda).*(1-exp(-
Al26_lambda.*t_exposure));
        Al26muon_buildup = (Al26_mubuildup./Al26lambdamu).*(1-exp(-
Al26lambdamu.*t_exposure));
        Al26_conc_buildup = Al26spall_buildup + Al26muon_buildup;
   % end
```

```
%%%%%%%%%%%%%%%%%%%%%%%%%%%%%%%%%%%%%%%%%%%%%%%%%%%%%%%%%%%%%%%%%%%%%%%%%%%%%%%
%%%
% calculate buildup at depth
t_burial=10000; % for a rate of 10cm/1000yr, burial time for deposition
of one package
for j=1:50;
    depth=100:100:5000;
    depth=depth(j);
%decay constants (1/s)
Be10_lambda = log(2)/1387000; %Korschinek et al. (2010)
Al26_lambda = log(2)/705000; %Nishiizumi (2004)

%neutron attenuation length (g/cm^2)
neutron_atten = 160; %Follows Balco et al. (2008); see Gosse and
Phillips (2001)

%spallogenic production (atoms/g/a)
refspalprod = 4.48; %Value from Balco et al. (2008); 4.96/1.106 to
reflect recalibration of Nishiizumi et al. (2007)
ratio_init = 6.75; %Follows Balco et al. (2008); 6.1/1.106 to reflect
recalibration of Nishiizumi et al. (2007)

%Get LSD scaling factors
maxage = 100000; %age over which to integrate production rates
LSD10 = LSD(lat,long,elev,1,maxage,-1,10);
LSD26 = LSD(lat,long,elev,1,maxage,-1,26);
agegrid = 0:1:maxage;

%average spallogenic surface production rate over age range
Be10_spalsurf =
mean(refspalprod.*interpolate(LSD10.tv,LSD10.Be,agegrid));
Al26_spalsurf =
mean(refspalprod.*ratio_init.*interpolate(LSD26.tv,LSD26.Al,agegrid));
```

```
%average total muogenic surface production rate over age range
meanRC = mean(interpolate(LSD10.tv,LSD10.Rc,agegrid));
meanSPhi = mean(interpolate(LSD10.tv,LSD10.SPhi,agegrid));
Be10_musurf =
P_mu_totalLSD(0,LSD10.pressure,meanRC,meanSPhi,consts,10,'no');
Al26_musurf =
P_mu_totalLSD(0,LSD10.pressure,meanRC,meanSPhi,consts,26,'no');

%muonic production at depth
if muontype == 0 %no muon production
    Be10_mudepth = 0;
    Al26_mudepth = 0;
else if muontype == 1 %Use LSD rates based on
        Be10_mudepth =
P_mu_totalLSD(depth*density,LSD10.pressure,meanRC,meanSPhi,consts,10,'no
');
        Al26_mudepth =
P_mu_totalLSD(depth*density,LSD10.pressure,meanRC,meanSPhi,consts,26,'no
');
    else if muontype == 2
            Be10_mudepth =
muonproduction_heisinger(depth*density,elev,1);
            Al26_mudepth =
muonproduction_heisinger(depth*density,elev,0);
        end
    end
end

%override buildup production rates here (for example, to assume basin-
wide
%production rate for source)
Be10_spalbuildup = Be10_spalsurf;
Al26_spalbuildup = Al26_spalsurf;
Be10_mubuildup = Be10_musurf;
Al26_mubuildup = Al26_musurf;

%rock density used during buildup phase (g/cc)
```

```
r_density = 2.0;

%burial production; assume buildup is inheritance

    %function Be10_conc_burial = Be10_burial(t_exposure, t_burial)
        Be10spall_burial = (Be10_spalsurf/Be10_lambda)*exp(-
depth*density/neutron_atten)*(1-exp(-Be10_lambda*t_burial));
        Be10muon_burial = (Be10_mudepth/Be10_lambda)*(1-exp(-
Be10_lambda*t_burial));
        %Be10inheritance = Be10_buildup(t_exposure)*exp(-
Be10_lambda*t_burial);
        Be10_conc_burial = Be10spall_burial + Be10muon_burial; %+
Be10inheritance;
    %end

    %function Al26_conc_burial = Al26_burial(t_exposure, t_burial)
        Al26spall_burial = (Al26_spalsurf/Al26_lambda)*exp(-
depth*density/neutron_atten)*(1-exp(-Al26_lambda*t_burial));
        Al26muon_burial = (Al26_mudepth/Al26_lambda)*(1-exp(-
Al26_lambda*t_burial));
        %Al26inheritance = Al26_buildup(t_exposure)*exp(-
Al26_lambda*t_burial);
        Al26_conc_burial = Al26spall_burial + Al26muon_burial; %+
Al26inheritance;
    %end

vector_Be10(j)= Be10_conc_burial; % i think this is just decayed till
the end of that interval
vector_Al26(j)= Al26_conc_burial;
end

assignin('base', 'vector_Be10', vector_Be10)
assignin('base', 'vector_Al26', vector_Al26)

%%%%%%%%%%%%%%%%%%%%%%%%%%%%%%%%%%%%%%%%%%%%%%%%%%%%%%%%%%%%%%%%%%%%%%%%%%%%
%%%
```

```
% decay by different times for each depth
decay_time=[490000 480000 470000 460000 450000 440000 430000 420000
410000 400000 390000 380000 370000 360000 350000 340000 330000 320000
310000 300000 290000 280000 270000 260000 250000 240000 230000 220000
210000 200000 190000 180000 170000 160000 150000 140000 130000 120000
110000 100000 90000 80000 70000 60000 50000 40000 30000 20000 10000 0];
conc_after_500000yrs_Be10=vector_Be10.*(exp(-Be10_lambda*decay_time));
conc_after_500000yrs_Al26=vector_Al26.*(exp(-Al26_lambda*decay_time));

% undecay



% add surface exposure
Be10_surface_decayed=Be10_conc_buildup*(exp(-Be10_lambda*500000));
Al26_surface_decayed=Al26_conc_buildup*(exp(-Al26_lambda*500000));
total_conc_after_500000yrs_Be10=Be10_surface_decayed;
total_conc_after_500000yrs_Al26=Al26_surface_decayed;
for j=1:10

total_conc_after_500000yrs_Be10=total_conc_after_500000yrs_Be10+conc_aft
er_500000yrs_Be10(j);

total_conc_after_500000yrs_Al26=total_conc_after_500000yrs_Al26+conc_aft
er_500000yrs_Al26(j);
end
```

Post-burial production

```
function muon_isochron_witherosion_2(t_exposure, ratio_init,
depth_above_030, erate, consts)

%This function plots a muon equilibration isochron for the samples at
%Section 9

% all the inputs are the sample for all samples:
% t_exposure = the exposure time of the samples prior to burial, in
years.
```

```
% for the Banks samples the average xposure time is 5600 years
% ratio_init = 6.75 unless inherited a depressed ratio
% depth_above_030 = 50m (hence, the deepest sample ~70m depth), constant
% erate in cm/a
% for all burial duration
% consts = a matlab structure containing constants used in the LSD
scaling
% model. This structure is loaded in the startup.m file.

%% This code block establishes the parameters, prod rate, etc. for the
% Section (to be computed only once when the function is called)

% muontype=1; variable not needed because only use this muon type
% sigma=1; variable not used
lat = 74.349917;
long = -123.18775;
elev = 50;
density = 2;
r_density = 2.0; %rock density used during buildup phase (g/cc) -
variable
% not used

%decay constants (1/s)
Be10_lambda = log(2)/1387000; %Korschinek et al. (2010)
Al26_lambda = log(2)/705000; %Nishiizumi (2004)
%neutron attenuation length (g/cm^2)
neutron_atten = 150; %Follows Balco et al. (2008); see Gosse and
Phillips (2001); changed from 160 to 150 (Lea, 31/10/14)
%spallogenic production (atoms/g/a)
refspalprod = 4.48; %Value from Balco et al. (2008); 4.96/1.106 to
reflect recalibration of Nishiizumi et al. (2007)
%Get LSD scaling factors
maxage = 100000; %age over which to integrate production rates
LSD10 = LSD(lat,long,elev,1,maxage,-1,10);
LSD26 = LSD(lat,long,elev,1,maxage,-1,26);
agegrid = 0:1:maxage;
%average spallogenic surface production rate over age range
```

```
Be10_spalsurf =
mean(refspalprod.*interpolate(LSD10.tv,LSD10.Be,agegrid));
Al26_spalsurf =
mean(refspalprod.*ratio_init.*interpolate(LSD26.tv,LSD26.Al,agegrid));
%average total muogenic surface production rate over age range
meanRC = mean(interpolate(LSD10.tv,LSD10.Rc,agegrid));
meanSPhi = mean(interpolate(LSD10.tv,LSD10.SPhi,agegrid));
Be10_musurf =
P_mu_totalLSD(0,LSD10.pressure,meanRC,meanSPhi,consts,10,'no');
Al26_musurf =
P_mu_totalLSD(0,LSD10.pressure,meanRC,meanSPhi,consts,26,'no');
%deleted code for overiding production rates (e.g. assuming basin-wide
%production rates)
Be10_spalbuildup = Be10_spalsurf;
Al26_spalbuildup = Al26_spalsurf;
Be10_mubuildup = Be10_musurf;
Al26_mubuildup = Al26_musurf;

%% This code block calculates the initial buildup from exposure
% Exposure can be on the catchment, during transport, or at the burial
site
Be10spall_buildup = (Be10_spalbuildup/Be10_lambda)*(1-exp(-
Be10_lambda*t_exposure));
Be10muon_buildup = (Be10_mubuildup/Be10_lambda)*(1-exp(-
Be10_lambda*t_exposure));
Be10_conc_buildup = Be10spall_buildup + Be10muon_buildup;

Al26spall_buildup = (Al26_spalbuildup/Al26_lambda)*(1-exp(-
Al26_lambda*t_exposure));
Al26muon_buildup = (Al26_mubuildup/Al26_lambda)*(1-exp(-
Al26_lambda*t_exposure));
Al26_conc_buildup = Al26spall_buildup + Al26muon_buildup;

%% erosion
    %lambda term spallation
    function Be10lambda = Be10_elambda(erate)
        Be10lambda = Be10_lambda + erate*r_density/neutron_atten;
```

```
    end
    function Al26lambda = Al26_elambda(erate)
        Al26lambda = Al26_lambda + erate*r_density/neutron_atten;
    end
    %lambda fast muons
    effective_fastmuon_atten = 5300;
    function Be10lambdafastmu = Be10_elambdafastmu(erate)
        Be10lambdafastmu = Be10_lambda +
erate*r_density/effective_fastmuon_atten;
    end
    function Al26lambdafastmu = Al26_elambdafastmu(erate)
        Al26lambdafastmu = Al26_lambda +
erate*r_density/effective_fastmuon_atten;
    end
    %lambda neg muons
    effective_negmuon_atten = 1300;
    function Be10lambdanegmu = Be10_elambdanegmu(erate)
        Be10lambdanegmu = Be10_lambda +
erate*r_density/effective_negmuon_atten;
    end
    function Al26lambdanegmu = Al26_elambdanegmu(erate)
        Al26lambdanegmu = Al26_lambda +
erate*r_density/effective_negmuon_atten;
    end
% effective_muon_attenuation_fastneutrons = 5300 (Braucher is an author,
2012)
% effective_muon_attenuation_slowneutrons = 1300
% dont use heisenger 4800


%% This code block calculates concentration (a) at each time (b) for
each sample

% times
t_burial = [0:0.1:2].*200000;
% samples
```

```
%depth = [0 225 700 943.4 2057.3]+depth_above_030; % Section 9 group
average sample depth - shallowest (030) sample depth (3705 cm)
depth = [0 500 1000 1500 2000]+depth_above_030;
% storing results
Be10_data = zeros(length(depth), length(t_burial));
Al26_data = zeros(length(depth), length(t_burial));
Be10_muon = zeros(length(depth), length(t_burial));
Al26_muon = zeros(length(depth), length(t_burial));

for i=1:length(t_burial);
    for j=1:length(depth);
        %muonic production at depth
        Be10_mudepth=
P_mu_totalLSD(depth(j)*density,LSD10.pressure,meanRC,meanSPhi,consts,10,
'yes'); %this stores both fast and neg muon production rates
        Al26_mudepth =
P_mu_totalLSD(depth(j)*density,LSD10.pressure,meanRC,meanSPhi,consts,26,
'yes');
        %burial production
        Be10spall_burial = (Be10_spalsurf/Be10_elambda(erate))*exp(-
depth(j)*density/neutron_atten)*(1-exp(-
Be10_elambda(erate)*t_burial(i)));
        Be10fastmuon_burial =
(Be10_mudepth.P_fast/Be10_elambdafastmu(erate))*(1-exp(-
Be10_elambdafastmu(erate)*t_burial(i)));
        Be10negmuon_burial =
(Be10_mudepth.P_neg/Be10_elambdanegmu(erate))*(1-exp(-
Be10_elambdanegmu(erate)*t_burial(i)));
        Be10inheritance = Be10_conc_buildup*exp(-
Be10_lambda*t_burial(i));
        Be10_conc_burial = Be10spall_burial + Be10fastmuon_burial +
Be10negmuon_burial + Be10inheritance;

        Al26spall_burial = (Al26_spalsurf/Al26_elambda(erate))*exp(-
depth(j)*density/neutron_atten)*(1-exp(-
Al26_elambda(erate)*t_burial(i)));
```

```
        Al26fastmuon_burial =
(Al26_mudepth.P_fast/Al26_elambdafastmu(erate))*(1-exp(-
Al26_elambdafastmu(erate)*t_burial(i)));
        Al26negmuon_burial =
(Al26_mudepth.P_neg/Al26_elambdanegmu(erate))*(1-exp(-
Al26_elambdanegmu(erate)*t_burial(i)));
        Al26inheritance = Al26_conc_buildup*exp(-
Al26_lambda*t_burial(i));
        Al26_conc_burial = Al26spall_burial + Al26fastmuon_burial +
Al26negmuon_burial + Al26inheritance;
        %store data
        Be10_data(j,i) = Be10_conc_burial;
        Al26_data(j,i) = Al26_conc_burial;
        Be10_muon(j,i) = Be10fastmuon_burial + Be10negmuon_burial;
        Al26_muon(j,i) = Al26fastmuon_burial + Al26negmuon_burial ;
    end
end

% separate fast and slow muons from lsd output (be10_mudepth) and make
two
% equations with different attenuations lengths

assignin('base', 'Be10_data', Be10_data) % copy result variables to the
base workspace
assignin('base', 'Al26_data', Al26_data)
assignin('base', 'Be10_muon', Be10_muon)
assignin('base', 'Al26_muon', Al26_muon)

% see buildup production code for including erosion

end

% plots are made in the muon_isochronn_makeplots.m file
```

Post-incision production

```
function [Be10_integrated_conc, Al26_integrated_conc] =
post_incision(erate, t_postincision)
%erate in cm/a
%t_postincision in a
    % CONSTANTS FOR THIS SITE AND INPUT
    lat = 74.349917;
    long = -123.18775;
    elev = 50;
    density = 2;
    r_density = density;
    ratio_init = 6.75;
    %decay constants (1/s)
    Be10_lambda = log(2)/1387000; %Korschinek et al. (2010)
    Al26_lambda = log(2)/705000; %Nishiizumi (2004)
    %neutron attenuation length (g/cm^2)
    neutron_atten = 160; %Follows Balco et al. (2008); see Gosse and
Phillips (2001)
    %new lambda term spallation
    Be10lambda = Be10_lambda + erate*r_density/neutron_atten;
    Al26lambda = Al26_lambda + erate*r_density/neutron_atten;
    %spallogenic production (atoms/g/a)
    refspalprod = 4.48; %Value from Balco et al. (2008); 4.96/1.106 to
reflect recalibration of Nishiizumi et al. (2007)
    %Get LSD scaling factors
    maxage = 100000; %age over which to integrate production rates
    LSD10 = LSD(lat,long,elev,1,maxage,-1,10);
    LSD26 = LSD(lat,long,elev,1,maxage,-1,26);
    agegrid = 0:1:maxage;
    %average spallogenic surface production rate over age range
    Be10_spalsurf =
mean(refspalprod.*interpolate(LSD10.tv,LSD10.Be,agegrid));
    Al26_spalsurf =
mean(refspalprod.*ratio_init.*interpolate(LSD26.tv,LSD26.Al,agegrid));
    %average total muogenic surface production rate over age range


    % depth = erate*t_postincision -erate*t
```

```
    % shieldingfactor = 0.6867*exp(-0.9196*depth_fnc(t)) + 0.2344*exp(-
3.82*depth_fnc(t));
    % shieldingfactor = 0.6867*exp(-0.9196*(erate*t_postincision -
erate*t)) + 0.2344*exp(-3.82*(erate*t_postincision -erate*t));
    syms t
    Be10spall_conc = @(t) (0.6867.*exp(-0.9196.*(erate.*t_postincision -
erate.*t)) + 0.2344.*exp(-3.82.*(erate.*t_postincision -
erate.*t))).*Be10_spalsurf/Be10lambda.*exp(-(erate.*t_postincision -
erate.*t).*density/neutron_atten).*(1-exp(-Be10lambda.*t));
    Be10_integrated_conc = integral(Be10spall_conc, 0, t_postincision);
    Al26spall_conc = @(t) (0.6867.*exp(-0.9196.*(erate.*t_postincision -
erate.*t)) + 0.2344.*exp(-3.82.*(erate.*t_postincision -
erate.*t))).*Al26_spalsurf/Al26lambda.*exp(-(erate.*t_postincision -
erate.*t).*density/neutron_atten).*(1-exp(-Al26lambda.*t));
    Al26_integrated_conc = integral(Al26spall_conc, 0, t_postincision);

end
```

Post-burial production forward model

```
%forward model
% change from forward model 2: misfit is compared to trends not conc
%clear results results_Be10_concentrations results_Al26_concentrations

results = zeros(300,7);
results_Be10_concentrations=zeros(300, 5);
results_Al26_concentrations=zeros(300, 5);

for i=1:300;
% (1)randomly sample parameter ranges
time_vector_all = 0:5000:5000000; % timesteps of 5 ka up to potential
for 5 Ma depositional age
% zero inheritance in forward_model_2
Be10_inheritance = datasample(0:1000000,1);
Al26_inheritance = datasample(0:1000000,1);
effective_fastmuon_atten = datasample(4300:6300,1);
id = datasample(5000:25000,1); %ice depth expressed in sediment depth
(2x the density) [cm]
```

```
e = datasample(0:0.000001:1,1); %cm/yr
erate_cycle = [e,0,0,0,0,0,0,0,0,0,0,0,0,0,0,0,0,0,0,0]; % 20 time steps
of 5ka
depth_cycle =
[id+3600,3600,3600,3600,3600,3600,3600,3600,3600,3600,3600,3600,3600,360
0,3600,3600,3600,3600,3600,3600]; % 20 time steps of 5ka (3600 is depth
above 030 in cm from highest peak of 84m)
% 'id + 3600' above must be changed if different sediment erosion
scenarios are introduced

index = datasample(4:length(time_vector_all),1); %this is the number of
5ka timesteps that the model will run for
cycles = floor((index-3)/20); % this is the number of glacial cycles,
since there are 20 time steps in each cycle (100 ka/ 5ka),
% I subtract 3 for the first 3 timesteps before the LGM, which are an
incomplete cycle
remainder = rem((index-3),20); % this is the remaining number of 5ka
time steps that need to be accounted for after accounting for the 100 ka
cycles

% there are 3 parts to erate_vector and depth_above_030_vector below:
% (1) the first three timesteps are an incomplete cycle (before the LGM,
and the first cycle starts at 15ka)
% (2) the number of glacial cycles, each of 20 time steps
% (3) the remaining time steps
time_vector = time_vector_all(1:index);
erate_vector = horzcat([e, e, e],repmat(erate_cycle, 1,
cycles),erate_cycle(1:remainder));
depth_above_030_vector = horzcat([3600, 3600, 3600], repmat(depth_cycle,
1, cycles), depth_cycle(1:remainder));

% different scenarios of sediment erosion
depth_above_030_vector(1)=1200; %simple solution for now
depth_above_030_vector(2)=1200;
depth_above_030_vector(3)=1200;

% plot variables:
```

```
% scatter(time_vector,erate_vector)
% plot(time_vector,depth_above_030_vector)

% (2)compute concentrations
muon_isochron_erosion_changingdepth_manysteps_3(Be10_inheritance,
Al26_inheritance, time_vector, depth_above_030_vector, erate_vector,
effective_fastmuon_atten, consts);
%0 inheritance
Be10_data = [[0; 0; 0; 0; 0] Be10_data_reversed]; % only flip data once!
Al26_data = [[0; 0; 0; 0; 0] Al26_data_reversed];
Be10_spall = [[0; 0; 0; 0; 0] Be10_spall_reversed];
Al26_spall = [[0; 0; 0; 0; 0] Al26_spall_reversed];
Be10_muon = [[0; 0; 0; 0; 0] Be10_muon_reversed];
Al26_muon = [[0; 0; 0; 0; 0] Al26_muon_reversed];
t_burial= fliplr(time_vector);

% (3)compute misfits using chi-squared

%calculate slopes
x=Be10_data(:,end);
y=Al26_data(:,end);
z=[0 225 700 943.4 2057.3]';
P=polyfit(x,y,1);
slope=P(1);
P=polyfit(x,z,1);
Be10depth_slope=P(1);
P=polyfit(y,z,1);
Al26depth_slope=P(1);

%calcualte misfit
% isochron_slope_misfit = ((slope-7.99)/(0.4752))^2;
% Be10depth_slope_misfit = ((slope+0.4588)/(0.0456))^2;
% Al26depth_slope_misfit = ((slope+0.065)/(0.0107))^2;
% misfit = isochron_slope_misfit + Be10depth_slope_misfit +
Al26depth_slope_misfit;
Be10_misfit_030 = ((Be10_data(1,end)-1.62E+04)/565)^2; %formula calls
for measured standard error but i used total error (may be wrong)
```

```
Be10_misfit_029 = ((Be10_data(2,end)-1.46E+04)/509)^2;
Be10_misfit_032 = ((Be10_data(3,end)-1.24E+04)/446)^2;
Be10_misfit_upperA3 = ((Be10_data(4,end)-12051)/231)^2;
Be10_misfit_lowerA3 = ((Be10_data(5,end)-10537.05)/215.187)^2;
Be10_misfit = Be10_misfit_030 + Be10_misfit_029 + Be10_misfit_032 +
Be10_misfit_upperA3 + Be10_misfit_lowerA3

Al26_misfit_030 = ((Al26_data(1,end)-6.15E+04)/8729)^2;
Al26_misfit_029 = ((Al26_data(2,end)-4.98E+04)^2/(7635))^2;
Al26_misfit_032 = ((Al26_data(3,end)-4.00E+04)^2/(8100))^2;
Al26_misfit_upperA3 = ((Al26_data(4,end)-33608)^2/(1906))^2;
Al26_misfit_lowerA3 = ((Al26_data(5,end)-20021.98)^2/(2465.35))^2;
Al26_misfit = Al26_misfit_030 + Al26_misfit_029 + Al26_misfit_032 +
Al26_misfit_upperA3 + Al26_misfit_lowerA3

misfit = Be10_misfit + Al26_misfit;
% (4)store data
results(i,1) = time_vector_all(index);
results(i,2) = Be10_inheritance;
results(i,3) = Al26_inheritance;
results(i,4) = e; %erosion rate of sediment
results(i,5) = id/100*2; %ice depth (m)
results(i,6) = misfit;
results(i,7) = effective_fastmuon_atten;

% also store concentration information
results_Be10_concentrations(i,1:5)=Be10_data(:,end)';
results_Al26_concentrations(i,1:5)=Al26_data(:,end)';

fprintf('done\n');
end



% (4)make plots

% caculate slopes
```

```
% caculate isochron slopes
number_runs=length(results(:,1))
%slopes = zeros(number_runs,1)
for j = 1:number_runs
    x=results_Be10_concentrations(j,:);
    y=results_Al26_concentrations(j,:);
    z=[0 225 700 943.4 2057.3];
    P=polyfit(x,y,1);
    slopes(j,1)=P(1);
    P=polyfit(x,z,1);
    Be10depth_slopes(j)=P(1);
    P=polyfit(y,z,1);
    Al26depth_slopes(j)=P(1);
end

% scatter(results(97:end,1),slopes(97:end),[],results(97:end,6))
% plot misfits
% blue = lower misfit
subplot(4,1,1);
scatter(slopes(1:number_runs),results(1:number_runs,6),[],results(1:numb
er_runs,6))
xlabel('decrease in ratio with depth'); ylabel('misfit wrt to all
concs')
subplot(4,1,2);
scatter(Be10depth_slopes(1:number_runs),results(1:number_runs,6),[],resu
lts(1:number_runs,6))
xlabel('decrease in 10Be conc with depth'); ylabel('misfit wrt to all
concs')
subplot(4,1,3);
scatter(Al26depth_slopes(1:number_runs),results(1:number_runs,6),[],resu
lts(1:number_runs,6))
xlabel('decrease in 26Al conc with depth'); ylabel('misfit wrt to all
concs')
subplot(4,1,4); scatter(results(:,7),results(:,6),[],results(:,6))
xlabel('Time since deposition (yrs)');ylabel('misfit (unit?)')

% what do we need to get spread??
```

```
subplot(2,1,1); scatter(results(1:number_runs,1),
Be10depth_slopes(1:number_runs),[],results(1:number_runs,6))
ylabel('decrease in 10Be conc with depth'); xlabel('time since
deposition (yrs)')
subplot(2,1,2); scatter(results(1:number_runs,1),
Al26depth_slopes(1:number_runs),[],results(1:number_runs,6))
ylabel('decrease in 26Al conc with depth'); xlabel('time since
deposition (yrs)')

subplot(2,1,1); scatter(results(1:number_runs,2),
Be10depth_slopes(1:number_runs),[],results(1:number_runs,6))
ylabel('decrease in 10Be conc with depth'); xlabel('10Be inheritance')
subplot(2,1,2); scatter(results(1:number_runs,3),
Al26depth_slopes(1:number_runs),[],results(1:number_runs,6))
ylabel('decrease in 26Al conc with depth'); xlabel('26Al inheritance')

subplot(2,1,1); scatter(results(1:number_runs,2),
results(1:number_runs,1),[],results(1:number_runs,6))
ylabel('time'); xlabel('10Be inheritance')
subplot(2,1,2); scatter(results(1:number_runs,3),
results(1:number_runs,1),[],results(1:number_runs,6))
ylabel('time'); xlabel('26Al inheritance')

% just for misfit scale
scatter(results(:,6), results(:,6),[],results(:,6))

%%%%%%%%%%%%%%%%%%%%%%%%%%%%%%%%%%%%%%%%%%%%%%%%%%%%%%%%%%%%%%%%%%%%%%%%%%%%%%%
%%%
% previous results stored in mat file
% results1 (150 rows, some of which have concs results too)
results1_Be10_concentrations = results_Be10_concentrations
results1_Al26_concentrations = results_Al26_concentrations

results2=results
results2_Be10_concentrations = results_Be10_concentrations
results2_Al26_concentrations = results_Al26_concentrations
```

```
results3=results
results3_Be10_concentrations = results_Be10_concentrations
results3_Al26_concentrations = results_Al26_concentrations

    % time_vector_all = [0:5000:5000000]; % timesteps of 5 ka up to
potential for 5 Ma depositional age
    % Be10_inheritance = datasample(0:1000000,1);
    % Al26_inheritance = datasample(0:1000000,1);
    % id = datasample(5000:25000,1); %ice depth expressed in sediment
depth (2x the density) [cm]
    % e = datasample(0:0.000001:1,1); %cm/yr
    % erate_cycle = [e,0,0,0,0,0,0,0,0,0,0,0,0,0,0,0,0,0,0,0]; % 20 time
steps of 5ka
    % depth_cycle =
[id+3600,3600,3600,3600,3600,3600,3600,3600,3600,3600,3600,3600,3600,360
0,3600,3600,3600,3600,3600,3600]; % 20 time steps of 5ka (3600 is depth
above 030 in cm from highest peak of 84m)
    % index = datasample(4:length(time_vector_all),1); %this is the
number of 5ka timesteps that the model will run for
    % cycles = floor((index-3)/20); % this is the number of glacial
cycles, since there are 20 time steps in each cycle (100 ka/ 5ka),
    % remainder = rem((index-3),20); % this is the remaining number of
5ka time steps that need to be accounted for after accounting for the
100 ka cycles
    % time_vector = time_vector_all(1:index);
    % erate_vector = horzcat([e, e, e],repmat(erate_cycle, 1,
cycles),erate_cycle(1:remainder));
    % depth_above_030_vector = horzcat([3600, 3600, 3600],
repmat(depth_cycle, 1, cycles), depth_cycle(1:remainder));
    % depth_above_030_vector(1)=1200; %simple solution for now
    % depth_above_030_vector(2)=1200;
    % depth_above_030_vector(3)=1200;
```